NANYANG TECHNOLOGICAL UNIVERSITY
SINGAPORE

IN-SITU MONITORING OF SELECTIVE LASER MELTING PROCESS

LU QINGYANG

SCHOOL OF MECHANICAL AND AEROSPACE ENGINEERING

2020

IN-SITU MONITORING OF SELECTIVE LASER MELTING PROCESS

LU QINGYANG

SCHOOL OF MECHANICAL AND AEROSPACE ENGINEERING

A thesis submitted to Nanyang Technological University
in partial fulfilment of the requirements for the degree of
Doctor of Philosophy

2020

Statement of Originality

I hereby certify that the work embodied in this thesis is the result of original research, is free of plagiarised materials, and has not been submitted for a higher degree to any other University or Institution.

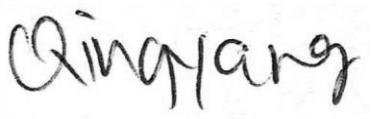

10 January 2020

. . . . . .

Date

. . . . . .

Lu Qingyang

Supervisor Declaration Statement

I have reviewed the content and presentation style of this thesis and declare it is free of plagiarism and of sufficient grammatical clarity to be examined. To the best of my knowledge, the research and writing are those of the candidate except as acknowledged in the Author Attribution Statement. I confirm that the investigations were conducted in accord with the ethics policies and integrity standards of Nanyang Technological University and that the research data are presented honestly and without prejudice.

10 January 2020

. . . . . .

Date

. . . . . .

Assoc Professor Tran Anh Tuan

Authorship Attribution Statement

This thesis contains material from 2 paper(s) published in the following peer-reviewed journal(s) in which I am listed as an author.

Chapters 3 and 4 were published in the following articles:

1. Q.Y. Lu, N.V. Nguyen, A.J.W. Hum, T. Tran, C.H. Wong, Optical in-situ monitoring and correlation of density and mechanical properties of stainless steel parts produced by selective laser melting process based on varied energy density. *Journal of Materials Processing Technology* **271**, 520-531 (2019). DOI: 10.1016/j.jmatprotec.2019.04.026.

The contributions of the co-authors are as follows:

- A/Prof Tran and Dr Wong provided the initial project direction and edited the manuscript drafts.
- I prepared the manuscript drafts. The manuscript was revised by all authors.
- I co-designed the study with A/Prof Tran, Dr Wong, Dr Nguyen and Hum Jun Wee Allen and performed all the laboratory work at the Singapore Centre for 3D Printing and the School of Mechanical and Aerospace Engineering. I also analysed the data.
- I co-conducted the print jobs with Dr Nguyen.
- All image analyses, density tests, micro computed tomography and scanning electron microscopy of specimens were done by me.
- Dr Nguyen assisted in the calibration of the in-situ monitoring system, wire cutting, optical microscopy and tensile testing of specimens.

2. Q.Y. Lu, N.V. Nguyen, A.J.W. Hum, T. Tran, C.H. Wong, Identification and evaluation of defects in selective laser melted 316L stainless steel parts via in-situ monitoring and micro computed tomography. *Additive Manufacturing* (2020). DOI: 10.1016/j.addma.2020.101287.

The contributions of the co-authors are as follows:

- A/Prof Tran and Dr Wong provided the initial project direction and edited the manuscript drafts.
- I prepared the manuscript drafts. The manuscript was revised by all authors.
- I co-designed the study with A/Prof Tran, Dr Wong, Dr Nguyen and Hum Jun Wee Allen and performed all the laboratory work at the Singapore Centre for 3D Printing and the School of Mechanical and Aerospace Engineering. I also analysed the data.
- I co-conducted the print jobs with Dr Nguyen.
- All image analyses, density tests, micro computed tomography and scanning electron microscopy of specimens were done by me.
- Dr Nguyen assisted in the calibration of the in-situ monitoring system and wire cutting of specimens.

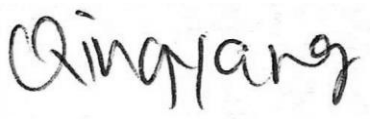

10 January 2020

. . . .

Date Lu Qingyang

ACKNOWLEDGEMENTS

The author would like to express her sincere gratitude to her Ph.D. supervisors, Dr Wong Chee How and Associate Professor Tran Anh Tuan, for their great patience, invaluable academic inspiration, knowledge, guidance and support to her study and research.

The author would also like to express her gratitude to Dr Nguyen Ngoc Vu and Mr Hum Jun Wee Allen for sharing their knowledge and experience in their specific field and contribute to this research.

The author is grateful to Mr Daniel Yeo Yin Ping from the Singapore Centre for 3D Printing, Mr Thomas Lew Sui Leung from Materials Laboratory 2, Mr Joel Lim Choon Wee, Mr Gregory Chua and all the Final Year Project students (Ms Tan Hui Ling, Mr Teo Zhi Jie, Ms Xu Xiao Zhe) for their assistance in the research.

The author would also like to express her gratitude to the University for presenting her the NTU Research Scholarship to pursue her Ph.D. studies. The author the Ministry of Education (MOE), Singapore, for the financial support.

Lastly, the author would like to thank her family and friends for their unconditional love and support throughout the process of study and research.

TABLE OF CONTENTS

ABSTRACT

Additive manufacturing (AM) has progressively transited from being regarded as a tool for rapid prototyping to the efficient production of individually customised, and highly complex functional parts. AM of metals, in particular, is an emerging field of interest with exponential growth in metallic parts manufactured for end-use applications via laser melting processes. Powder bed fusion (PBF) and directed energy deposition are the main processes for metal printing. One of the most promising PBF processes is selective laser melting (SLM), which is capable of fabricating metal components near full density with little post-processing.

While SLM allow design freedoms unequalled by conventional manufacturing methods, production techniques require strict control of processing parameters and conditions to build a metallic part of high quality. The printing process is vulnerable to defects generation and is inevitable. In-situ measurements can be utilised to optimise part-to-part reproducibility. The implementation of in-situ monitoring systems (IMSs) in AM printers render both time and cost savings as the process can be stopped if a failure is detected.

A myriad of in-situ monitoring studies has been carried out focusing on identification of defects and irregularities during the printing process. Despite the advancement of IMSs in defects detection, the impact of these defects on the printed part's structural integrity remains unknown. The effects of these defects identified during printing on the density and mechanical properties of the printed part have yet to be adequately investigated by researchers and industrial experts.

This thesis focuses on the development of a self-developed in-situ monitoring system (IMS) and the establishment of relationships between features (i.e., process signatures)

captured in images during fabrication and the mechanical properties of the printed parts. The establishment of a correlation between features captured in images during printing and the actual defects present in the printed parts has also been explored.

The self-developed IMS proposed in this research has several advantages over existing commercial IMSs. It is portable as it is an independent system and does not require any modification of the printer's existing optical components. This makes the IMS flexible for installation on any SLM printers. The self-developed IMS captures high-resolution optical and thermal images, allowing for easy identification and evaluation of features. Coupled with the fast and robust algorithm, real-time image-based measurements of features can be correlated with mechanical properties of the printed part. Simultaneous monitoring of the powder bed is possible through the use of optical and infrared sensors. It enables different types of defects to be detected during the printing process.

The design of the proposed IMS allowed monitoring of the powder bed via optical and infrared cameras. Ten sets of 316L stainless steel specimens were fabricated by the SLM process. Each set of specimens consisted of a cylinder and a sub-size tensile coupon. The specimens were printed with varying energy densities. Features captured in optical images of the powder bed were examined. They are represented by pixels that are either brighter or darker than that of the metal powders. A relationship has been established between features captured in optical images during fabrication and the mechanical properties of the printed parts. Cylinders with percentage area of features greater than 2% exhibit lower densities, ultimate and yield strengths, and vice versa. These cylinders have densities lower than 7.82 gcm^{-3}, ultimate strength lesser than 565 MPa and yield strength lesser than 462 MPa. The implementation of the IMS based on optical imaging enables

end users to distinguish between specimens with relatively higher density and better mechanical properties and specimens with relatively lower density and weaker mechanical properties.

A correlation has been established between features captured in optical images during printing and the actual defects present in the printed part. Micro computed tomography (CT) was used to validate the correlation of features in two-dimensional optical images to actual three-dimensional defects in the printed samples through reconstruction of the CT images, and more importantly, to justify the viability of using optical imaging as a solution for evaluating defects in printed parts. A positive correlation exists between the percentage area of features in each resultant optical image, $OP_{features}$, and the percentage area of defects in each resultant CT image, $CT_{defects}$, for the ten cylinders. Their Pearson correlation coefficients range between 0.30 and 0.78. Similarities in trends between $OP_{features}$ and $CT_{defects}$ were established across the layers of the cylinders, where a higher $OP_{features}$ translates to higher $CT_{defects}$. This enables end users to directly evaluate the area of defects present in parts based on real-time analysis of optical images, eliminating the need for long hours of defects detection in printed parts by CT.

A relationship between regions with high normalised temperature gradients captured in thermal images and the densities of selectively laser melted parts has been demonstrated. Cylinders with more pixels of high normalised temperature gradients across their cross sections exhibit lower densities. This finding potentially aids in the fabrication of parts with improved density via thermal imaging.

Based on the established relationships, the proposed IMS has a strong potential in aiding the production of parts with better mechanical properties. Printing parameters can be adjusted in-situ to improve the quality of the printed part if the number of features or thermal signatures present in optical or thermal images correlate to weak mechanical properties, rendering both time and cost savings. The results also illustrated the capability of the system in differentiating the extent of defects present in specimens fabricated with varying energy densities. The findings presented in this thesis also lay the foundation for the development of closed-loop IMSs associated with the SLM process.

LIST OF FIGURES

LIST OF TABLES

CHAPTER 1: INTRODUCTION

1.1 Background

Additive manufacturing (AM) is the process of joining materials to fabricate objects from three-dimensional (3D) computer aided design data, usually layer upon layer, as opposed to subtractive manufacturing methodologies [1]. It produces the final shape of the part by the addition of materials [2]. AM is divided into seven categories of technologies. They are, namely, material extrusion, powder bed fusion (PBF), vat photopolymerization, material jetting, binder jetting, sheet lamination and directed energy deposition [3].

AM has progressively transited from being regarded as a tool for rapid prototyping to the efficient production of individually customised, and highly complex functional parts. Biologically inspired scaffolding structures with high strength-to-weight ratio can be created through AM processes, such as stereolithography. AM technology is also used to fabricate tissue constructs for the rectification or replacement of damaged human tissues and organs in the biomedical field. AM presents a broad range of applications [4]. Titanium cabin bracket connectors produced by AM are used in Airbus A350 XWB. Compared to milling and machining of aluminium alloy, the connectors are now made of titanium powder material, leading to more than 30% weight reduction [5]. Material extrusion technology is applied for the printing of tailored breast prostheses [6].

AM of metals, in particular, is an emerging field of interest with exponential growth in metallic parts manufactured for end-use applications via laser melting processes. PBF processes, such as selective laser melting (SLM), are commonly employed for the AM of metallic components.

However, the extensive adoption of AM technologies is hindered by challenges including the lack of certification standards, geometric inaccuracies and presence of defects in finished parts [7, 8]. There are also major concerns regarding the repeatability and reliability of the technology from part-to-part and machine-to-machine [9]. Non-destructive testing (NDT) techniques offer solutions to some of the challenges mentioned above through pre-, in-situ and post-process control. They have primarily been used for inspection and assurance of product's reliability without destructing and damaging it. Continual advancements in NDT instruments are fuelled by the growing need in establishing control of manufacturing processes and maintaining the reliability of the product. These techniques also play an important role in establishing an in-situ diagnostic system for monitoring of defects generated in additively manufactured parts. Furthermore, in-situ measurements can be utilised to optimise part-to-part reproducibility.

The implementation of in-situ monitoring systems to AM printers render both time and cost savings as the process can be stopped if a failure is detected. Partially built parts that do not meet the standards can be stopped automatically before further parts are manufactured. The mechanical properties and structural integrity of the additively manufactured parts will be consistent across different print jobs and machines. Integration of in-situ monitoring systems to AM processes will potentially alleviate issues concerning the volume production of 3D printed parts.

1.2 Motivation

The future for AM of metals is promising as major engineering materials including steel, titanium and aluminium can be fabricated to fully dense parts with remarkable properties

via PBF processes. AM of metals has gradually gained acceptance among industries, evident from the successful printing of fuel nozzles for General Electric's leading edge aviation propulsion engine [10, 11]. Nonetheless, a more in-depth understanding of the PBF process and the resulting material properties is required for the mass production of structurally sound and reliable metallic parts.

While PBF processes allow design freedoms unequalled by conventional manufacturing methods, production techniques require strict control of processing parameters and conditions to build a metallic part of high quality. The printing process is vulnerable to defects generation and is inevitable. Computed tomography (CT), being one of the few NDT techniques that can detect both internal and external defects of additively manufactured parts, is costly and time consuming [12]. The implementation of CT to an in-situ monitoring system (IMS) is further complicated by safety issues. A high voltage, which is necessary for generating x-rays, can be hazardous and dense shielding metals are required to minimize the operator's exposure to x-rays [13]. Hence, there is a crucial need for the development of robust in-situ monitoring systems (IMSs) in the AM industry for quality assessment of parts.

Visual inspection and thermography are two widely researched NDT techniques for the development of IMSs to monitor defects created during PBF processes as parts are built layer-by-layer. A myriad of in-situ monitoring studies has been carried out focusing on identification of defects and irregularities during the printing process. Jacobsmühlen et al. [14] worked on acquiring high-resolution images of deposited powder layers for the SLM process. Elevated regions which were not covered by the metal powders were detectable from the images of the powder layers. These regions were then characterised by image

processing techniques. H. Krauss, C. Eschey, and M. Zaeh [15] demonstrated the possibility of utilizing an infrared camera to track the quality of powders deposited during the SLM process. Variations in powder layer thickness can be identified immediately after recoating based on the theory that a thinner layer of powder will heat up more rapidly than that of a thicker layer.

Despite the advancement of IMSs in defects detection, the impact of these defects on the printed part's structural integrity remains unknown. The effects of these defects identified during printing on the density and mechanical properties of the printed part have yet to be adequately investigated by researchers and industrial experts. Research in this area can potentially aid in the production of parts with better mechanical properties while reducing the reliance for post-process control. Printing parameters can be adjusted in-situ to improve the quality of the fabricated part if the extent of defects present in the captured data correlate to weak mechanical properties, rendering both time and cost savings. Moreover, limited efforts have been made to establish a relationship between the defects detected during printing and the actual defects present in the printed part. This is critically pertinent as it opens prospects for real-time detection and quantification of defects. The extensiveness of defects present in the part is updated layer-by-layer, allowing users to decide on the continuation of a job during printing. Mass production is attainable with improved consistency in the quality of the additively manufactured parts.

1.3 Research objectives

A self-developed IMS proposed in this research has several advantages over existing commercial IMSs. It is portable as it is an independent system and does not require any modification of the printer's existing optical components. This makes the IMS flexible

for installation on any SLM printers. Commercial IMSs are designed to be integrated with their own printers and are not applicable to printers of other brands. Various metrics are also used by different manufacturers to define a printed part of high quality. Some systems utilise concealed figures as indicators which only provide information on the acceptance or rejection of a printed part. This poses an issue as efforts are made to achieve a common understanding in the definition of a high-quality part across the AM community where a wide range of printers are used.

The self-developed IMS captures high-resolution optical and thermal images, allowing for easy identification and evaluation of features. Coupled with the fast and robust algorithm, real-time image-based measurements of features can be correlated with mechanical properties of the printed part. This information acquired helps to build the database of mechanical tests results associated with various process parameters and images. The resolution of commercial IMSs is not publicly available and the correlation between process signatures captured in-situ and actual quality of the printed part has not been adequately investigated.

Simultaneous monitoring of the powder bed is possible through the use of optical and infrared sensors. It enables different types of defects to be detected during the printing process. Some examples include the detection of non-uniformly recoated powder bed, overheated regions, delamination and elevated regions of the printed part. A comprehensive approach has been taken for monitoring a range of process signatures during SLM. Such a feature, however, is absent in commercial IMSs. The sensor fusion methodology (i.e., using optical and infrared sensors to monitor the powder bed during

printing) also ensured that the data analysed corresponded to the same physical structure, which has yet been widely explored by machine manufacturers [16].

The aims of this research are to (1) develop an IMS to capture optical and thermal images of the SLM process, (2) establish a relationship between features (i.e., process signatures) captured in images during fabrication and the mechanical properties of the printed parts and (3) establish a correlation between features captured in images during printing and the actual defects present in the printed parts. The SLM process is chosen as it is extensively used in the domain of metal printing. Metals, among the many materials used in AM is gaining its increasing share of the pie, especially in the automotive and aerospace sectors.

1.4 Scopes

The scopes are summarised as follows:

1. Design the set-up for mounting of digital single lens reflex (DSLR) and infrared cameras where their field of views are at the SLM 500 machine's powder bed.
2. Install light emitting diode (LED) light strips onto the chamber walls to ensure optical images are captured with adequate contrast.
3. Evaluate the performances of the DSLR and infrared cameras and correct any distortions present in the captured images.
4. Analyse and evaluate features in optical and thermal images for correlation studies.
5. Perform mechanical testing of printed specimens to establish a relationship between features captured in optical and infrared images during fabrication and the mechanical performance of printed parts.

6. Perform micro CT to identify defects in printed parts and establish a correlation between features captured in optical images during fabrication and the actual defects present.

1.5 Organisation of thesis

Chapter 1 introduces the background and motivation of this research. The objectives and scopes of this research are also included in this chapter.

Chapter 2 focuses on the state-of-the art of IMSs and major shortfalls associated with current IMSs. The AM of metals and its significance and challenges involved in the implementation of AM technologies are discussed.

Chapter 3 highlights the design of the IMS which encompasses the optical and infrared cameras. The procedures taken to achieve uniform illumination of the powder bed and examine the emissivity of 316L stainless steel specimens with different surface textures are outlined. The steps taken to evaluate the modulation transfer functions of the optical and infrared cameras and correct the distortions present in thermal images are explained. The design of specimens, materials used for the experiments and mechanical tests performed are discussed.

Chapter 4 presents the established correlation between features captured in optical images during fabrication and the mechanical properties of printed parts. It illustrates the established correlation between features captured in optical images during fabrication and the actual defects identified by micro CT. Defects and process signatures identifiable by the IMS during SLM are summarised. The feasibility of using optical imaging as a solution to evaluate defects in selectively laser melted parts is stressed in this chapter.

Chapter 5 analyses the relationship between regions with high temperature gradients captured in thermal images and the densities of selectively laser melted parts. The findings in this chapter potentially aids in the fabrication of parts with improved density via thermal imaging.

Chapter 6 summarises the significant findings in this research and proposes recommendations to improve on the self-developed IMS for future work.

1.6 Summary

AM of metals is an emerging field of interest with exponential growth in metallic parts manufactured for end-use applications via laser melting processes. PBF processes are commonly employed for the AM of metallic components. However, the extensive adoption of AM technologies is hindered by challenges including the lack of certification standards, geometric inaccuracies and presence of defects in finished parts. The repeatability and reliability of the technology from part-to-part and machine-to-machine are also cause for concern. Integration of IMSs to AM processes will potentially alleviate issues related to these challenges. Several in-situ monitoring studies have been carried out focusing on identification of defects and irregularities during the printing process. Despite the advancement of IMSs in defects detection, the impact of these defects on the printed part's structural integrity remains unknown.

A self-developed IMS proposed in this research has several advantages over existing commercial IMSs. It is portable as it is an independent system and does not require any modification of the printer's optical components. Additionally, the self-developed IMS captures high-resolution optical and thermal images, allowing for easy identification and evaluation of features. The use of optical and infrared sensors enables different types of

defects to be detected during the printing process. To this end, the aims of this research are to (1) develop an IMS to capture optical and thermal images of the SLM process, (2) establish a relationship between features captured in images during fabrication and the mechanical properties of the printed parts and (3) establish a correlation between features captured in optical images during printing and the actual defects present in the printed parts.

CHAPTER 2: LITERATURE REVIEW

2.1 Overview of additive manufacturing technologies

The seven classifications of additive manufacturing (AM) technologies are discussed. Material extrusion involves the dispensing of the material through a nozzle where it will be heated and deposited in a layer-by-layer fashion to produce an object [3]. The process is illustrated in Figure 2.1. The materials used in material extrusion are usually thermoplastics such as acrylonitrile butadiene styrene and nylon in a spool of filament [17]. The resolution of the printed part is highly dependent on the geometry of the nozzle and the layer thickness. The layer thickness of material extrusion processes typically ranges from 0.178 to 0.356 mm [18]. Fused deposition modelling and fused filament fabrication are some examples of the material extrusion technology.

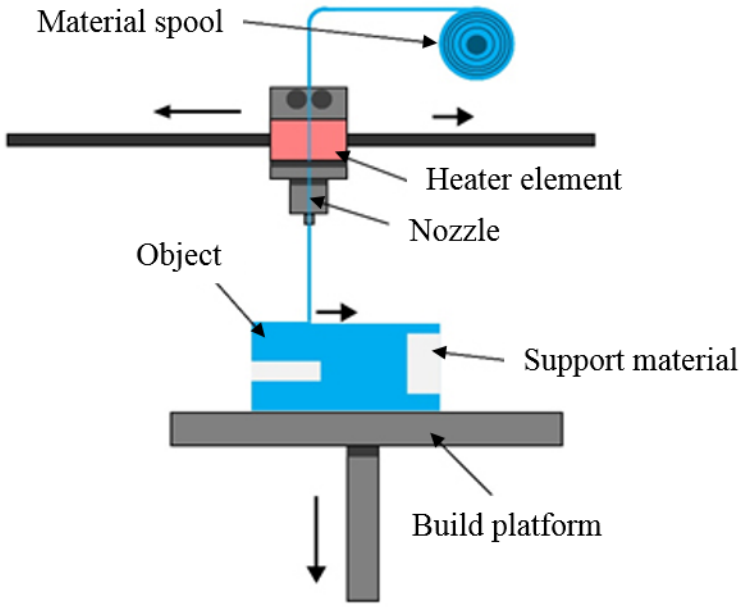

Figure 2.1 Schematic representation of material extrusion technology [18].

The powder bed fusion (PBF) technology employs the use of thermal energy to selectively fuse regions of a powder bed [3]. The process is shown in Figure 2.2. The thermal source can be either a laser or an electron beam. Powder is sintered or melted in accordance to the CAD data. The build platform lowers by the layer thickness after one layer is scanned and the roller spreads a new layer of powder. The process repeats until the part is fully printed. A hopper is present to provide continuous supply of fresh materials needed for printing. The common materials used in PBF include nylon, 316L stainless steel and titanium alloys [19]. The resolution of the printed part is dependent on the powder size. Direct metal laser sintering (DMLS), electron beam melting (EBM), selective laser melting (SLM) and selective laser sintering are some examples of the powder bed fusion technology [20].

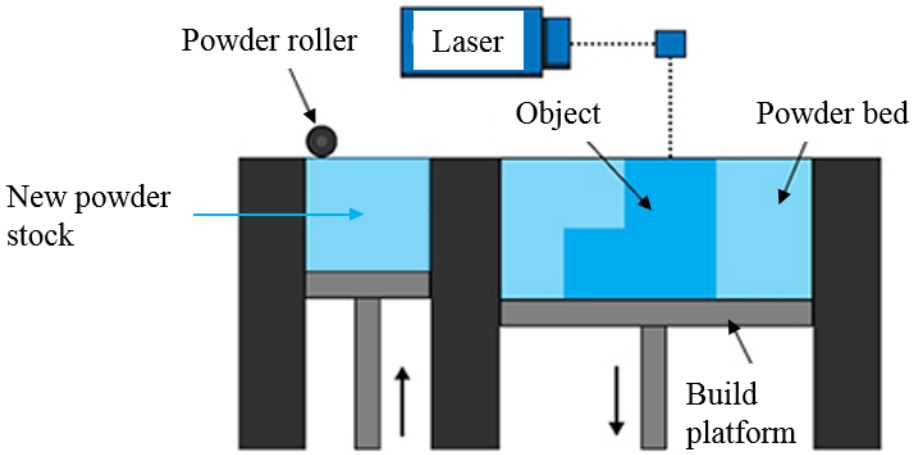

Figure 2.2 Schematic representation of PBF technology [19].

Liquid photopolymer in a vat is selectively cured by light activated polymerization during vat photopolymerization. Ultraviolet (UV) light or laser is used to cure the vat of liquid photopolymer resin where required as seen in Figure 2.3. The build platform lowers from

the top of the resin vat by the layer thickness after each new layer is cured [21, 22]. Upon completion of the print job, liquid photopolymer is drained from the vat and the part is removed. Polymers are used as materials for vat photopolymerization. Parts produced have high level of accuracy and a good surface finish as compared with other AM technologies. Stereolithography and digital light processing are grouped under vat photopolymerization technology [23].

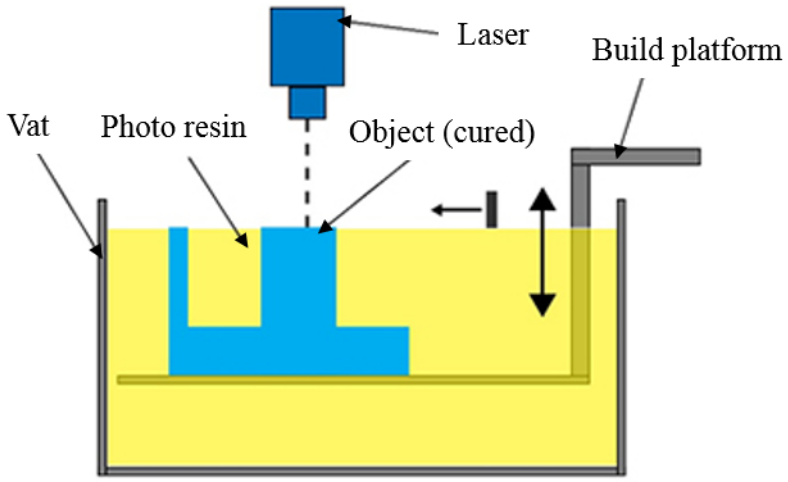

Figure 2.3 Schematic representation of vat photopolymerization technology [22].

Droplets of build material and support material are selectively deposited in material jetting whose principle of operation is similar to a 2D ink jet printer [3, 24]. A schematic presentation of the material jetting technology is depicted in Figure 2.4. A nozzle, which moves horizontally across the build platform, deposits the build and support materials on the substrate. The materials are cured using UV light and the part is built layer-by-layer. The support material is dissolvable, allowing it to be removed during the post processing step. Polymers and waxes are commonly used materials due to their viscous nature and

their capability to form droplets [25]. Drop-on-demand, polyjet and nanoparticle jetting printers belong to material jetting technology [26].

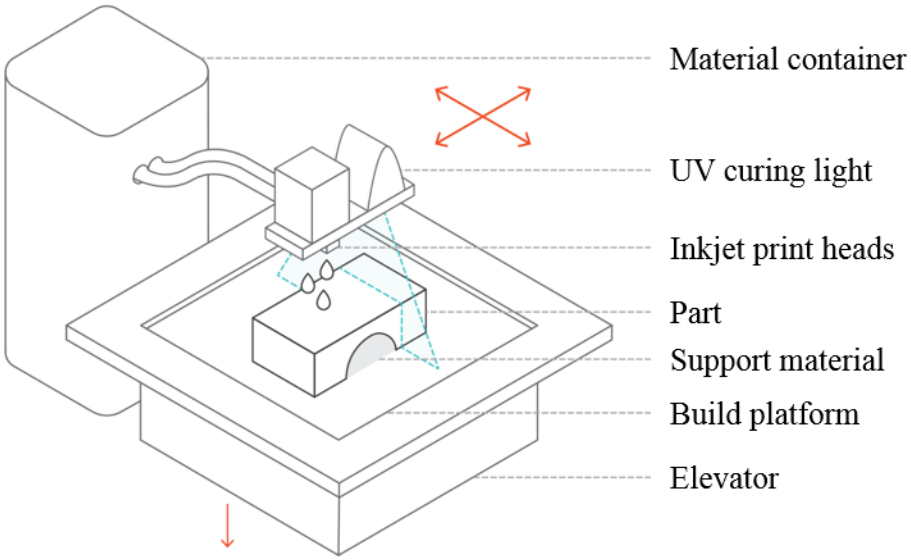

Figure 2.4 Schematic representation of material jetting technology [24].

A liquid bonding agent is selectively deposited to join powder materials in binder jetting via an inkjet printhead [3]. A schematic presentation of the binder jetting technology is depicted in Figure 2.5. Binder droplets form spherical agglomerates of the binder liquid and powder particles. The droplets also ensure bonding to the previous printed layer. After the printing of each layer, the powder bed lowers and the roller spreads a new layer of powder onto the build platform, until printing is completed [27]. Metals, polymers and ceramics powders are the materials that can be used in binder jetting [28]. Three types of binders are commonly used in binder jetting: water-based binders, phosphoric acid-based and citric acid-based binders and polymer solution binders [29].

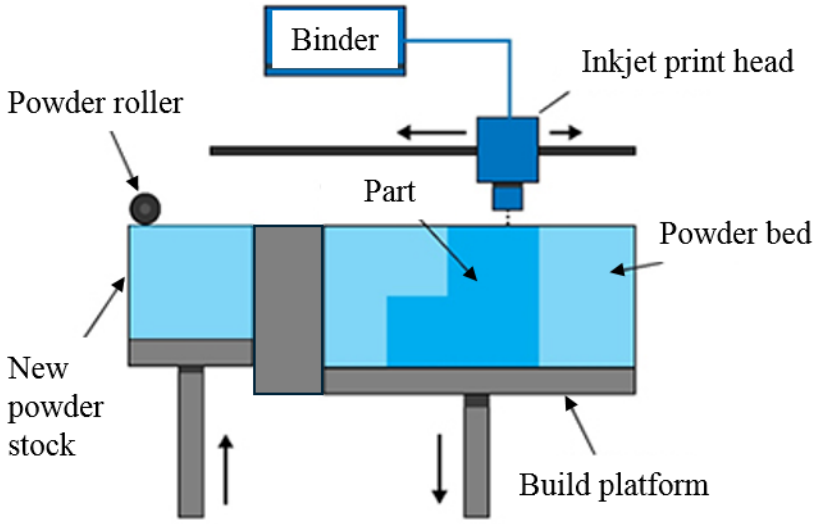

Figure 2.5 Schematic representation of binder jetting technology [28].

Sheet lamination is an AM technology in which sheets of material are bonded to form an object [3]. It includes laminated object manufacturing and ultrasonic consolidation. The former produces parts through layer-by-layer lamination of paper sheets, cut using a carbon dioxide laser, with each sheet constituting to one cross-sectional layer of the CAD model of the part. The printing process is highlighted in Figure 2.6. The material is bonded to the previous layer using an adhesive. Cross hatches are drawn on the remaining surface to facilitate the removal of waste materials. The used material is collected as a spool. The latter operates with a similar layer-by-layer approach but uses metal sheets as material and ultrasonic welding instead of adhesive for bonding of the material [30].

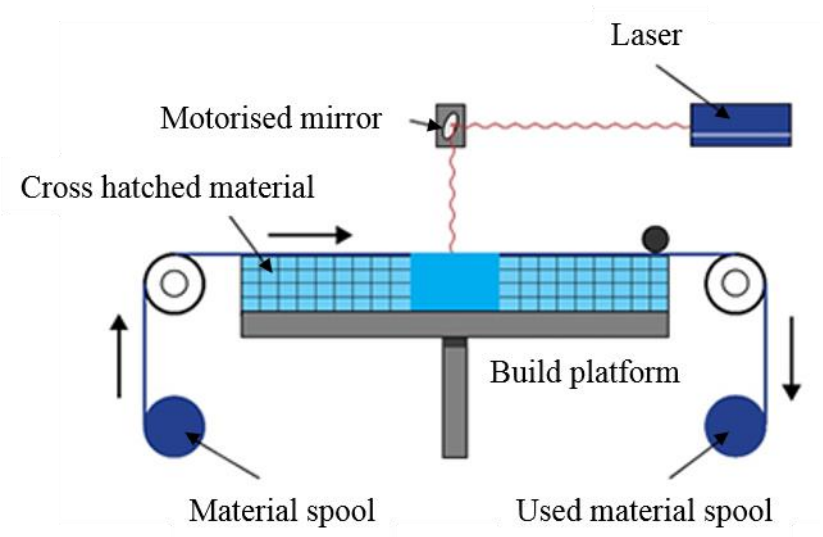

Figure 2.6 Schematic representation of sheet lamination technology [30].

Directed energy deposition (DED) technology utilises focused thermal energy to melt the substrate, simultaneously melting the material that is being deposited into the substrate's melt pool. The thermal source can be either a laser or an electron beam. This technology is primarily used for metal powders although parts can also be fabricated by melting polymers, ceramics and metal matrix composites [31]. Materials can be in the form of powders or wires. Common processes include laser engineered net shaping and electron beam AM.

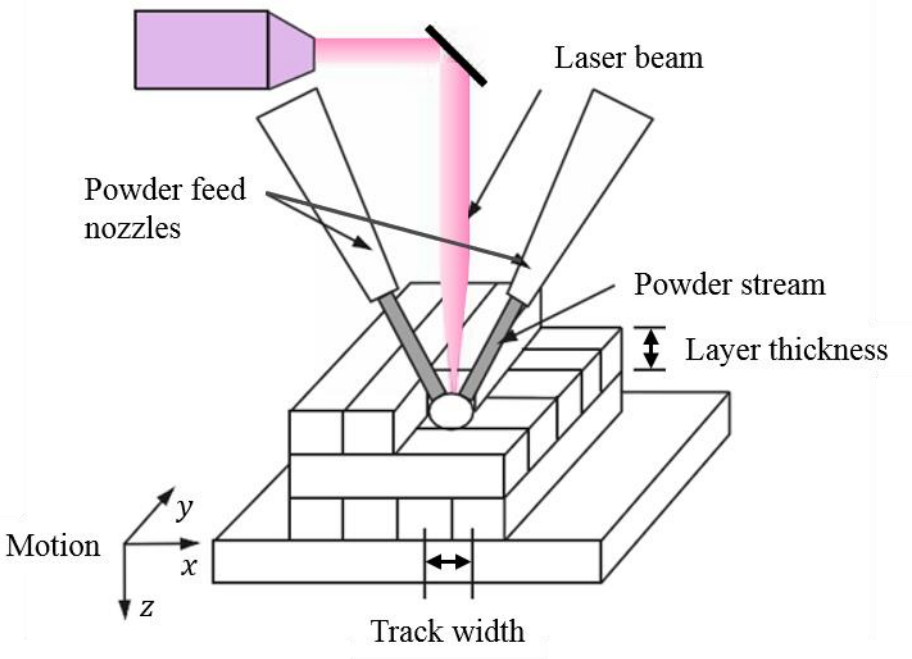

Figure 2.7 Schematic representation of DED technology [31].

AM has been widely adopted in the aerospace industry throughout all processes and functions; from design conceptualisation to near-end-of-life repairs [5, 32]. High-performance titanium alloys, in particular, Ti-6Al-4V, is favoured for the manufacturing of advanced aerospace structures such as engine parts [33, 34]. A significant portion of the AM equipment sales is attributed to the demand from business machines and motor vehicles industries, where both sectors have an indispensable need for metals [22]. Being a relatively new type of material introduced to the realm of AM, there is a growing trend for the sales of metals, driving the need for research of metallic materials [35]. Among the seven classifications of technologies for AM, PBF and DED are the main processes for metal printing [36]. One of the most promising PBF processes is SLM, which is highly utilised across most industries mentioned above [37]. SLM is capable of fabricating metal components near full density with little post-processing. Some

materials, which will be discussed in the next section, when processed via SLM, attain mechanical properties that are superior than their wrought counterparts. However, the quality of as-printed selectively laser melted parts is usually inconsistent [38]. Therefore, SLM was chosen as the process for development in this thesis.

2.1.1 Selective laser melting

SLM is one of the processes under PBF technology. It involves depositing a thin layer of powder on the build platform by a powder recoating system, as seen in Figure 2.8. A high intensity laser is used as an energy source to selectively melt and fuse regions of powder in a layer-by-layer fashion, in accordance to the CAD data [39]. The scanner system focuses the laser as it reaches the powder bed. Upon completion, the build platform is lowered and the recoater blade deposits the next layer of powder. The laser then scans a new layer. The sequence of depositing and scanning is repeated until the part is fully built [40].

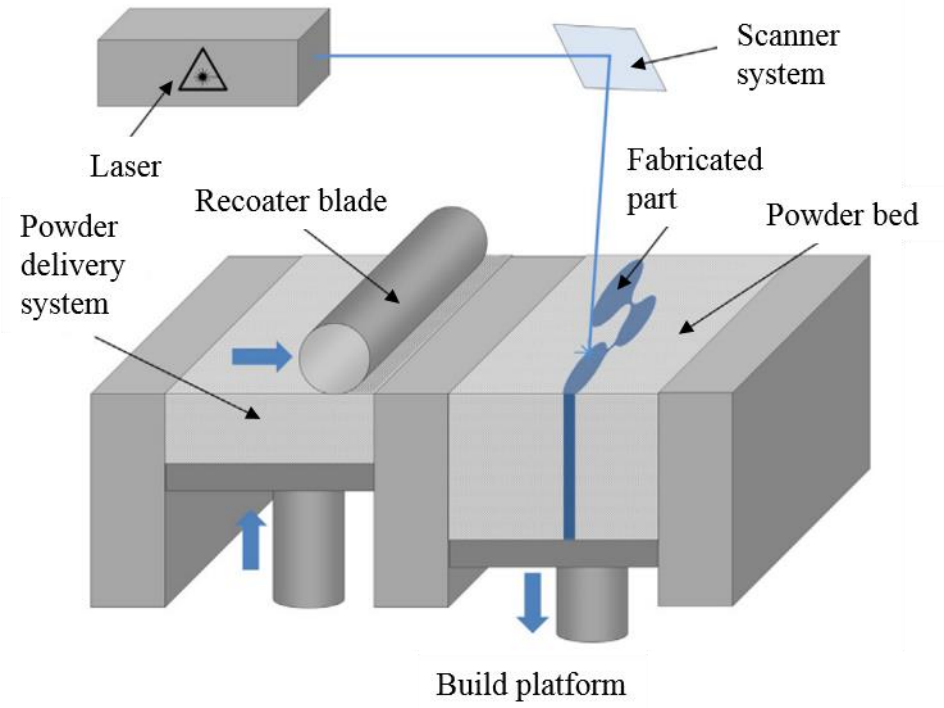

Figure 2.8 Schematic of the SLM process [36].

SLM is a promising technology for the mass production of metallic components as it produces near net-shape parts. Moreover, selectively laser melted parts can achieve near full density (up to 99.9% relative density) with optimised printing parameters [41]. Choi et al. [42] fabricated stainless steel specimens with 99.2% relative density with optimised parameters, i.e., laser power, scanning speed, hatch spacing and layer thickness. Engineering alloys, such as titanium, Inconel, stainless steel and cobalt chromium, are the common materials used for SLM. As the metal powders are rapidly melted and solidified, it results in some mechanical properties surpassing their cast or wrought counterparts [4]. Trosch et al. [43] reported superior tensile properties of selectively laser melted Inconel 718 parts when compared to conventionally produced specimens at room temperature and 450°C.

2.2 Challenges associated with additive manufacturing

The challenges hindering large-scale implementation of AM processes revolve mainly around (1) the lack of standards for certification of additively manufactured parts and (2) the repeatability and reliability of the technology from part-to-part and machine-to-machine.

2.2.1 Standards and certifications of additively manufactured parts

The constituents of each AM technology must be standardised and certified in ensuring the reproducibility of fabricated components. The constituents for SLM, for instance, will include metal powders and printing parameters. Without standardization procedures, the production of first few high-quality parts are problematic. Standards are particularly crucial for the emerging AM industry as they form the basis for common understanding between researchers and industrial experts and are utilised as tools to facilitate the manufacturing process. Yet, there has been a lack of standards pertaining to AM technologies. This is due to the absence of a public database which would otherwise enable access to materials properties and their design allowables for specific processes [9]. The acquisition of materials data is also challenged by the number of machine manufacturers and the evolution of control software. Collaborations between researchers and industrial experts are necessary for the establishment of materials databases.

There also exists an urgent need to establish certification schemes for AM processes. There is a lack of certification guidelines for additively manufactured parts on the market. Certification schemes must be put in place to ensure the safety and reliability of these parts. This is especially important with the substantial increase in the number of industries adopting AM technologies for their manufacturing processes. The

establishment of certification schemes will instil confidence in manufacturers and end users that parts produced by AM are robust and of high quality.

2.2.2 Repeatability and reproducibility of additive manufacturing technologies

The consistency of a part's quality has been a major concern for AM processes, questioning the fidelity and reliability of the technology from part-to-part and across different machines [5]. Production techniques require strict control of processing parameters and conditions to build a part of high quality. There are numerous factors affecting the overall quality of the printed part. Using PBF as an example, laser beam optics, spot size, wavelength, power and raster speed all have a direct impact on the energy transfer to metal powders [44]. Laser absorption, which is affected by variations in powder alloy composition, surface chemistry, morphology, particle size distribution, powder layer thickness and packing density, influences the material properties and quality of the build [45]. Printing parameters including hatch spacing and thickness must be optimised to reduce lack of fusion defects and porosity during solidification. The design of support structures, build orientation and placement of parts relative to one other can vary the local heat accumulation, resulting in the generation of residual stresses and thermal distortion.

As many printing parameters are involved in AM processes, defects are inevitably generated when any of these parameters are inappropriately selected. Thus, there is a crucial need for in-situ monitoring and control technologies in the AM industry for quality assessment of parts. In-situ monitoring methods are essential for the detection of discontinuities and possible failures of a part while maintaining its structural integrity. This also creates the possibility of arresting further build-up of defective parts while

printing continues for the remaining parts, rendering time and cost savings. However, the absence of real-time sensors for process control and monitoring of AM processes has been ascertained as a main challenge [9]. The development of in-situ monitoring systems (IMSs), which can aid in the provision of materials data, is inadequate. Furthermore, limited efforts have been made to employ non-destructive testing (NDT) methods for in-situ monitoring and performance indication of the SLM process.

2.3 State-of-the-art of in-situ monitoring systems

IMSs for AM processes drive the possibility for identification of defects during printing. This renders both time and cost savings as the process can be stopped if a failure is detected. Semi-built parts that do not meet the standards can be stopped automatically before further parts are manufactured. As the systems monitor the actual printing process, the results are representative of the printed part and no extrapolation or scaling is needed as in the case for simulations.

Amongst the various NDT techniques, visual inspection with optical aids and thermography are the main methods integrated with current IMSs. Visual inspection can be performed quickly, is simple and applies to most specimens [46, 47]. The principle of visual inspection is based on the illumination of the specimen with light, which is usually in the visible light region of the electromagnetic spectrum. The specimen is then examined with the eye or light sensitive optical aids. Although the equipment required for visual inspection is relatively simple, ample illumination is necessary. The amount of light falling upon the specimen can be quantified with a light meter. Mechanical and or optical aids may be required for visual inspection. Mechanical aids include apparatus such as callipers and micrometres. Optical aids are used when direct viewing of the test

specimen is not possible. The equipment ranges from simple mirrors to intricate devices, such as microscopes and borescopes [48].

Thermography relies on the infrared band of the electromagnetic radiation spectrum. This infrared band is further categorised into four smaller bands. They are near-infrared, short-wavelength infrared, medium-wavelength infrared and long-wavelength infrared with wavelengths of 0.8 to 1.7 μm, 1 to 2.5 μm, 2 to 5 μm and 8 to 14 μm respectively [49]. The intensity of the emitted spectrum depends on the absolute temperature of the body. Three factors that affect the thermal measurement include emissivity, surrounding and atmosphere. Calibration of emissivity is the most important step for quantitative measurement of temperature using infrared radiation. It can be interpreted as the ratio of the radiance of a body at a particular temperature to the corresponding radiance of a black body at the same temperature [12]. The emissivity of a black body is 1.0 but objects rarely have emissivity of 1.0. High-emissivity materials emit more infrared radiation than materials with low-emissivity at the same temperature [49].

Thermography measures the temperature field of the surface of the studied body [50]. The principle behind thermography is based on the difference in thermal behaviour between the internal structure of the examined object and its flaws. Discontinuities affect the heat flow and will be heated or cooled at rates different from the bulk of the material. Hence, temperature differences exist on the surface of the object, resulting in variations of the emitted radiation captured by the infrared camera [15].

Apart from visual inspection and thermography, there has been an increase in the application of acoustic emission testing and laser ultrasonic testing for in-situ monitoring of AM processes [51]. Acoustic emission testing is based on the principle of sound waves

transmission through the test part. This technique has the potential to be employed for monitoring of additively manufactured parts. Variations in microstructure, surface defects, surface roughness and geometric divergence will influence the signature of sound travelling through the part. The difficulty associated with this method lies in the recognition of the source causing the change in sound signature. Hence, this technique is only practical when the detected sound signature caused by an impact can be compared to a reference signature.

Laser ultrasonic testing, being a non-contact measurement technique, is a potential candidate for in-situ process monitoring of metallic AM processes [16, 52]. A laser pulse is focused at the material's surface and an ultrasonic pulse is generated to disseminate into the material. Rayleigh wave, which is a surface wave, is the dominant wave mode produced. Longitudinal and shear waves are also generated. Diffraction and scattering of the Rayleigh wave occurs in the presence of subsurface defects and when returned to a receiver, it comprises of shear waves and mode converted compressional waves. The returned signal, which is received by the detection laser, is processed for further investigation on the details of the defects [53]. This technique allows the inspection of inaccessible areas and on curved surfaces and can be applied at elevated temperatures. The application of this NDT technique allows the examination of defect information during each build layer, which accentuates the processing errors and enables real-time alteration of processing parameters. Laser ultrasonic testing presents opportunities for in-situ monitoring of AM processes with improved part quality.

2.3.1 Existing in-situ monitoring systems

A myriad of in-situ monitoring studies has been carried out focusing on identification of defects during the printing process. Jacobsmühlen et al. [14] worked on acquiring high-resolution images for each layer of deposited powder during the SLM process. Figure 2.9 illustrate the scanned and recoated layer captured during printing respectively. The images were processed for the characterization of defects. Elevated regions, which had minimal metal powders recoated on them, appeared as light structures and were detectable from the images of the powder layer.

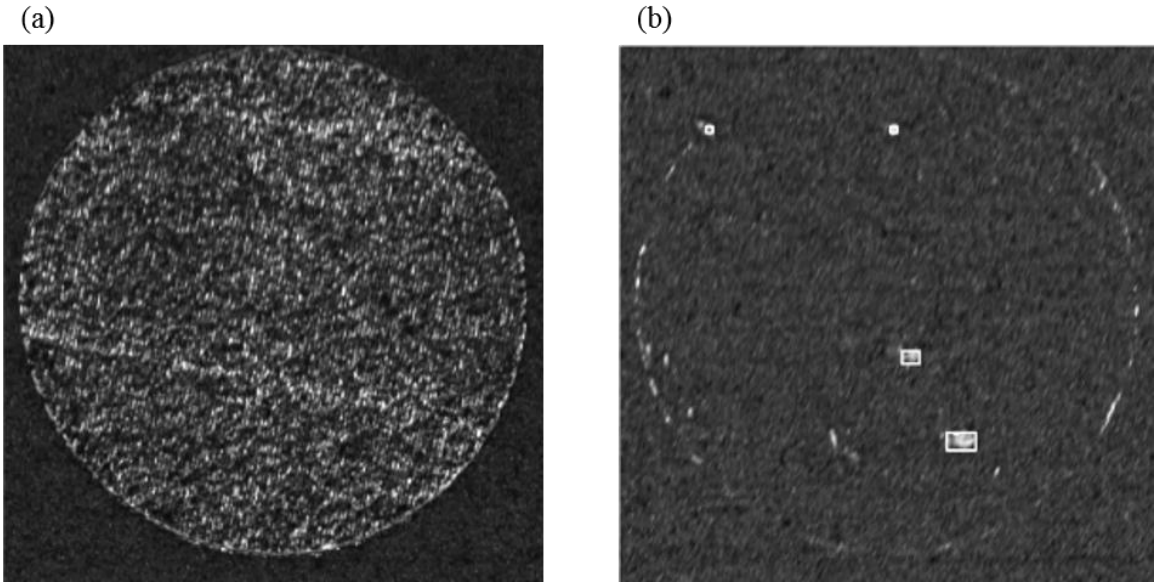

Figure 2.9 Image captured (a) after scanning and (b) after recoating illustrating the presence of elevated regions [14].

Foster et al. [44] developed a high-resolution powder bed monitoring system using a consumer grade digital single lens reflex (DSLR) camera to compare the acquired images of parts with actual characteristic defects generated during printing. They designed a series of cylinders with intentional variation of laser power and hatch spacing to create

lack-of-fusion defects. Non-uniform linear perturbations in the powder layer due to dragged agglomerated powder were observable in Figure 2.10 (a). A cantilevered part, shown in Figure 2.10 (b), was fabricated with inadequate support structures. Deformation of the part resulted in a portion of it elevating from the surface of the powder bed. Subsequently, the recoater blade was affected, causing non-uniform deposition of powders.

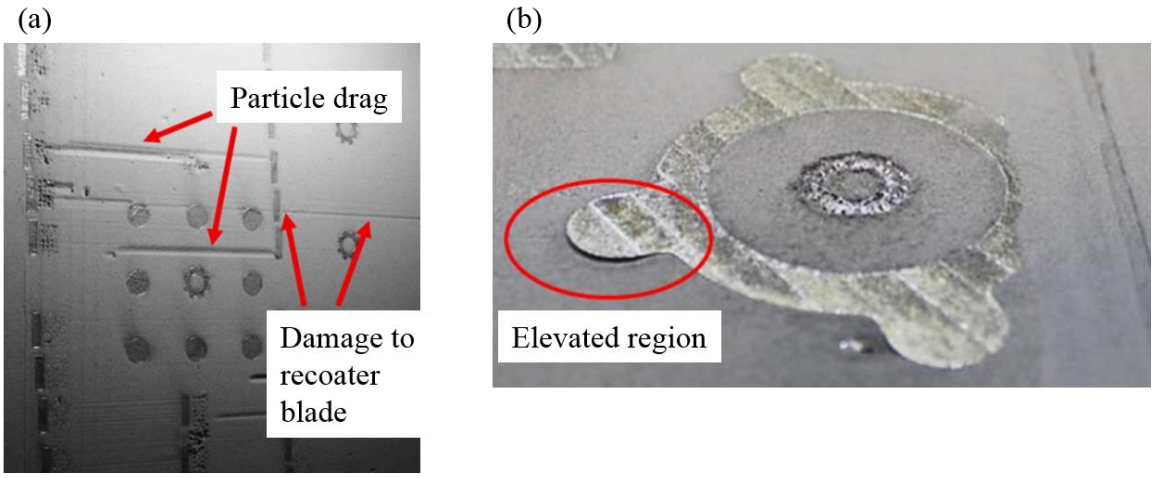

Figure 2.10 (a) Image captured in-situ illustrating non-uniform linear perturbations in the powder bed and (b) deformation during the printing of a cantilevered part [44].

Craeghs et al. [40] developed an optical inspection system to analyse the recoating of powders using visual camera and light sources, and a melt pool monitoring system using a high-speed camera, a semi-reflective mirror, a beam splitter and a photodiode. The detrition and local damage of the recoater blade resulted in tiny scratches spread all around the powder bed. Localised deep scratches were also observed on the powder bed as seen in Figure 2.11 (a). Vertical lines were constructed on the captured image (Figure 2.11 (a)). An average line profile (red line in Figure 2.11 (b)) was computed based on the grey values of multiple line profiles. The green lines represented the allowed tolerances

for the detection of damaged recoater blade. A damaged recoater blade causes the presence of peaks and valleys of the line profile as illustrated in Figure 2.11 (b). The monitoring system can be used to detect process errors during printing, which include porous parts.

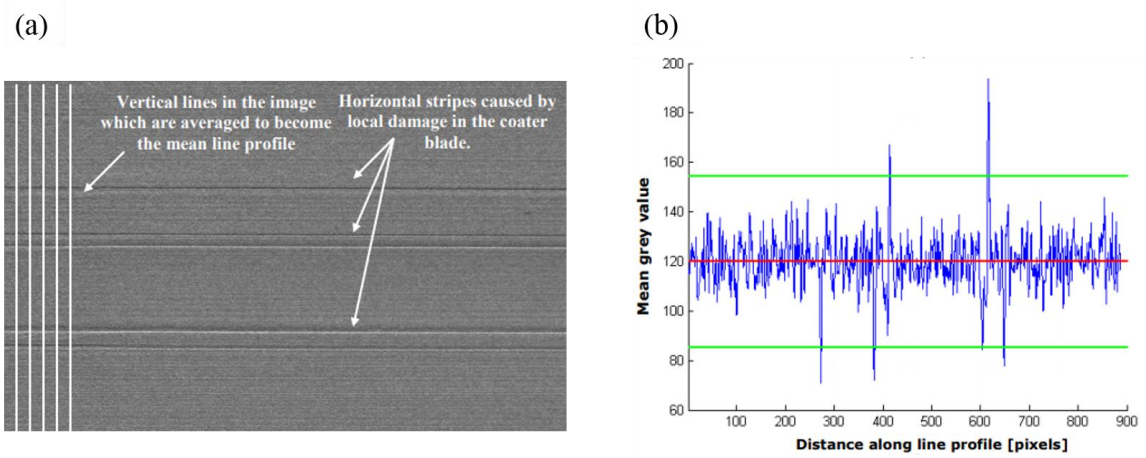

Figure 2.11 (a) Image of powder bed with worn recoater blade and (b) line profile depicting the mean grey value of 120 [40].

H. Krauss, C. Eschey, and M. Zaeh [15] demonstrated the possibility of utilising infrared camera to track the solidification process and the quality of powder layer deposition during the print process of a SLM machine. The variation in powder layer thickness can be identified by thermography immediately after recoating based on the theory that a thinner layer of powder will heat up more rapidly than that of a thicker layer. Artificial flaws with size up to 100 μm in diameter were also distinguishable through the measurement of the temporal evolution and the spatial distribution of the total irradiance during each exposure of a new layer [15]. The solidification and deposition of powders were monitored and evaluated. Hot spots can be distinguished at an early stage during the solidification process to aid in the rectification of print parameters. Pivotal indicators,

such as the highest temperature and cool-down behaviour of the powder bed were monitored for the whole layer. Through the review of individual layer data, information based on one image per key indicator and layer (tomography) can be obtained as illustrated in Figure 2.12.

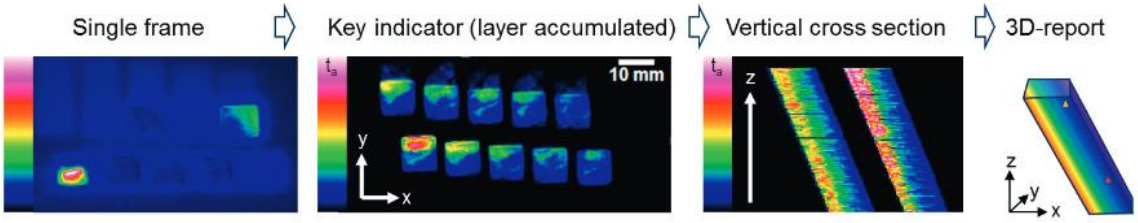

Figure 2.12 Thermal images of the powder bed captured are analysed based on a key indicator and stacked in the build height direction to generate a three-dimensional (3D) report of the printed part (colour map represents the temperature field) [15].

While the feasibility of adopting thermography for in-process inspection of the SLM process has been proven [54-56], it is worthwhile to note the technical difficulties associated with this technique. The broad temperature range of the melt pool should be taken into consideration for the calibration of the infrared camera. The temperature distribution of the powder bed ranges from approximately 2000°C, the instant which the laser beam melts the powder, to 400°C upon cooling, with a time on the order of milliseconds [57, 58]. The chosen infrared camera should have a measurable temperature range corresponding to the melt pool evaluation of the powder bed during the melting process. The emissivity of the printed specimen must be determined to ensure an accurate representation of its true temperature. As a material property, emissivity is dependent on factors including the object's surface structure, geometry and temperature. The determination of a specimen's emissivity under printing conditions is further complicated

by its dependence on the lens and filter combinations and the material of the window between the lens and the imaged subject [58].

Rieder et al. [59] have employed ultrasonic testing to detect the presence of porosities during SLM. An ultrasonic transducer was placed below the build platform to monitor the printing of cylindrical specimens. They reported the feasibility of using ultrasonic signals to detect porosities. The layer at which these porosities occurred were also traceable.

Cerniglia et al. [60] explored the use of laser ultrasonic for in-line inspection of laser powder deposition process. A proof-of-concept laser system prototype was constructed. Intentional defects were fabricated in standard geometries to evaluate the sensitivity of this technique for defect identification. Holes with varying diameters and depths below the surface of Inconel specimens were created. Results have confirmed the feasibility of utilising laser ultrasonic for detecting defects of micro sizes in Inconel specimens. Minimum defect size of 0.1 mm in diameter near the surface and larger defect of up to 0.8 mm deep can be detected. As additively manufactured parts can be complicated in geometry, it is challenging to use conventional NDT techniques for flaw detection. The quality of components produced by laser powder deposition is commonly evaluated by destructive testing or by x-ray computed tomography (CT) after fabrication. Successful demonstration of the laser ultrasonic system has proven its potential for detection of flaws during manufacturing [60]. Table 2.1 is a summary on IMSs developed by various researchers for PBF processes.

Table 2.1 Summary on IMSs developed by various researchers for PBF processes.

Researchers	**NDT technique**	**Equipment / machine (process)**	**Equipment location**	**Captured area / resolution**	**Defects identifiable**
Jacobsmühlen et al.	Visual inspection with optical aids	Monochrome 29-megapixel (MP) charged couple device camera / EOSINT M 270 (DMLS)	Outside chamber	Entire layer / 25 – 35 µm per pixel	Elevated edges
Foster et al.	Visual inspection with optical aids	36.3-MP DSLR Nikon D800E / EOS M 280 (DMLS)	Inside chamber	- / 50 µm per pixel, 15 µm per pixel	Non-uniform perturbations to powder layer
Craeghs et al.	Visual inspection with optical aids	High-speed camera / in-house developed SLM machine (SLM)	Outside chamber	- / 10 µm per pixel	Porous parts, balling of overhang structure, overheating of acute corners, non-uniform powder bed

Krauss et al.	Thermography	Infrared camera / EOSINT M 270 (DMLS)	Outside chamber, view angle of 45°	160 mm × 120 mm / 250 µm per pixel	Flaws identified up to size of 100 µm
Rieder et al.	Ultrasonic testing	Ultrasonic transducer / EOSINT M 270 (DMLS)	Underneath build platform	Entire layer / temporal resolution of 4 ns	Unmelted metal powders
Cerniglia et al.	Laser ultrasonic testing	Infrared Nd:YAG pulsed laser and laser receiver / laser powder deposition machine (DED)	Outside chamber	- / Micro defects of 0.1 mm in diameter near surface and larger defect of up to 0.8 mm deep	Micro defects

There are several commercial systems available for in-situ monitoring of AM processes, providing process control and quality assurance of printed parts. Some commercial IMSs feature the capturing of images layer by layer for inspection of defects. EOS GmbH [61, 62] introduced EOSTATE Monitoring Suite – an automated and real-time process monitoring system for direct metal laser sintering. During the build process, monitoring is carried out at each layer and each part. EOSTATE Monitoring Suite software registers data by capturing images of the powder bed, which can be used to draw conclusions on the presence of defects in printed parts. A 1.3 megapixels industrial camera was installed in the ceiling of the chamber which is significantly lower than consumer grade DSLR cameras with image sensors of 24.2 megapixels or higher [44]. As the optical system is unable to capture high-resolution images, the detection of small-sized defects based on the images captured by the system may therefore be challenging.

Arcam EBM [63, 64] has developed process validation technology for AM. Arcam LayerQam is a high-resolution camera system for the detection of defects through each layer. Porosities detected are reported as an entire build. Other systems enable the visualization of defects through the stacking of images from the start to the end of the print job, similar to that of a CT scan. Concept Laser GmbH [16, 65] developed an in-situ quality assurance system, QMmeltpool 3D that utilises coaxial sensors consisting of a photodiode and an optical camera to identify the melt pool area and the melt pool intensity. The system documents position-related characteristics of the melt pool when the part is being printed, providing local indications of defects in the part. A 3D image illustrating the locations and sizes of defects in the printed part is generated after the build process.

SLM Solutions [66] has developed the Melt Pool Monitoring tool for resolving of melt pool thermal radiation using pyrometry. Two IR sensors are implemented to collect information of the melt pool through two beam splitters. Measurements can be taken with a rate up to 100 kHz (10 µs) and be recorded and displayed in real time. Intensity (temperature) profile of the individual melting lines can be accessed. The saved data can be probed and visualised layer by layer for analysis of the melt pool. Further details of the set-up can in found in [66, 67]. The resolution of the system and the area of monitoring, however, were not reported. The nature and size of the defects identifiable by the system remains unknown.

General Electric [68] has developed an acoustic monitoring system for measuring acoustic signals using sensors in powder bed fusion processes. The acoustic sensors are placed underneath the build substrate. Monitoring of these signals allows for the detection of defects in the printed part. The monitoring system can be activated upon completion of the printed part or in real time. Defects identification is achieved by comparing the signal profile of a known piece of qualified and defect-free specimen and the measured signal profile of the printed part. While the acoustic profile shows acoustic signals with constant amplitude in a defect-free part, sudden dips in the amplitude of acoustic signals are present in the acoustic profile for printed parts with defects [69]. Intelligent Optical Systems, Inc. [70] has embarked on developing an in-situ layer-by-layer part qualification process using laser ultrasonic testing. During the build process, each layer will be examined in real time and completed parts will not require any further tests. Table 2.2 is a summary on commercially available IMSs for PBF processes.

Table 2.2 Summary on commercial IMSs for PBF processes.

Company / software	**NDT technique**	**Equipment / machine (process)**	**Equipment location**	**Captured area / resolution**	**Defects identifiable**
EOS e-Manufacturing Solutions / EOSTATE MeltPool	Visual inspection with optical aids	1.3-MP industrial camera / EOS M 290 (DMLS)	Inside ceiling of chamber	-	Insufficient recoating
Arcam EBM / Arcam LayerQam	Visual inspection with optical aids	Optical camera / Arcam Q10plus, Arcam Q20plus (EBM)	-	200 × 200 mm / 100 µm	Porosities
CONCEPT Laser GmbH / QMmeltpool	Visual inspection with optical aids	High-speed camera and photodiode, coaxial with laser / M1 cusing, M2 cusing (SLM)	-	4 cm^2 / 35 µm	Irregularities in melting process

SLM Solutions / Melt Pool Monitoring	Thermography	Photodiodes / SLM 280 (SLM)	Inside chamber	-	Irregularities during fusion
General Electric / -	Acoustic emission testing	Acoustic sensors / - (SLM)	Underneath build platform	-	Cracks and voids
Intelligent Optical Systems, Inc / -	Laser ultrasonic testing	Pulsed laser / - (DED)	Integrated to deposition head of printer	- / 500 µm	Porosities and lack-of-fusion defects

2.3.2 Limitations of current in-situ monitoring systems

Most IMSs developed by researchers and industrial experts identify single source of defects, such as porosities or non-uniformly recoated powder bed. A more comprehensive approach is needed to improve the robustness of IMSs in identifying different defects during printing. Commercial IMSs are exclusive to their own brand of machines. The in-situ monitoring system (IMS) is not transferrable to similar AM machines of other brands. EOS Monitoring Suite, for instance, is only applicable to EOS DMLS machines. The nature of data collected across different commercial IMSs varies and some feature the use of concealed figures as quality indicators. The downside of Arcam LayerQam and QMmeltpool 3D is the extremely small areas of monitoring. Both systems feature a 4 cm^2 area of monitoring. The area of a part that can be monitored is therefore limited. Thus, the results obtained based on captured images may not be a good representative of the entire part if its size exceeds the area of monitoring. Furthermore, the number of small-sized specimens that can be monitored per print job is restricted.

While researchers and industrial experts have successfully detected defects using IMSs, limited efforts have been made to establish the relation between defects identified during printing and the mechanical properties of the printed part. This information is vital as it bridges the gap between the defects identified by the monitoring system and the actual performance of the part. Moreover, the correlation between the defects detected during printing and the actual defects present in the printed part must be studied for the development of a robust IMS. This is critically pertinent as the mechanical properties of a part are dictated by the extent of defects present.

Ultimately, the performance of a printed part is evaluated by examining its density, mechanical properties and chemical composition. Yet, many research works and commercial systems focused only on the defects identifiable during in-situ monitoring of the SLM process. There is, however, a crucial need in establishing the relationship between defects identified during printing to the actual mechanical performance of the printed part for advancements in the development of IMSs.

Despite the advancement of commercial IMSs in defects detection, the impact of these defects on the structural integrity of the printed part remains unknown. Since the optical resolution of these commercial systems is not publicly available, the correlation between captured images and structural integrity of the printed parts can only be established through high-resolution imaging. This enables fine details of the printed and recoated layers to be captured before accurate quantification of defective regions can be performed for correlation with the parts' mechanical properties.

2.4 Summary

The demand of metal-based parts has increased over the years across many industries, including automotive and aerospace. SLM is one of the main AM processes adopted for printing of metals. AM technologies, however, have not been implemented on a large scale. This is due to the lack of standards for additively manufactured parts and concerns regarding the repeatability and reliability of the technology from part-to-part and machine-to-machine. IMSs are needed for the identification of defects during printing, ensuring parts fabricated are of high quality. IMSs for AM processes also render time and costs savings since semi-built parts that fail to meet the standards can be stopped automatically.

Visual inspection with optical aids and thermography are the main methods integrated with current IMSs. There has been an increase in the application of acoustic emission testing and laser ultrasonic testing for in-situ monitoring of AM processes. Researchers and industrial experts have developed various IMSs, each aimed at identifying specific defects. Nonetheless, limited efforts have been made to establish the relation between defects identified during printing and the mechanical properties of the printed part. Furthermore, the correlation between the defects detected during printing and the actual defects present in the printed part must be studied for the development of a robust IMS.

The development of IMSs must be focused on:

1. the ability to detect and quantify multiple sources of defects during printing,
2. their portability for installation on printers of different brands,
3. the possibility to infer the mechanical properties of printed parts based on captured signals,
4. the possibility to determine the sizes and locations of the defects in printed parts based on captured signals and
5. the establishment of a closed-loop system, providing end users with feedback on the quality of the print job.

Continuous research in these areas will constitute an improvement on IMSs with enhanced defects detection capabilities and flexible integration to a range of printers.

CHAPTER 3: EXPERIMENTAL METHODS

Visual inspection with the aids of optics and thermography are the two non-destructive testing techniques employed for developing the proposed in-situ monitoring system (IMS). High-resolution optical images of the powder bed can be captured. The implementation process is simple and optical-based in-situ monitoring is applicable to most specimens. Optical aids allow the powder bed to be monitored even when direct viewing is not possible. Thermography measures the temperature field of the surface of the studied body. An infrared camera detects and captures temperature-related defects based on the radiation emitted by a body, which is unattainable via optical imaging. This section first discusses on the development of the IMS. The materials and methods which include the design of specimens and choice of mechanical tests are subsequently outlined.

3.1 Development of in-situ monitoring system

The development of the IMS takes into consideration several factors including its design and calibration procedures for the optical and thermal systems. Other considerations include distortion correction of optical and thermal images. The machine used was SLM 500 HL from SLM Solutions Group AG. The laser beam focus diameter was 80 – 115 μm.

3.1.1 Design of in-situ monitoring system

The IMS is, in essence, a separate set of equipment installed onto the selective laser melting (SLM) machine to monitor the printing process. The system is portable and independent of the make of the SLM machine. The development of the IMS can be summarised into two designs — (1) optical system for visual inspection of the powder bed and (2) thermal system for thermographic inspection of the powder bed.

3.1.1.1 Design of optical system

A NIKON D850 digital single lens reflex (DSLR) camera was employed for visual inspection. It has a sensor size of 23 × 15 mm (45.7 million pixels). The lens attached to it has a focal length of 200 mm. A resolution of 10 to 13 µm / pixel is obtained. The design involved placing the DSLR camera outside of the machine to capture optical images of the powder bed. Light was reflected from the powder bed and directed to the lens of the DSLR camera using a silver coated mirror. The mirror was mounted at an angle of 45° between the walls of the chamber using a tensioning rod as shown in Figure 3.1 (a). Strings were used to mark out the laser path and the mirror was placed outside of this boundary. This prevents the mirror from being damaged by the high intensity laser during printing. The mirror was mounted near the front door of the chamber. The mirror measured 80 × 60 mm and the field of view provided by the mirror measured 69 × 49 mm.

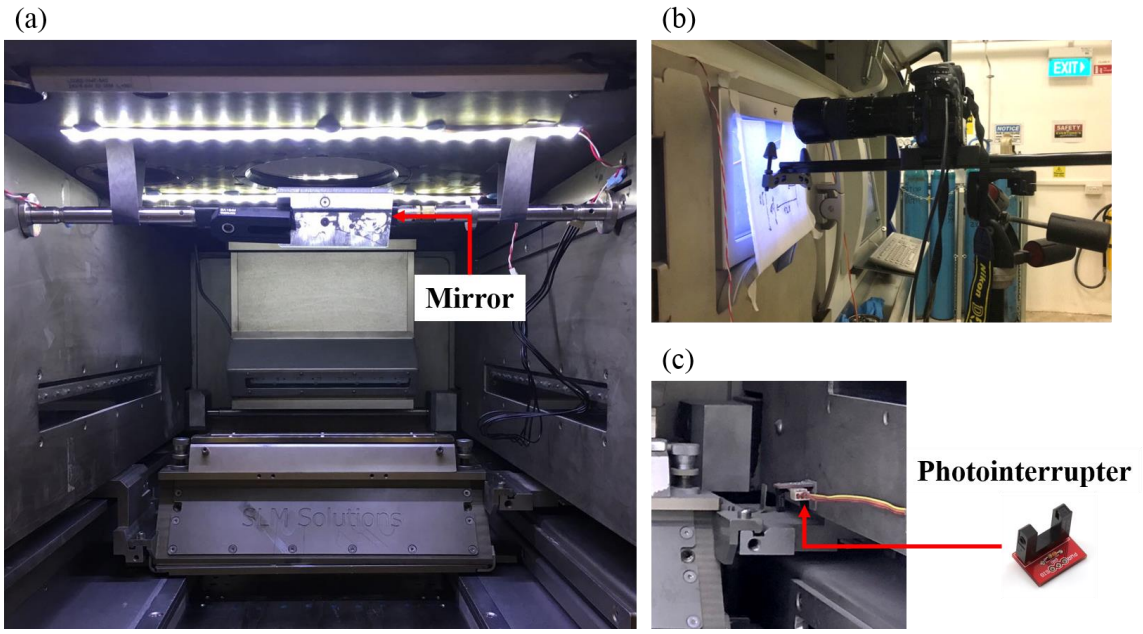

Figure 3.1 Experimental set-up comprising of a (a) mirror, (b) camera on a tripod and (c) photointerrupter.

3.1.1.2 Design of thermal system

The infrared camera was placed above the chamber of the machine, which differed from the optical camera. The infrared camera is more susceptible to environmental disturbances than the optical camera. One major disturbance is changes in light intensity of the environment. An example is the switching on and off of laboratory lights during printing. Before each print job, the infrared camera must be calibrated to take into account various factors that may introduce errors during the monitoring process. Significant changes to the working environment of the infrared camera during printing will lead to inaccurate information captured in thermal images. As such, it was decided that the infrared camera has to be placed above the chamber of the machine to reduce the probability of disturbance to the set-up.

An ImageIR 8355 hp infrared camera from Infratec GmbH was utilised for thermographic inspection. It detects medium-wavelength infrared and has a sensor size of 9.6 × 7.7 mm (640 × 512 pixels). The lens attached to it has a focal length of 50 mm. A resolution of 170 to 173 µm / pixel is obtained. Some of the emitted infrared energy from the powder bed was transmitted through the viewport of the chamber before reaching the silver coated mirror as depicted in Figure 3.2. The viewport of the machine was replaced from the original glass material to that of calcium fluoride. Glass blocks infrared wavelengths while calcium fluoride enables the transmission of mid-wavelength infrared signals. The viewport measured 75 mm in diameter. The mirror measured 100 × 75 mm and was mounted at an angle of 50° measured from the vertical position as seen in Figure 3.2. Prior to installation of the thermal system, an optical camera from the machine manufacturer was mounted at an angle of 50°. This camera was subsequently removed and was replaced by the mirror mounted at the same angle which optimised the area of monitoring. The infrared radiation path, represented by red arrows in Figure 3.2, was deflected by the mirror before reaching the gold dichroic beam splitter at 45° angle of incidence. The dichroic beam splitter allows transmission of visible wavelengths and reflects infrared wavelengths (short to medium wavelengths), enabling the infrared sensor to detect the signals. The gold dichroic beam splitter measured 50.8 mm in diameter. The infrared radiation path was 585 mm in length. The field of view is dependent on the distance of infrared radiation path from the powder bed to the sensor, the size of the beam splitter, the size of the mirror and the lens of the infrared camera. The field of view associated with this set-up is 85 × 51 mm.

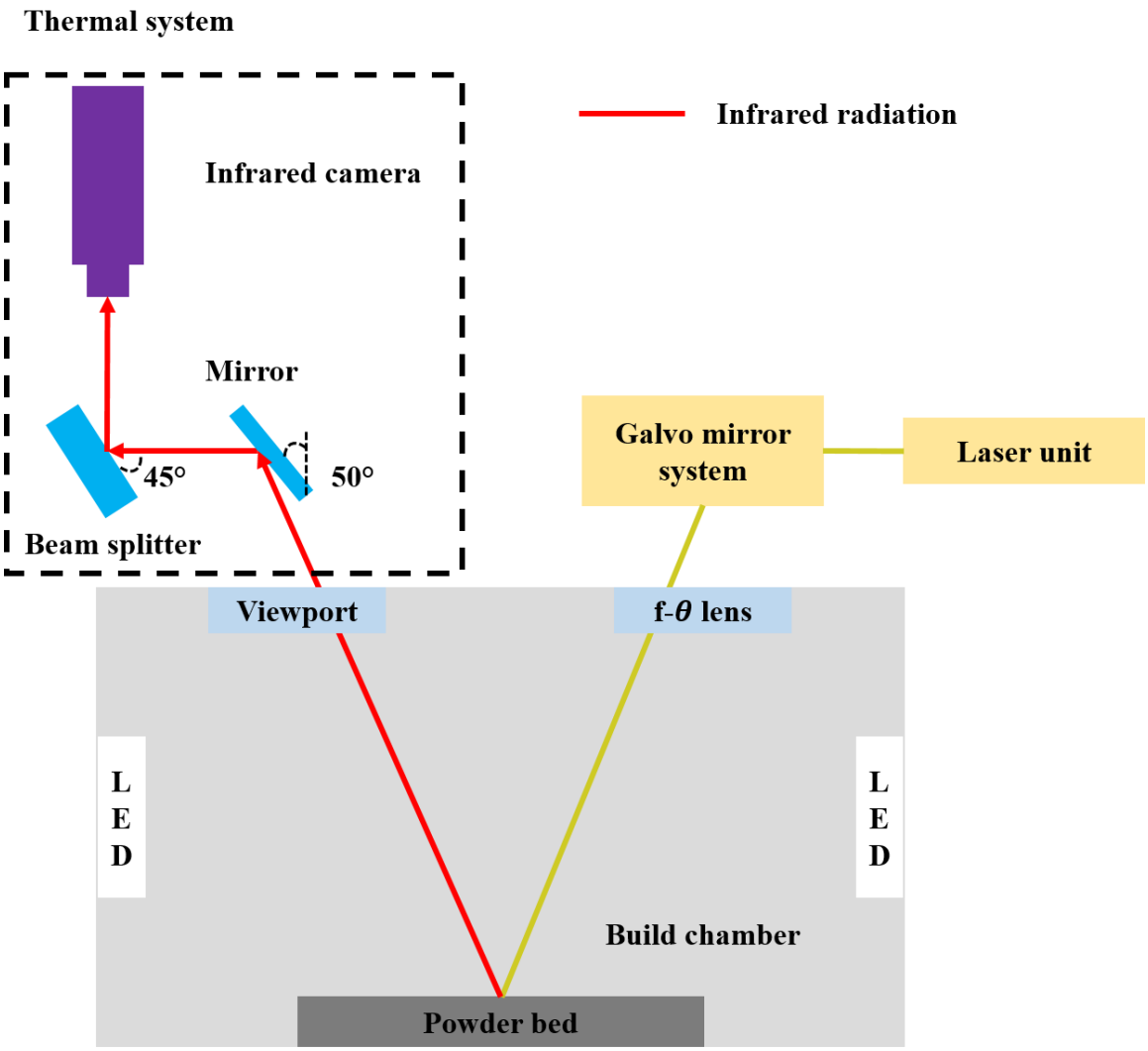

Figure 3.2 Schematic representation of the thermal system (front view).

The SLM 500 machine employs the use of ytterbium fibre laser with a wavelength of 1.06 µm [71]. Near infrared and short-wavelength infrared cameras have spectral bands of 0.8 to 1.7 µm and 1 to 2.5 µm respectively. These infrared cameras were not considered as the operating wavelength of the laser falls within this range. The purpose of the infrared camera is to examine the temperature profiles of the printed specimens rather than the temperature profile of the laser. Choosing an infrared camera in either of these spectral bands will result in information of the laser being captured, interfering the

collection of data with respect to the printed specimens. Therefore, the spectral range of the infrared camera must not coincide with the operating wavelength of the laser. Between the selection of mid-wavelength and long-wavelength infrared cameras, the former is more suitable for inspection of high-temperature objects while the latter is best suited for assessment of objects at room or low temperatures [72]. The solidified metal could reach a temperature of approximately 2000 K or higher immediately after the laser scans the powder bed, necessitating the use of a mid-wavelength infrared camera [73].

3.1.2 Calibration of light source

Foster et al. [44] attributed uniform lighting within the machine's chamber to be the most critical factor in obtaining optical images with sufficient contrast. It also facilitates the procedures involved in automating the process of defects detection. Although there is one set of in-built white light emitting diode (LED) lights installed at the chamber ceiling, it does not provide sufficient illumination. Images captured had poor intensity and contrast. Hence, the use of additional white LED lights was considered as the solution to achieve uniform illumination within the chamber.

Two lighting conditions were evaluated — (1) in-built white LED lights in the machine's chamber and (2) additionally installed white LED lights without in-built lighting. LED lights were used in both conditions as they provide diffuse illumination, reducing non-uniform illumination in the chamber. While the platform has a printing area measuring 280 × 500 mm, the area used for actual printing was 280 × 250 mm. This corresponds to the front half of the substrate that is nearer to the machine's front door. Therefore, additionally installed LED lights were placed at areas near the front door of the chamber. As space is a constraint, the LED lights were installed without diffusers which would

otherwise improve the uniformity of illumination within the chamber. Certain regions of the powder bed may be more illuminated (brighter) than others, complicating the process of segregating important features or process signatures from the captured optical images. Histograms of the captured images were used to evaluate the uniformity of illumination within the chamber. Ideally, the images of the objects being captured should be uniformly lit and their histograms should illustrate intensity values spread out across the 256 grey levels.

3.1.2.1 In-built LED lights

The optical images captured were generally dark in intensity (Figure 3.3 (a)) as there is only one set of in-built LED lights located at the ceiling of the chamber. The intensity of the light source is low as represented by the histogram in Figure 3.3 (b), where the peak greyscale intensity value is 63. Moreover, the image's greyscale intensity values ranged between 30 to 215, which is far from the total 256 grey levels. This indicates the lack of contrast between printed parts and unmelted powders.

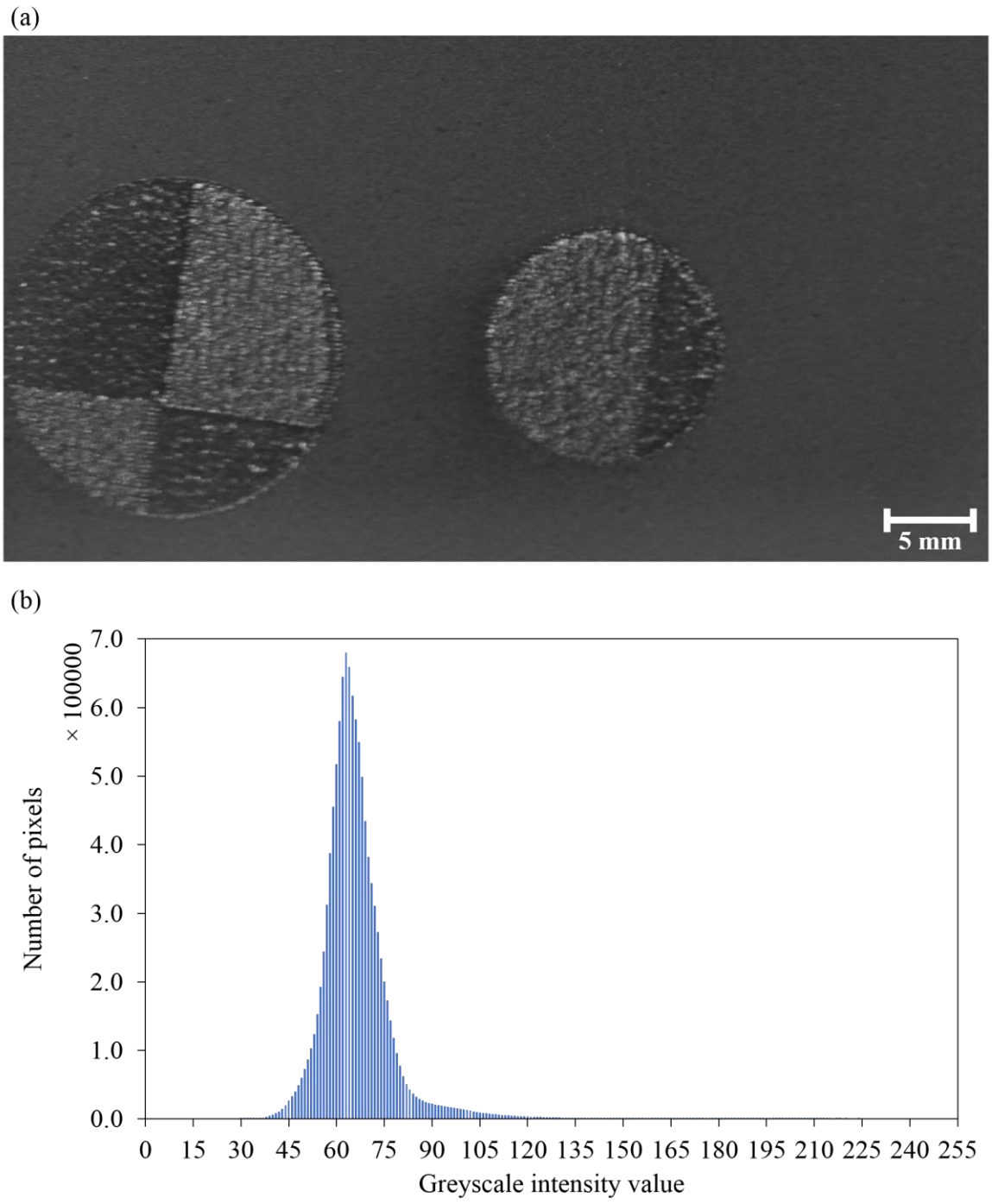

Figure 3.3 (a) Greyscale image of printed parts captured under in-built LED lighting and (b) histogram of (a) representing the distribution of pixels' greyscale intensity values.

3.1.2.2 Additional LED lights

A separate print was carried out where additional sets of white LED light (without using the in-built white LED light) were installed at the ceiling and the side walls of the chamber. The powder bed was more uniformly lit and images were captured with high contrast. A comparison between Figures 3.3 (a) and 3.4 (a) reveals an improvement in the light source's intensity and the contrast of captured image. The histogram in Figure 3.4 (b) depicts a peak greyscale intensity value of 116, an improvement in the light source's intensity as compared to the previous configuration of in-built lighting. The image's contrast is also notably enhanced as supported by the larger range of greyscale intensity values from 49 to 255 (Figure 3.4 (b)). Therefore, this configuration of white LED lights was chosen for in-situ monitoring of the SLM process.

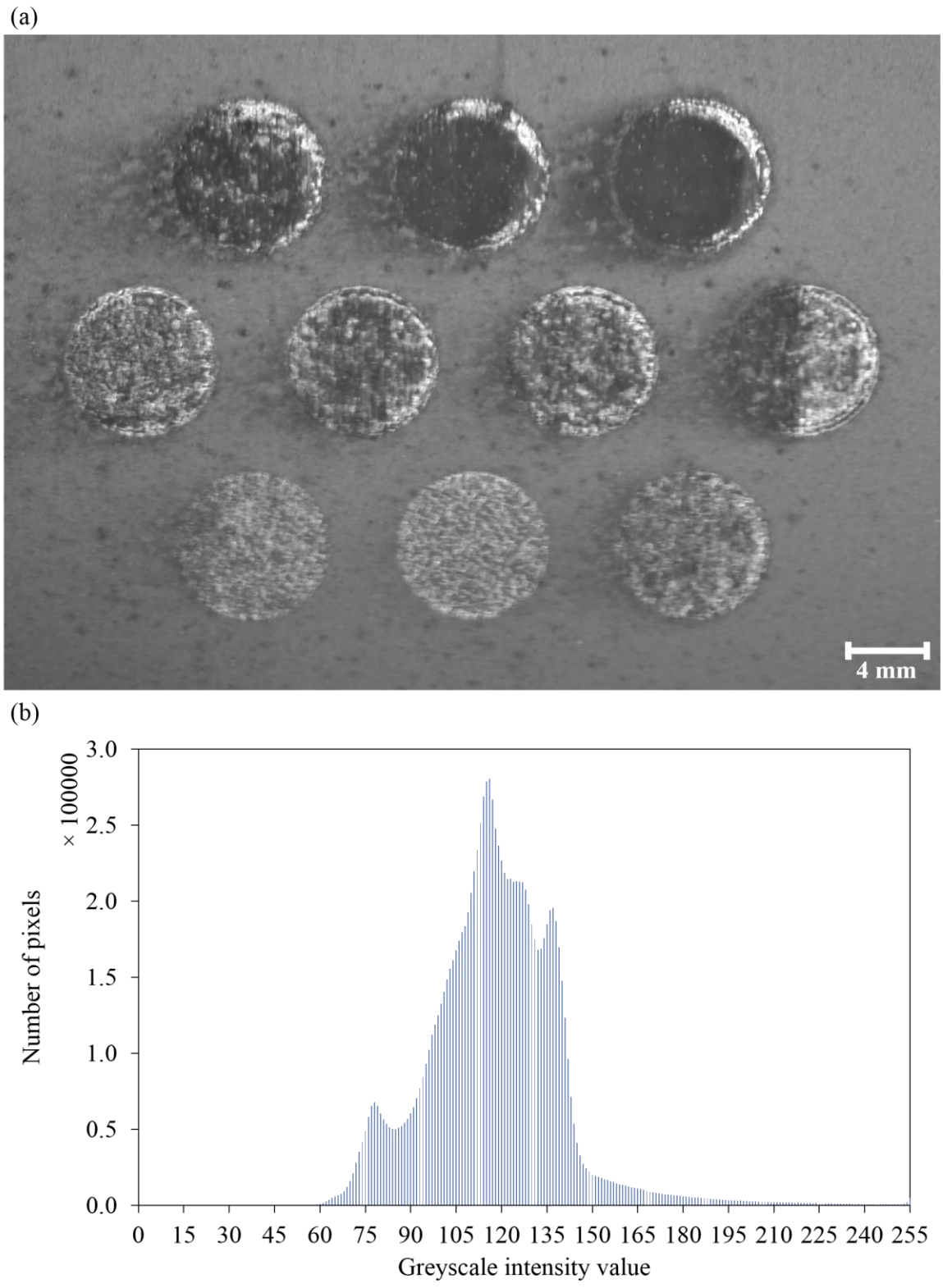

Figure 3.4 (a) Greyscale image of printed parts captured under additional sets of LED lighting and (b) histogram of (a) representing the distribution of greyscale intensity values.

3.1.3 Automatic capturing of optical images

A photointerrupter was affixed to the chamber wall at a height above the homing position of the recoater to automate the capturing of optical images during printing. The location of the photointerrupter is shown in Figure 3.1 (c). The recoater blocks the amount of light detected by the photointerrupter momentarily due to its movement from the back to the front of the machine's platform, and vice versa, as it recoats after each printed layer. Signals were then sent to a script to trigger the shutter of the DSLR camera.

3.1.4 Emissivity study for true temperature measurements

Emissivity data of the material is required for the calculation of an object's true temperature, T_{true}. This information, however, is difficult to obtain given the extensive parameters that could influence the accuracy of the data. Two factors were considered to determine a specimen's emissivity — (1) calibration for temperature error caused by optical components of the thermal system and (2) calibration for emissivity of a specimen with specific printing parameters. This ensures the emissivities determined are compensated for the errors incurred and are representative of the material during real-time printing.

The overall transmittance of the dichroic beam splitter, mirror and the viewport must be determined. These optical accessories are attenuating mediums, introducing sources of errors which lead to inaccurate temperature measurements. The procedures for compensating the transmittance when using an infrared camera to measure the surface temperature of a specimen through attenuating mediums were referenced to ASTM E1897-14 [74]. A blackbody simulator was used for calibration. CEM's BX-500 portable infrared calibrator has an emissivity value of 0.95. The schematic representation of the

set-up is depicted in Figure 3.5 (a). The infrared camera was placed at the top of the machine's chamber. The blackbody simulator was placed in the chamber and heated up to 200 °C. Accurate temperature reading of the blackbody simulator is provided by its in-built thermal sensor. The transmittance associated with the optical accessories, $\tau_{optical\ accessories}$, was adjusted in the infrared camera's software until the temperature measured matched the value indicated by the blackbody simulator. $\tau_{optical\ accessories}$ was found to be 0.044.

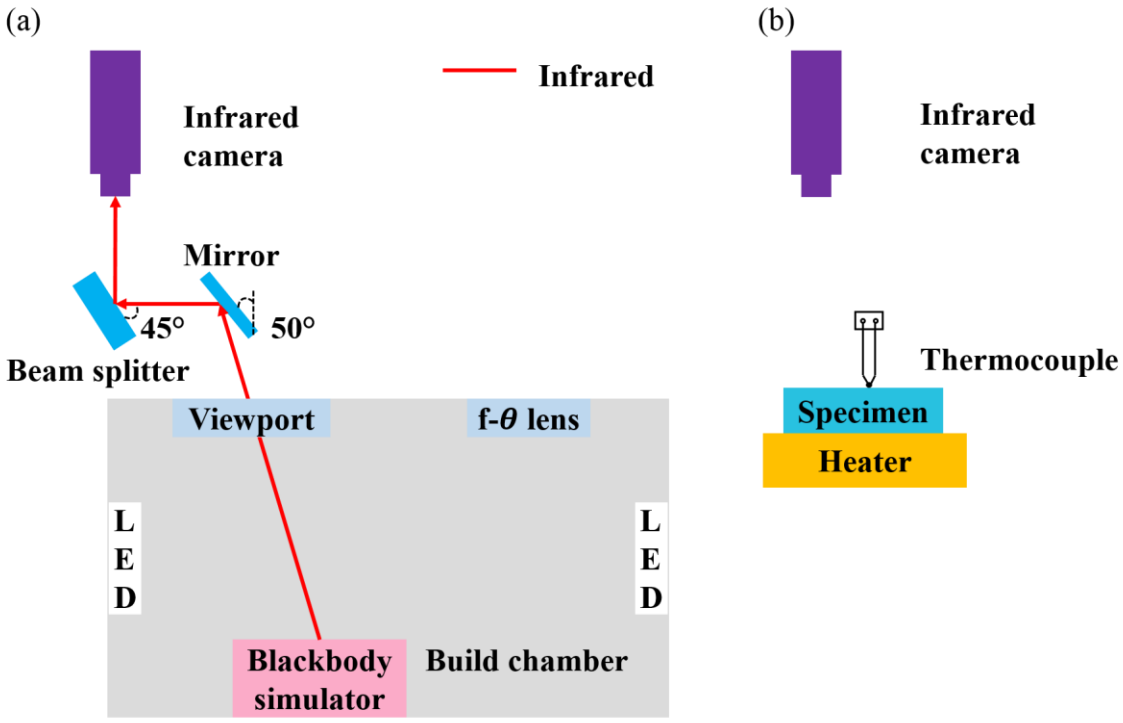

Figure 3.5 Schematic representation of set-up to determine (a) transmittance associated with optical accessories and (b) emissivities associated with the surface textures of the specimens.

Ten cylindrical specimens measuring 8 mm in diameter and 8 mm in height were printed for the investigation of the material's change in emissivity with surface texture. 316L

stainless steel powders were used for printing and the cylinders were printed with varying energy densities, resulting in the different surface textures obtained. Micro computed tomography (CT) images in Figure 3.6 illustrate notable differences in the surface texture across the ten cylinders. The printing parameters associated with the ten cylinders are replicated for subsequent print jobs and they will be further discussed in section 3.2.2.2.

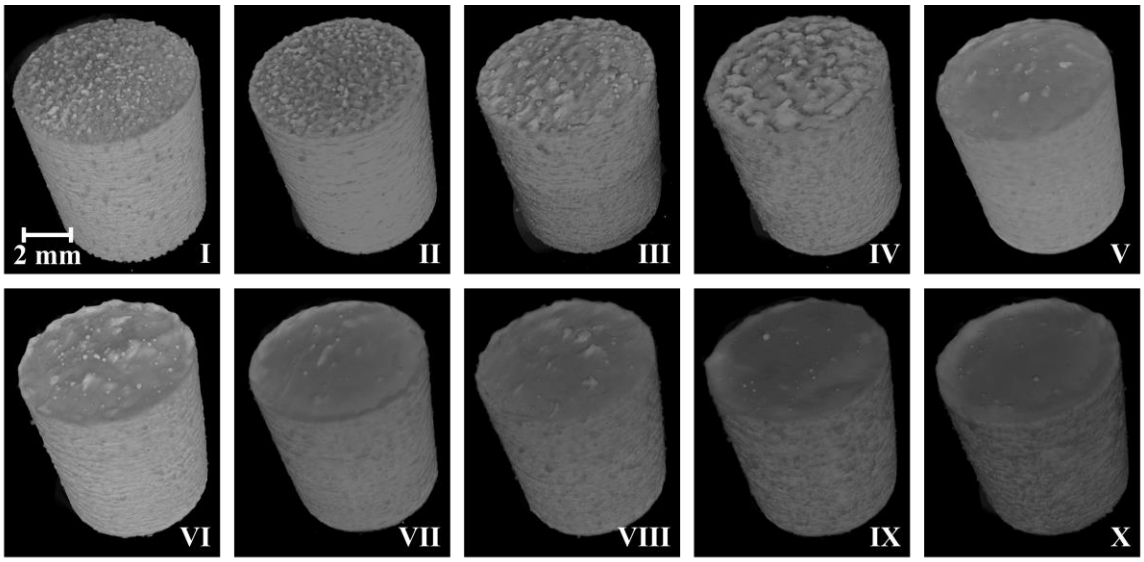

Figure 3.6 Surface texture of cylinders printed with varying energy densities.

The procedures for compensating the emissivity of a specimen when measuring its surface temperature using an infrared camera were referenced to ASTM E1933-14(2018) [75]. A heater was heated to 200 °C and the cylindrical specimens were placed on the heater, one at a time. The probe of a calibrated thermocouple was placed onto the surface of the cylinder to measure its T_{true}, as seen in Figure 3.5 (b). The infrared camera was set up with the configuration shown in Figure 3.5 (b) to capture thermal images of the cylinder. The cylinder was heated to 200 °C and its T_{true} was measured. Thermal images of the cylinder were also captured before the heater was turned off. T_{true} was used as the

reference data. Emissivity was then adjusted in the infrared camera's software until the temperature measured matched T_{true}. This process was repeated for the remaining nine cylinders printed with different parameters. The emissivities associated with the surface textures of the cylindrical specimens, $\varepsilon_{specimen}$, were recorded and consolidated in Table 3.1. It is worthwhile to note that no optical accessories, such as the dichroic beam splitter and mirror, were placed between the infrared camera and the cylinder. Table 3.1 also shows the $E_{overall}$ of the ten cylindrical specimens which will be used for subsequent temperature measurements. The combined emissivity and transmittance correction value, $E_{overall}$, is given as [74]

$$E_{overall} = \tau_{optical\ accessories} \times \varepsilon_{specimen}. \quad (3.1)$$

Table 3.1 $\varepsilon_{specimen}$ and $E_{overall}$ of ten cylindrical specimens.

Cylinder	I	II	III	IV	V	VI	VII	VIII	IX	X
$\varepsilon_{specimen}$	0.27	0.30	0.23	0.25	0.21	0.24	0.22	0.22	0.20	0.24
$E_{overall}$ $(\times 10^{-2})$	1.2	1.3	1.0	1.1	0.92	1.1	0.97	0.97	0.88	1.1

3.1.5 Imaging resolution test

The modulation transfer function (MTF) was used to evaluate the performance of the optical and thermal systems. MTF evaluates the performance of an imaging system by integrating resolution and contrast (modulation) information into a single parameter. The ability of an imaging system to differentiate object detail is defined as resolution. Resolution is commonly expressed with reference to line-pairs per millimetre where each line-pair consists of one black line and one white line as illustrated in Figure 3.7 (a).

Frequency is the measure of line-pairs per millimetre. Contrast is interpreted as how well the maximum and minimum intensity values are transferred from object plane to image plane. The percentage contrast is given as [76]

$$Percentage\ contrast = \frac{I_{max} - I_{min}}{I_{max} + I_{min}} \times 100 \quad (3.2)$$

where I_{max} and I_{min} are the maximum and minimum intensity values respectively.

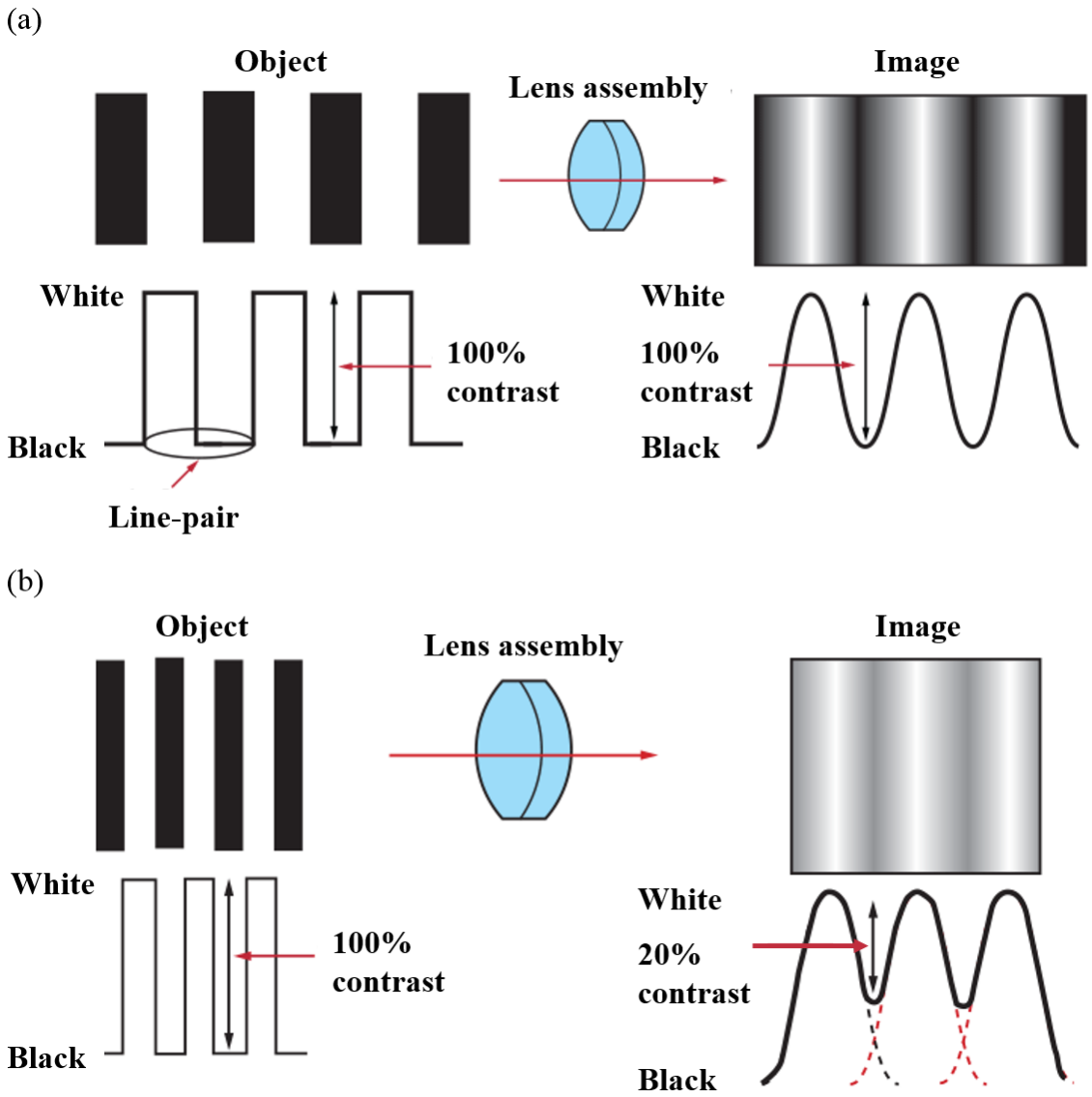

Figure 3.7 Contrast of an object and its image at (a) low spatial frequency of line-pair per unit length and (b) higher spatial frequency of line-pair per unit length [76].

A black pixel has an intensity value of 0 while a white pixel has an intensity value of 255. Grey pixels will have intensity values between 0 and 255 depending on their shade. Figure 3.8 (a) illustrates the contrast expressed as a square wave where the contrast between a black and white pixel is the highest and the contrast between two pixels of similar intensity values is the lowest. When the line spacing is large (black and white

lines are far apart), optical systems resolve these lines easily where I_{max} is 255 and I_{min} is 0. The percentage contrast in this case is 100% according to equation (3.2). When the spatial frequency of line-pair per unit length increases (black and white lines are nearer), it becomes increasingly challenging for an optical system to effectively resolve each line-pair of resolution [77]. I_{max} is less than 255 and I_{min} is more than 0. The percentage contrast in this case is less than 100% according to equation (3.2). The MTF of the system degrades accordingly as seen in Figure 3.7 (b). The MTF was determined using the 1951 United States Air Force (USAF) target as shown in Figure 3.8 (b).

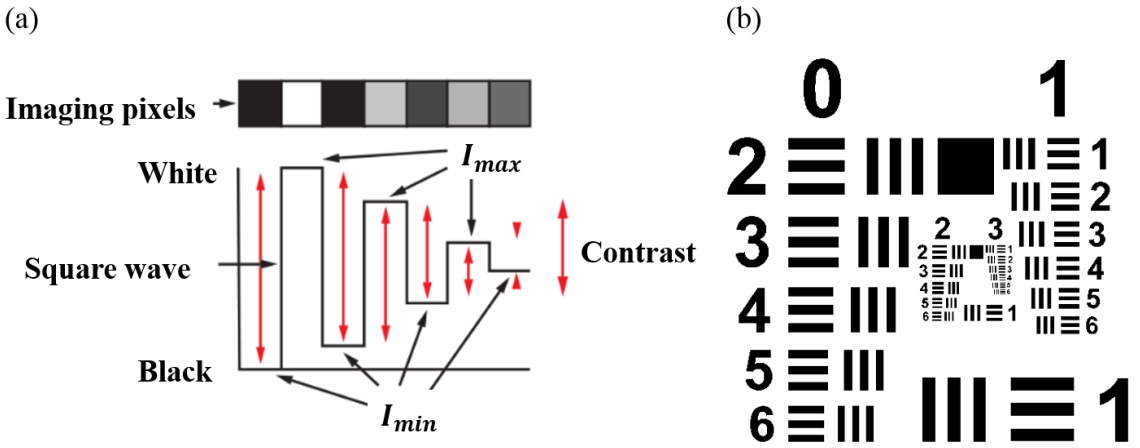

Figure 3.8 (a) Contrast represented as a square wave [76] and (b) a 1951 USAF target.

Common aberrations such as coma, spherical aberration and astigmatism can be effectively reduced by stopping down the aperture (i.e., increase f/number) of the lens. Stopping a lens to higher f/number also increases depth of field. This helps to reduce tilt aberration which is prominent in an off-axial monitoring system. The primary trade-off of stopping down a lens is lower light throughput and higher diffraction blur due to the inverse proportion of diffraction limit to f/number. These opposing factors indicate an ideal f/number at which optical aberrations and diffraction blur are compromised to yield

an optimal image quality. The ideal aperture stop is determined by plotting the MTF curves with various f/number. Figure 3.9 shows the images and close-up details of 1951 USAF resolution target captured by our optical system at various aperture stops. Blurs from optical aberration such as astigmatism and tilt are prominent at small f/number (wide aperture) while diffraction blur is influential at large f/number (small aperture).

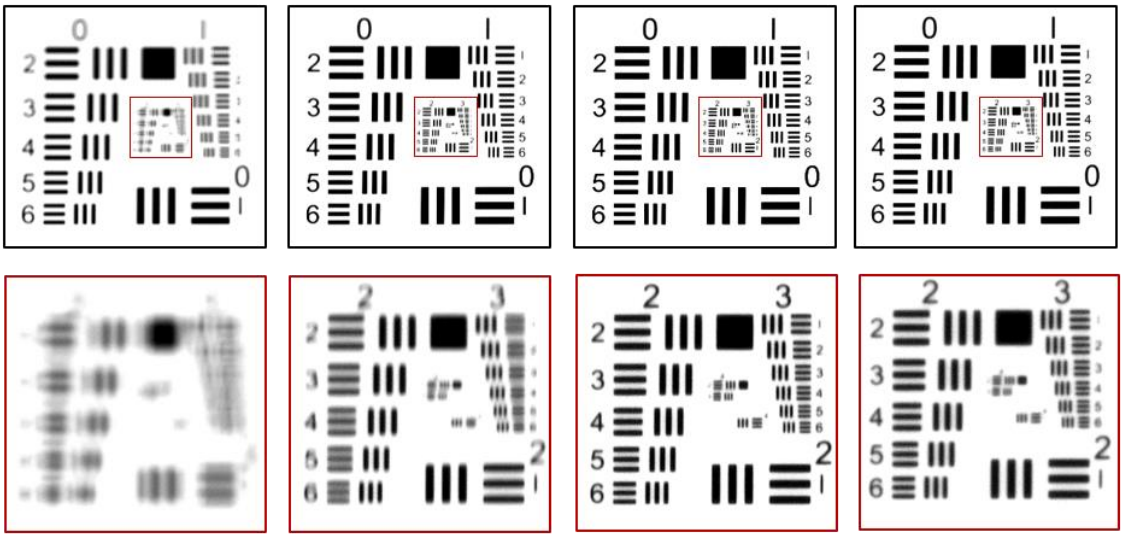

Figure 3.9 Images and close-up details (bottom row) of the 1951 USAF resolution target captured at various f/number.

Since the proposed monitoring system is off-axial in nature, its MTF was measured at both the centre and corner of the DSLR camera's field of view to find the ideal aperture stop for images taken at a given depth of field. The optical system was focused at the centre of the field of view and the exposure was kept constant for all aperture settings. Figures 3.10 (a) and (b) and illustrate the MTFs of the optical system. Aperture stop f/22 was chosen as the optimum f/number for the monitoring system as the percentage

contrasts were consistently high when images were taken at the centre and corner of the field of view.

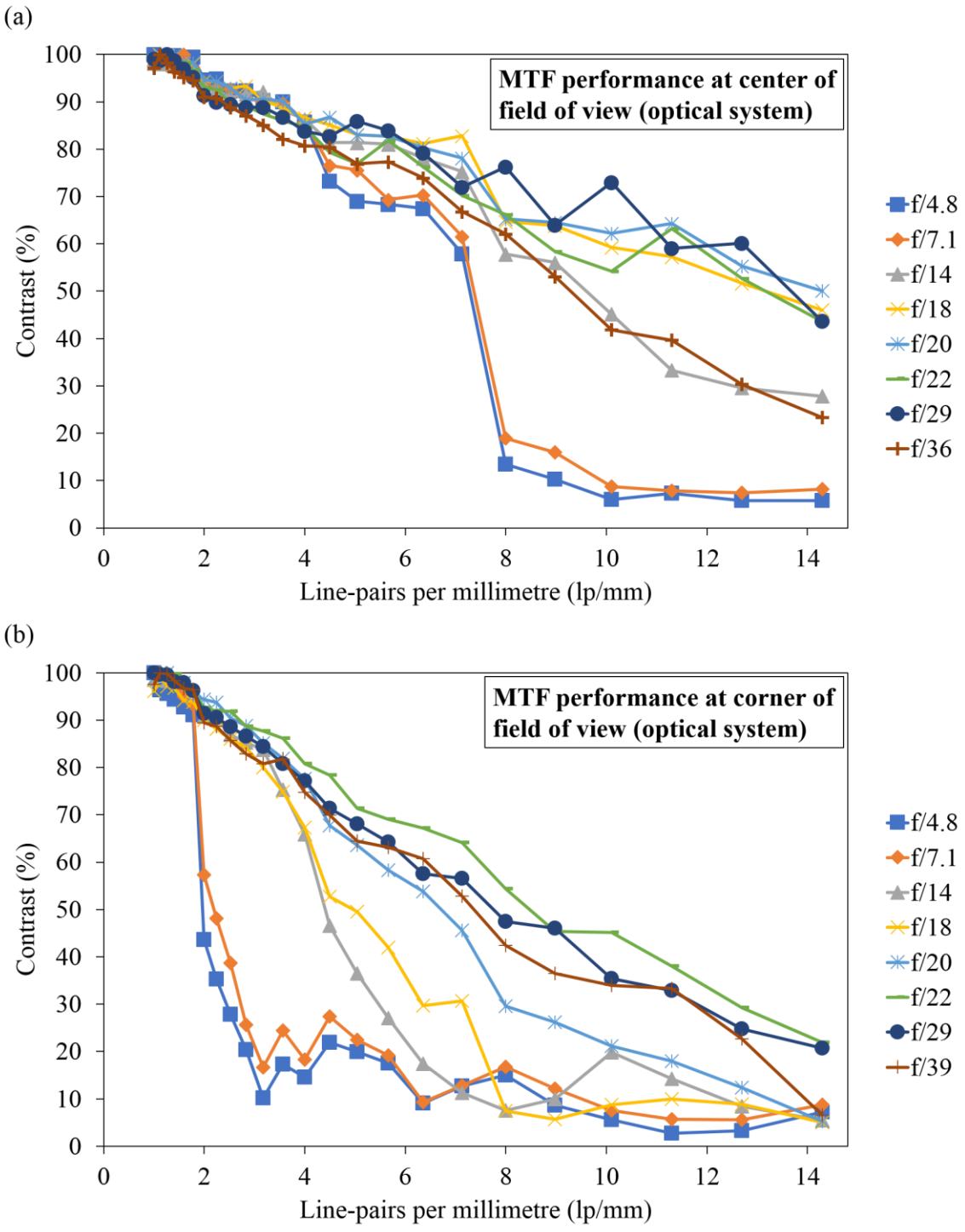

Figure 3.10 MTF of the optical system at (a) centre and (b) corner of the DSLR camera's field of view.

The MTF performance of the thermal system was also examined. A negative 1951 USAF target was used. The target was placed at the centre of the region of interest and a heater was used to illuminate it as represented in Figure 3.11. The MTF of the thermal system is shown in Figure 3.12. The MTF of the thermal system was not measured at the corner as its depth of field is relatively large and images formed at the corners are not blurred.

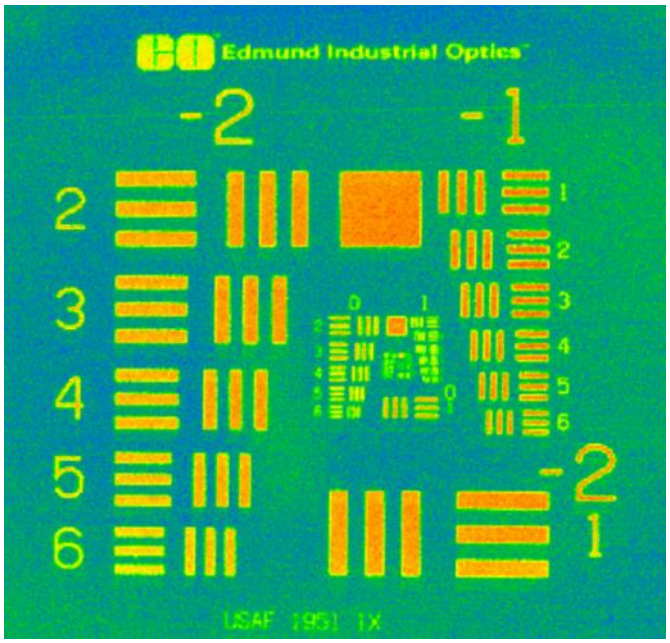

Figure 3.11 Negative 1951 USAF target.

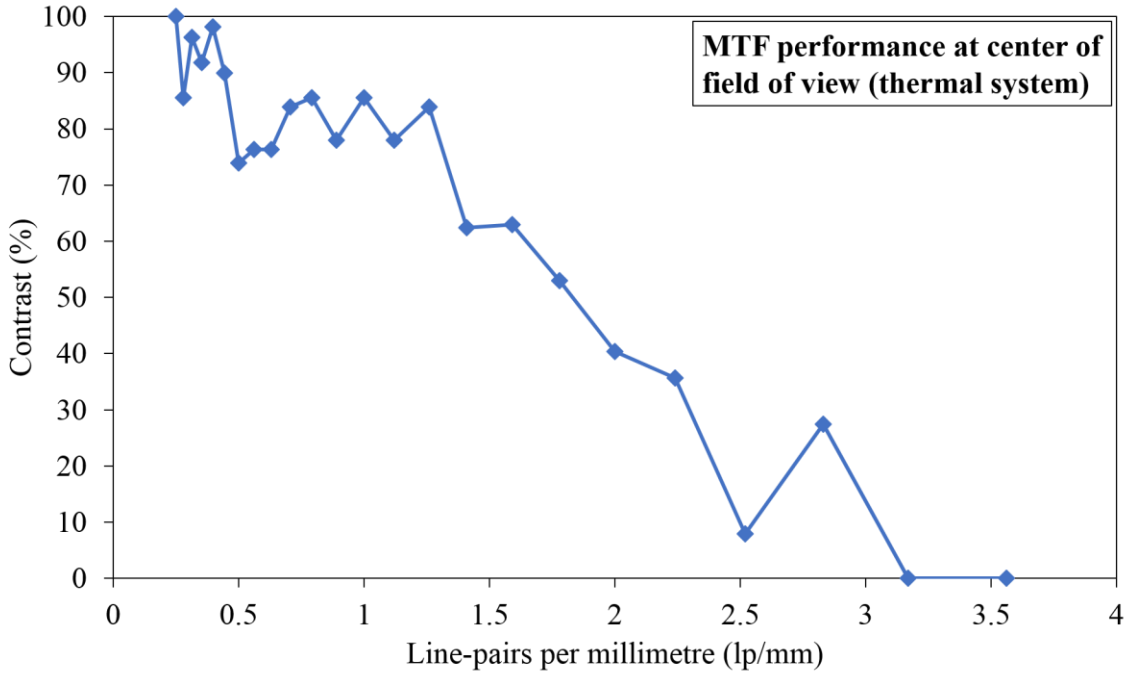

Figure 3.12 MTF of the optical system at centre of the infrared camera's field of view.

3.1.6 Distortion correction for thermal images

The images captured by the thermal system are distorted as the viewport is not situated directly above the powder bed. Infrared radiation reflected from the powder bed passed through the viewport at an angle before reaching the mirror. This caused the images captured to be distorted. The Camera Calibrator app in MATLAB was used to correct for the distortions present in the images. The app employs the calibration model developed by Zhang [78]. The calibration of a camera involves the approximation of the camera intrinsics, extrinsics and lens distortion parameters which are critical for accurate identification of defects. Camera calibration is also essential for post-processing operations, such as compositing images and matching of features between optical and infrared images.

The camera's location in a three-dimensional (3D) scene is represented by the extrinsic parameters which include a rotation, R and a translation, t as represented in Figure 3.13. The camera's optical centre (i.e., principal point, α) and focal length are represented by the intrinsic parameters. The intrinsic parameters are denoted by a matrix, K. The extrinsic parameters transform 3D world coordinates into 3D camera coordinates while the intrinsic parameters project 3D camera coordinates into the 2D sensor of camera.O_w, O_i and O_p are the origins of world coordinates, image and pixel respectively as illustrated in Figure 3.13. Radial and tangential distortions are also examined for the correction of distortions present in captured images. Radial distortions happen when light rays at the edges of a lens bend more than they do at its principal point. Tangential distortions happen when the lens and the image plane are not parallel.

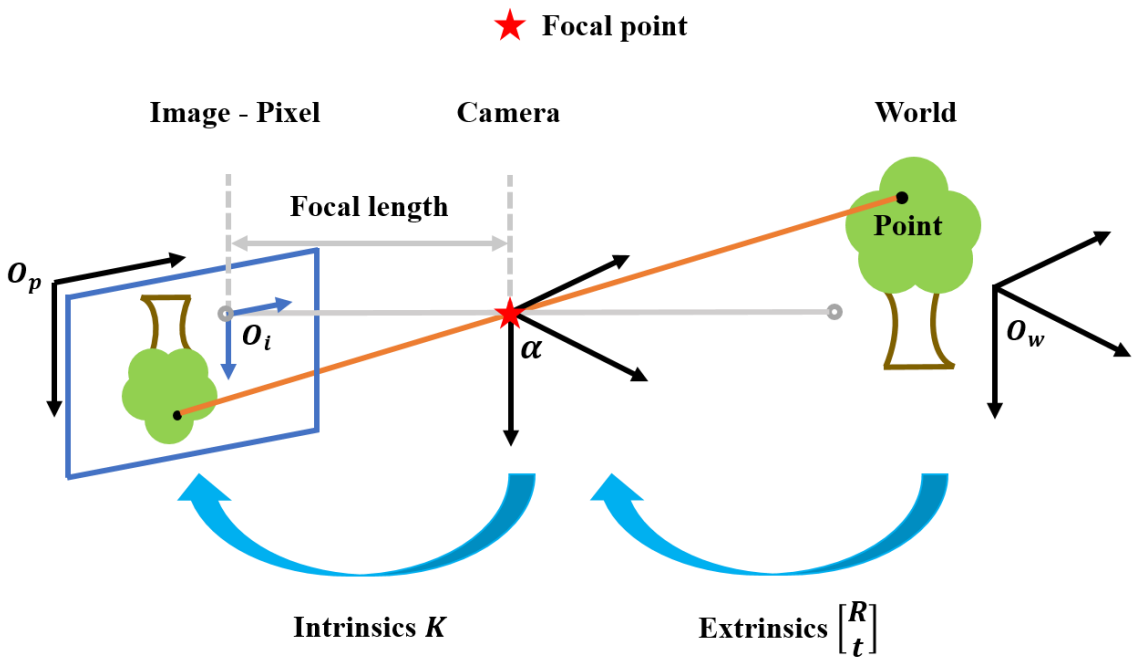

Figure 3.13 Transformation of world points to camera coordinates and mapping of camera coordinates into image plane [80].

A set of reference points on a calibration target is required to calibrate a camera. The world coordinates of these reference points are determined from the image of the calibration target. Their corresponding image coordinates are detected in the image. A checkerboard calibration pattern was printed by DragonFly 2020 Pro 3D Printer with silver and nonconductive thermoplastic. Each checkerboard square is 10 mm in length as shown in Figure 3.14 (a). The checkerboard was captured at different orientations relative to the infrared camera. The images of the checkerboard were captured at a distance equivalent to the actual working distance during in-situ monitoring of the powder bed. The infrared camera was placed above the chamber of the machine (Figure 3.2) and the checkerboard was positioned on the platform of the chamber. It is recommended to capture 10 to 20 checkerboard images to ensure the calibration is accurate. One of the checkerboard images must be captured at the same location as the monitored area for identifying the rotation and translation matrix associated with the inspected region. Calibration was performed by the Camera Calibrator app to compute the intrinsic parameters, extrinsic parameters and distortion coefficients. The calibration algorithm and detailed guidelines on the calibration of a camera can be found in [79-81]. The calibration results would then be evaluated by examining the reprojection errors. Reprojection errors are the distances, measured in pixels, between the points from the checkerboard image and the points projected using the camera parameters. Mean projections errors of one pixel or less are generally accepted [79, 81]. The corrected image is illustrated in Figure 3.14 (b) and the overall reprojection error is 0.45 pixels as seen in Figure 3.15.

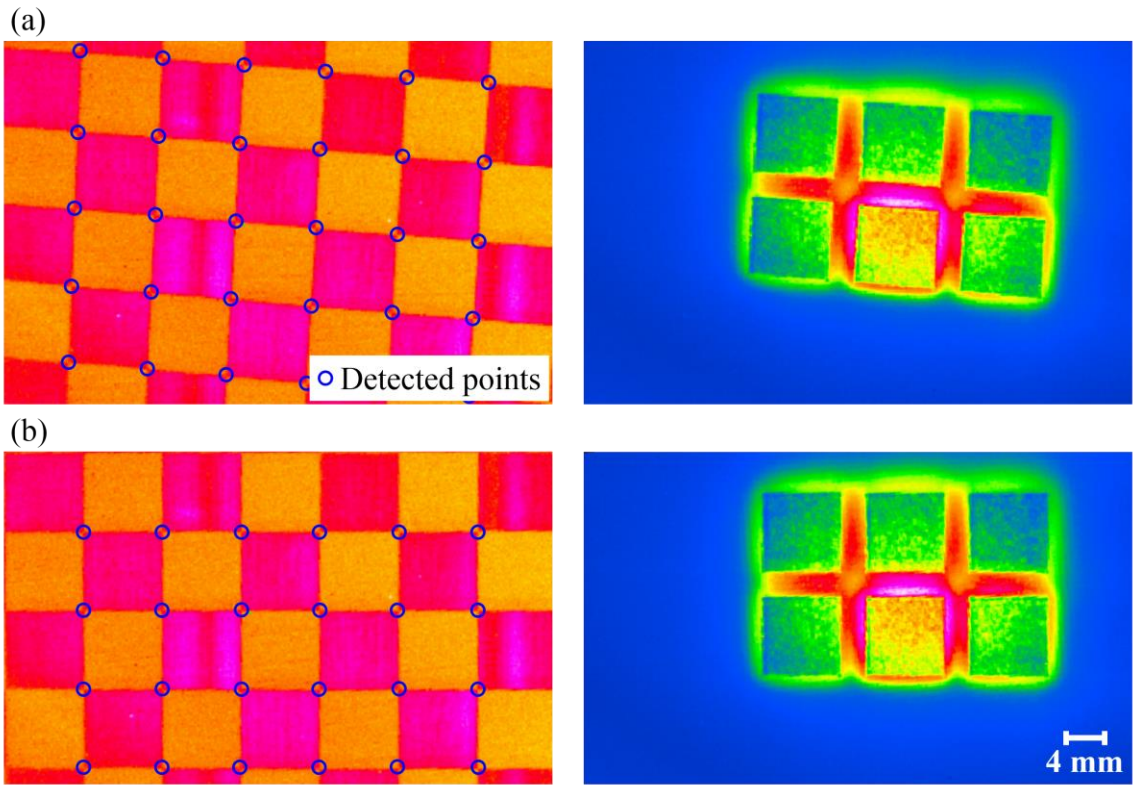

Figure 3.14 Images of the checkerboard and powder bed (a) captured by the thermal system and (b) corrected for distortion.

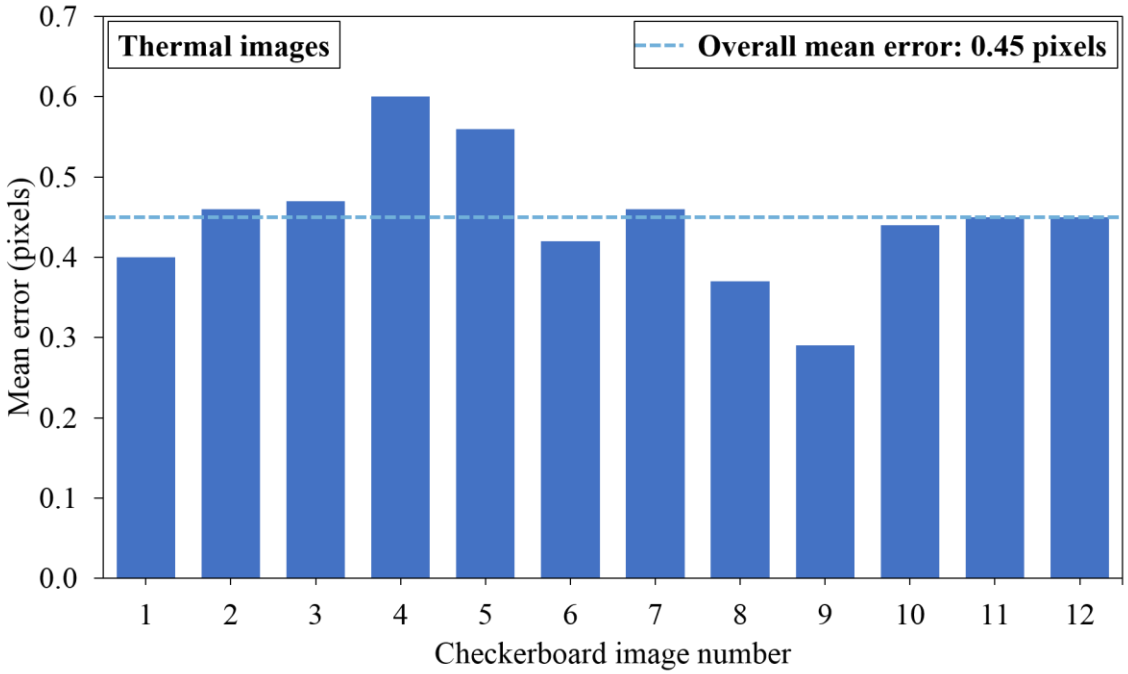

Figure 3.15 Mean reprojection errors associated with checkerboard images captured by infrared camera.

3.2 Materials and methods

3.2.1 Powder material

316L stainless steel powders were used in this research. The chemical compositions of the powders are listed in Table 3.2. The powders have a spherical shape with diameters ranging from 20 to 53 μm.

Table 3.2 Chemical composition of as-used 316L stainless steel powders.

Element	Fe	Cr	Ni	Mo	Mn	Si	O	C
Content (wt.%)	Balance	16 to 18	11 to 14	2 to 3	≤2.0	≤1.0	0.062	≤0.03

3.2.2 Design of specimens

3.2.2.1 Minimum defect size

Specimens were printed with cylindrical and square holes to study the minimum size observable from the DSLR and infrared cameras. These specimens were designed with embedded holes to simulate the presence of defects during printing. While the resolutions of these cameras have been stated in sections 3.1.1.1 and 3.1.1.2, the actual size of defects observable from the captured images is dependent on several factors. Different scanning parameters, such as laser power and scanning speed will produce printed parts with varying surface textures. The reflection of light off rough surfaces, for instance, is diffuse in nature. Furthermore, defects such as porosities, which are gases, interact with light differently as compared to solidified metal surfaces. The interaction of light with surfaces of different textures may result in porosities and solidified metal having similar greyscale intensity values. This signifies that defective regions are indistinguishable from non-defective regions of the printed part.

Defects, which have different emissivities and thermal conductivities from the bulk material, exhibit different temperature profiles and cooling rates. This principle allows defects to be identified in thermal images. However, when the size of a defect is significantly small, the difference in temperature between the defect and the bulk material is minimal. Similarly, this will result in defective regions being indistinguishable from non-defective regions of the printed part.

The actual defects present in selectively laser melted parts come in various geometries and sizes. Although cylindrical and square holes do not encompass all the possible defects present in printed parts, the study do shed light on the minimum size of defects

identifiable from the captured images. This information provides users with a better understanding on the smallest defects detectable visually for preliminary analysis of images.

Two sets of specimens were printed. Each set of specimens consisted of a rectangular bar and six cuboids. The difference between the two sets of specimens is the geometry of the holes. Cylindrical holes and square holes of varying sizes were printed for each set of specimens. Figure 3.16 (a) illustrate the design and dimensions of the rectangular bar with cylindrical holes of varying diameters and 8 mm depth. Figure 3.16 (b) illustrate the designs and dimensions of the six cuboids with cylindrical holes of varying diameters and 3 mm depth. Figure 3.17 (a) illustrate the design and dimensions of the rectangular bar with square holes of varying lengths and 8 mm depth. Figure 3.17 (b) illustrate the designs and dimensions of the cuboids with square holes of varying lengths and 3 mm depth. The dimensions are in millimetres. The six cuboids shown in Figure 3.16 (b) were placed 5 mm apart from each other during printing. The six cuboids shown in Figure 3.17 (b) were placed 5 mm apart from each other during printing.

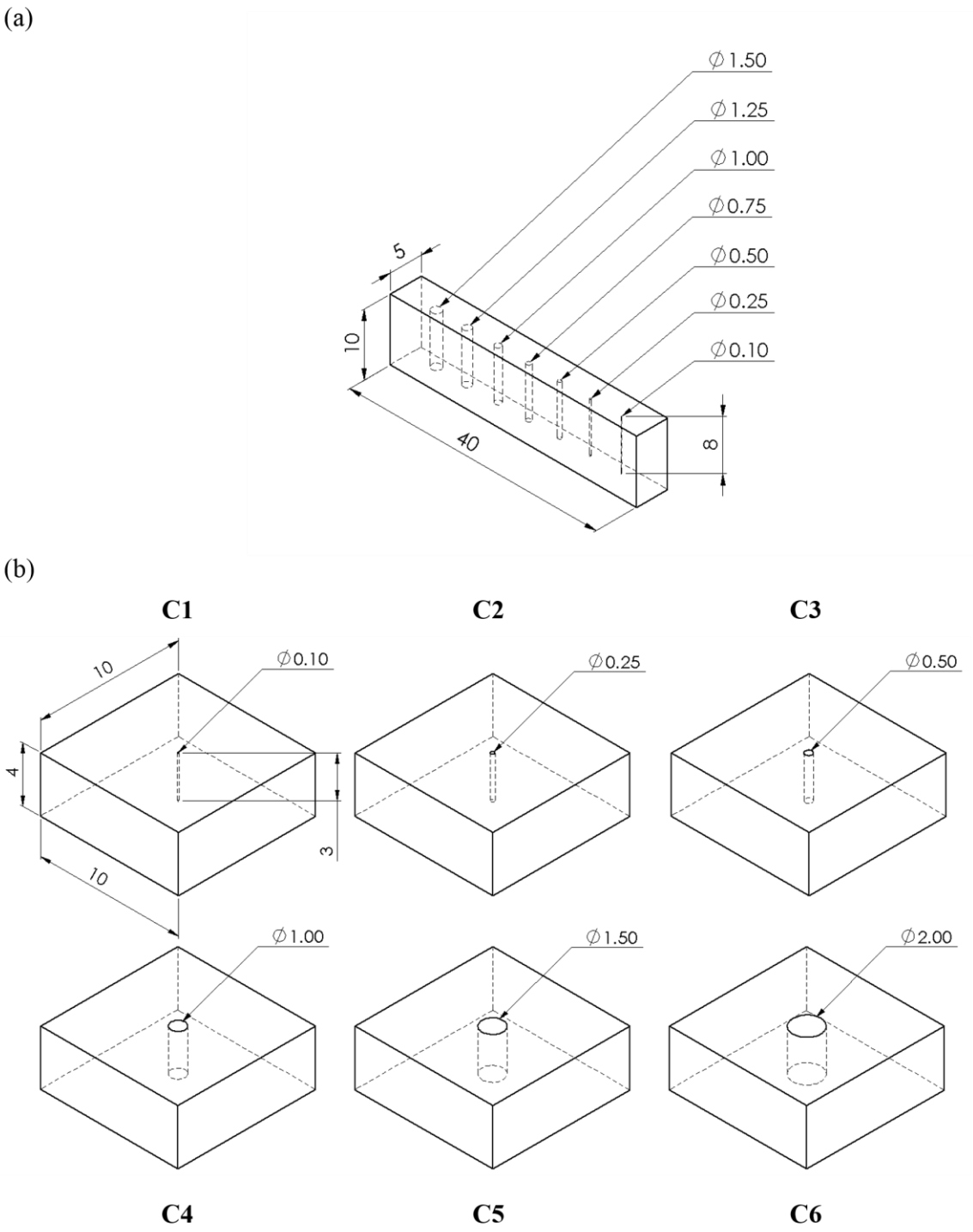

Figure 3.16 Dimensions of (a) rectangular bar with cylindrical holes and (b) cuboids with cylindrical holes in millimetres.

(a)

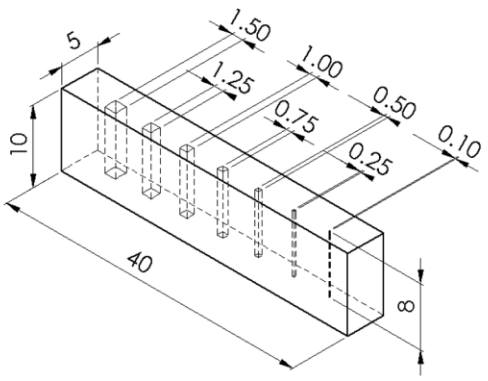

(b)

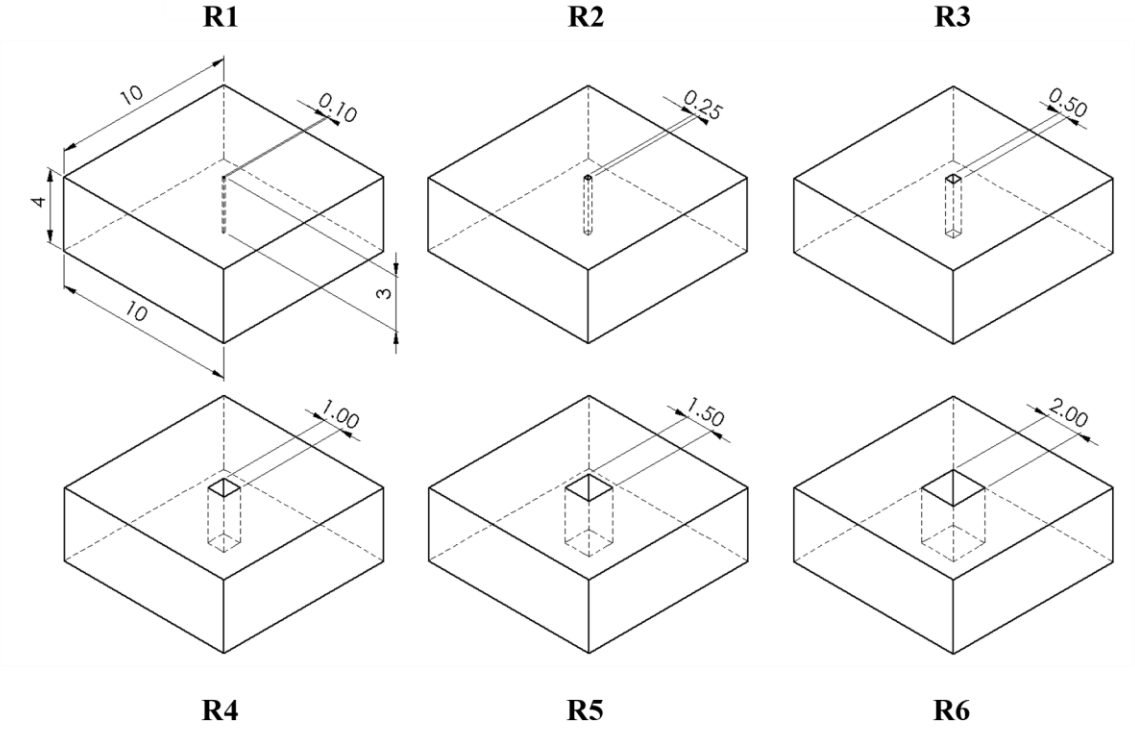

Figure 3.17 Dimensions of (a) rectangular bar with square holes and (b) cuboids with square holes in millimetres.

The printing parameters associated with the two sets of specimens were kept constant of which laser power was set to 350 W and scanning speed was set to 550 mms^{-1}. The hatch pattern was stripe with a hatch spacing of 0.14 mm and layer thickness was set to 50 µm.

It should be highlighted that both the rectangular bar and cuboids were designed with cylindrical holes. The difference lies in the number of cylindrical holes present in these specimens. The rectangular bar contains multiple cylindrical holes while each cuboid contains only one cylindrical hole. The design of the rectangular bar enables the temperature profile to be studied across a single specimen, i.e., the temperature variations across multiple cylindrical holes and the bulk material. While the rectangular bar containing multiple cylindrical holes was designed mainly for studying its thermal images, they were also printed for monitoring by the optical system to ensure consistency between the specimens studied for both systems. Likewise, the same rationale was applied to the design of the rectangular bar and cuboids with square holes.

3.2.2.2 Correlation studies

Thijs et al. [82] examined the influence of energy density on the microstructure of Ti-6Al-4V alloy processed by SLM. They noted the presence of martensitic and intermetallic phases when the rectangular specimens were printed with different energy densities. However, a more detailed study relating the effects of energy density on the occurrence of defects during printing is needed. Energy density E (in Jm^{-3}) is defined as the average applied energy per volume of material during the scanning of a powder layer and is computed as [82]

$$E = \frac{P}{v \times h \times t} \tag{3.3}$$

where P is the laser power (in Js^{-1}), v is the scanning speed (in ms^{-1}), h is the hatch spacing (in m) and t is the powder layer thickness (in m).

The laser power and scanning speed were varied while hatch spacing of 0.14 mm and layer thickness of 50 µm remained constant throughout the experiment. Hence, the energy density is expressed as a ratio between the laser power and scanning speed. Based on preliminary experiments, a laser power (P) of 175 W and scanning speed (v) of 550 mms^{-1} were considered as the reference data set, denoted as $E_{P,v}$. The details of the preliminary experiment can be found in Appendix A.

Ten sets of 316L stainless steel specimens were fabricated by the SLM process. Each set of specimens consisted of a cylinder and a sub-size tensile coupon. The cylindrical specimens are 8 mm in diameter and 8 mm in height. The printed cylinders are shown in Figure 3.18. Sub-size dog bone shaped tensile coupons were printed with dimensions in accordance to ASTM E8 / E8M-15a as shown in Figure 3.19 [83]. The images of the cylinders were captured by the IMS. Tensile tests were carried out to determine the ultimate and yield strengths of the tensile coupons. The results based on optical imaging of the cylinders will be correlated to the densities and mechanical properties of the cylinders and tensile coupons respectively. The results based on optical imaging of the cylinders will also be correlated to the actual defects present in them, validated via micro CT. The results based on thermal imaging of the cylinders will be correlated to their densities. Table 3.3 shows the scanning parameters used for printing each set of specimens.

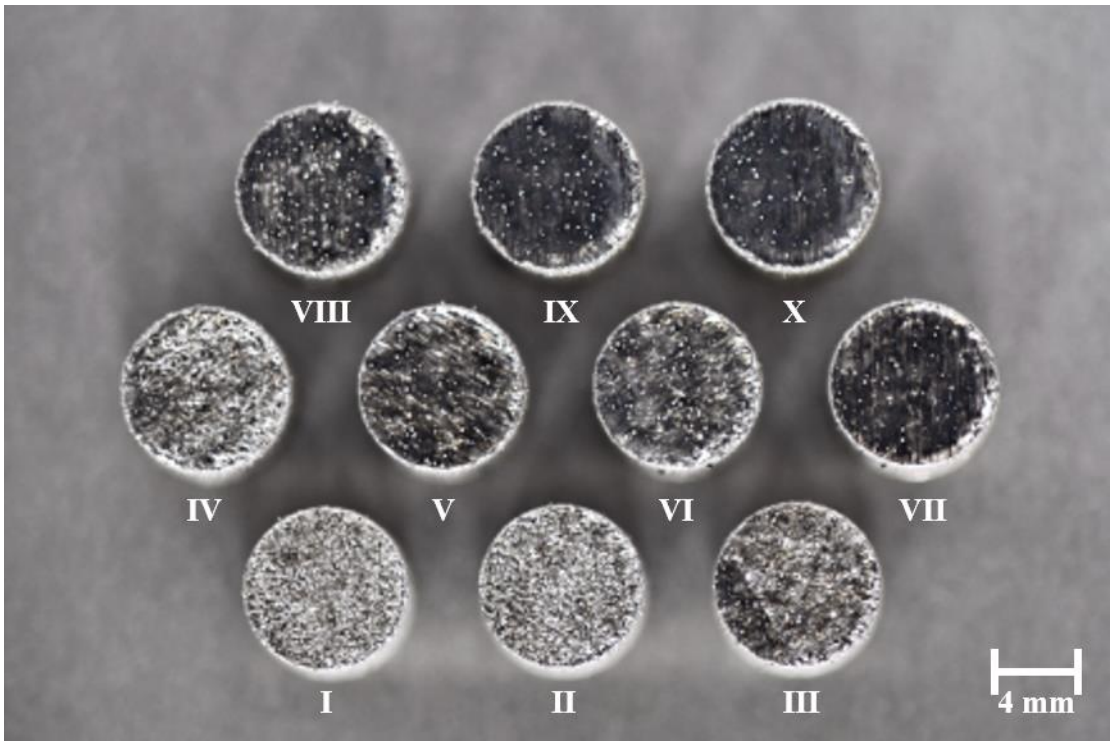

Figure 3.18 Cylinders printed by SLM process (top view).

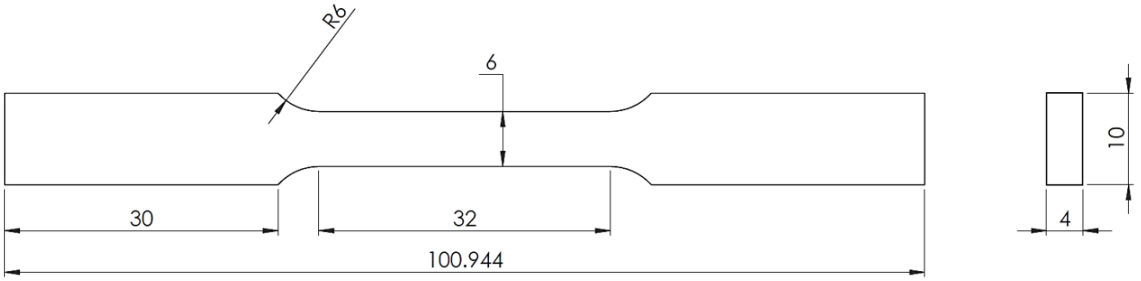

Figure 3.19 Dimensions of sub-size tensile coupon in millimetres.

Table 3.3 Printing parameters for ten sets of specimens and their energy density ratios.

Specimen	Laser power (W)	Scanning speed (mms^{-1})	Notation	Energy density ratio
I	87.5	550	$E_{0.5P,v}$	0.5
II	175	1100	$E_{P,2v}$	0.5
III	175	550	$E_{P,v}$	1.0
IV	350	1100	$E_{2P,2v}$	1.0
V	175	367	$E_{P,0.67v}$	1.5
VI	262.5	550	$E_{1.5P,v}$	1.5
VII	175	275	$E_{P,0.5v}$	2.0
VIII	350	550	$E_{2P,v}$	2.0
IX	350	367	$E_{2P,0.67v}$	3.0
X	350	275	$E_{2P,0.5v}$	4.0

Before the start of the print job, the optical system captures an initial image of the uniformly coated powder bed. During printing, two images are captured for each layer of powder deposition — one after scanning but before recoating, and another after recoating of the scanned layer. These optical images are then post processed via image processing for identification and evaluation of features. As the field of view does not cover the entire powder bed, only the cylinders will be monitored. The features evaluated for each

cylinder will be used to correlate with the mechanical properties of the respective tensile coupons. The features evaluated for each cylinder will also be used to correlate with the actual defects present in them.

The thermal system captures images with a frequency determined by the end user. A frequency of 10 Hz, for example, means ten thermal images are captured per second. These thermal images are then post processed via image processing for identification and evaluation of thermal signatures. The thermal signatures evaluated for each cylinder will be used to correlate with their densities.

Although cylindrical specimens were printed for correlation studies, it must be emphasised that the IMS is capable of detecting and evaluating anomalies in captured optical and thermal images, irrespective of the printed part's geometry. Correlation studies involve the development of robust algorithms in detecting and evaluating anomalies in optical and thermal images captured in-situ. These anomalies are referred as features and thermal signatures captured in optical and thermal images respectively. It is believed that the occurrence of these features and thermal signatures directly affects the mechanical properties and the generation of defects in printed parts. Their presence is independent of the printed parts' geometry. This is similar to the fact that defects are inevitably generated in printed parts during the SLM process, regardless of their geometries [84].

The focus is to develop and validate algorithms associated with image processing that can efficiently detect and quantify anomalies in captured images so that results collected can be correlated to the mechanical properties and actual defects present in the printed part. This can be achieved by analysing the greyscale intensity values of pixels for optical

images and temperature gradients of pixels for thermal images, which are not related to the shape of the specimens studied. The idea is to identify and examine pixels with either greyscale intensity values or temperature gradients that deviate significantly from what is deemed as a non-defective pixel, leading to the fabrication of high-quality parts. Cylindrical specimens are simply one of the many geometries that is being chosen to illustrate the feasibility of establishing correlations between images captured in-situ and the corresponding mechanical properties and actual defects present in printed parts. Chapters 4 and 5 will discuss in detail the steps involved in processing the optical and thermal images respectively.

Specimens of other geometries have been printed for other investigations including the minimum defect size identifiable from optical and thermal images. Some of the images captured belonged to parts fabricated for other projects and print jobs of other researchers. These results will be briefly discussed in section 4.4 which focuses on the types of defects identifiable by the IMS.

3.2.3 Archimedes' density test

Density measurements of the printed cylinders were carried out using the Mettler Toledo XS204 analytical balance with a specific density measurement device for solid materials. Vandenbroucke and Kruth [85] investigated the use of SLM as a rapid manufacturing technique for medical applications. They printed titanium alloy blocks and measured the density according to Archimedes' principle in which the mass of a solid is measured in air and subsequently in an auxiliary liquid with known density. The liquid used in this case is ethanol. The density of the solid can be calculated based on

$$\rho = \frac{A}{A-B} \times (\rho_0 - \rho_L) + \rho_L \quad (3.4)$$

where ρ is the density of the solid (in gcm^{-3}), A is the mass of the solid in air (in g), B is the mass of the solid in the auxiliary liquid (in g), ρ_0 is the density of the auxiliary liquid (in gcm^{-3}) and ρ_L is the density of air (in gcm^{-3}).

3.2.4 Tensile test

Sub-size dog bone shaped tensile coupons of 316L stainless steel were printed in $x - y$ (flat) direction and removed from the steel substrate using wire electrical discharge machining. Tensile tests were carried out in displacement control using an Instron 8501 universal testing machine at room temperature. An axial extensometer of 10 mm gauge length was attached to the gauge region of the tensile specimens for strain measurements. Displacement rate of crosshead was set at 1 mm/min. Tensile yield strength was determined by an offset yield point at 0.2% strain.

3.2.5 Micro computed tomography

The Bruker SkyScan 1173 micro CT system with SkyScan 1173 control software was used to scan the cylindrical samples. The micro focus x-ray source was set at 130 kV with a current of 62 µA. The spatial resolution for scanning of the cylinders was 9.9 µm. The acquisition parameters were set to a rotation step of 0.2° and frame averaging of 10. The images were then reconstructed into cross-sectional images with NRecon software. The interlayer distance between each CT image was 10 µm. The analysis of the dataset was carried out using CTAn software. The volume and size distribution of the defects were calculated during the analysis. CTVox software was used to visualise the reconstructed part.

3.2.6 Optical and scanning electron microscopy

Optical microscopy was conducted using the Axioskop 2 MAT. The magnification, focus and brightness were adjusted and images of the cylinders' top surface (polished and etched) were taken.

JEOL JSM-5600LV scanning electron microscope (SEM) was used to examine the surface morphology of the printed cylinders under vacuum. Each cylinder was placed on a carbon tape before being mounted on the microscope stage. The working distance, magnification, focus, brightness and contrast were adjusted and SEM images of the cylinders' top surface were taken.

3.3 Summary

The proposed IMS was designed to allow monitoring of the powder bed via optical and infrared sensors. The DSLR camera was placed outside of the machine to capture optical images of the powder bed. Light was reflected from the powder bed and directed to the lens of the DSLR camera using a silver coated mirror. The infrared camera was placed above the chamber of the machine as it is more susceptible to environmental disturbances than the optical camera. Optical accessories including a gold dichroic beam splitter and a silver coated mirror were used. The viewport of the machine was replaced from the original glass material to that of calcium fluoride, enabling the transmission of mid-wavelength infrared signals.

The procedures taken to achieve uniform illumination of the powder bed and examine the emissivity of 316L stainless steel specimens with different surface textures were outlined. The steps taken to evaluate the modulation transfer functions of the optical and infrared cameras and correct the distortions present in thermal images were explained.

Rectangular bars and cuboids were printed with cylindrical and square holes to study the minimum size observable from the DSLR and infrared cameras. These specimens were designed with embedded holes to simulate the presence of defects during printing. Ten sets of 316L stainless steel specimens were fabricated by the SLM process for correlation studies. Each set of specimens consisted of a cylinder and a sub-size tensile coupon. Archimedes' density test and tensile test were carried out to investigate the mechanical properties of the printed specimens. Micro CT was used to examine the actual 3D defects in the printed cylinders through reconstruction of the CT images, and more importantly, to justify the viability of using optical imaging as a solution for evaluating defects in printed parts.

CHAPTER 4: RESULTS AND DISCUSSION — OPTICAL IMAGES

This chapter begins with the discussion on the actual size of defects observable from the captured images. Subsequently, the correlation established between features captured in optical images during fabrication and the mechanical properties of printed parts are presented. The correlation between features captured in optical images during fabrication and the actual defects identified by x-ray micro computed tomography (CT) are also investigated.

4.1 Minimum defect size

The minimum size of cylindrical and square holes observable from the captured images were studied. As discussed in section 3.2.2.1, cylindrical holes and square holes of varying sizes were printed for each set of specimens consisting of a rectangular bar and six cuboids. Due to the layer-by-layer nature of printing, unmelted metal powders fill up the supposedly porous part of the printed specimens. The rectangular bar and cuboids C3 to C6 containing cylindrical holes designed with diameters of 0.5 mm and above are easily identified and captured in images as shown in Figure 4.1. Cylindrical holes with a diameter of 0.1 mm are unobservable from both Figures 4.1 (a) and (b). Cylindrical holes with a diameter of 0.25 mm are barely visible as well. Hence, it can be concluded that cylindrical holes with diameters of 0.5 mm and above are detectable from the raw images captured.

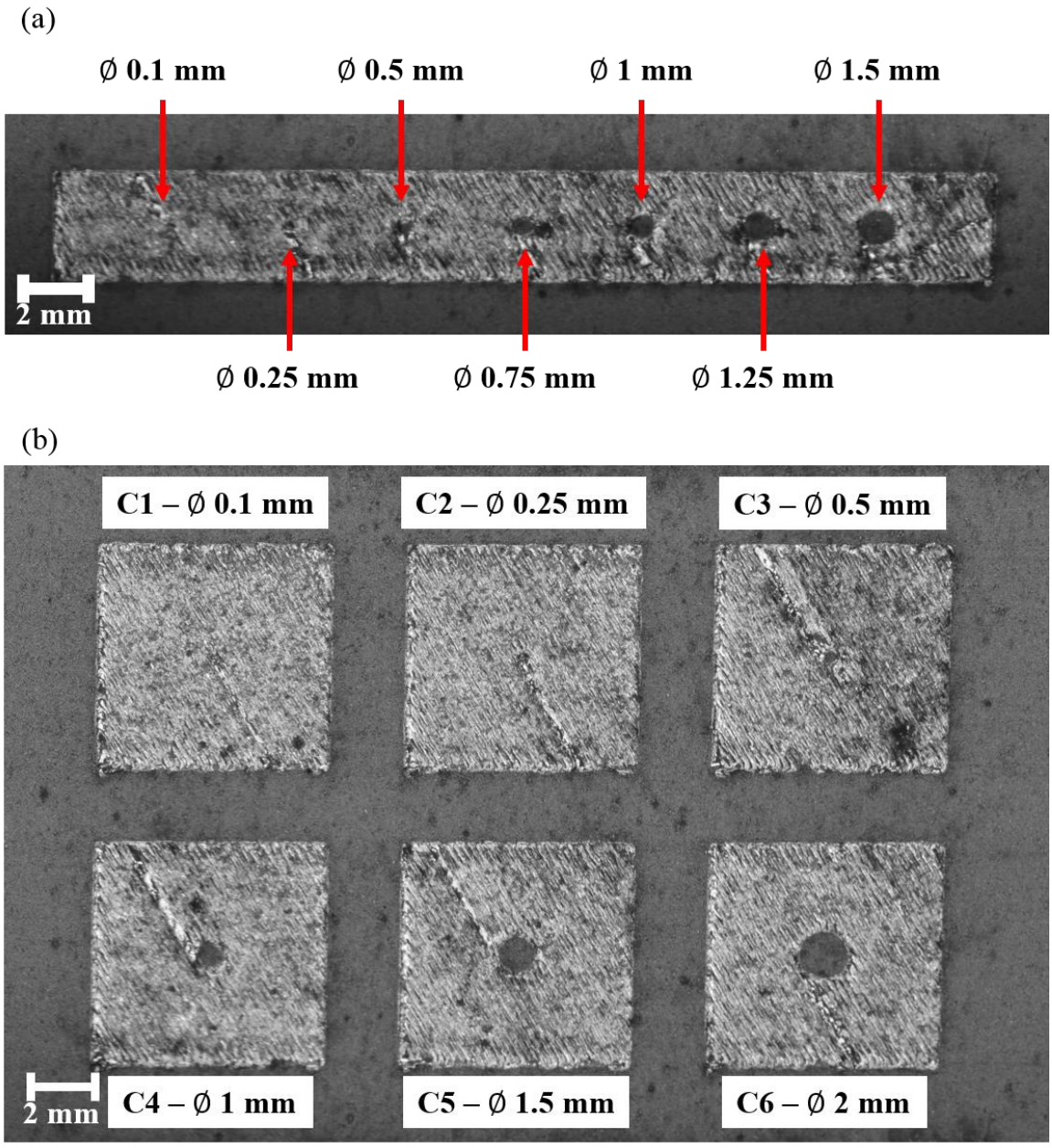

Figure 4.1 Captured images of (a) rectangular bar with cylindrical holes and (b) cuboids with cylindrical holes.

Similar to the case of cylindrical holes, the rectangular bar and cuboids R3 to R6 containing square holes with lengths of 0.5 mm and above are easily identified and captured in images as shown in Figure 4.2. Square holes with lengths of 0.1 mm are

unobservable from both Figures 4.2 (a) and (b). Square holes with lengths of 0.25 mm were barely visible as well. Hence, it can be concluded that square holes with lengths of 0.5 mm and above are detectable from the raw images captured.

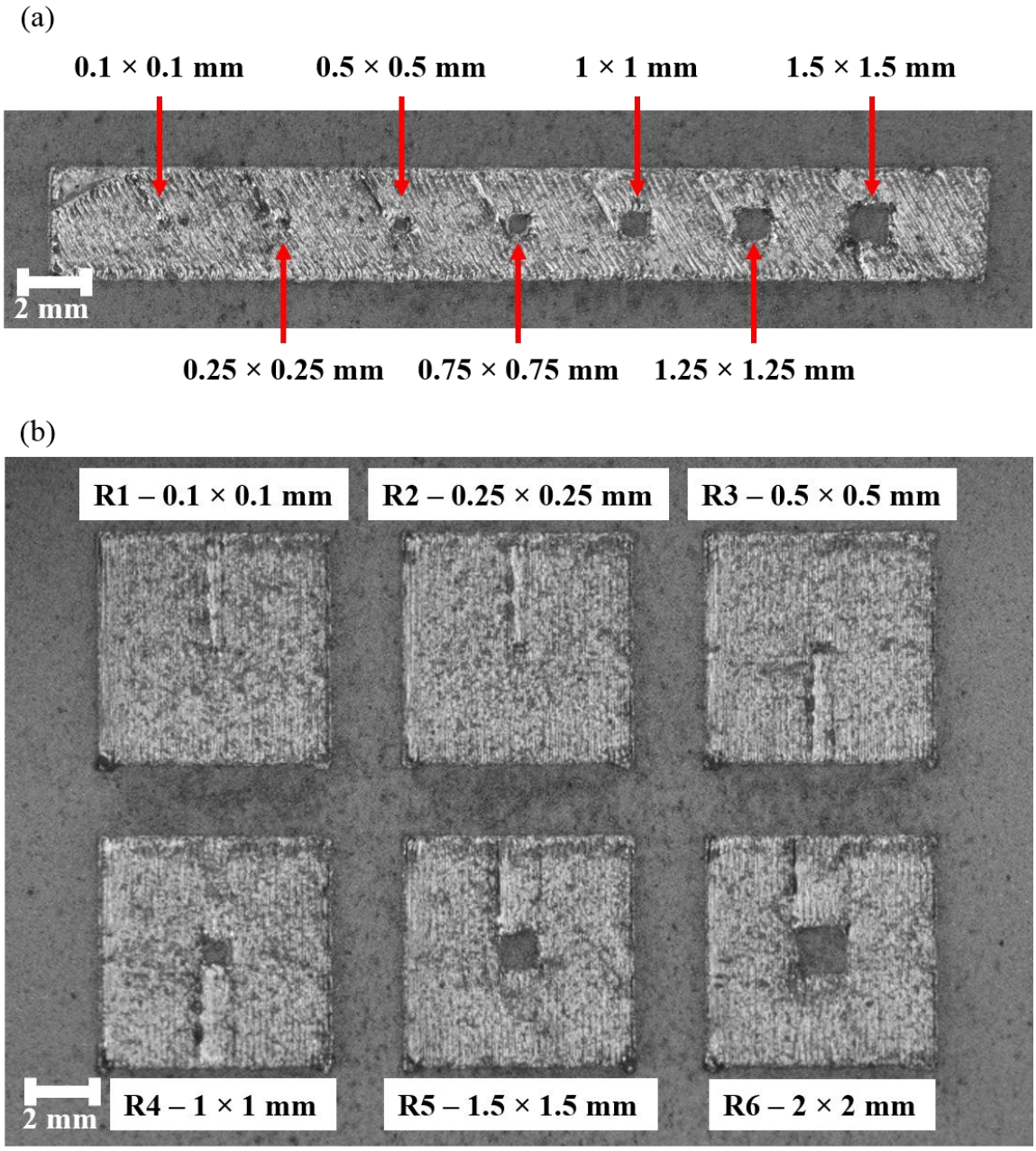

Figure 4.2 Captured images of (a) rectangular bar with square holes and (b) cuboids with square holes.

4.2 Correlation between optical images and mechanical properties of printed parts

This section examines the establishment of a relationship between the features present in optical images captured in-situ and the parts' mechanical properties. Features were segmented and evaluated from the optical images. They were then compared and correlated with the densities and mechanical properties of the respective printed parts.

Only the optical camera was used in this study. The printing of cylindrical specimens was monitored by the optical camera. As discussed in section 3.2.2.2, cylindrical specimens are simply one of the many geometries that is being chosen to illustrate the feasibility of establishing a correlation between images captured in-situ and the corresponding mechanical properties of printed parts. It is the development of robust algorithms for detecting and evaluating anomalies in optical images captured in-situ that is most critical. Nonetheless, cylindrical specimens were chosen due to their circular cross section. More cylindrical specimens can be fitted into the in-situ monitoring system's field of view as compared to specimens of other cross sections, such as square, enabling more printing parameters to be investigated in a single print job.

A preliminary investigation was carried out prior to the results represented in this section. Six sets of 316L stainless steel specimens were printed with varying energy densities. Each set of specimens consisted of a cuboid and a sub-size tensile coupon. The preliminary investigation was performed to explore the possibility of establishing a correlation between the features captured in optical images during printing and the specimens' mechanical properties. The findings of the preliminary investigation can be found in Appendix B. Upon the establishment of a correlation, the investigation was

further expanded to include specimens printed with more energy densities, i.e., ten sets of specimens presented in section 4.2.

4.2.1 Density and tensile tests

The average densities of the ten cylinders based on Archimedes' principle and ultimate and yield strengths of the tensile coupons are shown in Figure 4.3. Each data point for the densities of the cylinders is an average of three measurements. The individual density measurements for the ten cylinders can be found in Appendix C.

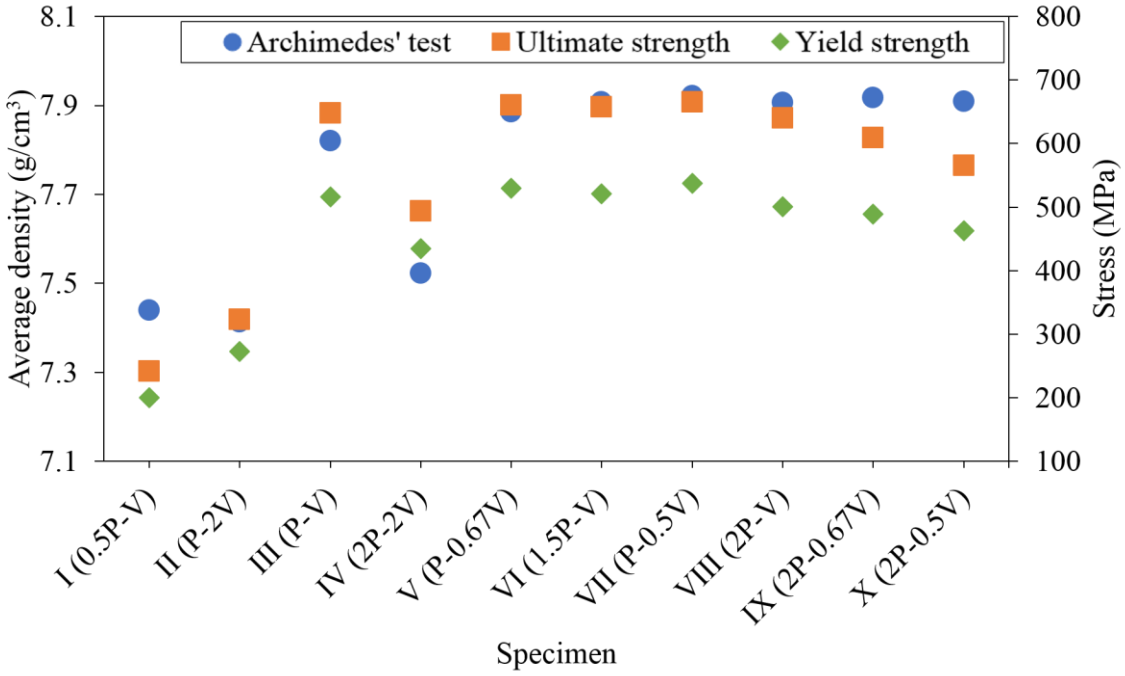

Figure 4.3 Average densities, ultimate and yield strengths of ten specimens.

Based on the results of Archimedes' test, a general trend shows that an increase in the energy density ratio from 0.5 to 2.0 leads to an increase in the average density of the cylinders. Following which, the average density remains relatively constant for cylinders with energy density ratios of 3.0 and 4.0 as powders are fully melted. It should be noted

that the average densities of cylinders II and IV are lower than cylinders I and III respectively. Despite having the same energy density ratio, a higher scanning speed has resulted in cylinders II and IV being less dense than their counterpart specimens.

The ultimate strength and the yield strength of the ten tensile coupons were measured and shown in Figure 4.3. Both properties exhibit an increase in value with an increase in energy density ratio of the tensile coupons from 0.5 to 2.0. Following which, the ultimate and yield strengths exhibit a slight decrease for tensile coupons of energy density ratios 3.0 and 4.0. Similarly, tensile coupon IV has notably lower ultimate and yield strengths as compared to tensile coupon III of a same energy density ratio. Tensile coupon IV was printed with a relatively high scanning speed as compared to tensile coupon III. This reduces the allowable time that the laser beam is in contact with each powder particle which may otherwise ensure complete melting. Therefore, the ultimate and yield strengths of tensile coupon IV have been compromised.

As the high energy laser scans across the powder bed for specimens VIII to X, the melting and solidification process are completed within an appreciably short period of time, generating a huge temperature gradient and a high stress field. An immense amount of residual thermal stress is accumulated in the fabricated specimen [86]. The thermal energy accumulated in the printed layer cannot be dissipated rapidly in materials with low thermal conductivity. As a result, cracks are formed to release the stresses as seen in Figure 4.4. These transverse cracks reduce the load-bearing section of the tensile coupons and act as stress concentration sites, lowering the ultimate and yield strengths. Density, on the other hand, remains relatively high as the high laser power ensured sufficient energy input into the melt pool to fully melt the stainless steel powders.

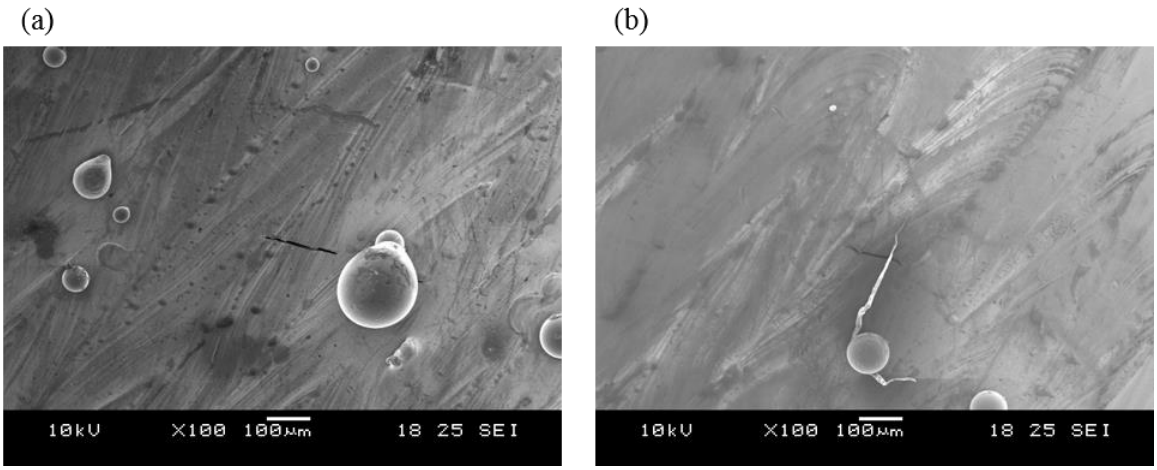

Figure 4.4 Scanning electron microscopy images of cylinders (a) IX and (b) X illustrating the presence of cracks.

It can be observed that the particles in Figure 4.4 have diameters in the range of 100 µm. These particles are much larger in diameter than the stainless steel powders used. They are formed via collision and coalescence of hot ejecta which are expelled from the melt pool during laser scanning. The hot ejecta (spheroidal agglomerate) are usually on the order of 100 to 200 µm in diameter [87, 88].

4.2.2 Extraction of features

The optical images of the cylinders after recoating for each layer were used for image processing and analysis. An image captured during the printing process is shown in Figure 4.5. These photographs were captured in greyscale and saved as 8-bit intensity images in TIFF format. The range of the 8-bit intensity images is between 0 and 255. Greyscale intensity values of 0 and 255 represent black and white pixels respectively.

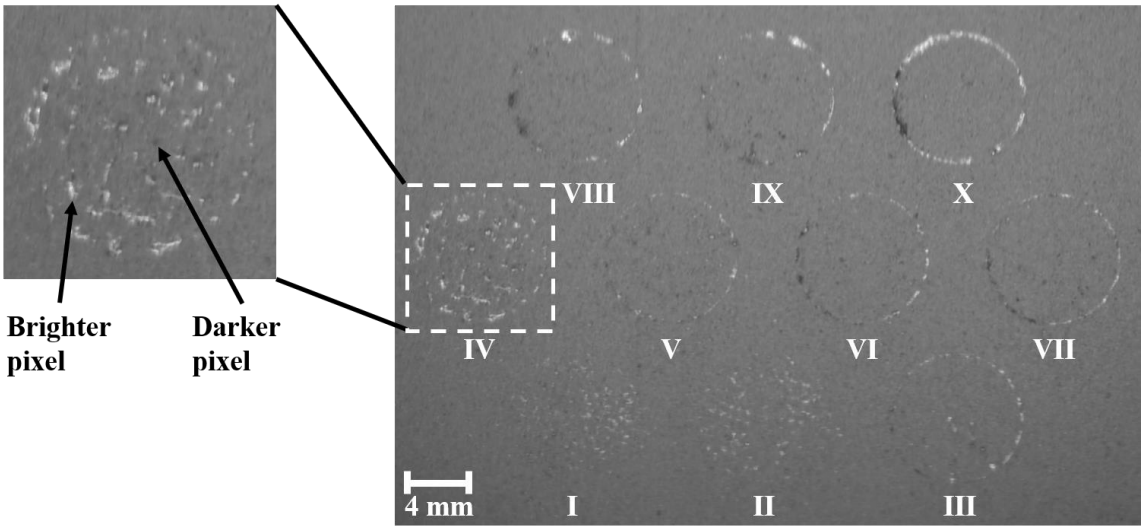

Figure 4.5 Recoated layer of powder bed captured during printing.

Features captured in the optical images are represented by pixels that are either brighter or darker than that of the metal powders as illustrated in Figure 4.5. Ideally, the powder bed should be uniformly recoated with powders after the scanning of each layer, i.e., there should not be any features elevated from the surface of the powder bed after recoating (Figure 4.6 (a)). However, features may arise from factors such as argon gas flow rate and the variations in printing parameters during the actual printing process. Their presence may be an indicator to the quality of a print. Information such as the number, area and location of the features can be extracted from the optical images captured after each layer of recoating for a print. MATLAB was used for image processing [89].

The initial layer of a uniformly recoated powder bed is captured as the background image before printing starts (Figure 4.6 (a)). The background image acts as a uniform target since the metal powders are of the same reflectivity and are laid evenly on the substrate.

It is needed to account for any non-uniformity of illumination in the captured images. The region of interest (ROI), where each cylinder will be printed is defined by a binary mask, as shown in Figure 4.6 (b). The white pixels of the mask are used to enclose image processing within the ROI. The average greyscale intensity value, I_{avg}, of the initial image is calculated for the area within the ROI. The region will then be filled with the average greyscale intensity value to produce an image, N_0, which will be used as a reference for subsequent image processing (Figure 4.6 (c)).

The black pixels of the binary mask are overlaid onto the optical image of the recoated layer as illustrated in Figure 4.6 (d). The absolute difference will be taken between each optical image of the recoated layers (Figure 4.6 (c)) and the reference image (Figure 4.6 (d)). This step is crucial as any non-uniformity of illumination in the captured images is subtracted away using the reference image, where the latter is derived from the background image. It should be highlighted that despite efforts made to ensure the uniformity of illumination, the edge of the camera's lens and the absence of diffusers for the light emitting diode lights will inevitably cause regions in the images to be non-uniformly lit. The corners of the captured images, for instance, appeared darker as seen in Figure 4.6 (a). While a non-uniformly lit background image (recoated powder bed) will directly influence the average greyscale intensity value of the reference image, the extraction of features from the optical images will not be affected. The important information revealed is represented by the absolute difference between the captured image of each recoated layer and the reference image, and not the average greyscale intensity value itself. The resulting image highlights the presence of features represented by pixels that are of higher greyscale intensity values (brighter) than the background

(Figure 4.6 (e)). Contrast-limited adaptive histogram equalisation is then applied to the image to enhance the contrast between the features and the background (Figure 4.6 (f)). The greyscale intensity range of the image is stretched to reveal more details of the features and allow these features to be distinguished at different illumination levels. The last step involves thresholding the resultant image to obtain binary images, where white pixels represent the features of each recoated layer as seen in Figure 4.6 (g). The flowchart in Figure 4.7 summarises the image processing algorithms used to extract features from the optical images. The features extraction process was performed separately for every cylinder. The layer thickness for each layer of print was 50 µm. Hence, optical images were captured after every 50 µm.

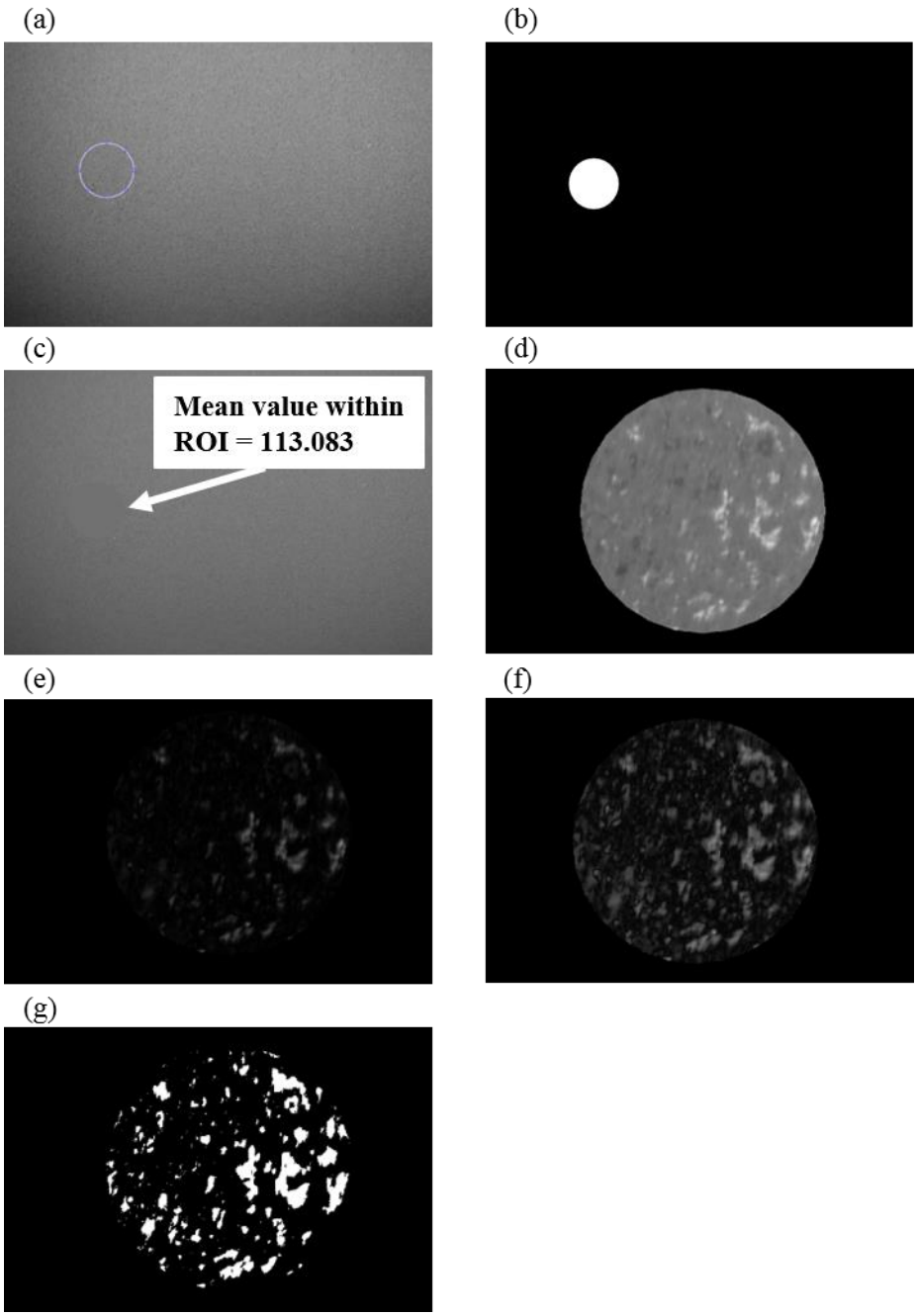

Figure 4.6 (a) Initial layer of recoated powder bed used for calculation of average greyscale intensity value at ROI, (b) binary mask for image processing within ROI, (c) reference image, N_0, ROI is filled with average greyscale intensity value and (d) black pixels of mask overlaid onto one of the cylinders (ROI), (e) revelation of features after difference is taken between (c) and (d), (f) features highlighted after contrast-limited adaptive histogram equalisation is applied and (g) binarised image containing features after thresholding.

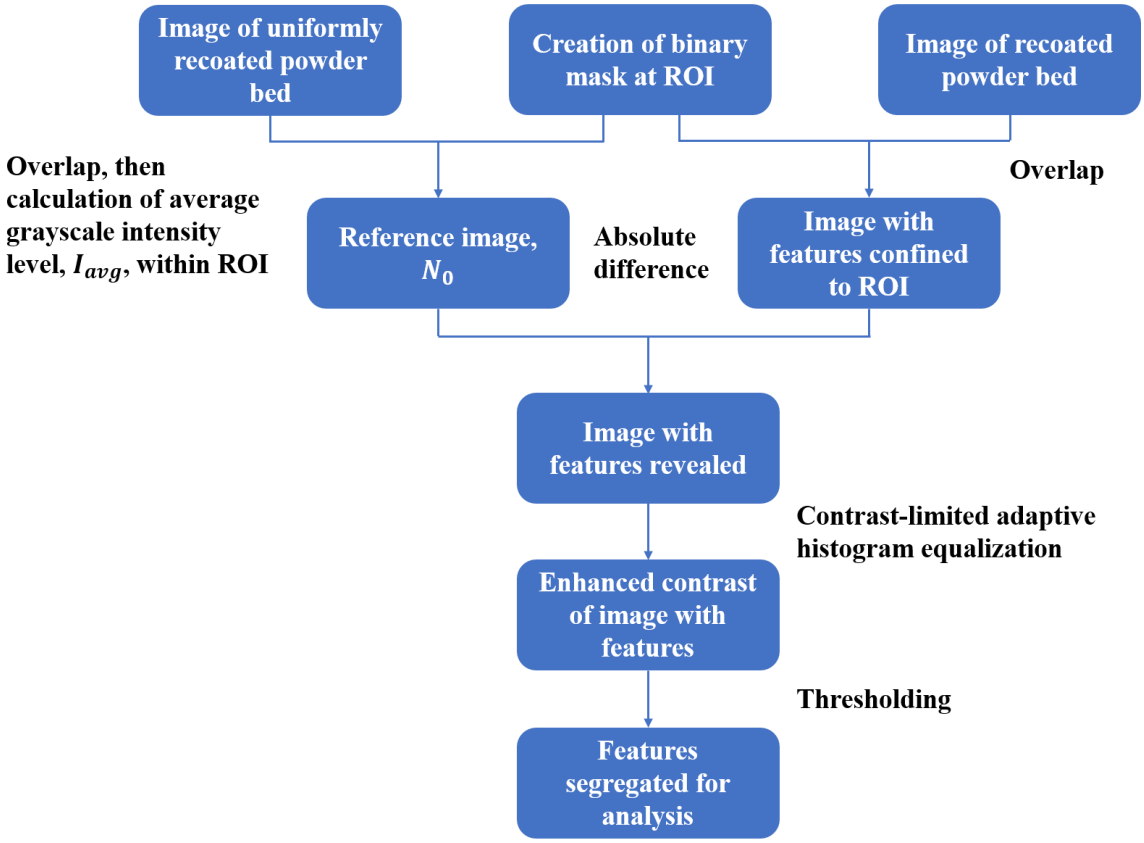

Figure 4.7 Procedures for features extraction from optical images.

A suitable threshold value must be determined in order to binarise an image. The distribution of the pixels' greyscale intensity values is plotted as a histogram. One method to select a threshold value is to locate the minimum number of pixels between two modes on a histogram, i.e., a valley in the histogram. An example is illustrated with Figure 4.8. A greyscale image and its histogram representing the distribution of the pixels' greyscale intensity values are shown in Figures 4.8 (a) and (b) respectively. Pixels with intensity values lesser than the threshold represent the background of the image, while pixels with intensity values more than the threshold depict the objects of the image. The binarised image is shown in Figure 4.8 (c).

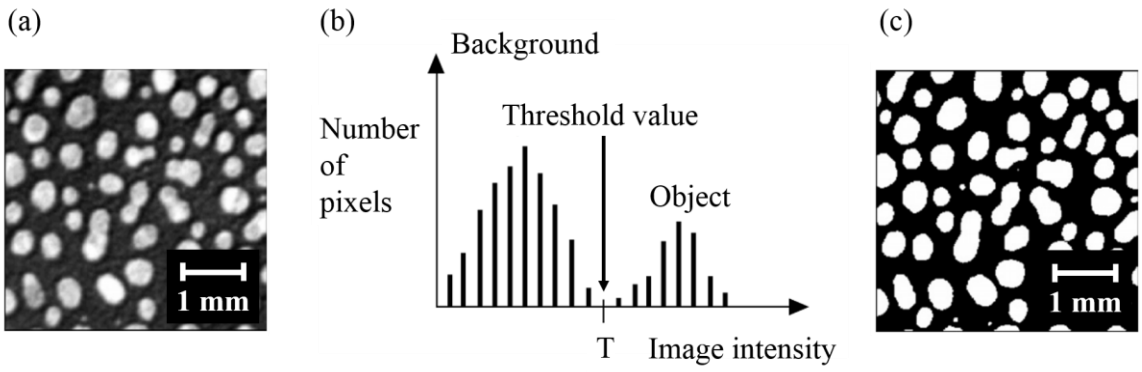

Figure 4.8 (a) Greyscale image, (b) histogram of (a) and (c) binarised image of (a).

The histogram of the obtained image in Figure 4.6 (e) was analysed and shown in Figure 4.9. However, it does not demonstrate the bimodal distribution. The determination of a threshold value based on Figure 4.9 was challenging. Upon enhancing the contrast of the image, a bimodal distribution can be seen from the histogram in Figure 4.10 (a). An enlarged view of the histogram is illustrated at the threshold value in Figure 4.10 (b). The threshold value was set to 52 to obtain the binarised image in Figure 4.6 (g). Other pre-processing steps such as median filtering and gaussian filtering have been carried out but the abovementioned method produced the best thresholding results.

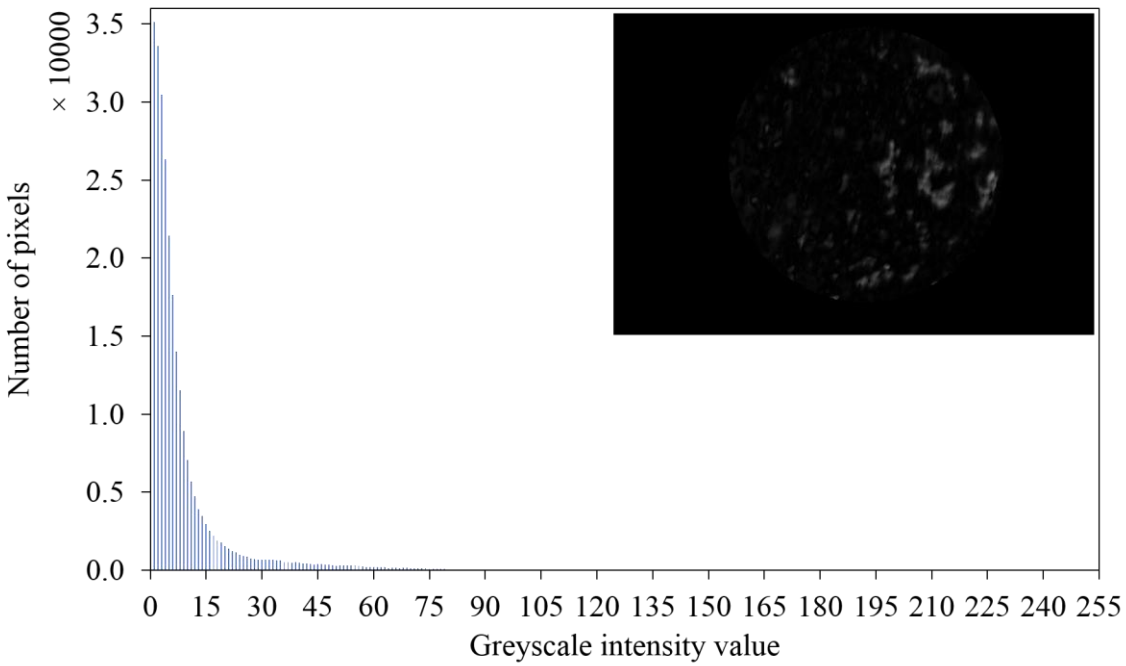

Figure 4.9 Histogram of image in Figure 4.6 (e) (before contrast enhancement).

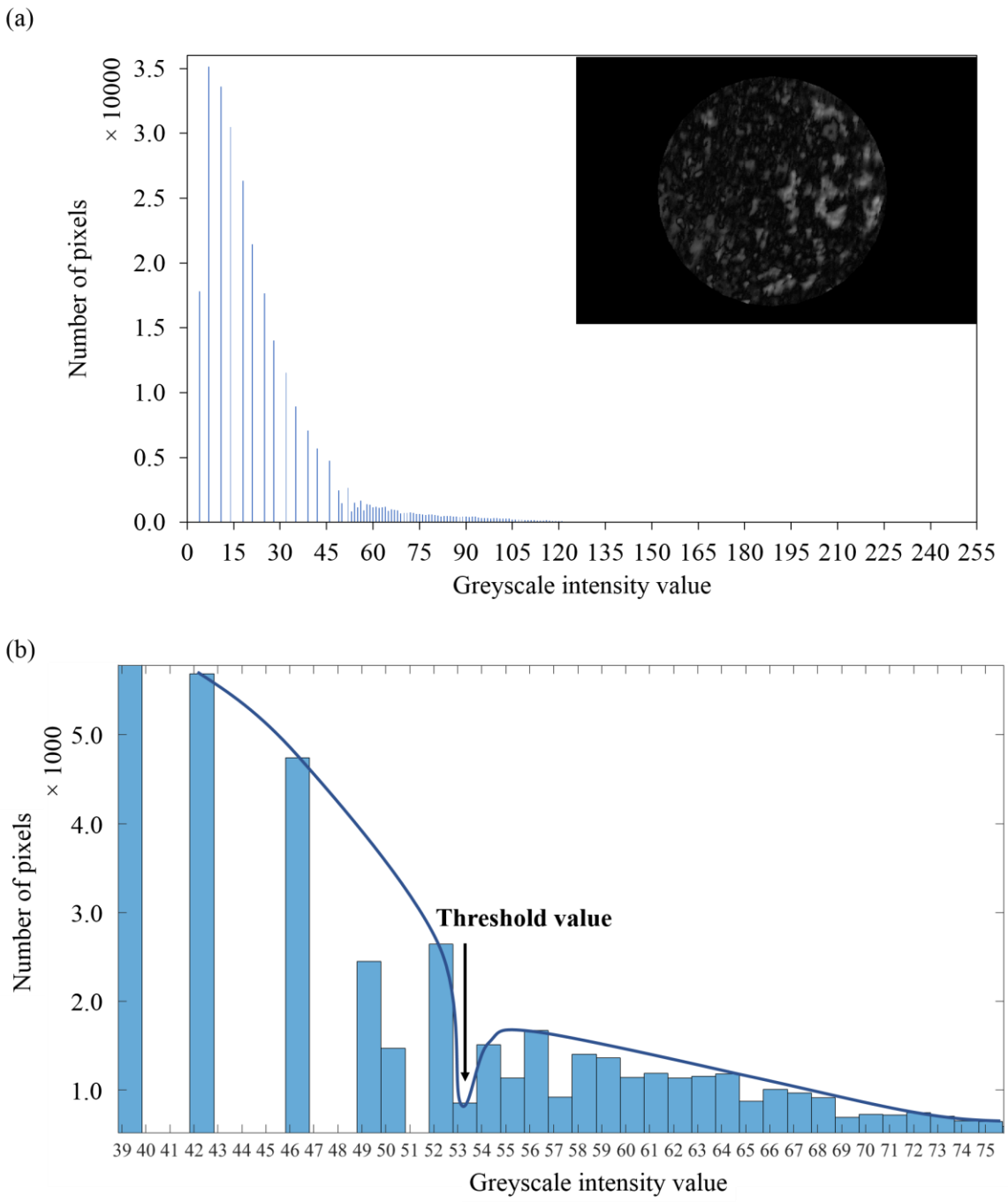

Figure 4.10 (a) Histogram of image in Figure 4.6 (f) (after contrast enhancement) and (b) enlarged view of (a) at threshold value.

The machine's scanning strategy requires the contour of the part to be scanned before the remaining regions are scanned. Insufficient overlap between the filling scan tracks and

the contour scan tracks may occur at regions of the contour with curvatures, resulting in porosities at the perimeters. It is therefore worthwhile to note that the perimeters of the cylindrical specimens were omitted for image processing due to inherent porosities as shown in Figure 4.11. As such, the mask, represented by the white pixels in Figure 4.6 (b), covers only 85% of the original cross-sectional area of each cylinder. This omits the evaluation of porosities near the perimeters.

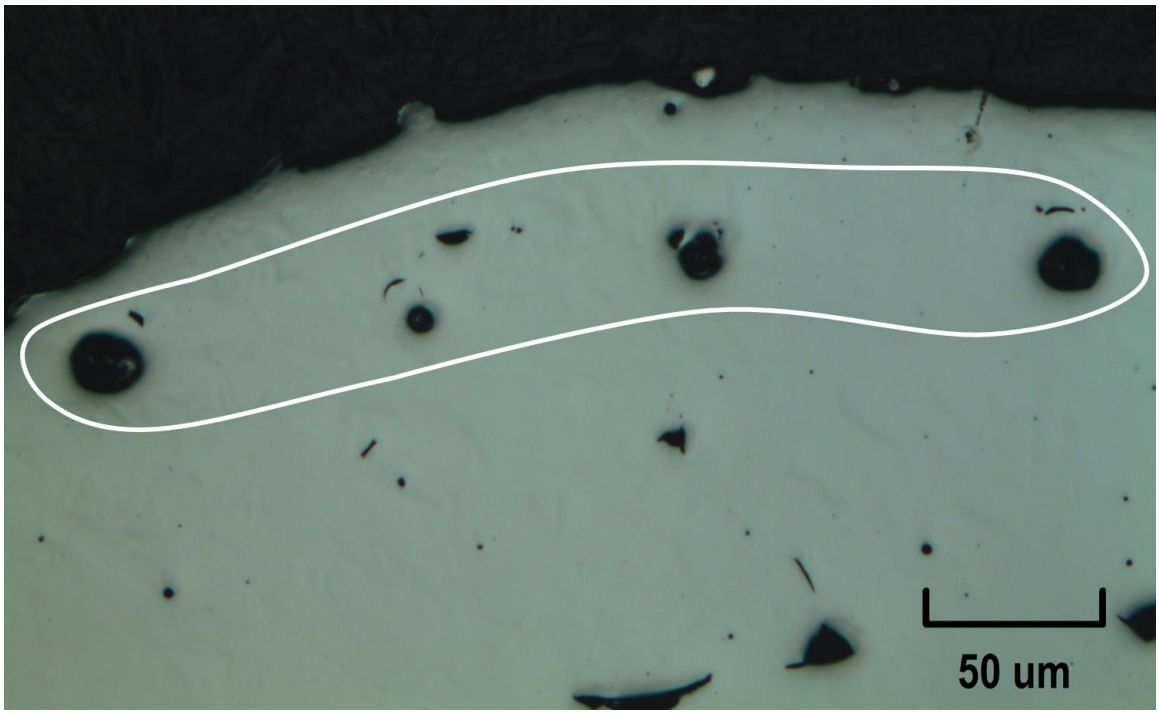

Figure 4.11 Optical micrograph showing the cross section of a cylinder with circled porosities present at its perimeter.

4.2.3 Evaluation of features

The area of features captured in the optical images after each layer of recoating is correlated to the density measurements from Archimedes' test. Optical images used for analysis are in binary form and the area of features is expressed as a percentage of its ROI for each layer. Each cylinder is analysed individually by cropping them out for a

total of N number of layers. The number of layers for each print job depends on the height of the parts. The masks' total area of white pixels (Figure 4.6 (b)) is equivalent to the cylinder's region of interest for each layer, denoted by P_{total}. The total area representing the features (or simply, the white pixels in Figure 4.6 (g)) for each layer is denoted by $P_{i,features}$, where i corresponds to the layer number. The percentage area of features for each layer, $\varphi_{i,features}$, is defined as

$$\varphi_{i,features} = P_{i,features}/P_{total} \times 100. \tag{4.1}$$

The average percentage area of features for each cylinder, $\varphi_{features,average}$, is expressed as

$$\varphi_{features,average} = \frac{\sum_{i=1}^{N} \varphi_{i,features}}{N}. \tag{4.2}$$

The average percentage area of non-features for each cylinder, $\varphi_{non-features,average}$ is defined as

$$\varphi_{non-features,average} = 100 - \varphi_{features,average}. \tag{4.3}$$

The percentage area of features for every layer of the ten cylinders is shown in Figure 4.12. Generally, it can be noted that an increase in the energy density ratio from 0.5 (specimens I and II) to 2.0 (specimens VII and VIII) leads to lower percentage area of features for the cylinders. However, the percentage area of features for cylinders II and IV are notably higher than that of other cylinders. A significant portion of the layers for these two cylinders fall in the range nearer to their upper limits. This suggests the presence of a substantial area of features in their captured images.

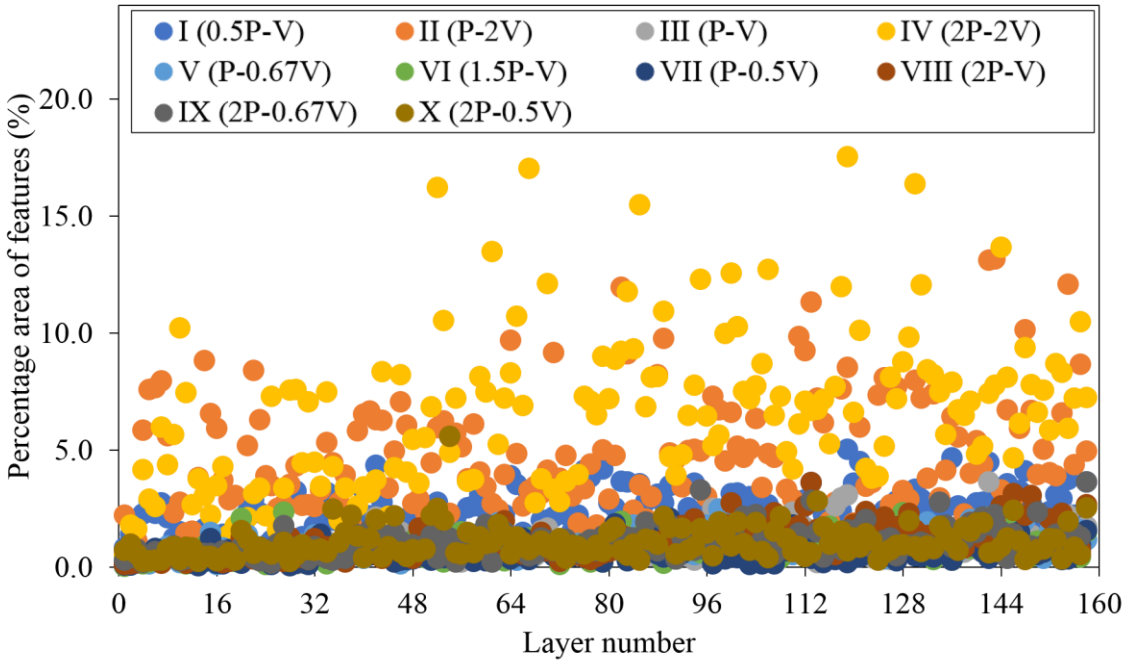

Figure 4.12 Percentage area of features present in each layer for ten cylinders.

It should be noted that the imaging processing results for cylinder IV indicated an extensive number of features present. Indeed, this could be due to the direction of argon gas flow and the positioning of cylinder IV during the printing process. Cylinder IV is at the left-most position as compared to the other cylinders. As the argon gas flows from right to left within the machine chamber, process by-products such as vaporised powders (condensates) and spatters that are removed tend to accumulate on the left side of the chamber (Figure 4.13). Spatters arise due to melt pool instabilities and high recoil pressure from the metal vapour plume [90]. A metal gas is produced when the melt pool reaches the material's vaporisation temperature. The fast-moving evaporated materials expand and give rise to a recoil pressure on the melt pool. Liquid metal is then expelled from the melt pool due to the high recoil pressure. The ejected material is known as spatter. Moylan et al. [91] presented a summary on the safety and environmental issues

on metal additive manufacturing and examined these condensates. The condensates, which tend to appear darker than the background, are oxides of the metal formed, contributing to the presence of darker pixels in the optical images. Liu et al. [92] investigated the spattering behaviour during selective laser melting (SLM) of 316L stainless steel powders. Energy dispersive spectroscopy analyses of fresh 316L powders and spatter particles revealed a higher oxygen content for the latter. These powders react with remaining oxygen in the chamber, generating iron oxides.

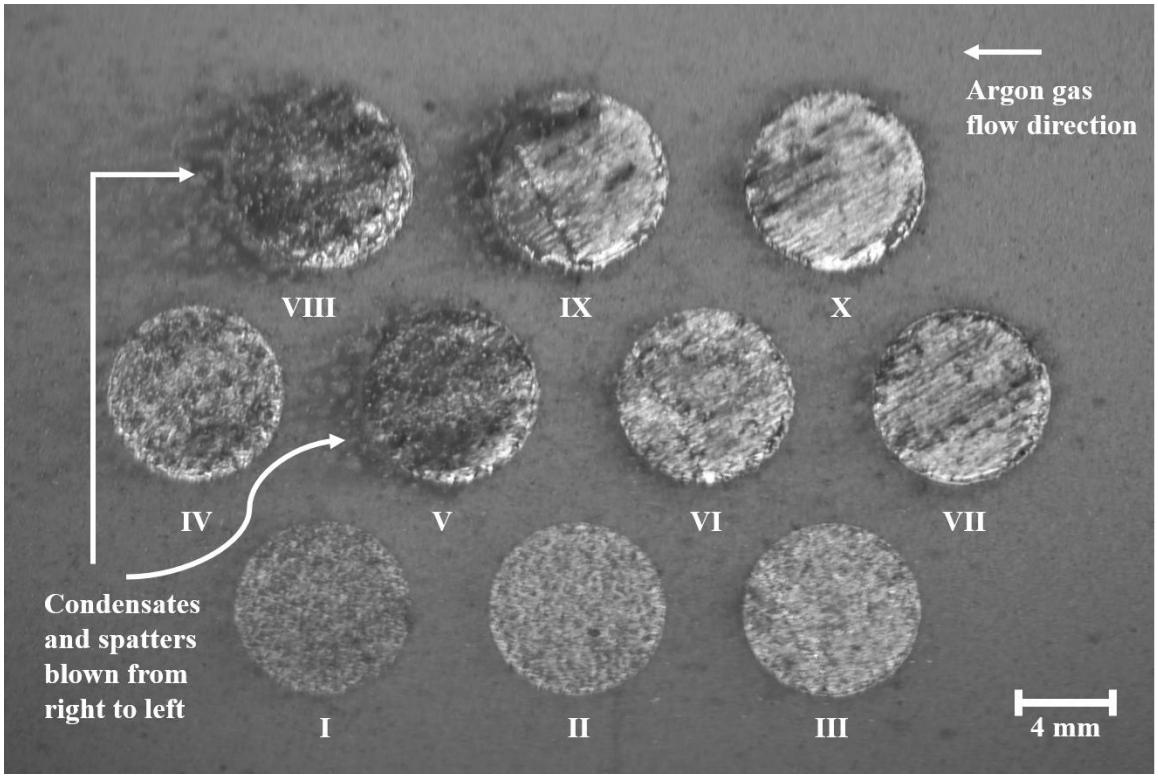

Figure 4.13 Condensates and spatters accumulated on the left of powder bed.

The condensates and spatters build up as the print proceeds after each layer of recoating, resulting in non-uniform heating when the laser beam is directed at the powder bed. This leads to significant amounts of elevated regions in cylinder IV. The excessive presence of

features in the recoated layer of cylinder IV is evident from the optical image in Figure 4.5. Foster et al. [44] also captured optical images illustrating uneven powder layers due to elevated regions, causing a change in the physical interaction of the laser beam with the material, leading to inconsistency in processing and sometimes, porosity. Consequently, the average density of cylinder IV is reduced.

The build-up of condensates and spatters is prominent for cylinders VIII to X, which are printed with high energy densities. This is evident from trails of dark particles concentrated at the left side of the specimens in Figure 4.13. However, their average densities are not significantly reduced and their percentage area of features are low based on the results from Archimedes' test and image processing. This is attributed to the high energy density during printing, which ensured complete melting of the metal powders.

A separate print was carried out to confirm the influence of condensates and spatters on the cylinders' quality. The positions of the cylinders were changed as shown in Figure 4.14. The printing parameters of the cylinders remained the same as stated in Table 3.3, section 3.2.2.2. Cylinder VII was subjected to the most condensates and spatters on its surface due to the direction of argon gas flow. The average densities of the ten cylinders based on Archimedes' principle were determined. The average density of cylinder VII decreases from 7.92 gcm^{-3} to 7.72 gcm^{-3} while the average density of cylinder IV increases significantly from 7.52 gcm^{-3} to 7.80 gcm^{-3}. Each of these reported values is an average of three measurements. More features are also observed on the recoated layer of cylinder VII as compared to cylinder IV, depicted in Figure 4.15. Despite the lower average density of cylinder VII, features present are not as extensive as compared to cylinder IV in the previous study. This can be explained by the relatively high energy

density ratio assigned to the printing of cylinder VII. Though condensates and spatters are present on its surface, the high energy density ensures more powders are melted than the case of cylinder IV from the previous study. The results have illustrated and validated the detrimental effect of excessive condensates and spatters on printed surfaces, notably affecting the part's density. Another print job was carried out to substantiate this finding where ten cylinders were printed with the same parameters listed in Table 3.3, section 3.2.2.2. The details and results of this print job can be found in Appendix D.

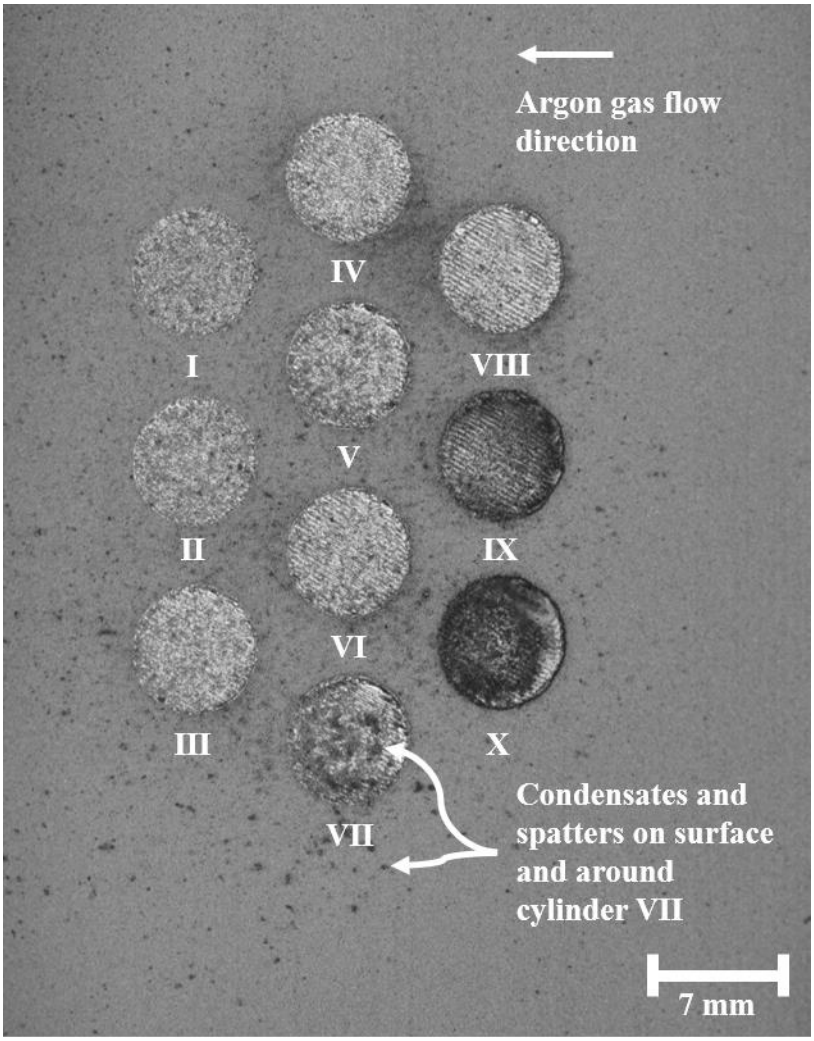

Figure 4.14 Condensates and spatters accumulated mostly around cylinder VII after rearrangement of cylinders' positions.

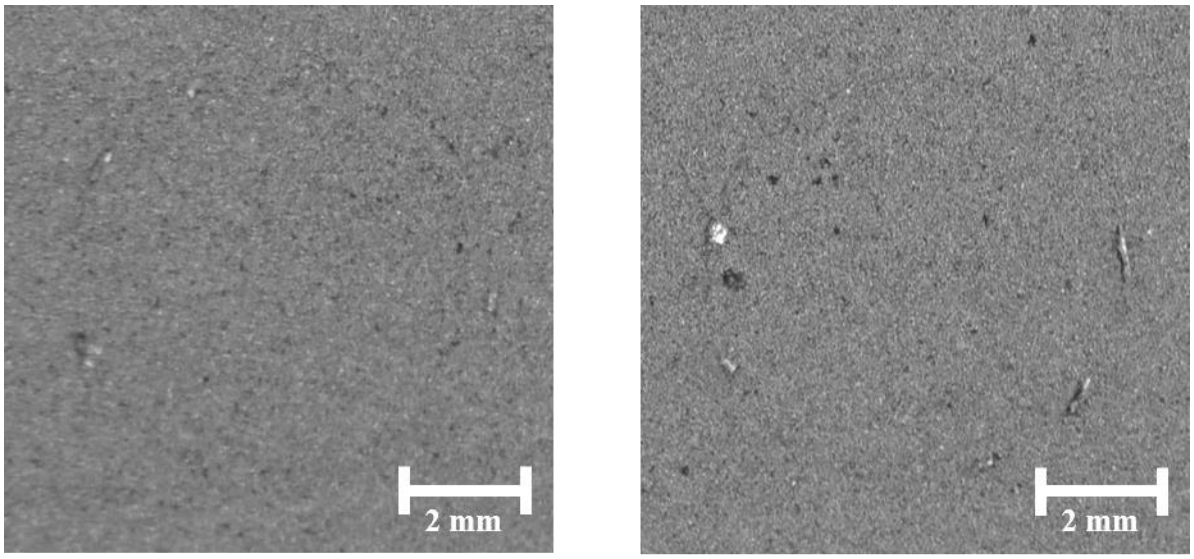

Figure 4.15 Recoated layer of cylinders IV and VII.

4.2.4 Correlation of results

Figure 4.16 (a) depicts the average percentage area of non-features across all 160 layers for each cylinder and their average densities. Figure 4.16 (b) illustrates the average percentage area of non-features across all 160 layers for each cylinder and the ultimate and yield strengths of the respective tensile coupons. These two figures provide an overview on the relationships established between the results of image processing and mechanical properties of the specimens.

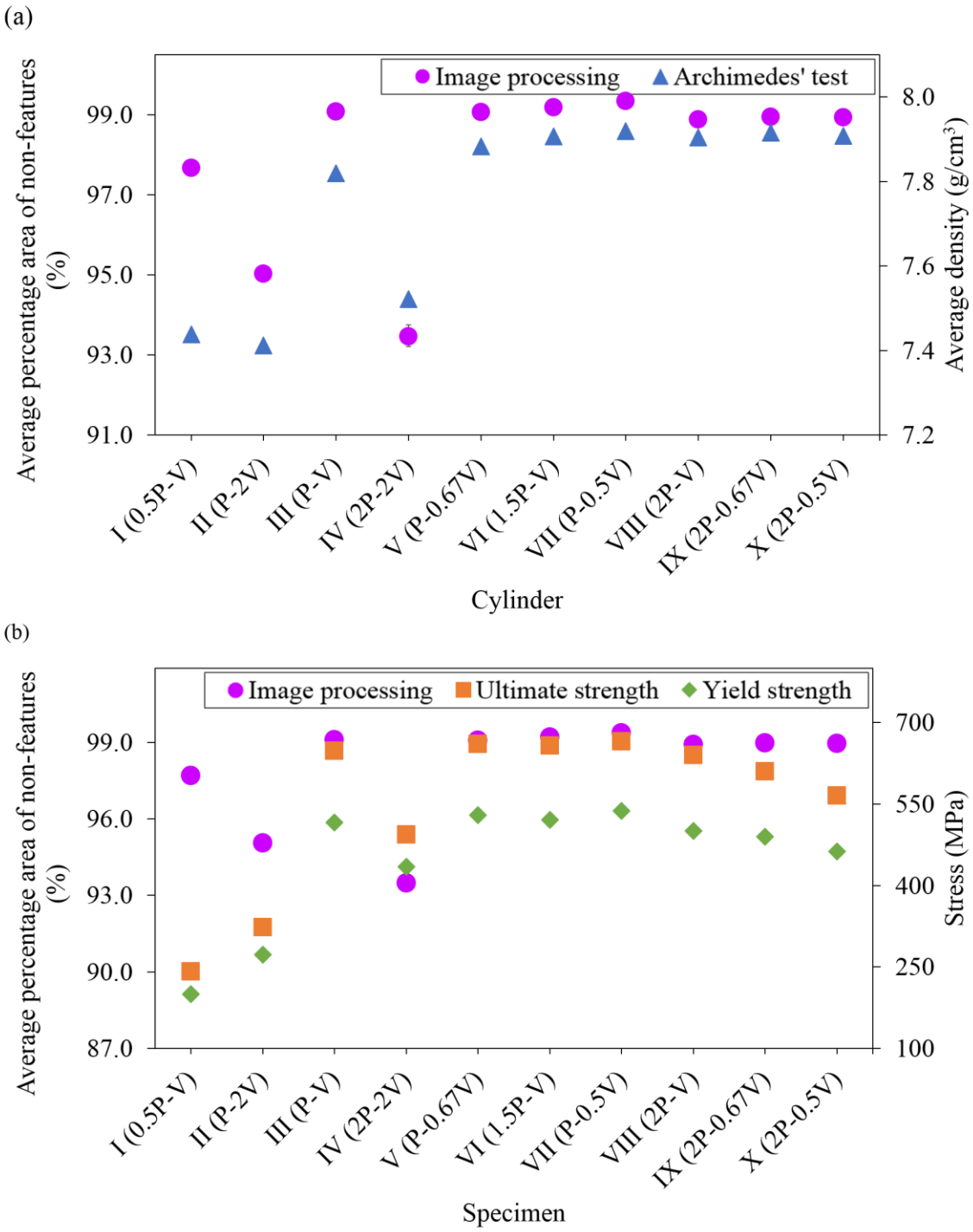

Figure 4.16 (a) Average percentage area of non-features across all 160 layers of each cylinder and densities of ten cylinders and (b) average percentage area of non-features across all 160 layers of each cylinder, ultimate and yield strengths of ten specimens.

The results from image processing indicated that cylinders I, II and IV, having relatively higher percentage area of features, displayed poorer mechanical properties as illustrated by Figures 4.12 and 4.3 respectively. Therefore, these cylinders had lower average percentage area of non-features across all 160 layers, translating to lower densities, ultimate and yield strengths as seen in Figures 4.16 (a) and (b). Cylinders III and V to X, having relatively lower percentage area of features, exhibited better mechanical properties as illustrated by Figures 4.12 and 4.3 respectively. Correspondingly, these cylinders had higher average percentage area of non-features across all 160 layers, translating to higher density, ultimate and yield strengths as illustrated in Figures 4.16 (a) and (b). The aforementioned relationship has demonstrated the feasibility of using the proposed in-situ monitoring system (IMS) to infer the density and mechanical properties of printed specimens based on the percentage area of features in optical images. Specimens with relatively higher percentage area of features have poorer mechanical properties while specimens with relatively lower percentage area of features have better mechanical properties.

4.2.4.1 Specimens I, II and IV

Specimens printed with a relatively low energy density ratio of 0.5 had printing parameters set to either low laser power (specimen I) or high scanning speed (specimen II). Gu et al. [93] studied the influence of energy density on porosity formation in 17-4 precipitation hardening stainless steel parts produced by SLM. They demonstrated that a relatively low laser power may cause insufficient penetration to the previous solidified layer for the attachment of newly formed liquid metal particles, resulting in poor wetting. Additionally, lower laser power also decreases the probability of powder ablation and

plasma formation near the surface of the powder bed, reducing the overall absorptivity of the metal powders.

A relatively high scanning speed reduces the allowable time that the laser beam is in contact with each powder particle which may otherwise ensure complete melting. These various effects lead to an increase in the presence of unmelted and partially melted powders, reducing the overall density of the printed specimens. X-ray micro CT of the ten cylinders revealed a large amount of porosities in cylinders I, II and IV as illustrated in Figure 4.17. There are also extensive regions of partially melted powders present in cylinders I and II (Figure 4.18). The metallurgical bonding between layers is weakened, affecting the structural integrity of the tensile coupons.

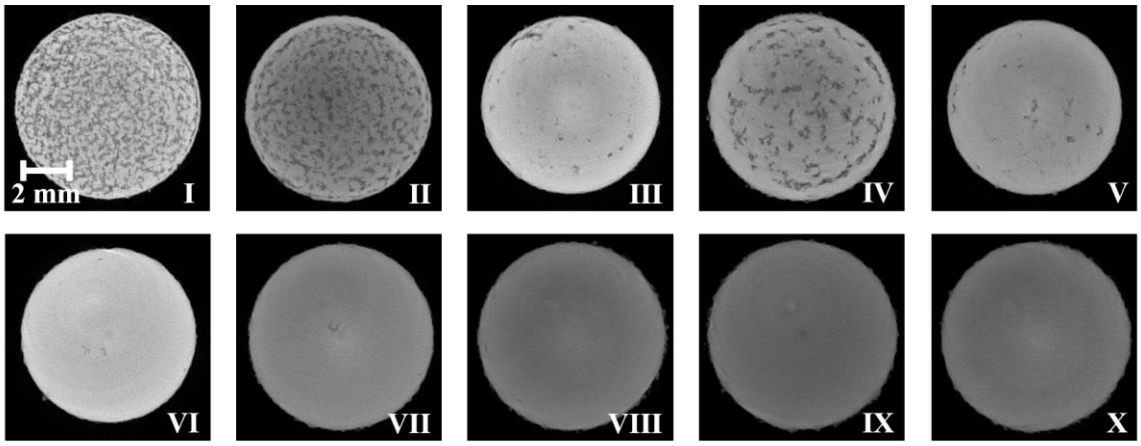

Figure 4.17 Micro CT images of cylinders showing the presence of porosities.

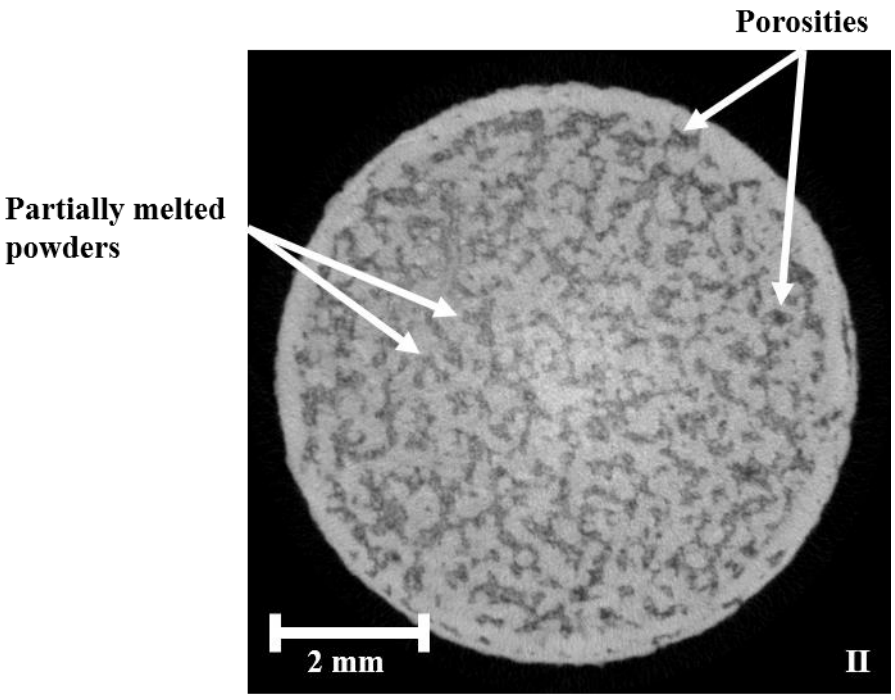

Figure 4.18 Micro CT image of cylinder II showing the presence of porosities and partially melted powders.

The effects of printing specimens with relatively low energy density ratio and high scanning speed are well reflected in the optical images captured by the IMS. Balling and instability of the melt pool give rise to regions of the printed parts to be elevated from the powder bed's surface, represented by pixels that are brighter than the powders. The presence of features in the optical images of cylinders I, II and IV are more pronounced than the remaining cylinders, evident from the higher percentage area of features in Figure 4.12. Cylinder I exhibits percentage area of features within 1 to 5%. Cylinders II and IV have percentage area of features in the range of 0 to 14% and 0 to 17% respectively. The density, ultimate and yield strengths of specimens I, II and IV, as discussed, are significantly lower than the rest of the specimens as seen in Figure 4.3. It can be concluded that cylinders with higher percentage area of features exhibit lower

densities and weaker mechanical properties. Hence, the implementation of the IMS based on optical imaging enables end users to distinguish specimens with relatively lower density and weaker mechanical properties.

The significantly lower densities and higher percentage area of features of specimens II and IV illustrated the influence of scanning speed on the densification of printed parts in SLM process. A high scanning speed results in reduced surface energy of the liquid and instability of the liquid track. Numerous small-sized liquid droplets tend to splash from the surface of the molten track [94, 95]. The build-up of these liquid droplets may cause uneven recoating of the metal powders and formation of elevated regions during printing, translating to brighter pixels in the optical images.

4.2.4.2 Specimens V to X

According to equation (3.3), with the hatch spacing and layer thickness kept constant, specimens of relatively high energy density ratios (with values ranging from 1.5 to 4.0 in this study) can be printed by setting the printing parameters to either high laser power (specimens VI and VIII) or low scanning speed (specimens V and VII) or a combination of both (specimens IX and X). A relatively high laser power ensures sufficient energy input into the melt pool to fully melt the stainless steel powders.

Kasperovich et al. [96] established a correlation between the processing parameters and porosity formation in selectively laser melted Ti-6Al-4V specimens. They revealed that a low scanning speed reduces the shear stress of the liquid phase of the metal, decreasing the surface tension within the melt pool. As a result, wettability between the molten metal and the underlying printed layer or substrate is enhanced, minimising the occurrence of balling and discontinuities forming on the melt track. The balling phenomenon is the

separation of melt pool into small spheres. The spattering of molten metal droplets caused by high scanning speeds which contribute to the formation of porosities will also be lessened in this case. The result is a diminution in the amount of unmelted powders and porosities. Hence, the overall density of the printed specimens increases.

As discussed, the formation of discontinuities in specimens is reduced as the energy density increases. The corresponding tensile coupons can sustain higher tensile stress when lesser amounts of defects are present within the structure. Significantly lesser amounts of defects are seen in the micro CT images of cylinders III and V to X (Figure 4.17), leading to higher measurements in their ultimate and yield strengths.

The improved stability of the melt pool due to increased energy density is notable from the optical images captured by the IMS. The powder bed is more uniformly recoated as compared to printing specimens with relatively low energy density. This is supported by a low percentage area of features for cylinders V to X, which falls within 2% across all layers as depicted in Figure 4.12. The occurrence of features in the optical images of these cylinders are drastically reduced as compared to cylinders I, II and IV. The printed layers of the cylinders do not have pronounced elevated regions (brighter pixels), condensates and spatters (darker pixels) in the optical images. It can be concluded that cylinders with lower percentage area of features exhibit higher densities and stronger mechanical properties. The implementation of the IMS based on optical imaging enables end users to distinguish specimens with relatively higher density and better mechanical properties.

Results from density tests based on Archimedes' principle and mechanical properties from tensile tests have demonstrated a correlation with the processed optical images of

the specimens. The established correlation has validated the potential of inferring the printed parts' mechanical performance based on features identified through optical-based IMS. This can potentially aid in the production of parts with better mechanical properties. Printing parameters can be adjusted in-situ to improve the quality of the printed part if the number of features present in optical images correlate to weak mechanical properties, rendering both time and cost savings.

4.3 Correlation between optical images and actual defects of printed parts

This section discusses on the establishment of a correlation between the features captured in optical images during fabrication and the defects captured in CT images. It can be achieved by leveraging the individual advantages of an IMS and CT. An optical-based IMS offers flexibility for the adjustment of printing parameters during fabrication if substantial features are captured. It also provides real-time updates such as the extensiveness of features present in each layer of the printed part. CT identifies defects such as porosities and the scan is not influenced by material characteristics such as the colour and reflectivity of surfaces, which may impede the detection process with other three-dimensional (3D) inspection methods [11]. Furthermore, a 3D model featuring the internal and external structures of a specimen can be attained through CT, making it an ideal non-destructive testing (NDT) technique for the identification of defects present in the printed parts. Hence, CT is primarily used to substantiate the viability of the proposed optical IMS as a means of defects identification.

A preliminary investigation was carried out prior to the results represented in this section. Six 316L stainless steel cuboids were printed with varying energy densities. The preliminary investigation was performed to explore the possibility of establishing a

correlation between the features captured in optical images during fabrication and the actual defects present in the printed part. The findings of the preliminary investigation can be found in Appendix E. Upon the establishment of a correlation, the investigation was further expanded to include specimens printed with more energy densities, i.e., ten specimens presented in section 4.3.

4.3.1 Extraction of features

The analysis of optical images by image processing should be simple, fast and accurate in order to be implemented for in-situ monitoring of the SLM process. The following section discusses the development of image processing algorithms for optical and CT images.

The images captured after recoating of the scanned layer were utilised for image processing and analysis. The images were taken in greyscale with intensity values ranging from 0 to 255. The same procedures as discussed in section 4.2.2 were taken to extract features from optical images. The captured and processed images are illustrated in Figures 4.19 (a) and (b) respectively. The processed images were in binary format where white and black pixels represented the features and the powder bed respectively. Subsequently, the total area of the features (white pixels) in each image was computed using MATLAB [89].

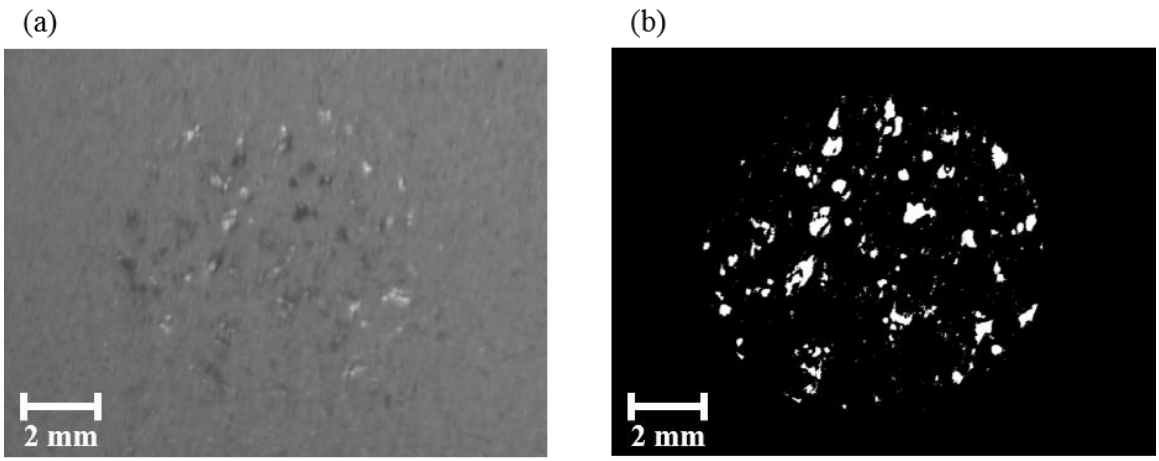

Figure 4.19 (a) Captured optical image during printing and (b) binarised image after processing.

Micro CT is an effective post-process NDT inspection technique in revealing internal defects of additively manufactured parts. Hence, it was used to validate the correlation between features in two-dimensional (2D) optical images to actual 3D defects in the printed cylinders through reconstruction of the micro CT images.

The cross-sectional images of the cylinders after reconstruction were used for analysis. Similar to that of optical images, they were also in greyscale as shown in Figure 4.20 (a). The common defects present in selectively laser melted metal parts are porosities and lack-of-fusion defects. The former consists of air while the latter comprises unmelted or partially melted metal powders. These defects, i.e., air, unmelted and partially melted metal powders, have densities that differ from the bulk material (316L stainless steel). Thus, there exists a difference in the amount of radiation absorbed by a defective part as compared to a defect-free part [5]. As defects and the bulk material are represented by their specific grey values, internal defects can be detected and segmented by carrying out thresholding on the slices of CT images. The same procedures as discussed in section

4.2.2 were taken to select a suitable threshold value for binarisation of the CT images. A bimodal distribution can be obtained upon enhancing the contrast of the CT image.

Defects, specifically porosities and lack-of-fusion defects, were represented by clusters of black pixels within the white pixels in the binarised image (Figure 4.20 (b)). The complement image of Figure 4.20 (b) was used to evaluate the area of defects in each CT image. The white pixels represent the defects while the black pixels represent the bulk of the material in Figure 4.20 (c). The area of defects in each CT image was computed using MATLAB.

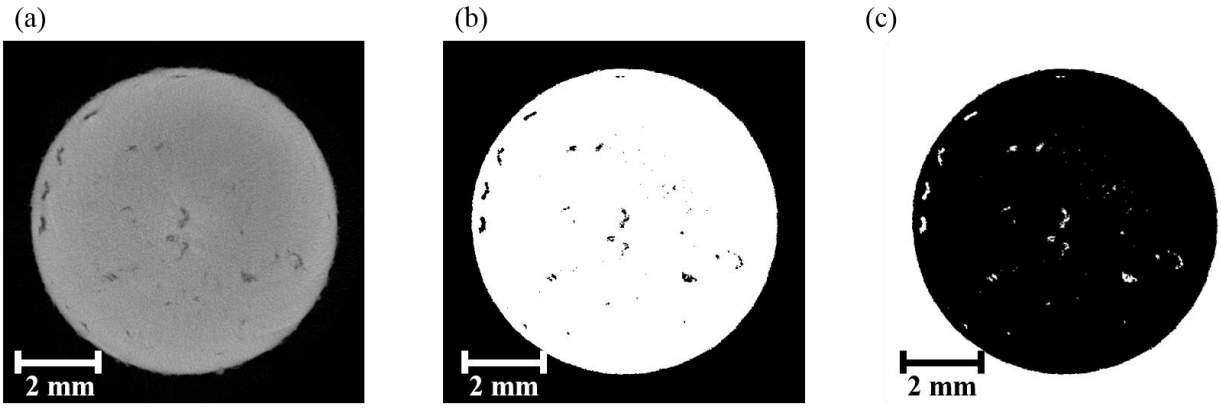

Figure 4.20 (a) CT image of cylinder, (b) binarised image of (a) after thresholding and (c) complement image of (b).

4.3.2 Evaluation of features

The optical images were enumerated according to the sequence during printing with image 1 representing the first layer, starting from the bottom of the print. Since the layer thickness was set to 50 µm, the interlayer distance between each image was therefore 50 µm. The optical images were analysed across every two consecutive layers for fast computation of the area of features in the optical images and to simulate real-time

printing conditions. The features were then combined into a single image for each of the two layers.

Figure 4.21 further illustrates the computation process. Images 1 and 2 contained features represented by white pixels. Image 1 was superimposed onto image 2 to form the resultant image, representing the accumulation of features across images 1 and 2. The percentage area of features in each resultant optical image, denoted as $OP_{features}$, was evaluated and correlated to the actual defects detected by micro CT.

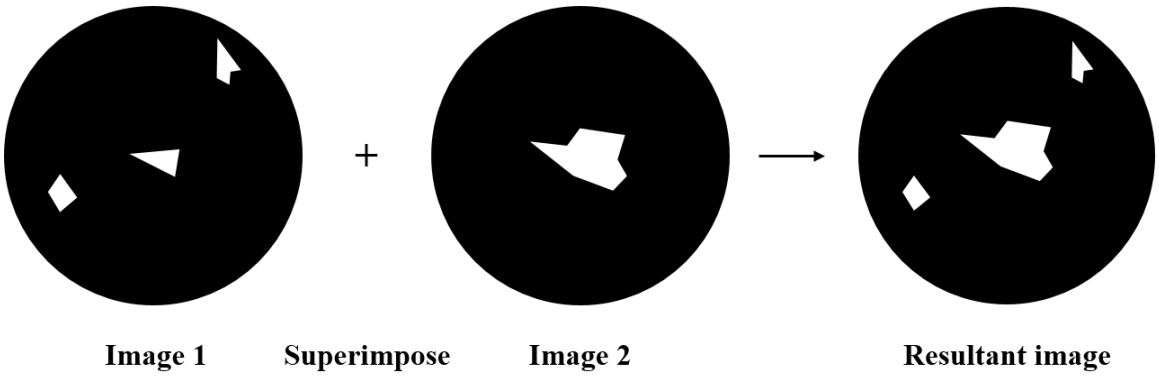

Figure 4.21 Illustration on processing of optical images for evaluating the area of features.

Micro CT imaging was used as a post-process inspection method in identifying internal defects within the cylinders. Similar to that of optical images, the white pixels represent defects in the binarised form of the CT images. These images were collated in the same manner as that of the optical images except for the number of CT images being compiled each time. The interlayer distance between each CT image was 10 µm. Hence, six CT images, equivalent to an interlayer distance of 50 µm were combined to form a single resultant image by the union of white pixels as seen in Figure 4.22. This ensures the net interlayer distance is equivalent between the optical and CT images before any analysis

was carried out. The percentage area of defects in each resultant CT image is denoted as $CT_{defects}$.

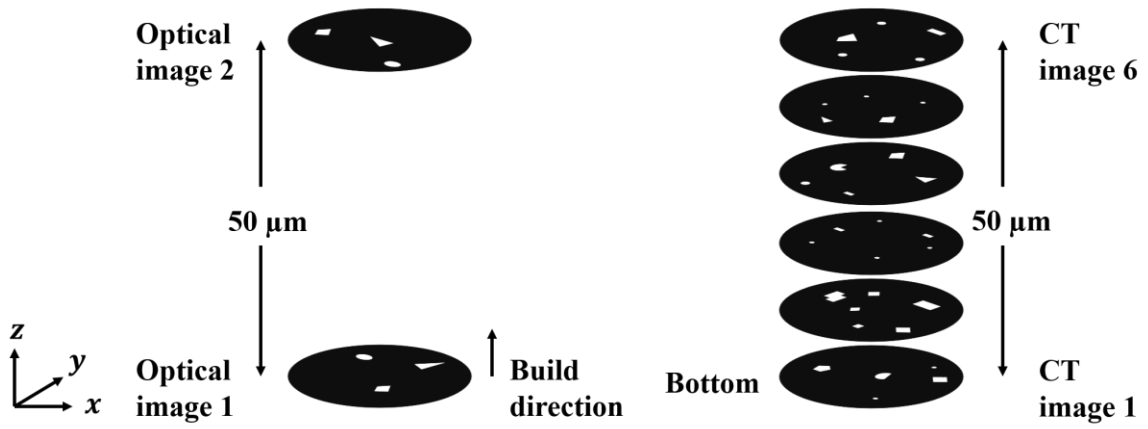

Figure 4.22 Perspective view on the compilation of optical and CT images for a net interlayer distance of 50 µm.

4.3.3 Correlation of results

Based on the compiled optical and CT images, the Pearson correlation coefficient was evaluated to illustrate the correlation of $OP_{features}$ to that of $CT_{defects}$. The Pearson correlation coefficient is a representation of the extent to which two variables are linearly related to each other [97]. When computed in a sample, it is denoted by r which ranges from -1 through +1, where -1 denotes a perfect negative correlation, 0 represents no correlation and +1 implies a perfect positive correlation between the variables. A sample (x_1, y_1), (x_2, y_2), …, (x_n, y_n) of size n has a Pearson correlation coefficient given as

$$r = \frac{\sum_{i=1}^{n}(x_i-\bar{x})(y_i-\bar{y})}{\sqrt{\sum_{i=1}^{n}(x_i-\bar{x})^2 \sum_{i=1}^{n}(y_i-\bar{y})^2}} \tag{4.4}$$

where x_i, y_i are the individual sample points indexed with i and $\bar{x}$, $\bar{y}$ are the sample means [97]. The Pearson correlation coefficients between $OP_{features}$ to that of $CT_{defects}$ for the ten cylinders are presented in Table 4.1.

Table 4.1 Pearson correlation coefficient of ten cylinders printed by SLM.

Cylinder	Pearson correlation coefficient
I	0.53
II	0.39
III	0.31
IV	0.78
V	0.60
VI	0.42
VII	0.45
VIII	0.51
IX	0.38
X	0.30

The correlation coefficient for cylinder X is the lowest. Defects were almost non-existent in cylinder X. As it was printed with a high energy density ratio of 4.0 (see Table 3.3, section 3.2.2.2), the powders were completely melted, minimising the formation of defects. Hence, the correlation between $OP_{features}$ and $CT_{defects}$ is low due to the limited number of data points associated with $CT_{defects}$ having values greater than 0%. Nonetheless, Figure 4.23 illustrates similarity in the trends between $OP_{features}$ and $CT_{defects}$ across the layers of cylinder X. Blue and orange dashed boxes corresponding to

$OP_{features}$ and $CT_{defects}$ are used respectively to demonstrate regions of coherent movement in the trends. Each set of blue and orange dashed boxes is numbered where the numeral represents a data point belonging to $OP_{features}$ and the numeral with an apostrophe represents a data point belonging to $CT_{defects}$. It is worthwhile to note that the main purpose of examining the correlation between $OP_{features}$ and $CT_{defects}$ across the layers of the ten cylinders is to accurately evaluate circumstances involving significant number of defects that could impair the printed part's quality. Consequently, coherence in the correlation between $OP_{features}$ and $CT_{defects}$ at regions where both values are significantly high is crucial. An example is shown in Figure 4.23 for blue and orange dashed boxes numbered 4 and 4' and 8 and 8'. The data points at which $OP_{features}$ reflect a high possibility of defects has to be validated by the corresponding data points associated with $CT_{defects}$. Such validation is important as it suggests the need for interference by the end user to mitigate the situation, producing parts with little defects. The data points at which both $OP_{features}$ and $CT_{defects}$ reflect little or no defects in the printed part are therefore not crucial. The Pearson correlation coefficient of 0.30 for cylinder X, albeit low, is not a cause for concern as the $OP_{features}$ and $CT_{defects}$ across its layers are relatively small.

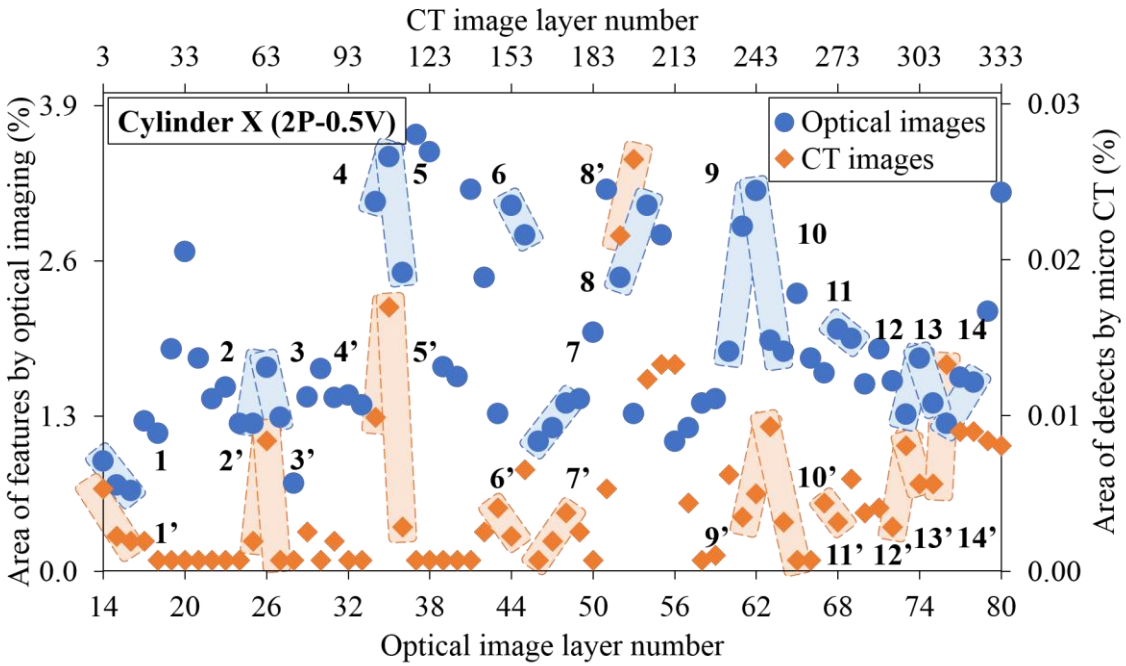

Figure 4.23 Area of features and defects across each layer for cylinder X (in percentages), where the numeral represents a data point belonging to $OP_{features}$ and the numeral with an apostrophe represents a data point belonging to $CT_{defects}$.

$OP_{features}$ and $CT_{defects}$ for cylinder IV are highly correlated with a coefficient of 0.78 and the trends between the two sets of data coincide well with each other as depicted in Figure 4.24. A higher $OP_{features}$ translates to higher $CT_{defects}$, and vice versa. The graphs of the remaining cylinders can be found in Appendix F. The proposed image processing algorithms for optical and CT images have been proven valid. This is supported by the Pearson correlation coefficient results which signify a positive correlation between $OP_{features}$ and $CT_{defects}$ for all ten cylinders. End users are therefore able to directly evaluate the area of defects present in parts based on real-time analysis of optical images. The results based on CT images, which is used to substantiate the viability of the proposed optical IMS as a means of defects indication, is well

represented by the results based on optical images. This eliminates the need for long hours of defects detection in printed parts by CT.

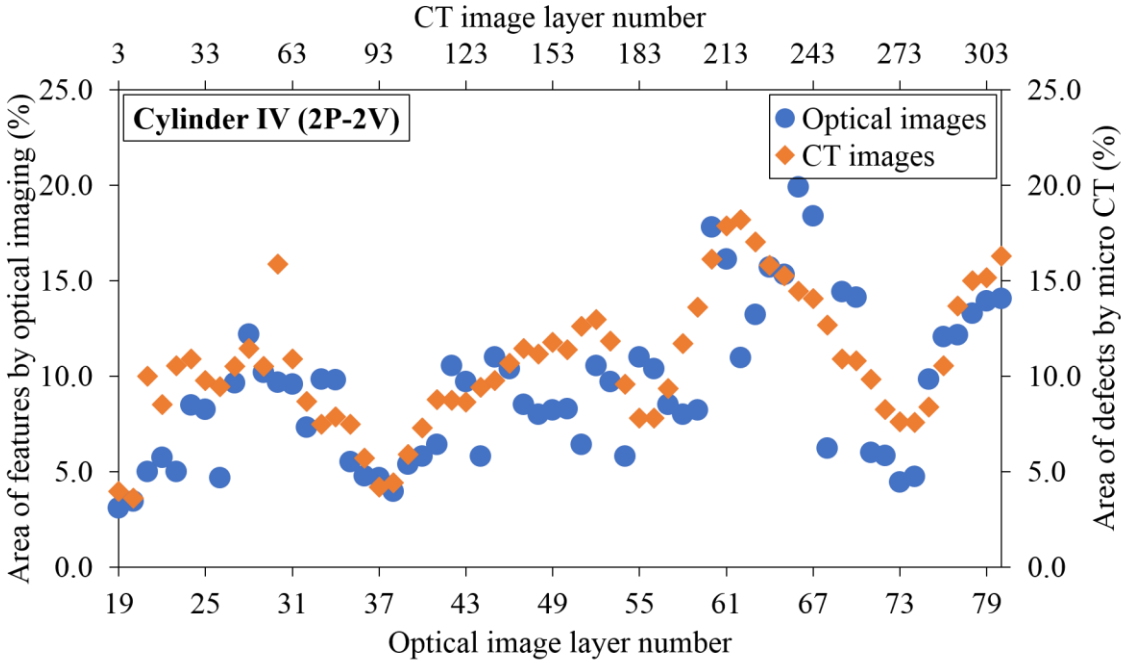

Figure 4.24 Area of features and defects across each layer for cylinder IV (in percentages).

Figures 4.25 (a) and (b) compare $OP_{features}$ to $CT_{defects}$. It can be concluded from Figure 4.25 (a) that cylinders I, II and IV exhibit significantly higher number of features than the other cylinders. These results, when validated against the results based on micro CT, are well correlated. $CT_{defects}$ is also notably higher for cylinders I, II and IV as depicted in Figure 4.25 (b). Similarly, the low $OP_{features}$ for cylinders III, and V to X coincide with the low $CT_{defects}$.

These results revealed the viability of implementing the proposed IMS to establish a correlation between the features captured during printing and the actual defects present in

the printed part. A higher $OP_{features}$ translates to higher $CT_{defects}$. A clear distinction in $OP_{features}$ and $CT_{defects}$ can be seen between cylinders I and II which were fabricated with relatively low energy density and cylinders V to X which were fabricated with relatively high energy densities. This illustrated the capability of the system in differentiating the extent of defects present in specimens fabricated with varying energy densities. This finding is critical as errors are commonly present during printing. Some errors include wrong printing parameters being set, uneven recoating of the powder bed due to damaged recoater blades and unoptimised argon gas flow. The effects of these errors often go unnoticed until defect inspection is performed on the part after printing. Furthermore, the extensiveness of defects in the printed parts due to these errors are unknown. Therefore, the ability of the proposed IMS to differentiate variations in the extent of defects is highly essential considering the possible occurrence of these errors in day-to-day print jobs.

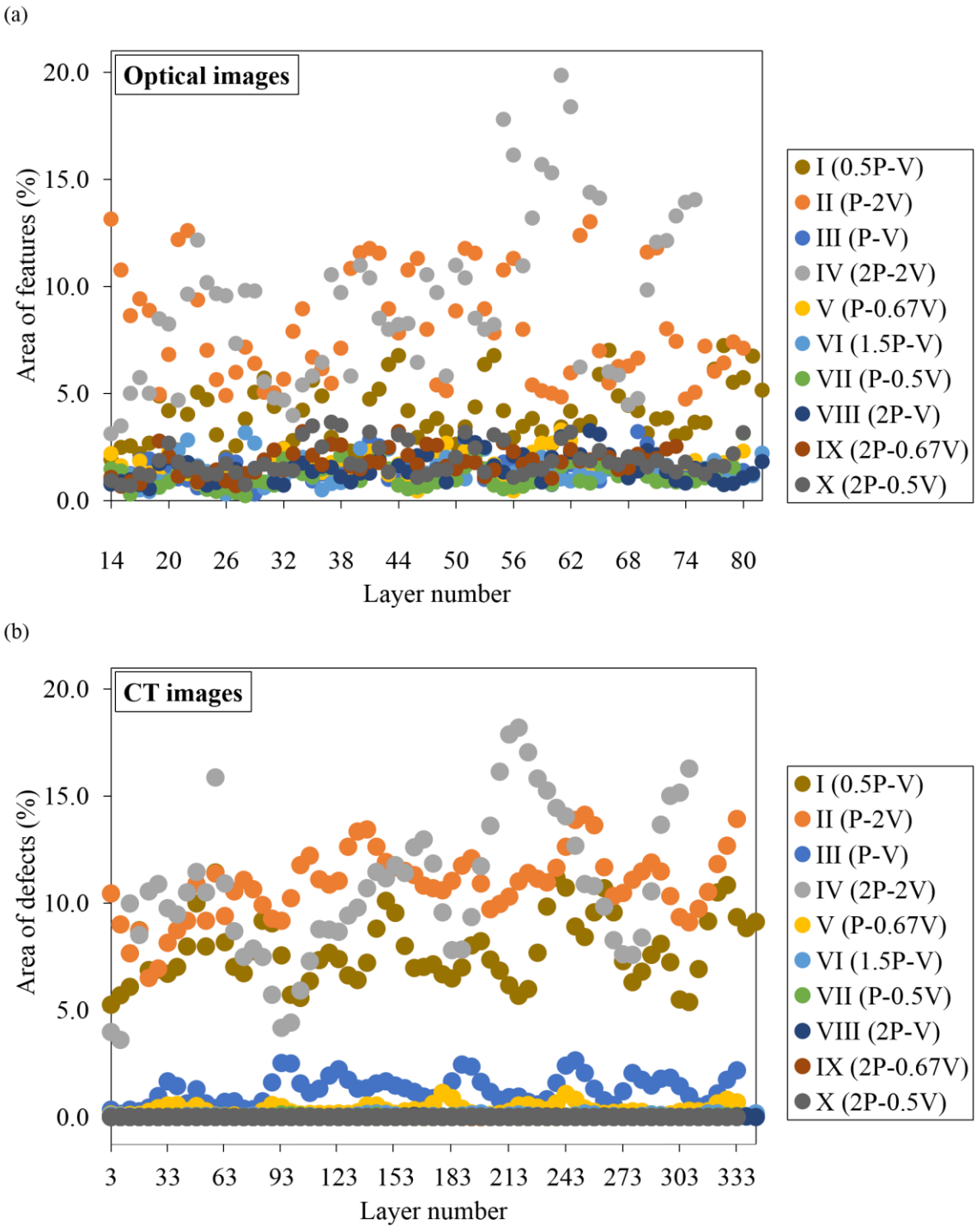

Figure 4.25 Area of (a) features across each layer for ten cylinders based on optical images and (b) defects across each layer for ten cylinders based on CT images (in percentages).

Cylinders II and IV were fabricated with relatively high laser scanning speed which promotes capillary instability in the melt pool. Balling is present due to non-linear solidification process. Small liquid droplets are splashed onto the surface and settled as irregularities, resulting in inhomogeneity in the deposition of the subsequent layers [17]. The non-uniform deposition of metal powders causes the build-up of regions that are raised above the recoated powder bed's surface. These regions, as observed in the optical images, are pixels with intensity values that are higher than the powders (i.e., features). This explains the significantly higher $OP_{features}$ and $CT_{defects}$ for cylinders II and IV as illustrated by Figures 4.25 (a) and (b).

Cylinders I and II were fabricated with comparatively low energy density which leads to insufficient melting of the metal powders and lack of fusion defects. The existence of incompletely melted and unmelted powders is reflected by the high $CT_{defects}$ in Figure 4.25 (b). $OP_{features}$ and $CT_{defects}$ for cylinders III and V to X are notably lower as the relatively high energy densities ensured the metal powders are fully melted. The formation of discontinuities is also minimised, improving the uniformity of the recoated powder bed. Hence, lesser features are observed in the optical images and the percentage area of features falls within 2% throughout every layer.

3D volumetric models of the cylinders were generated from 2D optical and CT images using the CTAn software. The volume of features and defects present in each cylinder were also evaluated by the software. The results are shown in Figure 4.26 and the 3D models of the cylinders are illustrated in Figure 4.27. The volume of features present in the 3D models of the cylinders generated from optical images are well correlated with the volume of defects based on the CT images. The data between optical and CT images

exhibit the same trend as seen in Figure 4.26. Large volumes of features generated from optical images are supported by large volumes of defects generated from CT images, and vice versa. The results have provided an affirmative answer for possible in-situ evaluation of defects in a part based on optical images captured. End users are able to obtain real-time information on the quality of the print, an advantage unique to an IMS. It therefore also offers end users the freedom and flexibility to make any adjustments during printing to improve the quality of the print.

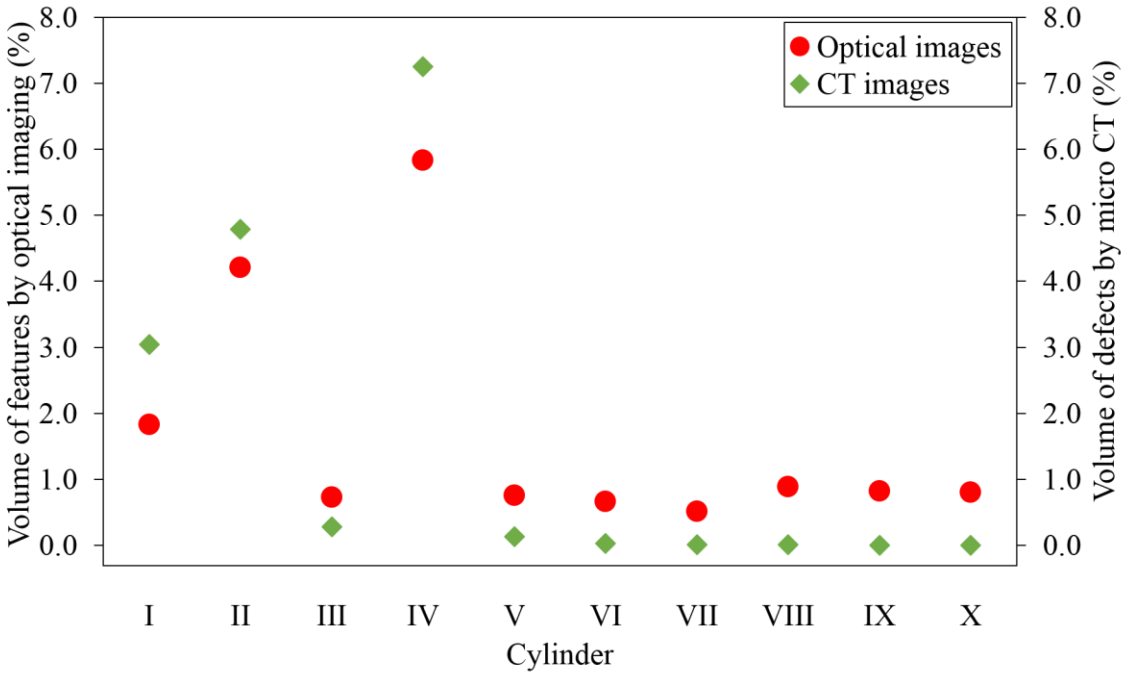

Figure 4.26 Percentage volume of features and defects for ten cylinders.

There is a drastic decrease in the volume of features and defects between cylinders IV and VIII as seen from the 3D models in Figure 4.27. The 3D models of the remaining cylinders can be found in Appendix F. These indicators provide an insight to the correlation between features captured in optical images and defects detected by micro

CT, where a large region of features present in optical images will represent an extensive number of defects in the printed part. The potential of utilising the proposed IMS for the establishment of a correlation between the features captured during printing and the actual defects present in the printed part has been reinforced.

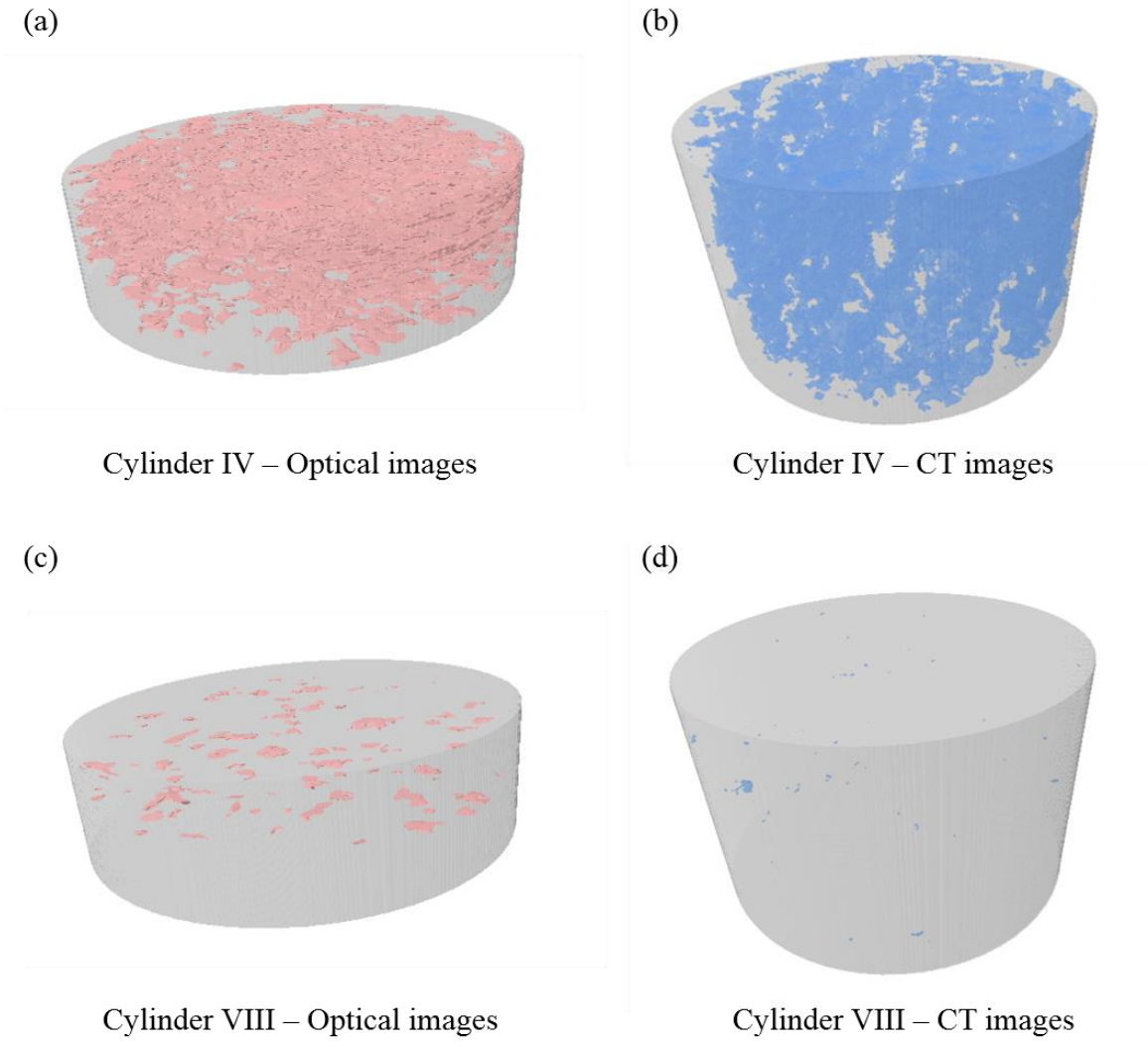

Figure 4.27 3D volumetric models of (a) cylinder IV based on optical images, (b) cylinder IV based on CT images, (c) cylinder VIII based on optical images and (d) cylinder VIII based on CT images.

4.3.4 Limitations of adopted approach

One limitation of the approach adopted is the detection of micro-scale porosities using the IMS and micro CT. The established correlation is not applicable to porosities which are below the spatial resolutions of the IMS and CT scanner. Cylinders IX and X exhibited high average densities and were assumed to contain minimal porosities based on the established correlation which can be found in Appendix F. Optical microscopy, however, revealed the presence of micro-scale porosities with sizes less than the spatial resolutions of the IMS and CT scanner. Figures 4.28 (a) and (b) illustrate the presence of micro-scale porosities in cylinder IX and X which are undetectable by the adopted approach.

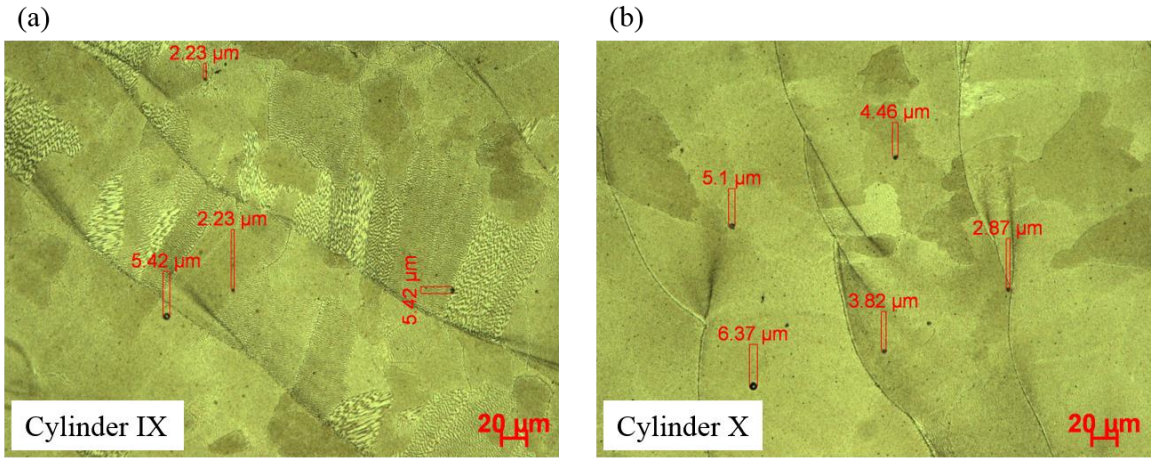

Figure 4.28 Optical microscopy images of cylinders (a) IX and (b) X illustrating the presence of micro-porosities.

4.4 Defects captured by in-situ monitoring system

The IMS was also employed for the inspection of other print jobs. Apart from the identification of features, other types of defects were detected by the IMS. Delaminations were captured during the printing process of tensile coupons with support structures. The

delaminated regions of the tensile coupons and their support structures are shown in Figure 4.29 (a). The optical images captured after recoating also revealed delamination of one tensile coupon and elevated regions corresponding to the support structures as shown in Figure 4.29 (b). They were thin-walled structures placed extensively throughout the base of the tensile coupons. These structures were designed with the purpose of minimising the materials needed for support. The tensile coupons can be easily removed due to the support structures' small area of contact with the substrate. However, the extensive presence of these support structures proved to be disruptive to the printing process's stability. This has led to inconsistencies in the resolution of printed parts.

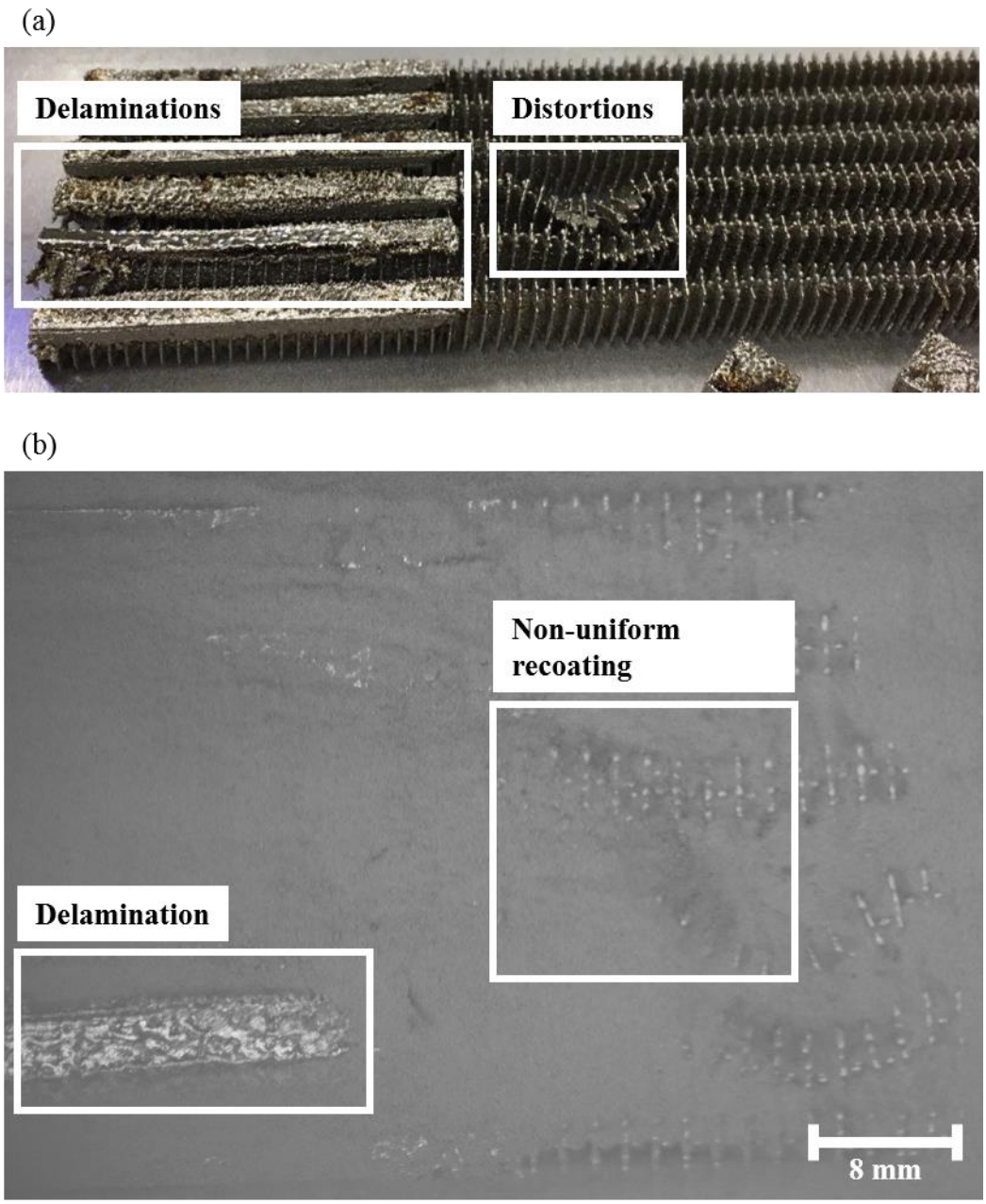

Figure 4.29 Delaminations and geometric distortions of tensile coupons and their support structures respectively and (b) image of (a) captured in-situ.

Elevated regions of the printed parts and non-uniform recoating of the powder bed due to damaged recoated blade were captured by the IMS. Overhang structures were printed with varying angles as shown in Figure 4.30 (a). Support structures, which act as a heat

diffuser while enhancing the structural rigidity of the printed parts, were absent. The metal powders below the unsupported structures have a low thermal conductivity, causing the accumulation of excessive heat and correspondingly, residual stresses to be present in the printed parts [98, 99]. Local overheating and elevation of the built parts have damaged the recoater blade. Sharp corners are seen in the printed overhang structures shown in Figure 4.30 (b). As a result, localised deep scratches are observed on the powder bed in Figure 4.31.

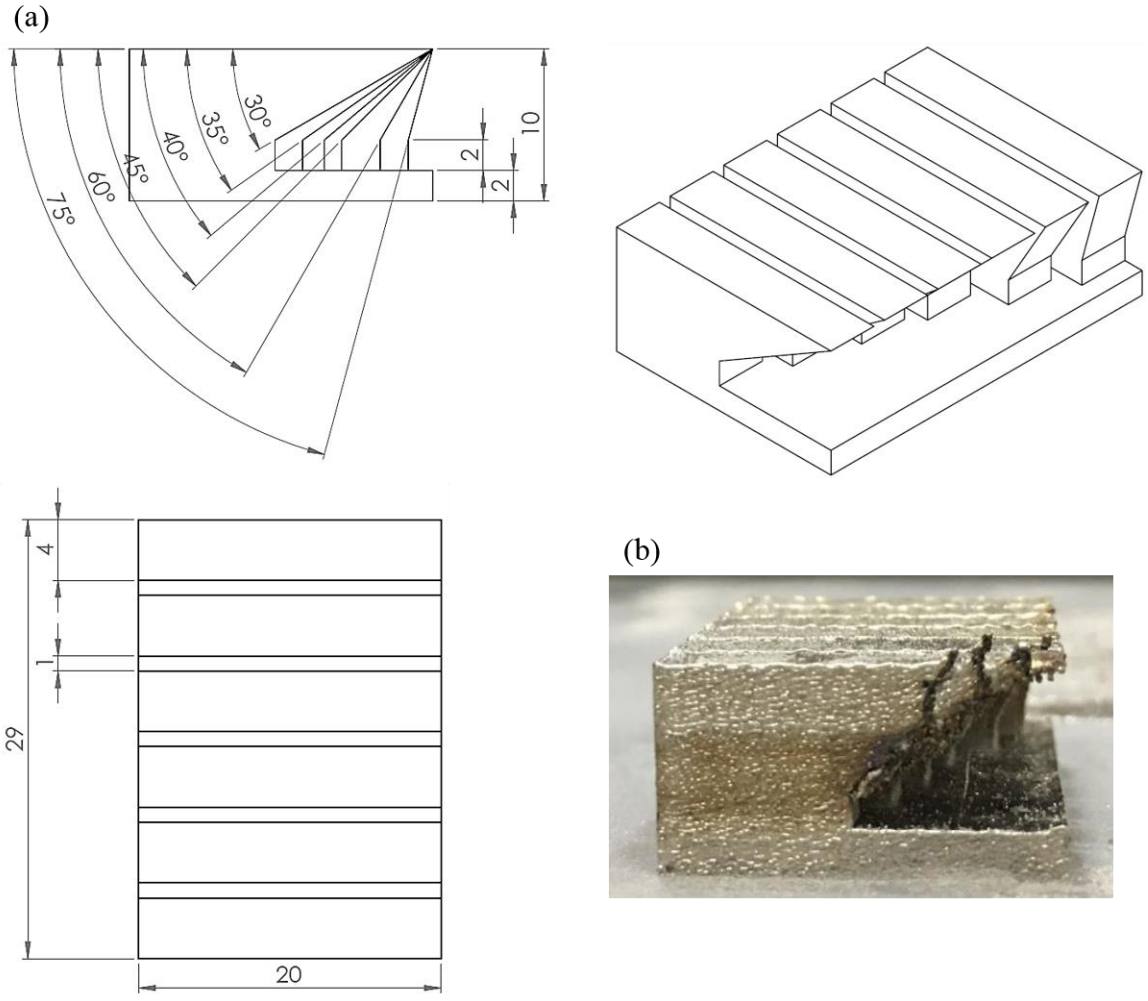

Figure 4.30 (a) Dimensions of overhang structures in millimetres and (b) overhang structures printed by SLM (side view).

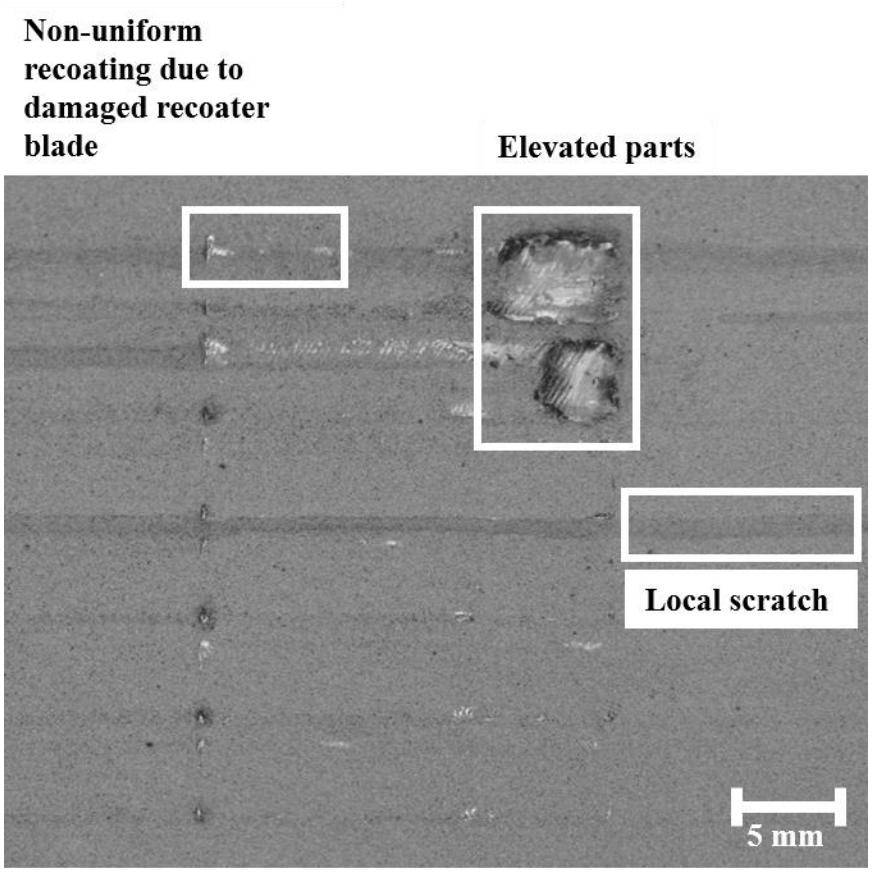

Figure 4.31 Recoated layer of overhang structures captured in-situ.

Porosities and balling were also observed on the surface of printed layers captured during other print jobs. A bridge was printed with increasing distance between consecutive supports as illustrated in Figure 4.32 (a). The lack of support structures in its design affected the part's printability. Heat accumulation could induce balling and adhesion of metal powders at regions without the supports [99]. Porosities and balling can be seen in Figure 4.32 (b), which was the image captured at the layer as indicated. The IMS can capture various types of defects through high-resolution imaging. This contrasts with many commercial systems that focus on the detection of a single type of defect.

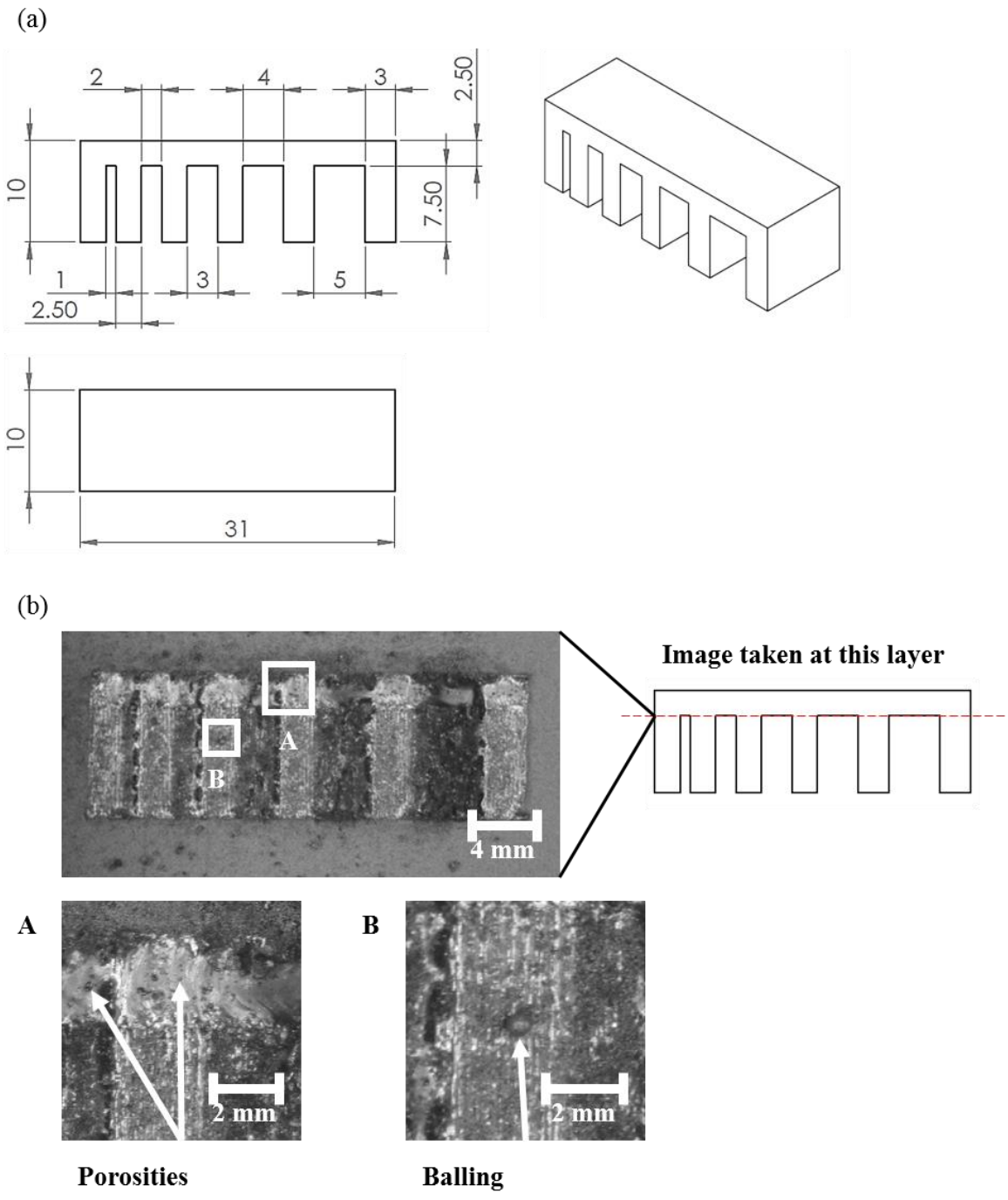

Figure 4.32 (a) Dimensions of bridge and (b) image of (a) captured at indicated layer.

4.5 Summary

The minimum size of cylindrical holes observable from captured optical images is 0.5 mm in diameter. The minimum size of square holes observable from captured optical images is 0.5 mm in length.

A relationship has been established between features captured in optical images during fabrication and the mechanical properties of the printed parts. Cylinders with higher percentage area of features exhibit lower densities and weaker mechanical properties, and vice versa. The implementation of the IMS based on optical imaging enables end users to distinguish between specimens with relatively higher density and better mechanical properties and specimens with relatively lower density and weaker mechanical properties.

Condensates and spatters play a crucial role in influencing the mechanical properties of the printed parts. Their presence on the surface of printed cylinders result in non-uniform heating when the laser beam is directed at the powder bed. This leads to significant amounts of elevated regions in optical images of affected cylinders, notably affecting their mechanical properties.

A correlation has been established between features captured in optical images during printing and the actual defects present in the printed part. Micro CT was used to validate the correlation of features in 2D optical images to actual 3D defects in the printed samples through reconstruction of the CT images, and more importantly, to justify the viability of using optical imaging as a solution for evaluating defects in printed parts. Similarities in trends between $OP_{features}$ and $CT_{defects}$ were established across the layers of the cylinders, where a higher $OP_{features}$ translates to higher $CT_{defects}$, and vice versa.

This enables end users to directly evaluate the area of defects present in parts based on real-time analysis of optical images, eliminating the need for long hours of defects detection in printed parts by CT.

Apart from the identification of features, other types of defects were detected by the IMS. Delaminations were captured during the printing process of tensile coupons with support structures. Elevated regions of the printed parts and non-uniform recoating of the powder bed due to damaged recoated blade were captured by the optical-based IMS. Porosities and balling were also observed on the surface of printed layers captured during other print jobs.

CHAPTER 5: RESULTS AND DISCUSSION — THERMAL IMAGES

5.1 Minimum defect size

The minimum size of cylindrical and square holes observable from captured images were studied. Referring to section 3.2.2.1, cylindrical holes and square holes of varying sizes were printed for each set of specimens consisting of a rectangular bar and six cuboids. The temperature profiles of the rectangular bars and cuboids were analysed. Unmelted powders and porosities have lower thermal conductivities than solidified metal, causing heat retention at regions where they are found [100]. Thermal imaging can detect their presence through variations in the temperature profiles of the bulk material. Thermal images were captured in a continuous process, similar to that of a video. Thus, images captured at different timeframes can be extracted for analysis. The thermal images of interest are those captured within two to three seconds after the laser scanned the powder bed. The temperature difference between the unmelted powders and the solidified metal is the highest, making it the easiest timeframe to examine for defects. More information on the selection of a suitable timeframe for analysing the thermal images can be found in section 5.2.2.

The rectangular bar and cuboids C4 to C6 containing cylindrical holes designed with diameters of 0.75 mm and above were easily identified and captured in the thermal images as shown in Figures 5.1 (a) and (b). Cylindrical holes with diameter of 0.5 mm were observable from Figure 5.1 (a), but not visible from Figure 5.1 (b). As cuboid C3 was printed alongside five other cuboids and was placed very close to one another (see section 3.2.2.1), there is lesser surface area available for heat to be dissipated to the cooler powder bed. Cuboids C2 and C6, which were placed beside cuboid C3, also

dissipated heat. This caused the powder bed surrounding cuboids C2 and C6 to be heated up. The temperature difference between the cylindrical hole with diameter of 0.5 mm (between 120°C and 140°C; containing unmelted powders) and the solidified metal (also between 120°C and 140°C) is smaller as compared to the case of the rectangular bar. The pixels' colours at regions of the cylindrical hole in cuboid C3 is indistinguishable from those at regions of the solidified metal in the thermal images. Cylindrical holes with diameters of 0.25 mm, 0.1 mm and 0.5 mm in the cuboids were not visible based on Figure 5.1 (b). It can be concluded that cylindrical holes of 0.75 mm and above were detectable from the thermal images captured.

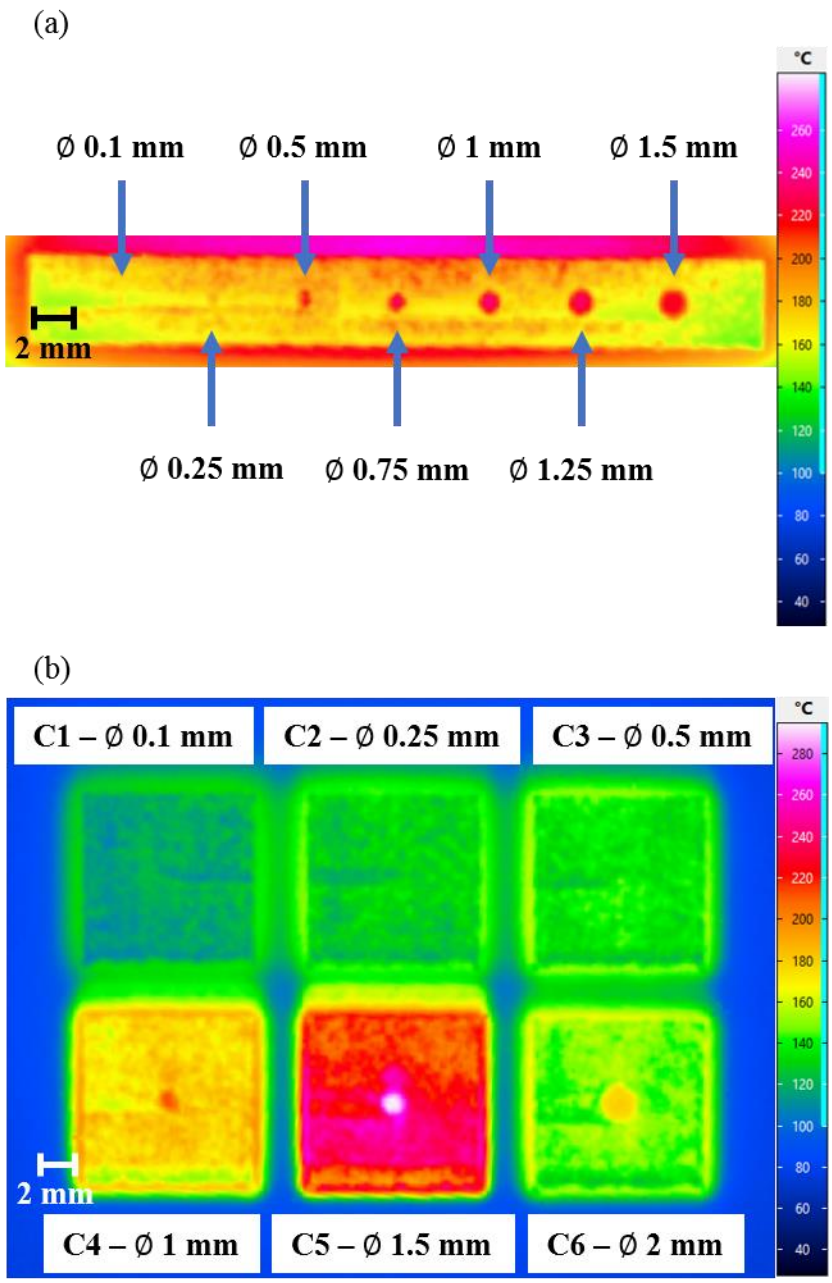

Figure 5.1 Thermal images of (a) rectangular bar and (b) cuboids with cylindrical holes of various diameters.

The cylindrical hole with diameter of 0.25 mm, however, was detectable from the temperature profile plot as illustrated in Figure 5.2. The spike in temperatures correspond to cylindrical holes of the rectangular bar. The detection of 0.25 mm and 0.1 mm

diameter cylindrical holes is challenging during actual printing. However, they are identifiable from the temperature profile plot since the location and size of the defects were known beforehand even though their peak temperatures are significantly lower than the bigger cylindrical holes due to the small amount of unmelted powders.

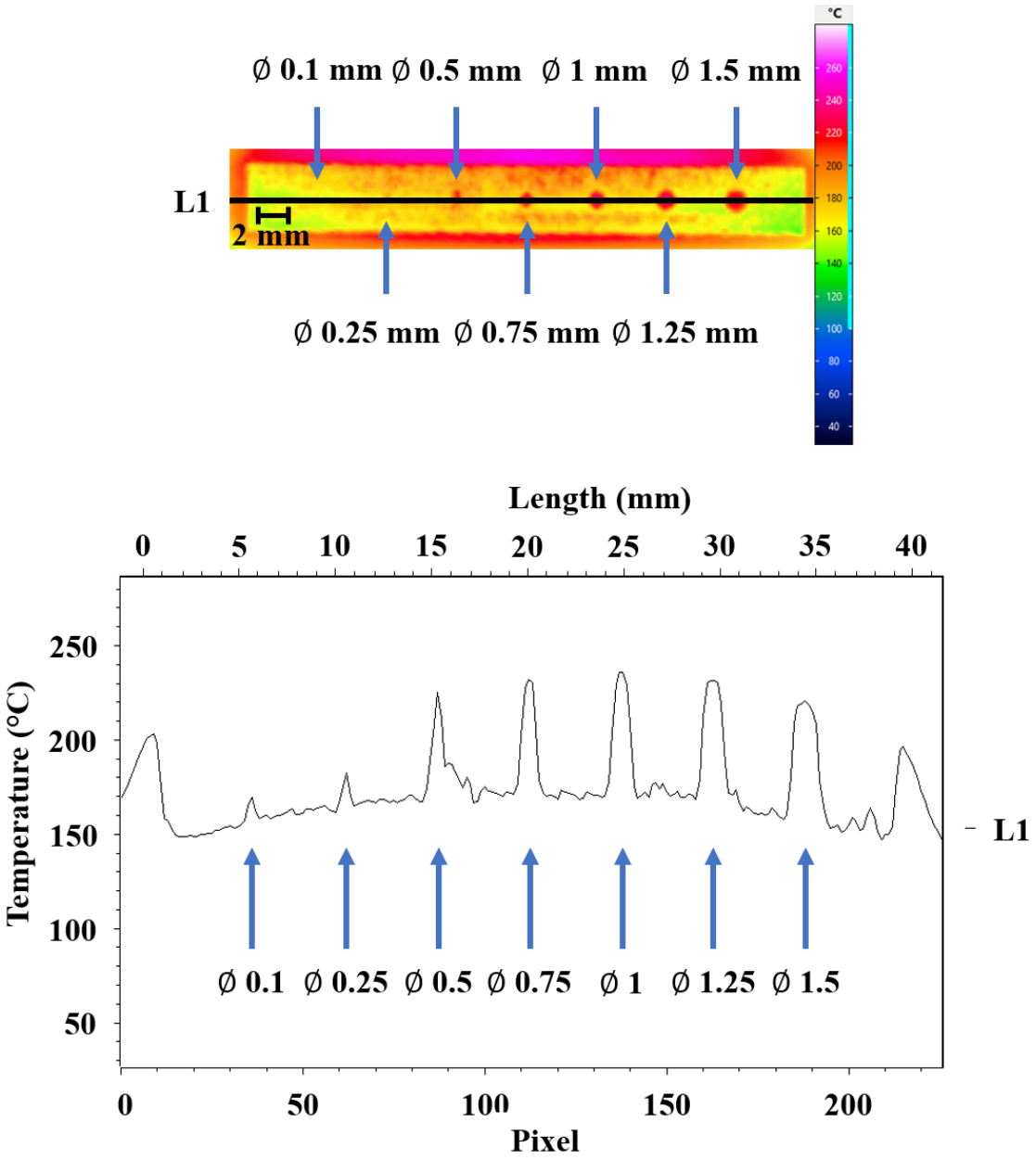

Figure 5.2 Pixels' temperature profile of the rectangular bar with cylindrical holes across the line, L1 (dimensions in millimetres).

Another set of experiments albeit with square holes was carried out. The rectangular bar and cuboids R4 to R6 containing square holes designed with lengths of 0.75 mm and above were easily identified and captured in the thermal images as shown in Figures 5.3 (a) and (b). Square holes with length of 0.5 mm were observable from Figure 5.3 (a), but

not visible from Figure 5.3 (b). The same reason, as explained for the case of cylindrical holes, is responsible for the square hole with length of 0.5 mm being not visible from the thermal image of cuboid R3. As cuboid R3 was printed alongside five other cuboids and was placed very close to one another (see section 3.2.2.1), there is lesser surface area available for heat to be dissipated to the cooler powder bed. The temperature difference between the square hole with length of 0.5 mm (containing unmelted powders) and the solidified metal is smaller as compared to the case of the rectangular bar. Square holes with lengths of 0.25 mm, 0.1 mm and 0.5 mm were not visible based on Figure 5.3 (b). It can be concluded that square holes with lengths of 0.75 mm and above were detectable from the thermal images captured.

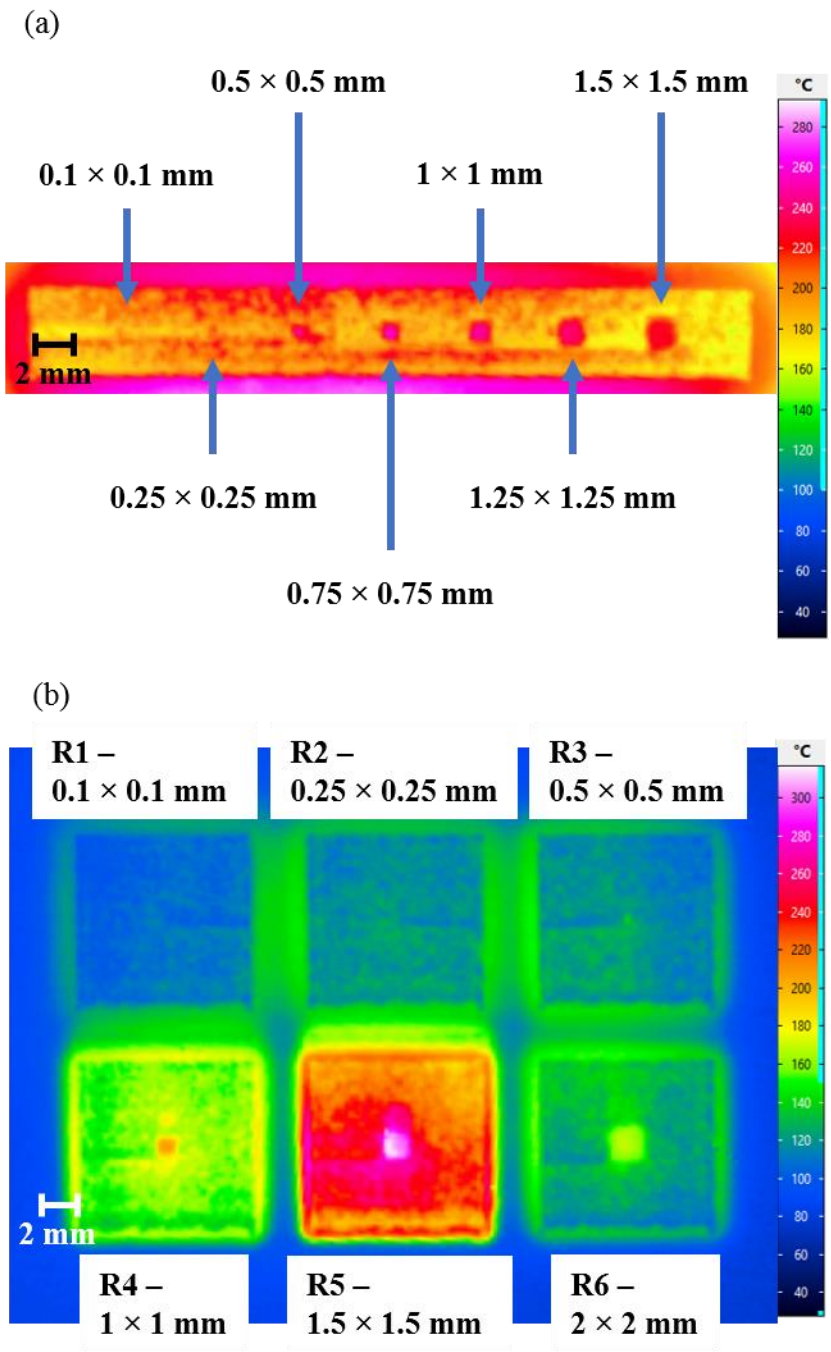

Figure 5.3 Thermal images of (a) rectangular bar (temperature scale bar is the same as (b) and (b) cuboids with square holes of various lengths.

Likewise, the detection of square holes with lengths of 0.25 mm and 0.1 mm is challenging during actual printing. Their peak temperatures, shown in Figure 5.4, are

significantly lower than the bigger square holes due to the small amount of unmelted powders.

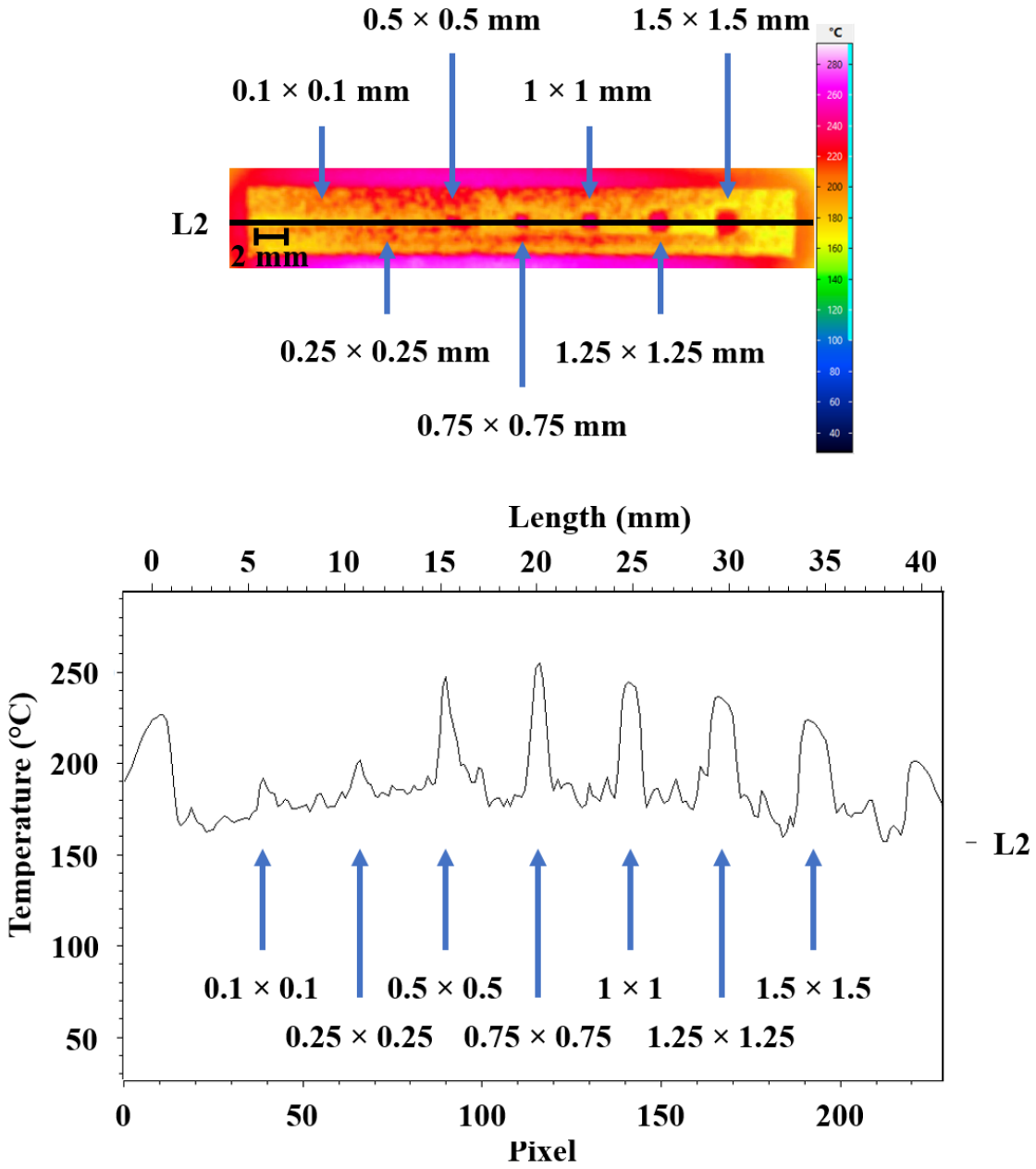

Figure 5.4 Pixels' temperature profile of the rectangular bar with square holes across the line, L2 (dimensions in millimetres).

5.2 Correlation between thermal images and densities of printed parts

This section examines the establishment of a relationship between the signatures present in thermal images captured in-situ and the parts' densities. The occurrence of pixels with high temperature gradients was evaluated from thermal images. They were then compared and correlated with the densities of the respective printed parts. Only the infrared camera was used in this study.

Ten cylinders measuring 6 mm in diameter and 6 mm in height were printed with the same parameters listed in Table 3.3, section 3.2.2.2. The placements of the cylinders are shown in Figures 5.5 (a) and (b). It should be highlighted that optical images of the cylinders were also captured in-situ for monitoring the presence of condensates and spatters. The cylinders were spaced apart from each other. This reduces the probability of inaccurate temperature readings recorded by the infrared camera due to interaction of thermal energy between the heated cylinders. The ten cylinders were fabricated in two print jobs of which each print job comprised five cylinders.

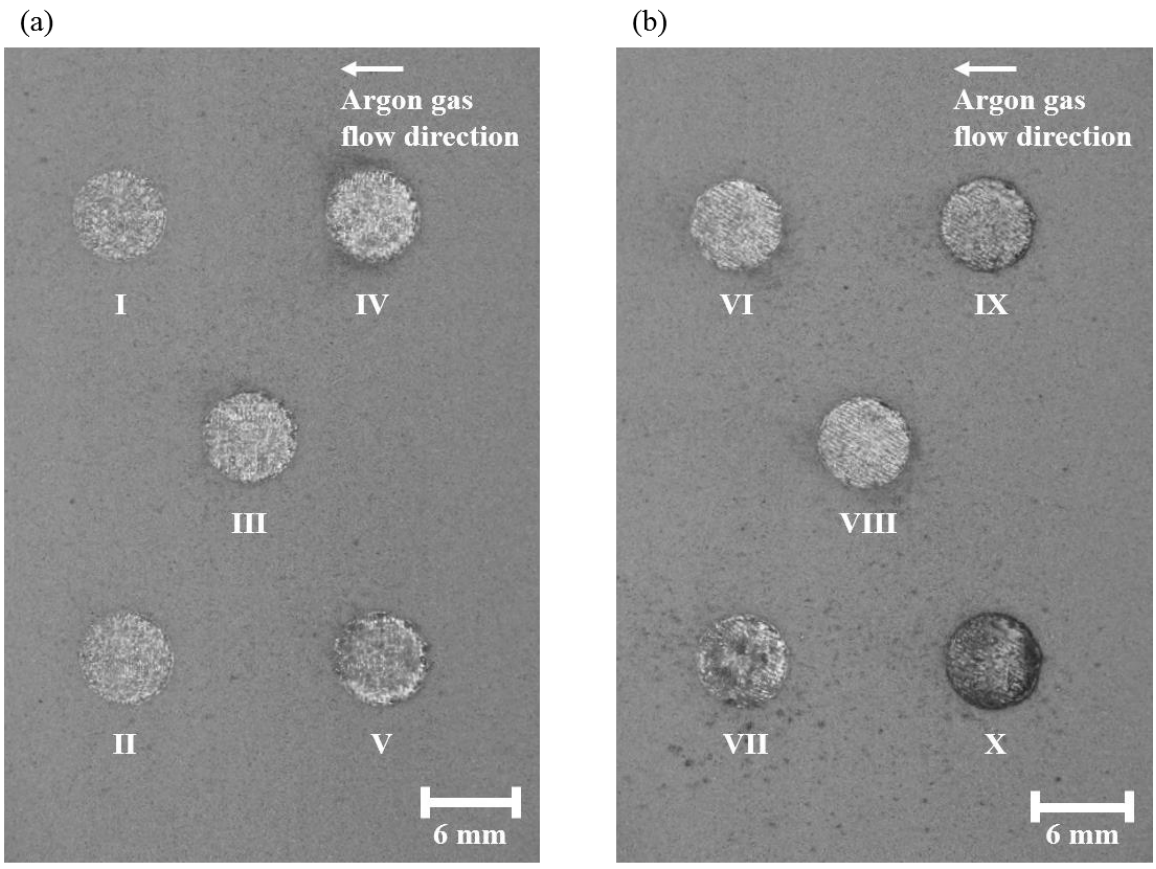

Figure 5.5 Placements of cylinders (a) I to V and (b) VI to X in each print job where condensates and spatters are the dark spots on the powder bed.

5.2.1 Density test

The average densities of the ten cylinders based on Archimedes' principle are shown in Figure 5.6. The results are similar to the findings obtained in section 4.2.1 since the printing parameters are identical. Each data point in Figure 5.6 is an average of three measurements for each cylinder. The individual density measurements for the ten cylinders can be found in Appendix D. A general trend shows that an increase in the energy density ratio from 0.5 to 2.0 leads to an increase in the average density of the cylinders. Following which, the average density remains relatively constant for cylinders with energy density ratios of 3.0 and 4.0 as powders are fully melted. The differences in

the results obtained between this study and that reported in section 4.2.1 are the improved average density of cylinder IV and the reduced average density of cylinder VII.

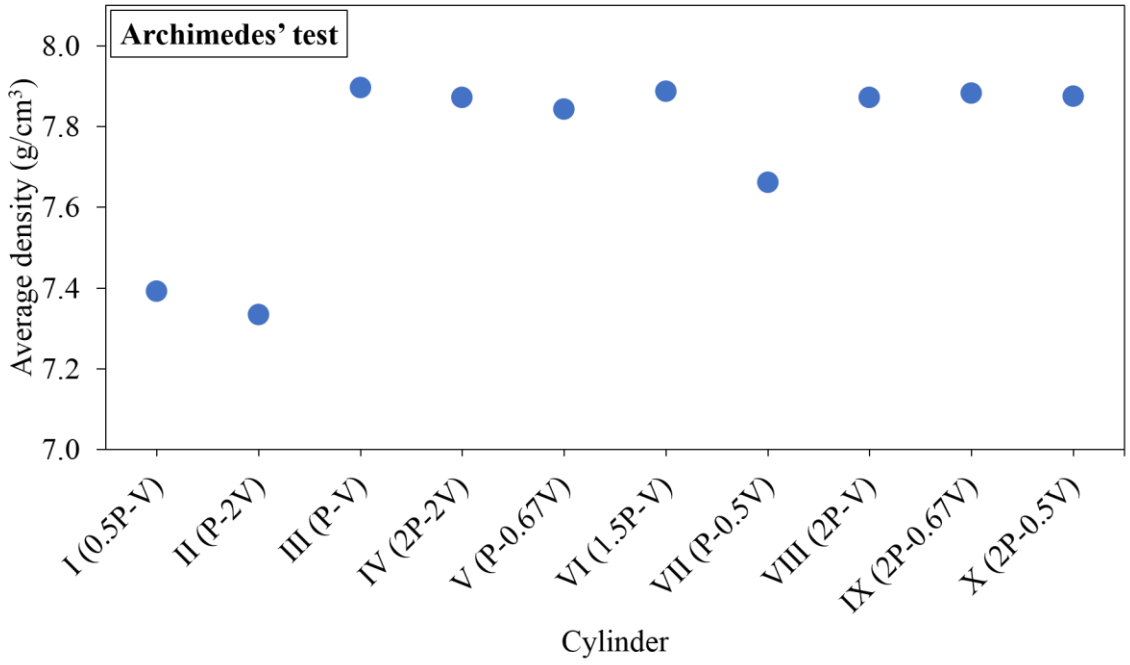

Figure 5.6 Average densities of ten cylinders.

Condensates and spatters have been found to play a crucial role in influencing the mechanical properties of the printed parts [92]. The average density of cylinder IV improved notably as minimal condensates and spatters was present on its surface during printing (Figure 5.5 (a)). Cylinder IV was printed together with cylinders I, II, III and V. These cylinders were printed with relatively low energy density ratios of 0.5 to 1.5. The temperature within the molten pool of these cylinders barely exceeds the powders' vaporisation point. Therefore, minimal condensates and spatters were present during printing. On the contrary, cylinder VII had significant amounts of condensates and spatters on its surface and regions around it during printing as depicted in Figure 5.5 (b).

Cylinder VII was printed together with cylinders VI, VIII, IX and X. These cylinders were printed with relatively high energy density ratios of 1.5 to 4.0. The temperature within the molten pool of these cylinders exceeds the powders' vaporisation point [92]. Liu et al. [92] reported that an increase in energy input to the printed specimens will lead to more condensates and spatters generated. Cylinder VII was placed beside cylinder X, which was printed with the highest energy density ratio of 4.0, generating significant amounts of condensates and spatters. As the argon gas flows from right to left within the machine chamber, these condensates and spatters settle on the left side of the powder bed. As a result, relatively large amounts of condensates and spatters were seen on cylinder VII's surface, notably affecting its density.

5.2.2 Analysis of thermal images

Defects such as unmelted powders, partially melted powders and porosities generated during printing will disrupt the temperature distribution across the surface of the printed cylinders. The analysis of thermal images was carried out based on this principle. Unmelted powders, partially melted powders and porosities possess lower thermal conductivities than solidified metal. A material of low thermal conductivity induces more heat retention within itself as compared to a material of higher thermal conductivity. During printing, more heat is retained at regions where unmelted powders, partially melted powders and porosities are found as compared to the solidified metal. Their presence is therefore characterised by regions of relatively high temperature gradients in processed thermal images. Thermal images were studied at two timeframes — (1) three and (2) ten seconds after the laser scanned the powder bed. The rationale behind this is to

determine the best timeframe to analyse the thermal images so that defects can be identified most accurately.

The following describes the procedures taken to analyse thermal images captured three and ten seconds after the laser scanned the powder bed. The thermal images captured were post processed to evaluate the temperature gradient across the pixels. The formulation of the temperature gradient across the pixels of each thermogram as suggested by Raplee et al. [101] requires the calculation of the temperature differences between the pixels computed as

$$\Delta T_x = \frac{|T_x - T_{x-1}| + |T_x - T_{x+1}|}{2} \text{ and} \tag{5.1}$$

$$\Delta T_y = \frac{|T_y - T_{y-1}| + |T_y - T_{y+1}|}{2} \tag{5.2}$$

where x and y are the pixel locations in the x and y directions of the image respectively. T_{x-1}, T_x, T_{x+1}, T_{y-1}, T_y and T_{y+1} are the temperatures (in °C) of each pixel at their subscripted locations.

The temperature gradient across the pixels, G (in °Cm^{-1}), as suggested by Raplee et al. [101] is given as

$$G = \sqrt{\left(\frac{\Delta T_x}{\Delta x}\right)^2 + \left(\frac{\Delta T_y}{\Delta y}\right)^2} \tag{5.3}$$

where Δx and Δy are the length per pixel in the x and y directions of the image respectively. Δx and Δy were evaluated to be 0.18 mm per pixel in the x direction and 0.19 mm per pixel in the y direction.

A raw thermal image illustrating the temperature information is captured as shown in Figures 5.7 (a). The raw data captured is a collection of temperature values, represented by pixels in Figure 5.7 (a). The brighter pixels indicate higher temperature. This image is alike coloured thermal pictures, but in greyscale format. The raw thermal image is then processed through a series of computation as explained by equations (5.1) to (5.3) to obtain information on the temperature gradient across the pixels (Figure 5.7 (b)). The brighter pixels indicate higher temperature gradients. Regions of high temperature gradients, represented by grey pixels in Figure 5.7 (b), are found at the perimeter of a printed part. This is due to the large temperature difference between unmelted metal powders and melted bulk material. A mask, depicted in Figure 5.7 (c), is applied onto the ROI which corresponded to the top surface area of the cylinder as shown in Figure 5.7 (d). The mask covers 90% of the original cross-sectional area of the cylinder. This omits the evaluation of high temperature gradient regions near its perimeter. The perimeter of the printed cylinder has inevitably high temperature gradients due to the large temperature difference between melted bulk material and unmelted metal powders of the powder bed. The maximum value of the temperature gradient, G_{max}, is then evaluated using equation (5.3) (Figure 5.7 (d)). The minimum value of the temperature gradient, G_{min}, also evaluated using equation (5.3), is set to 0 °Cm^{-1}. This value is also used as a reference to examine how extensive G_{max} has deviated from G_{min}.

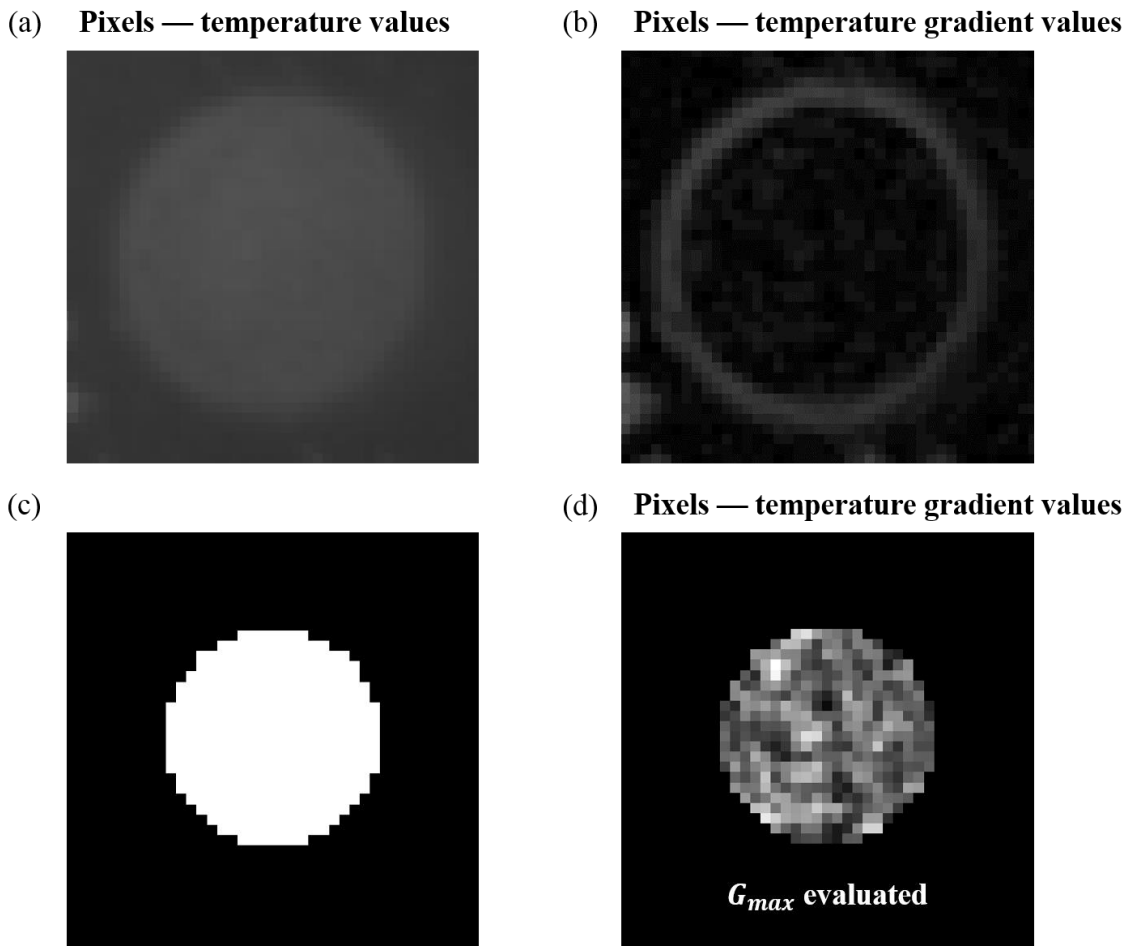

Figure 5.7 (a) Pixels representing temperature values (raw image), (b) pixels representing temperature gradient values (processed image), (c) binary mask created at ROI and (d) G_{max} evaluated within ROI after mask is applied to (b).

The temperature gradient across the pixels within the ROI is then normalised according to

$$G' = \frac{G - G_{min}}{G_{max} - G_{min}}. \tag{5.4}$$

G' ranges from 0 through 1. 0 denotes no normalised temperature gradient and hence, the corresponding temperature difference between the pixel of interest and its neighbouring pixels is also 0 based on equations (5.3) and (5.4). 1 represents maximum normalised

temperature gradient and hence, the corresponding temperature difference between the pixel of interest and its neighbouring pixels is also 1 based on equations (5.3) and (5.4). A value of 0 or values near 0 also signifies that defects are unlikely to be present around the pixel of interest. On the other hand, a value of 1 or values near 1 implies that defects are more likely to be present around the pixel of interest.

Ideally, the temperature gradient across pixels within the ROI is 0 $°Cm^{-1}$ as the absence of defects do not introduce perturbations to the temperature profile across the surface of the printed part. The presence of temperature gradients across pixels within the ROI is inevitable during printing. As the laser scans the powder bed, regions of metal powders that it first came into contact would have solidified and cooled down as compared to regions that were subsequently scanned. When a thermal image is analysed, a gradual increase in the normalised temperature gradient is observed across the indicated direction travelled by the laser in Figure 5.8.

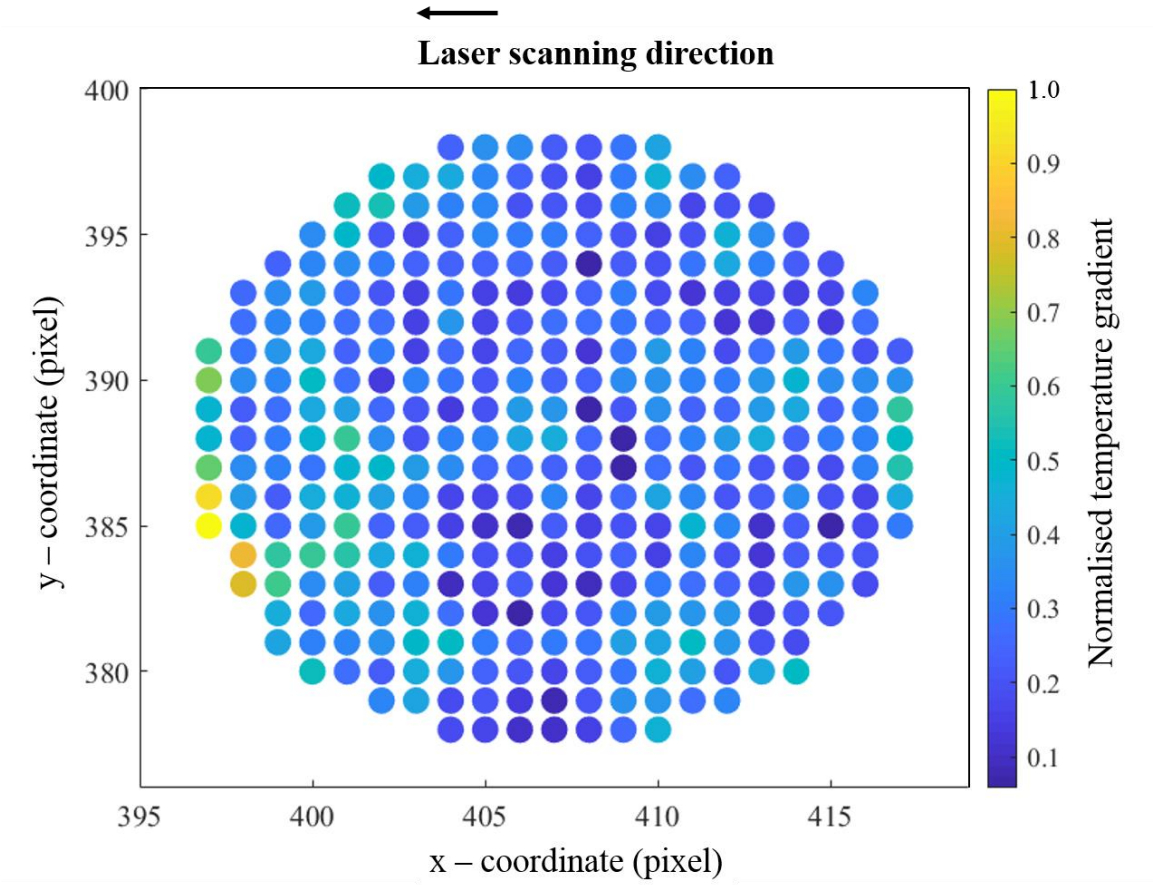

Figure 5.8 Normalised temperature gradient of thermal image three seconds after laser scanned the powder bed, illustrating its scanning direction (top view).

Figure 5.9 shows the temperature profiles of the solidified metal and unmelted powders immediately after the laser has stopped scanning. According to the figure, thermal images should be examined near the timeframe when the cylinders were just printed, i.e., within two to three seconds after the laser has scanned the part. This is the timeframe where temperature difference between defects and the bulk material is the largest. If the timeframe chosen is after a significant amount of time has passed, the defects and the bulk material will be approaching equilibrium temperature as seen in Figure 5.9. The normalised temperature gradient across the pixels will be values nearer to zero as the

temperature difference between defects and the bulk material decreases with time. Correspondingly, defects may not be identified easily from the processed thermal images. The time-dependent nature of thermal images will be further illustrated in sections 5.2.3 and 5.2.4. Additionally, the examination of thermal images within two to three seconds after the laser has scanned the part is only valid for specimens and process parameters studied in this experiment.

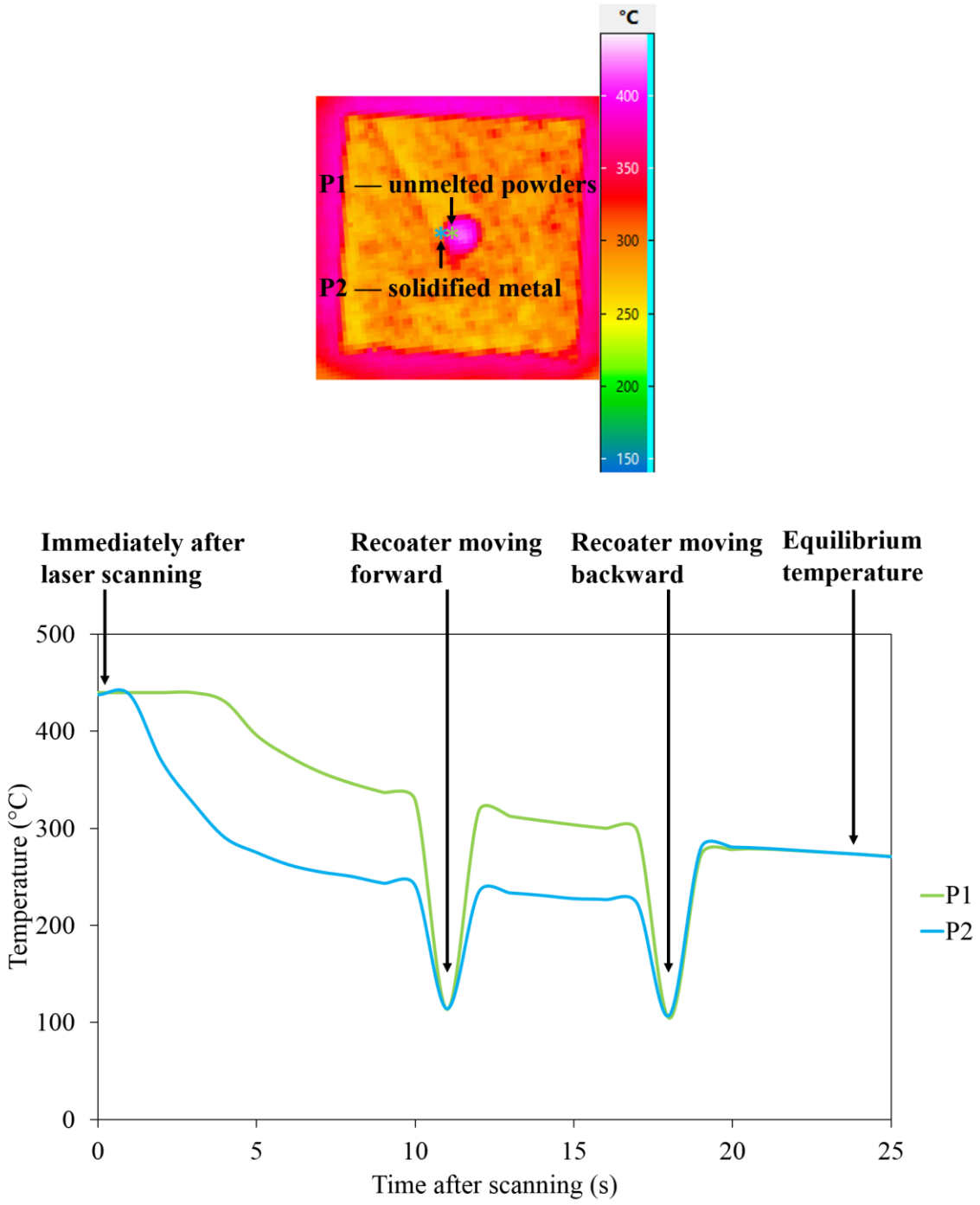

Figure 5.9 Temperature profiles of pixels located at unmelted powders (P1) and solidified metal (P2) with time.

Each cylinder is analysed individually by cropping their thermal images out for a total of N number of layers. The number of layers for each print job depends on the height of the

parts. G_{max} is computed for each layer. The number of pixels that falls within a certain range of normalised temperature gradients, denoted as $H_{a-b,n}$, is evaluated. Here, a represents the lower normalised temperature gradient limit, b represents the higher normalised temperature gradient limit and n corresponds to the layer number. $H_{0.0-0.1,1}$, for example, represents the number of pixels that falls between the normalised temperature gradients of 0.0 (exclusive) and 0.1 (inclusive) for the first layer. $H_{0.0-0.1,n}$ is computed from $n = 1$ to $n = N$.

The steps were repeated to obtain the data points for $H_{0.1-0.2,1}$, which means the number of pixels that falls between the normalised temperature gradients of 0.1 (exclusive) and 0.2 (inclusive) in the first layer. Similarly, $H_{0.1-0.2,n}$ is computed from $n = 1$ to $n = N$. The whole process is repeated until the number of pixels that fall between $H_{0.0-0.1,n}$ and $H_{0.9-1.0,n}$ are determined from $n = 1$ to $n = N$.

The average number of pixels that falls between the normalised temperature gradients of 0.0 (exclusive) and 0.1 (inclusive) for a cylinder with N layers is evaluated as

$$H_{0.0-0.1,average} = \frac{\sum_{n=1}^{N} H_{0.0-0.1,n}}{N}. \quad (5.5)$$

Similarly, $H_{0.1-0.2,average}$ to $H_{0.9-1.0,average}$ are evaluated for the cylinder. The abovementioned steps were repeated for the remaining cylinders and the results are reflected in Figure 5.10 (a). The results for the pixels' distribution based on thermal images studied at a timeframe of ten seconds after the laser scanned the powder bed are presented in Figure 5.10 (b).

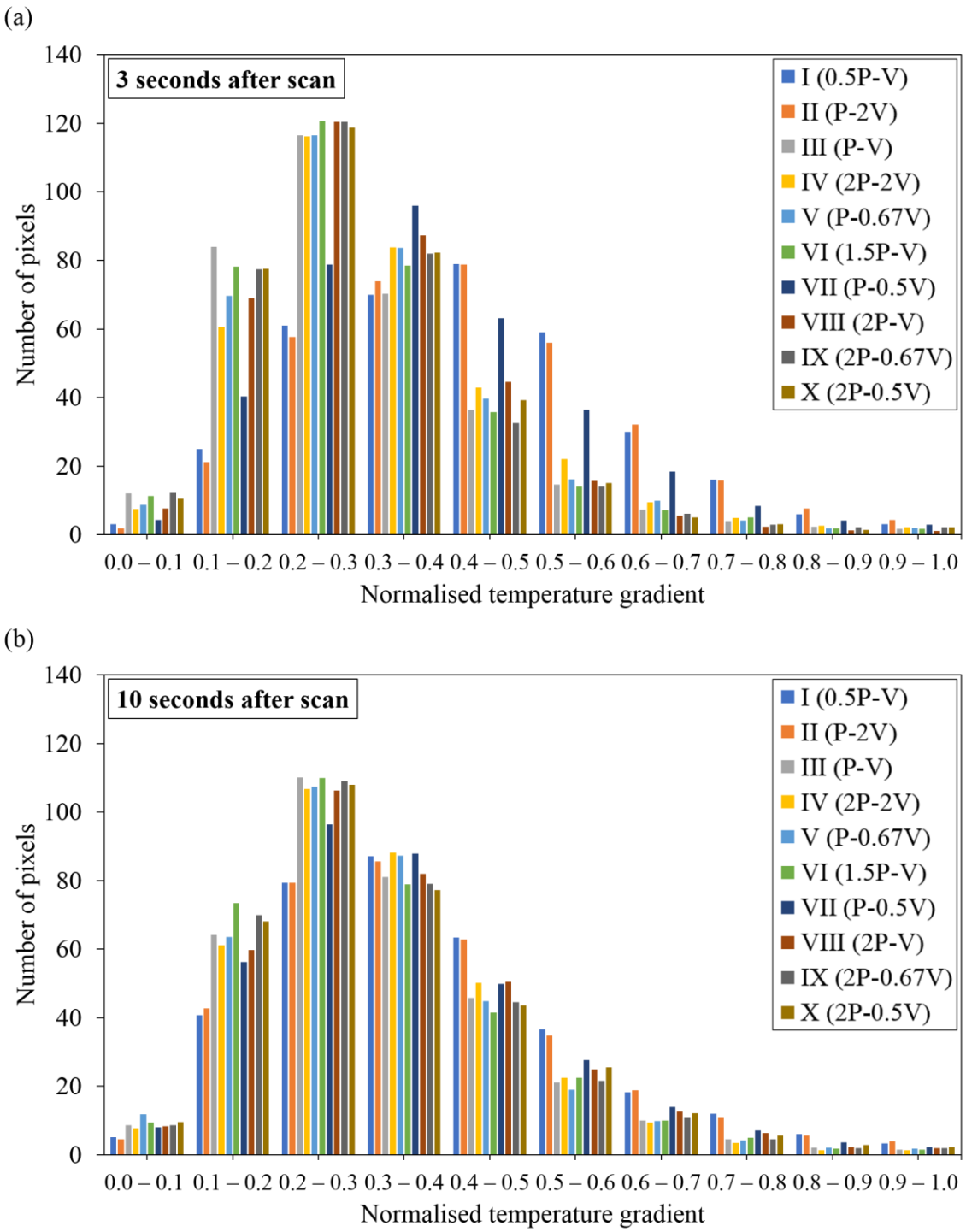

Figure 5.10 Frequency distribution of pixels at different normalised temperature gradients at timeframe of (a) three seconds and (b) ten seconds after the scanning.

As mentioned, thermal images were studied at two timeframes — (1) three and (2) ten seconds after the laser scanned the powder bed. The timeframe of ten seconds is studied as it is right before the recoater recoats the powder bed, i.e., before the temperature data of the pixels become inaccurate due to interference from the recoater as illustrated in Figure 5.9.

The timeframe at which thermal images are studied may vary according to the geometries and sizes of printed parts and the scanning speed. A preliminary study (similar to Figure 5.9) should be performed to determine an appropriate timeframe where the temperature difference between defective regions of printed part and its bulk material is the largest.

5.2.3 Correlation of results

As discussed, temperature gradient across the pixels is larger than 0 $°Cm^{-1}$ during actual printing due to the temperature difference between regions of the powder bed that the laser first came into contact and regions that were subsequently scanned. This explains for the small number of pixels that falls within 0.0 – 0.1 of the normalised temperature gradient as seen across all ten cylinders in Figures 5.10 (a) and (b). The finding also indicates that temperature gradients exist across the surfaces of printed parts.

While a region of high normalised temperature gradient may signify the presence of defects, the location at which high normalised temperature gradients occur is crucial. High normalised temperature gradients always exist across pixels located near and at the perimeter of the printed part due to large temperature differences between unmelted metal powders and solidified metal. Furthermore, within a short time span of three seconds, cooling of the solidified metal has just begun, accounting for the large temperature difference between unmelted metal powders and solidified metal. These regions, are

therefore, not of interest for defects detection. However, if a region of high normalised temperature gradient exists across pixels within the ROI of the cylinder, as illustrated in Figure 5.11, they should be further examined for the possible presence of defects.

5.2.3.1 Cylinders I, II, VII

Several regions of high normalised temperature gradients exist within the ROIs of cylinders I and II as supported by the presence of yellow and orange pixels in Figures 5.11 (a) and 5.12 (a). These regions are scattered throughout the cross sections of cylinders I and II, indicating a high possibility of defects. Indeed, CT images represented by Figures 5.11 (b) and 5.12 (b) show an extensive amount of unmelted and partially melted powders as the cylinders were printed with relatively low energy densities. These powder particles, together with the presence of gases (air) in between them, have lower thermal conductivities than that of solidified metal, allowing them to retain more heat. This leads to a notable difference in temperature between the defects and the bulk material. Correspondingly, the normalised temperature gradient between defects and the bulk material is large. Cylinders I and II were printed with a relatively low energy density ratio of 0.5. Insufficient energy input to the powder bed led to extensive regions of partially melted powders present in cylinders I and II, reducing their overall densities. As discussed in section 5.2.2, the mask covers 90% of the original cross-sectional area of each cylinder. The images presented in Figures 5.11 (a) and 5.12 (a) (including Figures 5.13 (a) and 5.14 (a)) omit the high temperature gradient regions near the cylinders' perimeters. The perimeter of the printed cylinder has inevitably high temperature gradients due to the large temperature difference between melted bulk material and unmelted metal powders of the powder bed. As a result, images in Figures 5.11 (a) and

5.12 (a) (including Figures 5.13 (a) and 5.14 (a)) do not illustrate the presence of porosities at the perimeters of the cylinders even though they can be seen from the corresponding CT images.

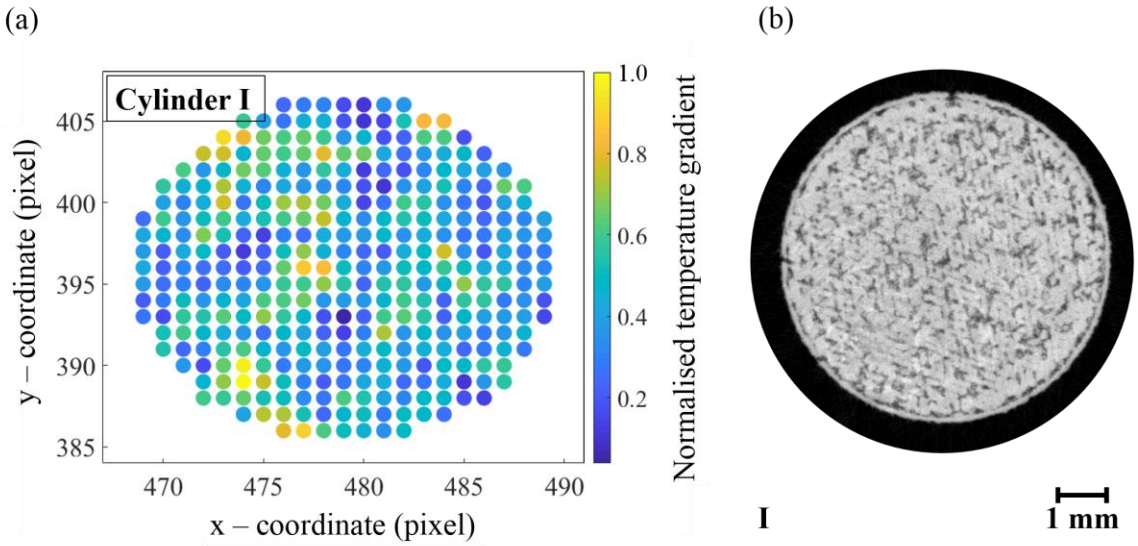

Figure 5.11 (a) Normalised temperature gradient of thermal image (90% of the original cross-sectional area) three seconds after laser scanned the powder bed (top view) and (b) CT image of cylinder I depicting porosities and partially melted powders.

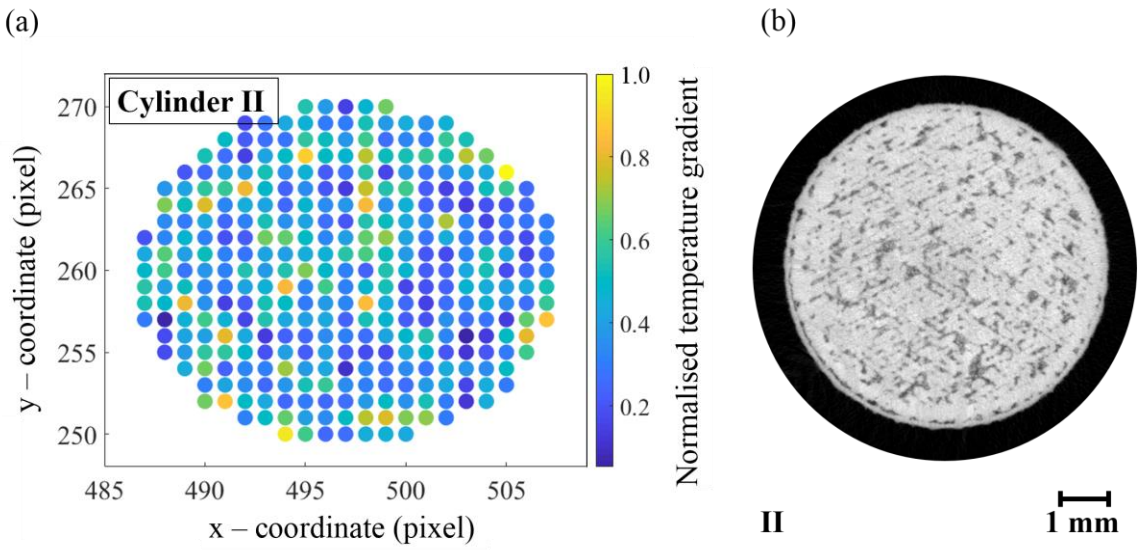

Figure 5.12 (a) Normalised temperature gradient of thermal image (90% of the original cross-sectional area) three seconds after laser scanned the powder bed (top view) and (b) CT image of cylinder II depicting porosities and partially melted powders.

Cylinder VII is expected to have a high density as it was printed with a relatively high energy density ratio of 2.0. However, the presence of condensates and spatters, as mentioned in sections 4.2.3 and 5.2.1, plays a crucial role in influencing the mechanical properties of the printed parts. Significant amounts of condensates and spatters on cylinder VII's surface and regions around it led to the occurrence of high normalised temperature gradient regions within the ROI of cylinder VII (Figure 5.13 (a)). The presence of porosities is illustrated in Figure 5.13 (b). Correspondingly, the average density of cylinder VII is relatively low as compared to cylinder VIII which was printed with the same energy density ratio.

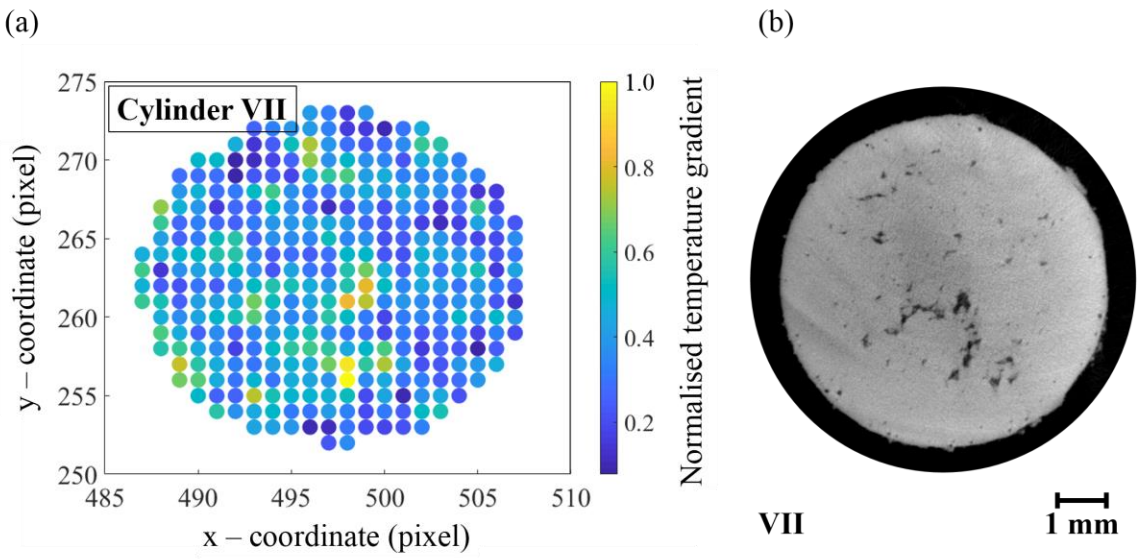

Figure 5.13 (a) Normalised temperature gradient of thermal image (90% of the original cross-sectional area) three seconds after laser scanned the powder bed (top view) and (b) CT image of cylinder VII depicting porosities.

It can be concluded that cylinders with more pixels of high normalised temperature gradients across their cross sections exhibit lower densities. Thus, the implementation of the IMS based on thermal imaging enables end users to distinguish specimens with relatively lower density.

5.2.3.2 Cylinders III to VI and VIII to X

Regions of high normalised temperature gradients are less prominent in cylinders III to VI. Most pixels have low normalised temperature gradients, supported by a large peak located towards the left in their distribution plots in Figure 5.10 (a). Likewise, similar trends are observed for the distribution plots of cylinders VIII to X. These cylinders showed minimal regions of high normalised temperature gradients within their ROIs. Using cylinder IX as an example, the number of yellow and orange pixels in Figure 5.14 (a) is limited and are located on the left of its perimeter. There is also no notable

difference in temperature across the bulk material. As a result, the normalised temperature gradient across the bulk material of cylinder IX is more uniform than cylinders I, II and VII. Most pixels of cylinders III to VI and VIII to X have low normalised temperature gradients, translating to a large peak located towards the left in their distribution plots as observed in Figure 5.10 (a).

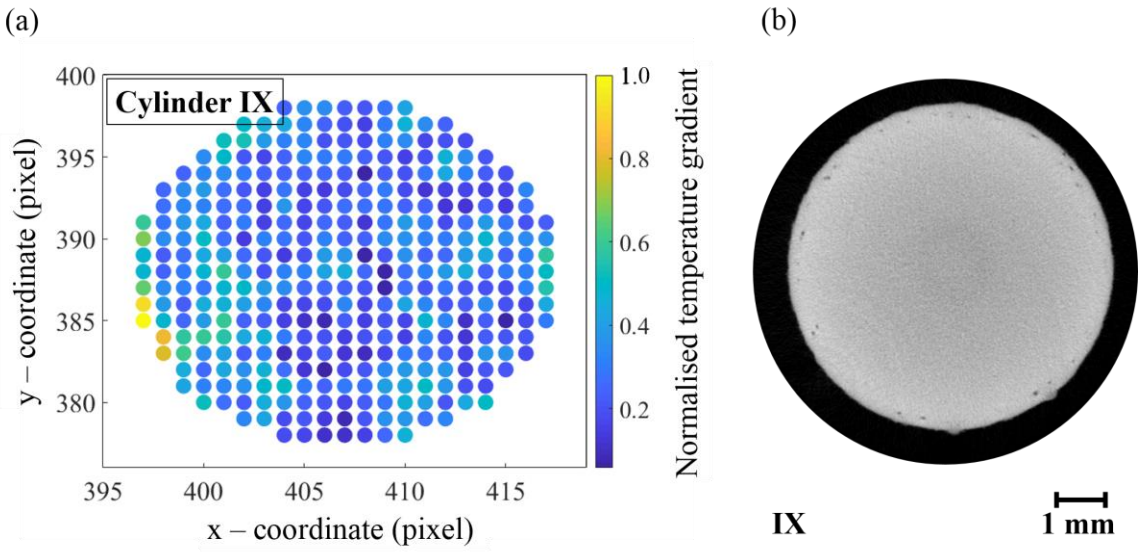

Figure 5.14 (a) Normalised temperature gradient of thermal image (90% of the original cross-sectional area) three seconds after laser scanned the powder bed (top view) and (b) CT image of cylinder IX.

Porosities, as seen from the CT image of cylinder IX in Figure 5.14 (b), were mostly present near its perimeter. The CT images of cylinders III to VI, VIII and X also demonstrated minimal porosities. Since these cylinders were printed with relatively high energy density ratios, complete melting of the metal powders leads to the formation of high-density parts.

It can be concluded that cylinders with more pixels of low normalised temperature gradients across their cross sections exhibit higher densities. The implementation of the

IMS based on thermal imaging enables end users to distinguish specimens with relatively higher density. Results from density tests based on Archimedes' principle have demonstrated a correlation with the processed thermal images of the cylinders. The established correlation has validated the potential of inferring the printed parts' mechanical performance based on features identified through infrared based IMS. This can potentially aid in the production of parts with improved densities. Printing parameters can be adjusted in-situ to improve the quality of the printed part if the number of pixels with high normalised temperature gradients across their cross sections features correlate to poor densities, rendering both time and cost savings.

5.2.4 Time dependence of temperature data

One challenge of analysing thermal images is the change in temperature values across each timeframe. As the printed part is heated or cooled, the pixels' values, which reflect the temperature, increase or decrease accordingly. An investigation has revealed an optimal timeframe for analysing the thermal images so that the defects are most easily identified. The frequency distribution of pixels as shown in Figures 5.10 (a) and (b) illustrate the time dependence of temperature data.

When the thermal images are studied at a timeframe of three seconds after scanning, the distribution plot of cylinder I shows a relatively high number of pixels, i.e., between 0.4 – 0.5 and 0.8 – 0.9 of the normalised temperature gradients (Figure 5.10 (a)). The distribution plot of cylinder I also shows a relatively small number of pixels between 0.0 – 0.1 and 0.2 – 0.3 of the normalised temperature gradients (Figure 5.10 (a)). The mean normalised temperature gradient is 0.43 and the standard deviation of the distribution plot is 0.17.

When the thermal images are studied at a timeframe of ten seconds after scanning, the normalised temperature gradient with the highest number of pixels (frequency) has decreased from 0.4 – 0.5 to 0.3 – 0.4 for cylinder I. Furthermore, it's mean normalised temperature gradient has decreased to 0.38 as compared to the case of examining thermal images at a timeframe of three seconds after scanning. This translates to a decrease in the temperature differences between pixels at regions that are defective and non-defective. The finding is supported by Figure 5.9, showing a decrease in the temperature difference between a pixel located within unmelted metal powders and another pixel located solidified metal as time increases. As such, studying the thermal images at a timeframe of ten seconds after scanning may lower the probability of locating porosities, unmelted and partially melted metal powders.

Similar observations are noted for cylinders II and VII (Figure 5.10). The normalised temperature gradient with the highest number of pixels (frequency) for cylinder II has changed from 0.4 – 0.5 to 0.3 – 0.4 as the timeframe used for analysis has changed from three to ten seconds after scanning. The normalised temperature gradient with the highest number of pixels (frequency) for cylinder VII has also changed from 0.3 – 0.4 to 0.2 – 0.3 as the timeframe used for analysis has been adjusted from three to ten seconds after scanning.

5.3 Summary

The minimum size of cylindrical holes observable from captured thermal images is 0.75 mm in diameter. The minimum size of square holes observable from captured thermal images is 0.75 mm in length.

A correlation has been established between cylinders' regions of high normalised temperature gradients and their corresponding densities. Cylinders with more pixels of low normalised temperature gradients across their cross sections (excluding pixels near or at their perimeters) exhibit higher densities. Cylinders with more pixels of high normalised temperature gradients across their cross sections (excluding pixels near or at their perimeters) exhibit lower densities. The implementation of the IMS based on thermal imaging enables end users to distinguish between specimens with relatively higher and lower densities. The feasibility of adopting thermography for in-process inspection of the SLM process has been proven.

One of the challenges associated with thermal images is the variation of pixels' temperature value with time. An investigation has revealed an optimal timeframe for analysing the thermal images such that the defects are most easily identified. It is found that three seconds after the laser scanned the powder bed to be suitable because the temperature difference between the defects and the bulk material at this timeframe is the largest. The timeframe at which thermal images are studied may vary according to the geometries and sizes of printed parts and the scanning speed. Hence, a preliminary study should be performed to determine an appropriate timeframe where the temperature difference between defective regions of printed part and its bulk material is the largest.

CHAPTER 6: CONCLUSIONS AND FUTURE WORK

6.1 Conclusions

This thesis mainly focuses on (1) the development of a self-developed in-situ monitoring system (IMS) that captures optical and thermal images of high resolution during the selective laser melting (SLM) process and (2) establishing correlations between features, thermal signatures and the mechanical properties of the printed parts. The proposed IMS has been successfully developed for monitoring the SLM process. Coupled with the proposed algorithms, it allows for easy identification and evaluation of process signatures. The feasibility of using the proposed IMS to infer the density and mechanical properties of printed parts based on processed optical and thermal images has been demonstrated and validated via micro computed tomography (CT) and mechanical tests. Moving forward, the findings presented in this thesis also lay the foundation for the development of closed-loop in-situ monitoring systems (IMSs) associated with the SLM process. The contributions from this thesis are summarised as follow:

1. The design of the proposed IMS allowed monitoring of the powder bed via optical and infrared cameras. The digital single lens reflex (DSLR) camera was used and placed outside of the machine to capture optical images of the powder bed. Using a silver coated mirror, light was reflected from the powder bed and directed to the lens of the DSLR camera. The infrared camera was placed above the chamber of the machine as it is more susceptible to environmental disturbances than the optical camera. Optical accessories including a gold dichroic beam splitter and a silver coated mirror were used, enabling thermal images of the powder bed to be captured.

2. A relationship has been established between features captured in optical images during fabrication and the mechanical properties of the printed parts. Features are represented by pixels that are either brighter or darker than that of the metal powders. Cylinders with higher percentage area of features exhibit lower densities and weaker mechanical properties. Cylinders with lower percentage area of features exhibit higher densities and stronger mechanical properties. The implementation of the IMS based on optical imaging enables end users to distinguish between specimens with relatively higher density and better mechanical properties and specimens with relatively lower density and weaker mechanical properties.
3. Condensates and spatters have been found to play a crucial role in influencing the mechanical properties of the printed parts. Cylinders positioned in the direction of argon gas flow are susceptible to the accumulation of condensates and spatters on their surfaces during scanning and after recoating. The condensates and spatters may build up after each layer of recoating, resulting in non-uniform heating when the laser beam is directed at the powder bed. This leads to significant amounts of elevated regions in optical images of affected cylinders, notably affecting their mechanical properties.
4. A correlation has been established between features captured in optical images during printing and the actual defects present in the printed part. Micro CT was used to validate the correlation of features in two-dimensional (2D) optical images to actual three-dimensional defects in the printed samples through reconstruction of the CT images, and more importantly, to justify the viability of using optical imaging as a solution for evaluating defects in printed parts. A positive correlation exists between

$OP_{features}$ and $CT_{defects}$ for the ten cylinders. Their Pearson correlation coefficients range between 0.30 and 0.78. Similarities in trends between $OP_{features}$ and $CT_{defects}$ were established across the layers of the cylinders, where a higher $OP_{features}$ translates to higher $CT_{defects}$, and vice versa. This enables end users to directly evaluate the area of defects present in parts based on real-time analysis of optical images, eliminating the need for long hours of defects detection in printed parts by CT.

5. Apart from the identification of features, other types of defects were detected by the IMS. Delaminations were captured during the printing process of tensile coupons with support structures. Elevated regions of the printed parts and non-uniform recoating of the powder bed due to damaged recoated blade were captured by the optical-based IMS. Porosities and balling were also observed on the surface of printed layers captured during other print jobs.
6. A relationship between regions with high normalised temperature gradients captured in thermal images and the densities of selectively laser melted parts has been demonstrated. Cylinders with more pixels of high normalised temperature gradients across their cross sections exhibit lower densities. Cylinders with minimal number of pixels with high normalised temperature gradients across their cross sections exhibit higher densities. This finding potentially aids in the fabrication of parts with improved density via thermal imaging.
7. The analysis of thermal images is a challenge as the pixels' temperature value changes with time. The timeframe at which thermal images are studied may vary according to the geometries and sizes of printed parts and the scanning speed. A

preliminary study should be performed to determine an appropriate timeframe where the temperature difference between defective regions of printed part and its bulk material is the largest.

Based on the established relationships, the proposed IMS can potentially aid in the production of parts with better mechanical properties. Printing parameters can be adjusted in-situ to improve the quality of the printed part if the number of features or thermal signatures present in optical or thermal images correlate to weak mechanical properties, rendering both time and cost savings. The results also illustrated the capability of the system in differentiating the extent of defects present in specimens fabricated with varying energy densities. This finding is critical as errors are commonly present during printing. Some errors include wrong printing parameters being set, uneven recoating of the powder bed due to damaged recoater blades and unoptimised argon gas flow. The effects of these errors often go unnoticed until defect inspection is performed on the part after printing. Furthermore, the extensiveness of defects in the printed parts due to these errors are unknown. Therefore, the ability of the IMS to differentiate variations in the extent of defects is highly essential considering the possible occurrence of these errors in day-to-day print jobs. Alongside the established relationships, an added advantage of the proposed IMS is its portability. It is suitable for small-scale workshops and can help small and medium enterprises kickstart their journey in additive manufacturing.

6.2 Future work

6.2.1 Protective housing for in-situ monitoring system

One major concern of placing the optical system outside of the machine is its susceptibility to environmental disturbances such as people walking pass the set-up and

accidentally shifting its position. This may cause inconsistencies in the quality of images captured during printing. A protective housing should be made for the optical system to minimise external disturbances. It also ensures the consistency in images captured.

6.2.2 Examination of surface defects

The evaluation of porosities near the perimeters was omitted for optical and thermal images due to inherent porosities. This signifies that surface defects are not considered in the analysis. Surface defects, however, are often the site where cracks initiate. The size of binary masks associated with optical images can be adjusted to cover the entire cross-sectional area of printed parts. This ensures that information related to surface defects of the printed parts will be included in the analysis of optical images. Adjusting the size of binary masks is not a viable solution for analysing surface defects based on thermal images. As discussed in section 5.2.2, regions of high temperature gradients are always found at the perimeter of a printed part. This is due to the large temperature difference between unmelted metal powders and melted bulk material. Instead, the printed parts can be examined for surface defects after printing. Some techniques will include optical microscopy and CT.

6.2.3 Correlation studies between condensates, spatters and mechanical properties of printed parts

The detrimental effect of significant amounts of condensates and spatters on printed surfaces have been demonstrated and validated in sections 4.2.3 and 5.2.1. Their presence plays a crucial role in influencing a part's density. Further studies must be carried out to investigate how the extensiveness of condensates and spatters affects the printed part's density and mechanical properties. Optical images of the powder bed can be captured by

the IMS. The area of condensates and spatters present on each layer of the printed surfaces can be extracted and evaluated by image processing. Thereafter, a correlative study between the area of condensates and spatters across each layer of the printed part and its resulting mechanical properties can be performed. The amounts of condensates and spatters present on printed surfaces that lead to the fabrication of a low-quality part can be determined. The area of condensates and spatters surrounding the printed parts should also be studied. As condensates and spatters are blown across the build chamber, they also settle at regions surrounding the printed parts. This examination could provide insights for establishing the correlation between the area of condensates and spatters across each layer of the printed part and its corresponding mechanical properties.

6.2.4 Correlation studies between optical and thermal images

A deeper understanding on the defect formation process can be achieved through the examination of optical and thermal images captured at the same layer. Simultaneous monitoring of the powder bed is possible through the use of optical and infrared cameras placed in a protective housing. Optical accessories such as the beam splitter that allows transmission of visible wavelengths and reflects infrared wavelengths must be included in the design. The sensor fusion methodology also ensured that the data analysed corresponded to the same physical structure, which has yet been explored by machine manufacturers. The combination of these sensors provides greater insights to improve the defect detection algorithm and enables the establishment of correlations between optical images, thermal images and mechanical properties of the printed parts. The two sensors complement each other, providing a holistic approach to examine different types of defects generated during SLM.

The material's microstructure may also be examined for its relationship with the pixels' temperature distributions and temperature gradients captured in thermal images. Various microstructures within a material may correlate to unique optical and thermal information captured in-situ. Future work in this area has the potential of tailoring parts with specific mechanical properties through in-situ monitoring of features and signals captured in optical and thermal images.

6.2.5 Three-dimensional examination of thermal data

The current image processing related to thermal data is a 2D ($x - y$ direction) analysis, i.e., pixels of interest are studied across one layer, for a total of N layers. Since heat is accumulated within the printed part as layers are built, the study of thermal images along its height direction (z direction) could possibly reveal the presence of defects. Defects generated in a certain layer, such as layer 20, will produce thermal signatures across previous and subsequent layers. Heat is retained at regions of the defects due to differences in their thermal conductivities and the bulk material. This retained heat may affect the temperature distributions of pixels for the subsequent layers, allowing defects to be identified. The cooling rates between defects and bulk material will also differ from each other across the layers (z direction).

Specimens can be printed with minimal defects by using the same printing parameters that were used to print cylinders of high densities. The printing parameters of cylinder VIII (Table 3.3, section 3.2.2.2) is one such example. The pixels' temperature values across these specimens should be studied as a reference for high-quality printed parts. Subsequently, the same process is repeated for cylinders with low densities. This corresponds to cylinders I and II (Table 3.3, section 3.2.2.2). A general understanding of

the pixels' thermal behaviour across printed layers will enable further studies to be carried out. It is speculated that regions where defects are present will cause a surge in temperature at the corresponding pixels. This increase in temperature is also speculated to last throughout multiple layers, easing the process of defects identification. Furthermore, the size of defects can be estimated by counting the number of pixels with unexpectedly high temperatures. This method is suitable for examining pixels at a specific timeframe across multiple layers.

Additionally, each pixel's cooling profile may also be examined across N layers. The presence of defects is signalled by notable deviations in the pixels' temperature values when compared to majority of the remaining pixels. Similarly, the cooling rates of pixels associated with high-density and low-density cylinders must be investigated and the results can be used as a reference for subsequent analyses. Pixels with abnormal cooling rates across each layer are flagged as defective and the number of defective pixels may be counted and further analysed to determine the sizes and locations of the defects. Thermal images will not be studied at a specific timeframe as the pixels' cooling rates are a function of time. Although the dataset will be large, this method is a more holistic approach since it involves studying the entire thermal history of the printed parts.

REFERENCES

[1] C. K. Chua, C. H. Wong, and W. Y. Yeong, *Standards, quality control, and measurement sciences in 3D printing and additive manufacturing*: Academic Press, 2017.

[2] S. H. Huang, P. Liu, A. Mokasdar, and L. Hou, "Additive manufacturing and its societal impact: a literature review," *International Journal of Advanced Manufacturing Technology*, vol. 67, pp. 1191-1203, 2013.

[3] ASTM ISO / ASTM52900-15, "Standard Terminology for Additive Manufacturing – General Principles – Terminology," ed. West Conshohocken, PA: ASTM International, 2015.

[4] I. Gibson, D. W. Rosen, and B. Stucker, *Additive manufacturing technologies* vol. 238. New York: Springer, 2010.

[5] Q. Y. Lu and C. H. Wong, "Applications of non-destructive testing techniques for post-process control of additively manufactured parts," *Virtual and Physical Prototyping*, vol. 12, pp. 301-321, 2017.

[6] F. P. Melchels, M. A. Domingos, T. J. Klein, J. Malda, P. J. Bartolo, and D. W. Hutmacher, "Additive manufacturing of tissues and organs," *Progress in Polymer Science*, vol. 37, pp. 1079-1104, 2012.

[7] J. M. Waller, B. H. Parker, K. L. Hodges, E. R. Burke, J. L. Walker, and E. R. Generazio, "Nondestructive evaluation of additive manufacturing state-of-the-discipline report," National Aeronautics and Space Administration, Las Cruces, New Mexico,2014.

[8] T. Srivatsan and T. Sudarshan, *Additive manufacturing: innovations, advances, and applications*. New York: CRC Press, 2015.

[9] Energetics Incorporated, "Measurement science roadmap for metal-based additive manufacturing," National Institute of Standards and Technology, Columbia, Maryland,2013.

[10] T. Kellner. (2014, 15 January). *Fit to print: new plant will assemble world's first passenger jet engine with 3D printed fuel nozzles, next-gen materials*. Available: http://www.gereports.com/post/80701924024/fit-to-print/

[11] Q. Y. Lu and C. H. Wong, "Additive manufacturing process monitoring and control by non-destructive testing techniques: challenges and in-process monitoring," *Virtual and Physical Prototyping*, vol. 13, pp. 39-48, 2018.

[12] B. Raj, T. Jayakumar, and M. Thavasimuthu, *Practical non-destructive testing*. Cambridge: Woodhead Publishing, 2002.

[13] P. J. Shull, *Nondestructive evaluation: theory, techniques, and applications*. New York: CRC Press, 2002.

[14] J. z. Jacobsmühlen, S. Kleszczynski, D. Schneider, and G. Witt, "High resolution imaging for inspection of laser beam melting systems," in *IEEE International Instrumentation and Measurement Technology Conference*, 2013, pp. 707-712.

[15] H. Krauss, C. Eschey, and M. Zaeh, "Thermography for monitoring the selective laser melting process," in *Proceedings of the Solid Freeform Fabrication Symposium*, Austin: Texas, 2012, pp. 999-1014.

[16] S. K. Everton, M. Hirsch, P. Stravroulakis, R. K. Leach, and A. T. Clare, "Review of in-situ process monitoring and in-situ metrology for metal additive manufacturing," *Materials & Design*, vol. 95, pp. 431-445, 2016.

[17] Stratasys Ltd. (2017, 28 May). *FDM thermoplastics 3D print durable parts in production-grade materials*. Available: http://www.stratasys.com/materials/fdm

[18] Loughborough University. (2017, 28 May). *Material extrusion*. Available: http://www.lboro.ac.uk/research/amrg/about/the7categoriesofadditivemanufacturing/materialextrusion/

[19] Loughborough University. (2017, 28 May). *Powder bed fusion*. Available: http://www.lboro.ac.uk/research/amrg/about/the7categoriesofadditivemanufacturing/powderbedfusion/

[20] Dassault Systèmes. (2018, 31 December). *Powder bed fusion*. Available: https://euw1-21dmo40125-3dprint.3dx-staging.3ds.com/processes/powder-bed-fusion

[21] I. Gibson, D. Rosen, and B. Stucker, "Vat photopolymerization processes," in *Additive Manufacturing Technologies: 3D Printing, Rapid Prototyping, and Direct Digital Manufacturing*, ed New York, NY: Springer New York, 2015, pp. 63-106.

[22] Loughborough University. (2017, 12 January). *Vat photopolymerisation*. Available: https://www.lboro.ac.uk/research/amrg/about/the7categoriesofadditivemanufacturing/vatphotopolymerisation/

[23] J. M. Lee, S. L. Sing, M. Zhou, and W. Y. Yeong, "3D bioprinting processes: a perspective on classification and terminology," *International Journal of Bioprinting*, vol. 4, 2018.

[24] L. Vassos. (2019, 12 January). *How to design parts for material jetting 3D printing*. Available: https://www.3dhubs.com/knowledge-base/how-design-parts-material-jetting-3d-printing/

[25] Loughborough University. (2017, 29 May). *Material jetting*. Available: http://www.lboro.ac.uk/research/amrg/about/the7categoriesofadditivemanufacturing/materialjetting/

[26] Dassault Systèmes. (2018, 31 December). *Material jetting*. Available: https://euw1-21dmo40125-3dprint.3dx-staging.3ds.com/processes/material-jetting

[27] I. Gibson, D. Rosen, and B. Stucker, "Binder jetting," in *Additive Manufacturing Technologies: 3D Printing, Rapid Prototyping, and Direct Digital Manufacturing*, ed New York, NY: Springer New York, 2015, pp. 205-218.

[28] Loughborough University. (2017, 12 January). *Binder jetting*. Available: https://www.lboro.ac.uk/research/amrg/about/the7categoriesofadditivemanufacturing/binderjetting/

[29] S. F. S. Shirazi, S. Gharehkhani, M. Mehrali, H. Yarmand, H. S. C. Metselaar, N. A. Kadri, *et al.*, "A review on powder-based additive manufacturing for tissue engineering: selective laser sintering and inkjet 3D printing," *Science and Technology of Advanced Materials*, vol. 16, p. 033502, 2015.

[30] Loughborough University. (2017, 29 May). *Sheet lamination*. Available: http://www.lboro.ac.uk/research/amrg/about/the7categoriesofadditivemanufacturing/sheetlamination/

[31] I. Gibson, D. Rosen, and B. Stucker, "Directed energy deposition processes," in *Additive Manufacturing Technologies: 3D Printing, Rapid Prototyping, and Direct Digital Manufacturing*, ed New York, NY: Springer New York, 2015, pp. 245-268.

[32] J. Hiemenz, "Additive manufacturing trends in aerospace," *White Paper, Stratasys, USA*, pp. 1-11, 2014.

[33] I. Inagaki, T. Takechi, Y. Shirai, and N. Ariyasu, "Application and features of titanium for the aerospace industry," *Nippon Steel & Sumitomo Metal Technical Report*, vol. 106, pp. 22-27, 2014.

[34] E. Uhlmann, R. Kersting, T. B. Klein, M. F. Cruz, and A. V. Borille, "Additive manufacturing of titanium alloy for aircraft components," *Procedia CIRP*, vol. 35, pp. 55-60, 2015.

[35] G. Alysia, H. Matthias, V. Hans, and Y. Aidong, "Redistributing material supply chains for 3D printing," University of Oxford, Oxford, England,2016.

[36] T. DebRoy, H. L. Wei, J. S. Zuback, T. Mukherjee, J. W. Elmer, J. O. Milewski, *et al.*, "Additive manufacturing of metallic components – process, structure and properties," *Progress in Materials Science*, vol. 92, pp. 112-224, 2018.

[37] S. Sun, M. Brandt, and M. Easton, "Powder bed fusion processes: an overview," in *Laser Additive Manufacturing*, M. Brandt, Ed., ed: Woodhead Publishing, 2017, pp. 55-77.

[38] National Academies of Sciences Engineering and Medicine, *Data-driven modeling for additive manufacturing of metals: proceedings of a workshop*. Washington, DC: The National Academies Press, 2019.

[39] K. H. Leitz, P. Singer, A. Plankensteiner, B. Tabernig, H. Kestler, and L. S. Sigl, "Multi-physical simulation of selective laser melting," *Metal Powder Report*, vol. 72, pp. 331-338, 2017.

[40] T. Craeghs, S. Clijsters, E. Yasa, and J.-P. Kruth, "Online quality control of selective laser melting," in *Proceedings of the Solid Freeform Fabrication Symposium*, Austin: Texas, 2011, pp. 212-226.

[41] C. Zhu, T. Liu, F. Qian, W. Chen, S. Chandrasekaran, B. Yao, *et al.*, "3D printed functional nanomaterials for electrochemical energy storage," *Nano Today*, vol. 15, pp. 107-120, 2017.

[42] J.-P. Choi, G.-H. Shin, M. Brochu, Y.-J. Kim, S.-S. Yang, K.-T. Kim, *et al.*, "Densification behavior of 316L stainless steel parts fabricated by selective laser melting by variation in laser energy density," *Materials Transactions*, vol. 57, pp. 1952-1959, 2016.

[43] T. Trosch, J. Strößner, R. Völkl, and U. Glatzel, "Microstructure and mechanical properties of selective laser melted Inconel 718 compared to forging and casting," *Materials Letters*, vol. 164, pp. 428-431, 2016/02/01/ 2016.

[44] B. Foster, E. Reutzel, A. Nassar, B. Hall, S. Brown, and C. Dickman, "Optical, layerwise monitoring of powder bed fusion," in *26th International Solid Freeform Fabrication Symposium*, Austin: Texas, 2015.

[45] M. S. Brown and C. B. Arnold, "Fundamentals of laser-material interaction and application to multiscale surface modification," *Laser Precision Microfabrication*, vol. 135, pp. 91-120, 2010.

[46] M. Allgaier, S. Ness, P. McIntire, and P. Moore, "Nondestructive testing handbook, visual and optical testing," *ASNT, Columbus, Ohio*, vol. 8, 1993.

[47] B. Craig. (2007, 25 July). *Editorial: the last starlifter*. Available: http://infohouse.p2ric.org/ref/41/40921.pdf

[48] G. A. Matzkanin. (2006, 25 July). *Selecting a nondestructive testing method: visual inspection*. Available: https://app.aws.org/itrends/2007/04/it200704/it0407-15.pdf

[49] R. Usamentiaga, P. Venegas, J. Guerediaga, L. Vega, J. Molleda, and F. G. Bulnes, "Infrared thermography for temperature measurement and non-destructive testing," *Sensors*, vol. 14, pp. 12305-12348, 2014.

[50] N. Avdelidis, T.-H. Gan, C. Ibarra-Castanedo, and X. P. Maldague, *Infrared thermography as a nondestructive tool for materials characterisation and assessment* vol. 8013: SPIE, 2011.

[51] M. Hirsch, R. Patel, W. Li, G. Guan, R. K. Leach, S. D. Sharples, *et al.*, "Assessing the capability of in-situ nondestructive analysis during layer based additive manufacture," *Additive Manufacturing*, vol. 13, pp. 135-142, 2017.

[52] J. Bamberg, K.-H. Dusel, W. Satzger, D. E. Chimenti, and L. J. Bond, "Overview of additive manufacturing activities at MTU aero engines," in *AIP Conference Proceedings*, 2015, pp. 156-163.

[53] S. Everton, P. Dickens, C. Tuck, and B. Dutton, "Evaluation of laser ultrasonic testing for inspection of metal additive manufacturing," in *SPIE LASE*, 2015, pp. 935316-935316-8.

[54] F. Bayle and M. Doubenskaia, *Selective laser melting process monitoring with high speed infra-red camera and pyrometer* vol. 6985: SPIE, 2008.

[55] J. Schwerdtfeger, R. F. Singer, and C. Körner, "In situ flaw detection by IR-imaging during electron beam melting," *Rapid Prototyping Journal*, vol. 18, pp. 259-263, 2012.

[56] R. Dinwiddie, R. Dehoff, P. Lloyd, L. Lowe, and J. Ulrich, *Thermographic in-situ process monitoring of the electron-beam melting technology used in additive manufacturing* vol. 8705: SPIE, 2013.

[57] B. Cheng and K. Chou, "Melt pool evolution study in selective laser melting," in *26th Annual International Solid Freeform Fabrication Symposium-An Additive Manufacturing Conference*, Austin: Texas, 2015, pp. 1182-1194.

[58] B. Lane, B. Lane, S. Moylan, S. Moylan, E. P. Whitenton, E. P. Whitenton, *et al.*, "Thermographic measurements of the commercial laser powder bed fusion process at NIST," *Rapid Prototyping Journal*, vol. 22, pp. 778-787, 2016.

[59] H. Rieder, A. Dillhöfer, M. Spies, J. Bamberg, and T. Hess, "Online monitoring of additive manufacturing processes using ultrasound," in *11th European Conference on Non-Destructive Testing*, 2014, pp. 6-10.

[60] D. Cerniglia, M. Scafidi, A. Pantano, and J. Rudlin, "Inspection of additive-manufactured layered components," *Ultrasonics*, vol. 62, pp. 292-298, 2015.

[61] T. G. Spears and S. A. Gold, "In-process sensing in selective laser melting (SLM) additive manufacturing," *Integrating Materials and Manufacturing Innovation*, vol. 5, p. 2, 2016.

[62] EOS GmbH. (2017, 24 October). *EOSTATE MeltPool: real-time process monitoring for EOS M 290*. Available: https://www.eos.info/software/monitoring-software/meltpool-monitoring

[63] Arcam EBM. (2012, 28 August). *Electron beam melting*. Available: https://static1.squarespace.com/static/534fa8d4e4b0a1a3d8a42c81/t/53761ceae4b002aab7ab8997/1400249578743/Pulverseminarium+PDF.pdf

[64] Arcam EBM. (2013, 28 May). *Just add*. Available: http://www.arcam.com/wp-content/uploads/justaddbrochure-web.pdf

[65] Concept Laser GmbH. (2015, 24 October). *QM Meltpool 3D*. Available: http://www.conceptlaserinc.com/in-situ-quality-assurance-with-qmmeltpool-3d-from-concept-laser/

[66] SLM Solutions. (2015, 28 August). *Selective laser melting*. Available: https://www.hs-owl.de/fb7/fileadmin/download/labore/konstruktion/06_Tagungen/01_RP_Tagungen/20_RP/20_FTRP_Schwarze_SLM_produktive_Fertigungstechnologie_Freigegeben.pdf

[67] SLM Solutions. (2017, 28 August). *Melt pool monitoring (MPM)*. Available: https://slm-solutions.com/products/machines/melt-pool-monitoring-mpm

[68] M. R. Redding, S. A. Gold, and T. G. Spears, "Non-contact acoustic inspection method for additive manufacturing processes," ed: US Patent 20,170,146,489, 2017.

[69] S. A. Gold and T. G. Spears, "Acoustic monitoring method for additive manufacturing processes," ed: US Patent 20,170,146,488, 2017.

[70] Navy STTR. (2015, 18 May). *In situ inspection of additive manufactured metallic parts using laser ultrasonics*. Available: https://navystp.com/vtm/print?project=N68335-17-C-0148

[71] H. Lee, C. H. J. Lim, M. J. Low, N. Tham, V. M. Murukeshan, and Y.-J. Kim, "Lasers in additive manufacturing: a review," *International Journal of Precision Engineering and Manufacturing-Green Technology*, vol. 4, pp. 307-322, 2017.

[72] V. Dhar, Z. Khan, R. Sharma, and R. Muralidharan, *Comparison of the performance of LWIR and MWIR thermal imagers for varying ambient temperature and humidity conditions* vol. 8014: SPIE, 2011.

[73] D. A. de Moraes and A. Czekanski, "Thermal modeling of 304L stainless steel for selective laser melting: laser power input evaluation," in *ASME 2017 International Mechanical Engineering Congress and Exposition*, 2017.

[74] ASTM E1897-14, "Standard Practice for Measuring and Compensating for Transmittance of an Attenuating Medium Using Infrared Imaging Radiometers," ed. West Conshohocken, PA: ASTM International, 2014.

[75] ASTM E1933-14(2018), "Standard Practice for Measuring and Compensating for Emissivity Using Infrared Imaging Radiometers," ed. West Conshohocken, PA: ASTM International, 2018.

[76] Edmund Optics. (2019, 12 January). *Introduction to modulation transfer function*. Available: https://www.edmundoptics.com.sg/knowledge-center/application-notes/optics/introduction-to-modulation-transfer-function/

[77] E. L. Dereniak and T. D. Dereniak, *Geometrical and trigonometric optics*. Cambridge: Cambridge University Press, 2008.

[78] Z. Zhang, "A flexible new technique for camera calibration," *IEEE Transactions on Pattern Analysis and Machine Intelligence*, vol. 22, pp. 1330-1334, 2000.

[79] P. F. Sturm and S. J. Maybank, "On plane-based camera calibration: a general algorithm, singularities, applications," in *1999 IEEE Computer Society Conference on Computer Vision and Pattern Recognition*, 1999, pp. 432-437 Vol. 1.

[80] MATLAB. (2019, 2 January). *What is camera calibration?* Available: https://www.mathworks.com/help/vision/ug/camera-calibration.html

[81] MATLAB. (2019, 2 January). *Single camera calibrator app*. Available: https://www.mathworks.com/help/vision/ug/single-camera-calibrator-app.html

[82] L. Thijs, F. Verhaeghe, T. Craeghs, J. Van Humbeeck, and J.-P. Kruth, "A study of the microstructural evolution during selective laser melting of Ti–6Al–4V," *Acta Materialia*, vol. 58, pp. 3303-3312, 2010.

[83] ASTM E8 / E8M-15a, "Standard Test Methods for Tension Testing of Metallic Materials," ed. West Conshohocken, PA: ASTM International, 2015.

[84] M. Zhang, C.-N. Sun, X. Zhang, P. C. Goh, J. Wei, D. Hardacre, *et al.*, "Effect of heat treatment on fatigue crack initiation of laser powder bed fusion stainless steel 316L," *MATEC Web of Conferences*, vol. 165, p. 22006, 2018.

[85] B. Vandenbroucke and J.-P. Kruth, "Selective laser melting of biocompatible metals for rapid manufacturing of medical parts," *Rapid Prototyping Journal*, vol. 13, pp. 196-203, 2007.

[86] S. Kleszczynski, J. Zur Jacobsmühlen, J. Sehrt, and G. Witt, "Error detection in laser beam melting systems by high resolution imaging," in *Proceedings of the 23rd Annual International Solid Freeform Fabrication Symposium*, 2012.

[87] S. Ly, A. M. Rubenchik, S. A. Khairallah, G. Guss, and M. J. Matthews, "Metal vapor micro-jet controls material redistribution in laser powder bed fusion additive manufacturing," *Scientific Reports*, vol. 7, p. 4085, 2017.

[88] A. R. Nassar, M. A. Gundermann, E. W. Reutzel, P. Guerrier, M. H. Krane, and M. J. Weldon, "Formation processes for large ejecta and interactions with melt pool formation in powder bed fusion additive manufacturing," *Scientific Reports*, vol. 9, p. 5038, 2019.

[89] MATLAB. (2018, 25 July). *MATLAB*. Available: https://www.mathworks.com/products/matlab.html

[90] L. Nastac and TMS., *CFD modeling and simulation in materials processing*: Springer, 2016.

[91] S. P. Moylan, J. A. Slotwinski, A. Cooke, K. Jurrens, and M. A. Donmez, "Lessons learned in establishing the NIST metal additive manufacturing laboratory," *NIST Technical Note*, 2013.

[92] Y. Liu, Y. Yang, S. Mai, D. Wang, and C. Song, "Investigation into spatter behavior during selective laser melting of AISI 316L stainless steel powder," *Materials & Design*, vol. 87, pp. 797-806, 2015.

[93] H. Gu, H. Gong, D. Pal, K. Rafi, T. Starr, and B. Stucker, "Influences of energy density on porosity and microstructure of selective laser melted 17-4PH stainless steel," in *2013 Solid Freeform Fabrication Symposium*, 2013, p. 474.

[94] D. Gu, *Laser additive manufacturing of high-performance materials*: Springer, 2015.

[95] M. Brandt, *Laser additive manufacturing: materials, design, technologies, and applications*: Woodhead Publishing, 2016.

[96] G. Kasperovich, J. Haubrich, J. Gussone, and G. Requena, "Correlation between porosity and processing parameters in TiAl6V4 produced by selective laser melting," *Materials & Design*, vol. 105, pp. 160-170, 2016.

[97] L. E. Eberly, "Correlation and simple linear regression," in *Topics in Biostatistics*, W. T. Ambrosius, Ed., ed Totowa, NJ: Humana Press, 2007, pp. 143-164.

[98] S. Kleszczynski, J. zur Jacobsmühlen, B. Reinarz, J. T. Sehrt, G. Witt, and D. Merhof, "Improving process stability of laser beam melting systems," in *Fraunhofer Direct Digital Manufacturing Conference*, 2014.

[99] S. Kleszczynski, A. Ladewig, K. Friedberger, J. Zur Jacobsmühlen, D. Merhof, and G. Witt, "Position dependency of surface roughness in parts from laser beam melting systems," in *Proceedings of the 26th Annual International Solid Freeform Fabrication Symposium*, 2015, pp. 10-12.

[100] J. L. Bartlett, F. M. Heim, Y. V. Murty, and X. Li, "In situ defect detection in selective laser melting via full-field infrared thermography," *Additive Manufacturing*, vol. 24, pp. 595-605, 2018.

[101] J. Raplee, A. Plotkowski, M. M. Kirka, R. Dinwiddie, A. Okello, R. R. Dehoff, *et al.*, "Thermographic microstructure monitoring in electron beam additive manufacturing," *Scientific Reports*, vol. 7, p. 43554, 2017.

[102] M. Yakout, M. A. Elbestawi, and S. C. Veldhuis, "Density and mechanical properties in selective laser melting of Invar 36 and stainless steel 316L," *Journal of Materials Processing Technology*, vol. 266, pp. 397-420, 2019.

APPENDIX A: DENSITY OF PRINTED 316L STAINLESS STEEL CUBES

Three 316L stainless steel cub with the parameters shown in Table A1 were printed and their densities measured by following the Archimedes' principle. The reported density of the 316L stainless steel powders is 8.000 gcm^{-3} [102]. The selection of a reference parameter was based on the density of the printed cube that is at least of 97% of the reported value. Hence, the printing parameters of cube III was chosen as a reference.

Table A1 Pearson correlation coefficient of ten cylinders printed by SLM.

Cube	Laser power (W)	Scanning speed (mms^{-1})	Density (gcm^{-3})	Percentage density (%)
I	87.5	550	7.013	87.7
II	175	1100	7.182	89.8
III	175	550	7.797	97.5

APPENDIX B: CORRELATION BETWEEN FEATURES AND MECHANICAL PROPERTIES OF PRINTED SPECIMENS

The preliminary investigation was performed to explore the possibility of establishing a correlation between the features present in optical images captured in-situ and the specimens' mechanical properties. Six sets of 316L stainless steel specimens were printed with varying energy densities. Each set of specimens consisted of a cuboid and a sub-size tensile coupon. The cuboids are 8 mm in length, 8 mm in breadth and 4 mm in height. The sub-size tensile coupon has the same measurements depicted in Figure 3.19, section 3.2.2.2. The scanning parameters used for printing each set of specimens from I to VI are illustrated in Table 3.3, section 3.2.2.2. The optical images of the cuboids after recoating for each layer were used for image processing and analysis. An image captured during the printing process is shown in Figure B1. The procedures involved in the extraction and evaluation of features captured in optical images are illustrated in sections 4.2.2 and 4.2.3 respectively.

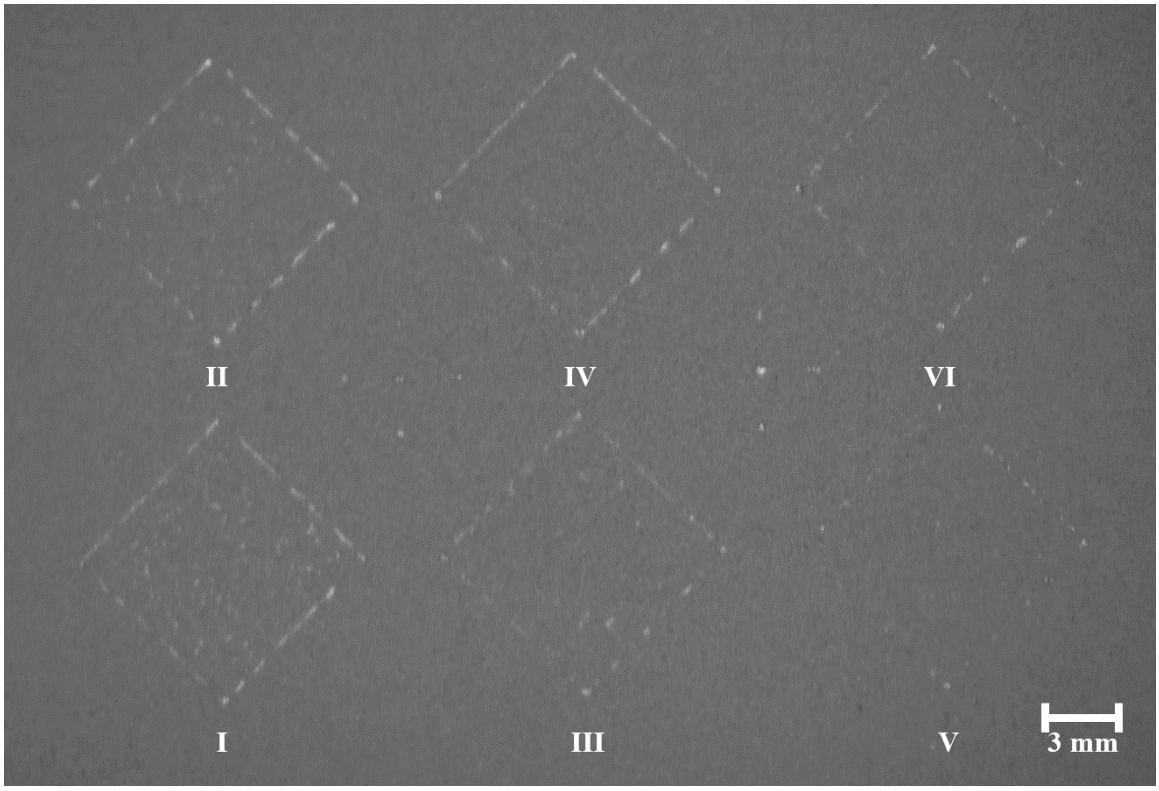

Figure B1 Recoated layer of powder bed captured during printing.

The average densities of the six cuboids based on Archimedes' principle and ultimate and yield strengths of the tensile coupons are shown in Figure B2. Each data point for the densities of the cuboids is an average of three measurements. The individual density measurements of the six cuboids based on Archimedes' principle are shown in Tables B1, B2 and B3. Based on the results of Archimedes' test, a general trend shows that an increase in the energy density ratio from 0.5 to 1.5 leads to an increase in the average density of the cuboids. The ultimate strength and the yield strength of the six tensile coupons were measured and shown in Figure B2. Both properties exhibit an increase in value with an increase in energy density ratio of the tensile coupons from 0.5 to 1.5.

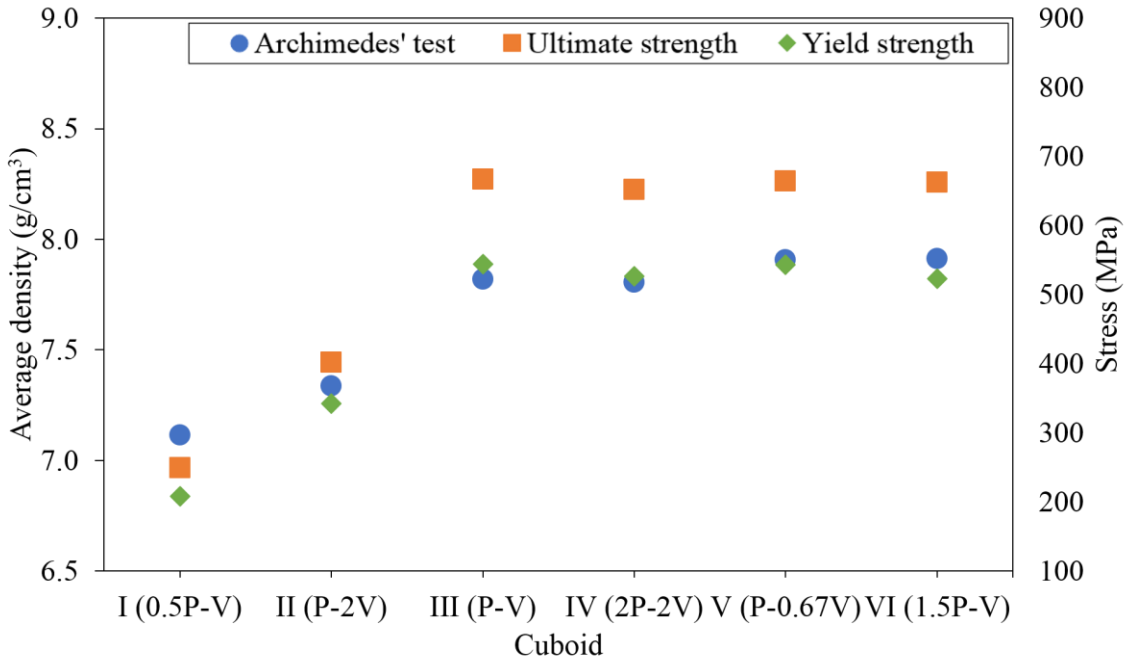

Figure B2 Average densities, ultimate and yield strengths of six specimens.

Table B1 First set of density measurements for six cuboids printed by SLM.

Cuboid	I	II	III	IV	V	VI
Density (gcm^{-3})	7.23	7.44	7.81	7.82	7.91	7.92

Table B2 Second set of density measurements for six cuboids printed by SLM.

Cuboid	I	II	III	IV	V	VI
Density (gcm^{-3})	7.27	7.41	7.81	7.81	7.91	7.92

Table B3 Third set of density measurements for six cuboids printed by SLM.

Cuboid	I	II	III	IV	V	VI
Density (gcm^{-3})	7.19	7.37	7.81	7.81	7.91	7.91

The percentage area of features for every layer of the six cuboids is shown in Figure B3. Generally, it can be noted that an increase in the energy density ratio from 0.5 (specimens I and II) to 1.5 (specimens V and VI) leads to lower percentage area of features for the cuboids.

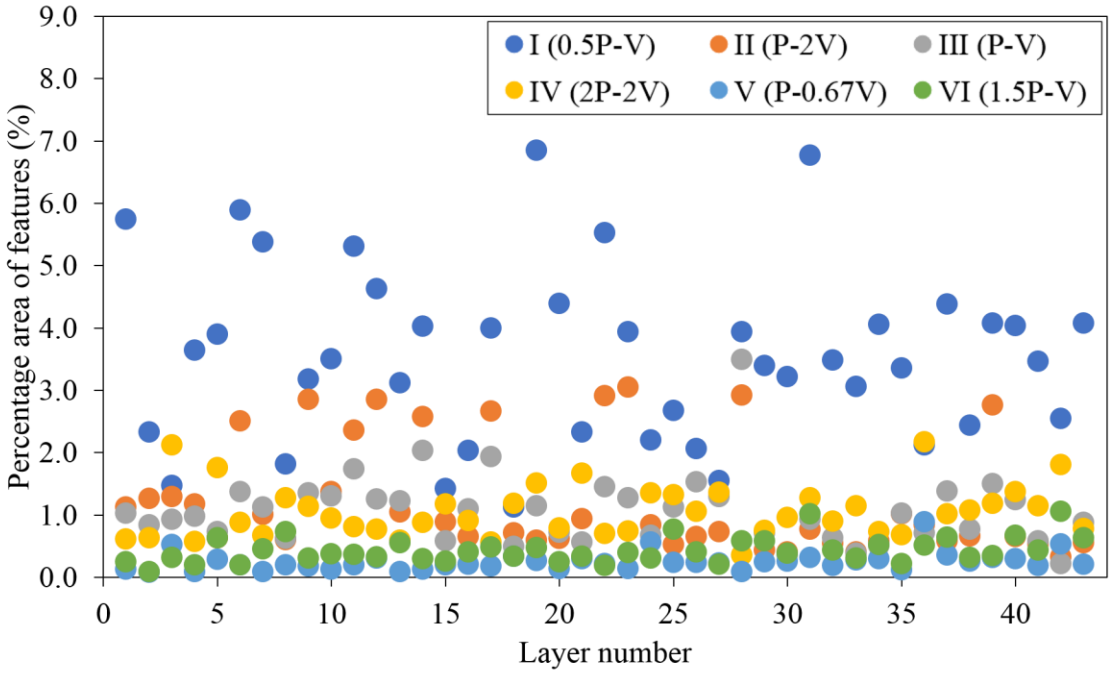

Figure B3 Percentage area of features present in each layer for six cuboids.

The results from image processing indicated that cuboids I and II, having relatively higher percentage area of features across their layers, displayed poorer mechanical

properties as illustrated by Figures B3 and B2 respectively. Cuboids III to VI, having relatively lower percentage area of features across their layers, exhibited better mechanical properties as illustrated by Figures B3 and B2 respectively. The aforementioned relationship has demonstrated the feasibility of using the proposed in-situ monitoring system (IMS) to infer the density and mechanical properties of printed specimens based on the percentage area of features in optical images. Specimens with relatively higher percentage area of features have poorer mechanical properties while specimens with relatively lower percentage area of features have better mechanical properties.

APPENDIX C: DENSITY MEASUREMENTS OF TEN PRINTED CYLINDERS

The individual density measurements of the ten cylinders based on Archimedes' principle are shown in Tables C1, C2 and C3.

Table C1 First set of density measurements for ten cylinders printed by SLM.

Cylinder	I	II	III	IV	V	VI	VII	VIII	IX	X
Density (gcm^{-3})	7.45	7.43	7.82	7.51	7.88	7.91	7.91	7.90	7.92	7.92

Table C2 Second set of density measurements for ten cylinders printed by SLM.

Cylinder	I	II	III	IV	V	VI	VII	VIII	IX	X
Density (gcm^{-3})	7.46	7.44	7.81	7.54	7.88	7.91	7.91	7.91	7.91	7.92

Table C3 Third set of density measurements for ten cylinders printed by SLM.

Cylinder	I	II	III	IV	V	VI	VII	VIII	IX	X
Density (gcm^{-3})	7.44	7.43	7.80	7.50	7.88	7.89	7.91	7.90	7.91	7.91

APPENDIX D: EFFECT OF CONDENSATES AND SPATTERS ON DENSITIES OF PRINTED CYLINDERS

Ten cylinders were printed with the same parameters listed in Table 3.3, section 3.2.2.2. The placements of the cylinders are shown in Figures D1 (a) and (b). As part of the investigation related to thermal images, the cylinders were spaced apart from each other. This reduces the probability of inaccurate temperature readings recorded by the infrared camera due to interaction of thermal energy between the heated cylinders. The ten cylinders were fabricated in two print jobs of which each print job comprised five cylinders.

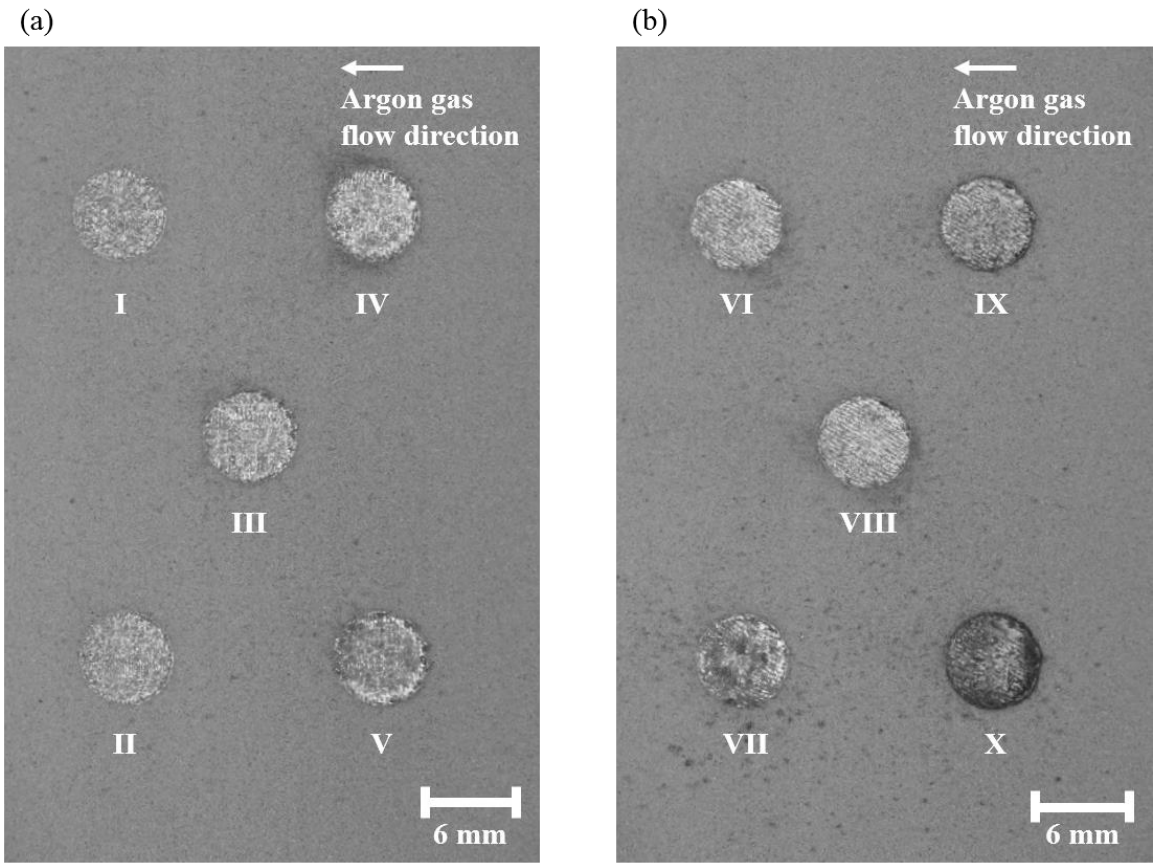

Figure D1 Placements of cylinders (a) I to V and (b) VI to X in each print job where condensates and spatters are the dark spots on the powder bed.

The average densities of the ten cylinders measured based on Archimedes' principle are shown in Figure D2. Each data point is an average of three measurements. The individual density measurements of the ten cylinders based on Archimedes' principle are shown in Tables D1, D2 and D3. The results are similar to the findings obtained in section 4.2.1 since the printing parameters are identical. A general trend shows that an increase in the energy density ratio from 0.5 to 2.0 leads to an increase in the average density of the cylinders. Following which, the average density remains relatively constant for cylinders with energy density ratios of 3.0 and 4.0 as powders are fully melted. The differences in the results obtained between this study and that reported in section 4.2.1 are the improved average density of cylinder IV and the reduced average density of cylinder VII.

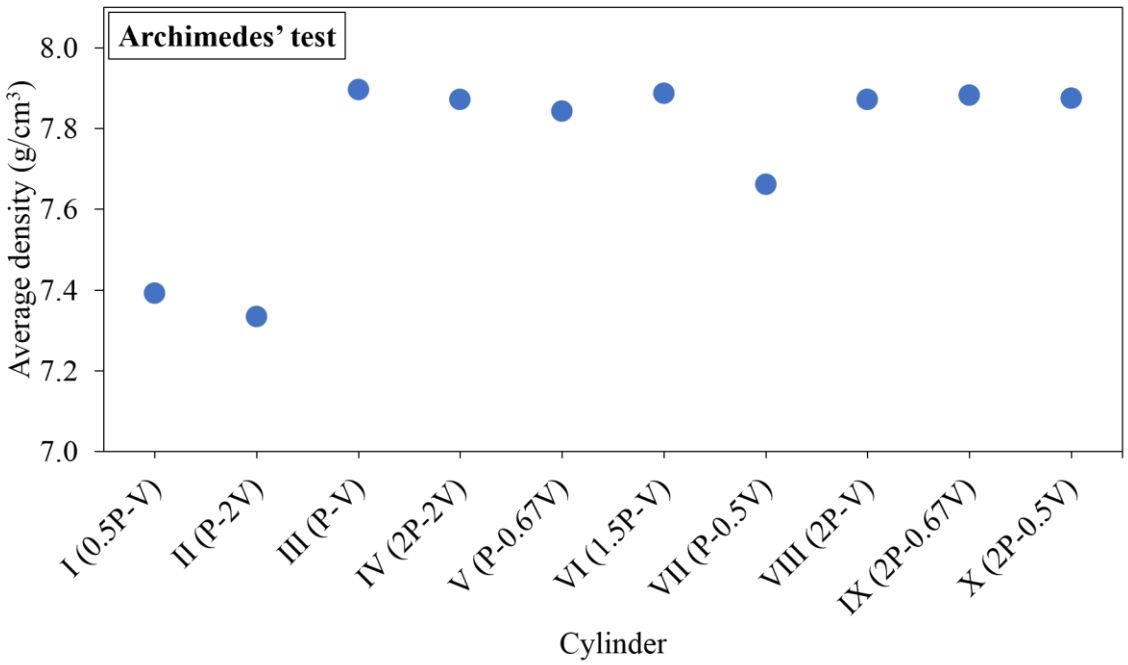

Figure D2 Average densities of ten cylinders.

Table D1 First set of density measurements for ten cylinders printed by SLM.

Cylinder	I	II	III	IV	V	VI	VII	VIII	IX	X
Density (gcm^{-3})	7.42	7.34	7.90	7.88	7.85	7.89	7.67	7.88	7.89	7.88

Table D2 Second set of density measurements for ten cylinders printed by SLM.

Cylinder	I	II	III	IV	V	VI	VII	VIII	IX	X
Density (gcm^{-3})	7.34	7.32	7.89	7.87	7.84	7.89	7.66	7.87	7.88	7.87

Table D3 Third set of density measurements for ten cylinders printed by SLM.

Cylinder	I	II	III	IV	V	VI	VII	VIII	IX	X
Density (gcm^{-3})	7.42	7.34	7.90	7.87	7.84	7.88	7.65	7.87	7.88	7.88

Condensates and spatters have been found to play a crucial role in influencing the mechanical properties of the printed parts. The average density of cylinder IV improved notably as minimal condensates and spatters was present on its surface during printing (Figure D1 (a)). Cylinder IV was printed together with cylinders I, II, III and V. These cylinders were printed with relatively low energy density ratios of 0.5 to 1.5. The temperature within the molten pool of these cylinders barely exceeds the powders' vaporisation point. Therefore, minimal condensates and spatters were present during

printing. On the contrary, cylinder VII had significant amounts of condensates and spatters on its surface and regions around it during printing as depicted in Figure D1 (b). Cylinder VII was printed together with cylinders VI, VIII, IX and X. These cylinders were printed with relatively high energy density ratios of 1.5 to 4.0. The temperature within the molten pool of these cylinders exceeds the powders' vaporisation point. An increase in energy input to the printed specimens will lead to more condensates and spatters generated. Cylinder VII was placed beside cylinder X, which was printed with the highest energy density ratio of 4.0, generating significant amounts of condensates and spatters. As the argon gas flows from right to left within the machine chamber, these condensates and spatters settle on the left side of the powder bed. As a result, relatively large amounts of condensates and spatters were seen on cylinder VII's surface, notably affecting its density.

APPENDIX E: CORRELATION BETWEEN FEATURES AND ACTUAL DEFECTS IN PRINTED CUBOIDS

The preliminary investigation was performed to explore the possibility of establishing a correlation between the features captured in optical images during fabrication and the actual defects present in the printed part. Six 316L stainless steel cuboids were printed with varying energy densities. The cuboids are 8 mm in length, 8 mm in breadth and 3 mm in height. The scanning parameters used for printing each cuboid from I to VI are illustrated in Table 3.3, section 3.2.2.2. The optical images of the cuboids after recoating for each layer were used for image processing and analysis. CT images of the cuboids after reconstruction were used for analysis. The procedures involved in the extraction and evaluation of features captured in optical images are illustrated in sections 4.3.1 and 4.3.2 respectively. Similarly, the procedures involved in the extraction and evaluation of defects captured in CT images are illustrated in sections 4.3.1 and 4.3.2 respectively.

The Pearson correlation coefficients between $OP_{features}$ to that of $CT_{defects}$ for the six cuboids are presented in Table E1. $OP_{features}$ and $CT_{defects}$ for cuboids I to V are highly correlated with coefficients above 0.66. The trends between the two sets of data coincide well with each other for cuboids I to V as depicted in Figures E1 to E6. The correlation coefficient for cuboid VI is the lowest. Minimal defects were present in cuboid X. As it was printed with a relatively high energy density ratio of 1.5 (see Table 3.3, section 3.2.2.2), the powders were completely melted, minimising the formation of defects. Hence, the correlation between $OP_{features}$ and $CT_{defects}$ is low due to the limited number of data points associated with $CT_{defects}$ having values greater than 0%.

Table E1 Pearson correlation coefficient of ten cylinders printed by SLM.

Cuboid	Pearson correlation coefficient
I	0.90
II	0.81
III	0.96
IV	0.66
V	0.89
VI	0.36

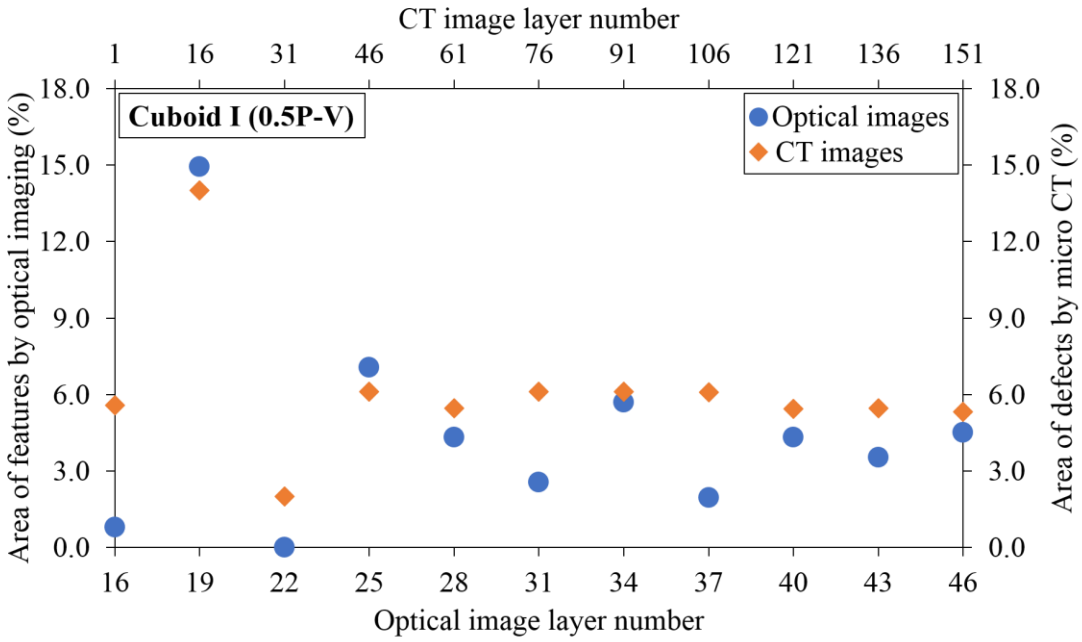

Figure E1 Area of features and defects across each layer for cuboid I (in percentages).

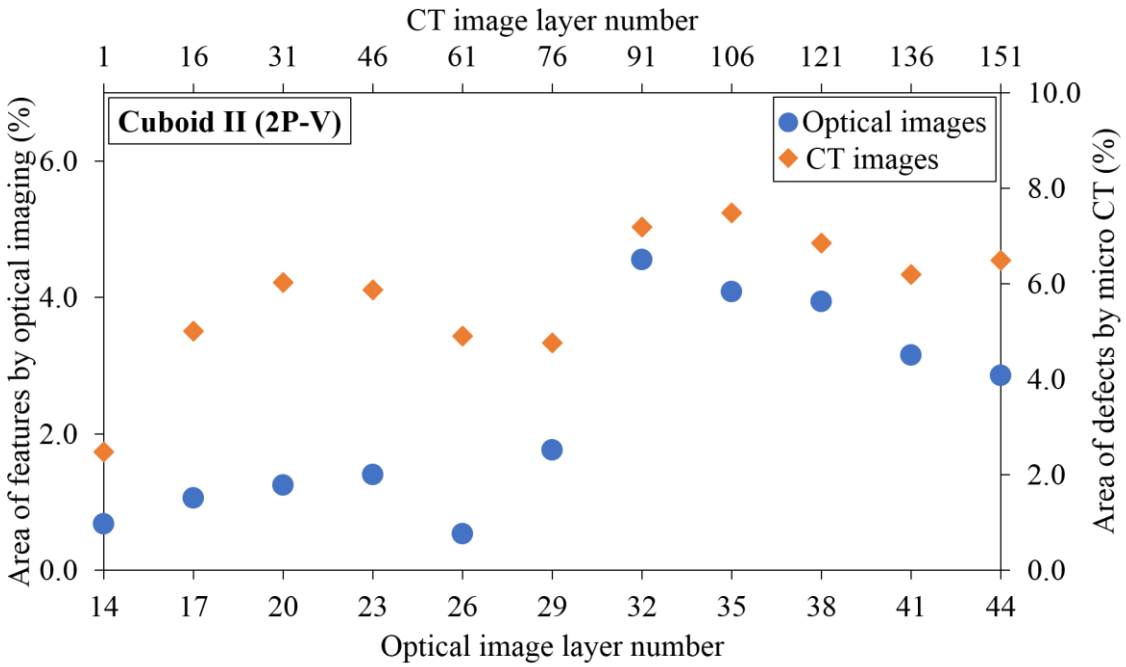

Figure E2 Area of features and defects across each layer for cuboid II (in percentages).

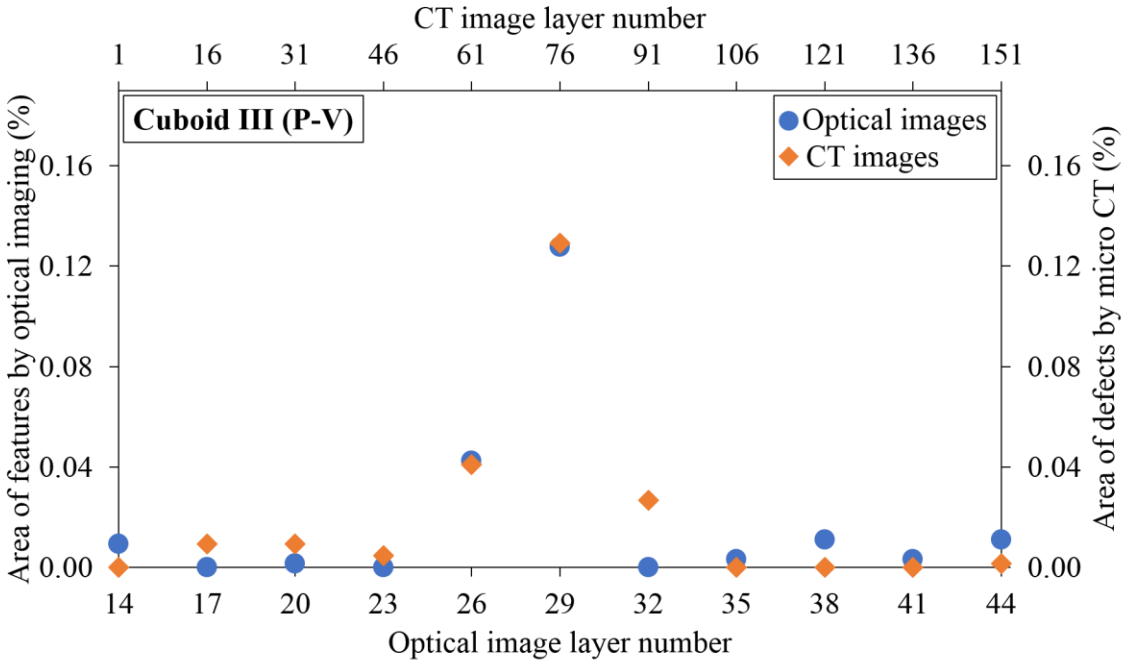

Figure E3 Area of features and defects across each layer for cuboid III (in percentages).

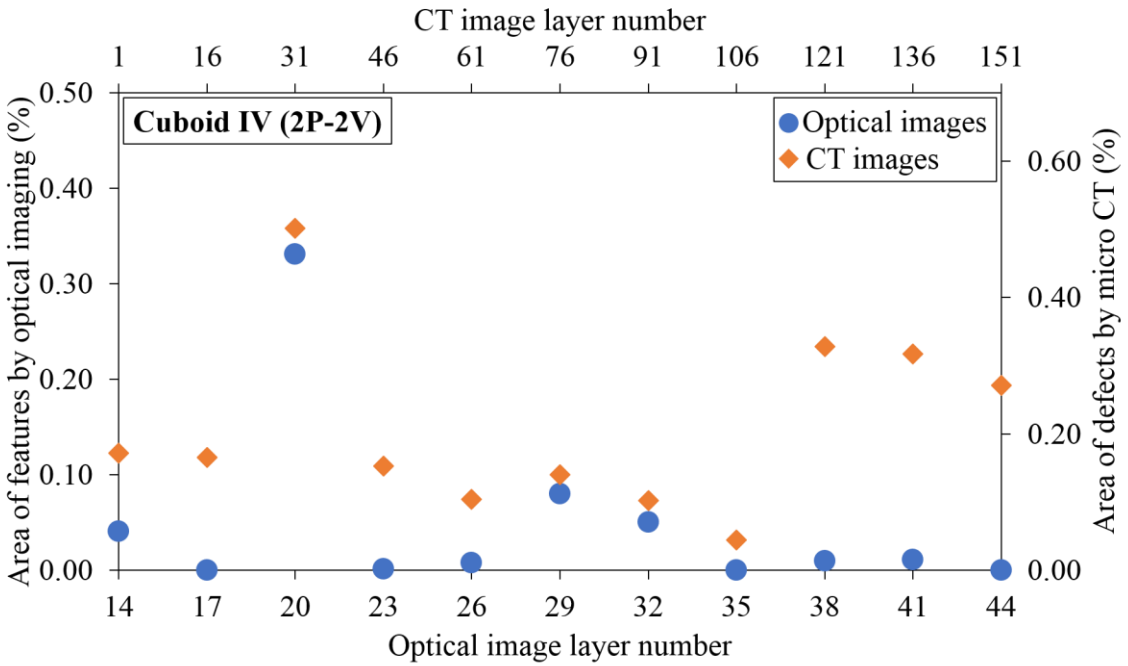

Figure E4 Area of features and defects across each layer for cuboid IV (in percentages).

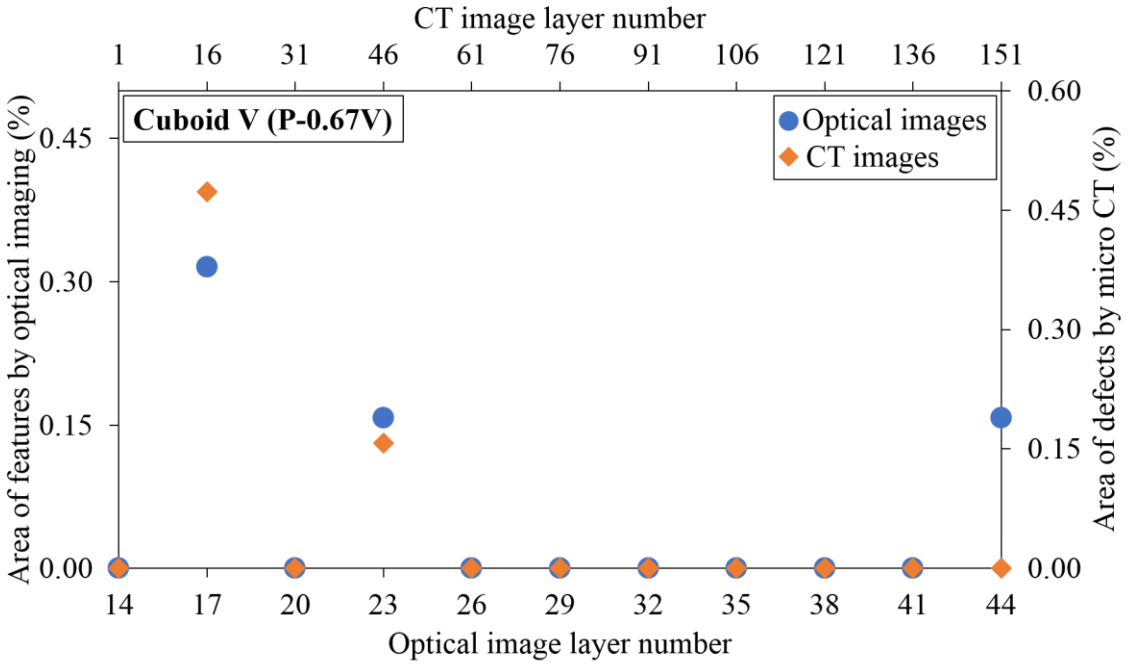

Figure E5 Area of features and defects across each layer for cuboid V (in percentages).

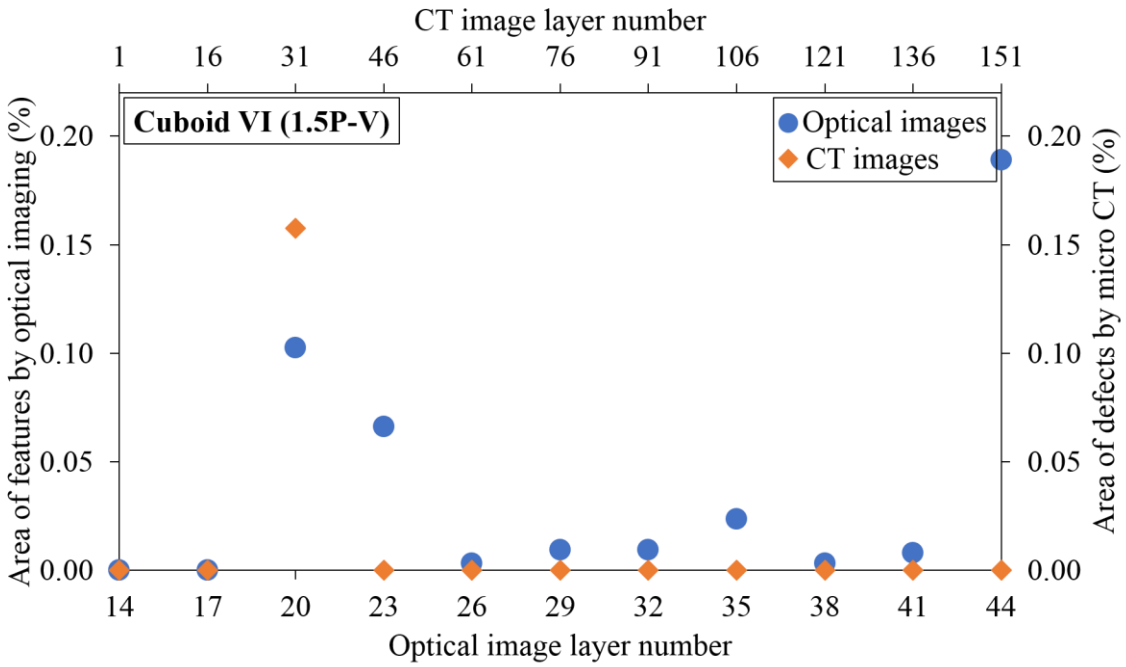

Figure E6 Area of features and defects across each layer for cuboid VI (in percentages).

The proposed image processing algorithms for optical and CT images have been proven valid. This is supported by the Pearson correlation coefficient results which signify a positive correlation between $OP_{features}$ and $CT_{defects}$ for all six cuboids. End users are therefore able to directly evaluate the area of defects present in parts based on real-time analysis of optical images. The results based on CT images, which is used to substantiate the viability of the proposed optical IMS as a means of defects indication, is well represented by the results based on optical images. This eliminates the need for long hours of defects detection in printed parts by CT.

APPENDIX F: GRAPHS AND 3D VOLUMETRIC MODELS OF PRINTED CYLINDERS

The percentage area of features present in optical images and the percentage area of defects detected by micro CT for cylinders I to III and V to IX are illustrated in Figures F1 to F8.

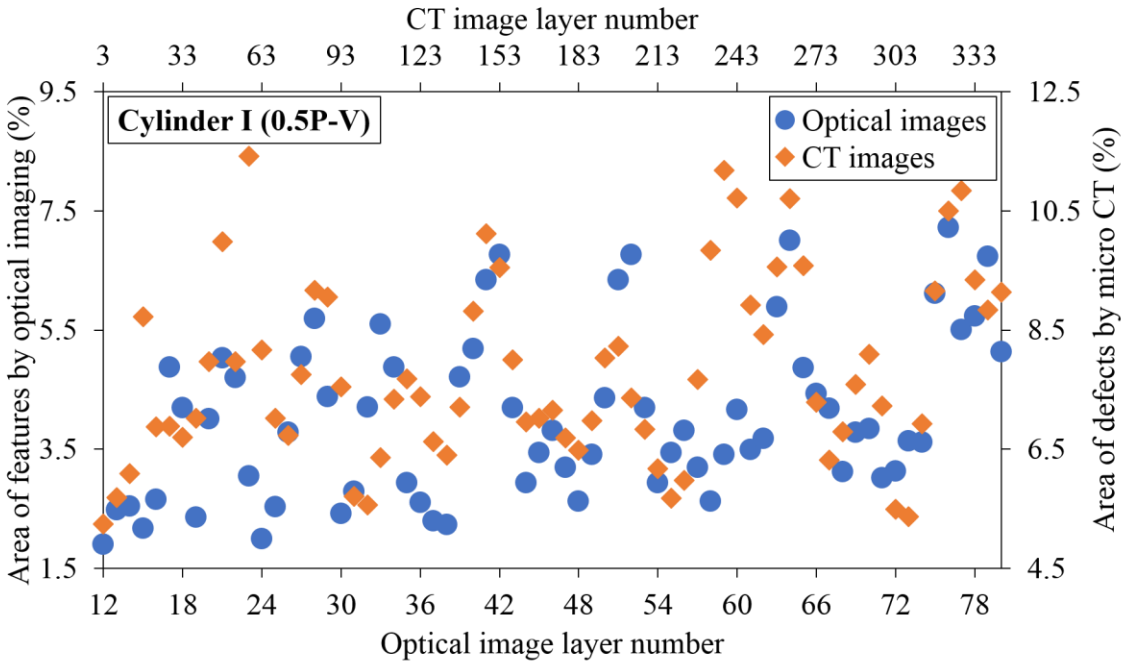

Figure F1 Area of features and defects across each layer for cylinder I (in percentages).

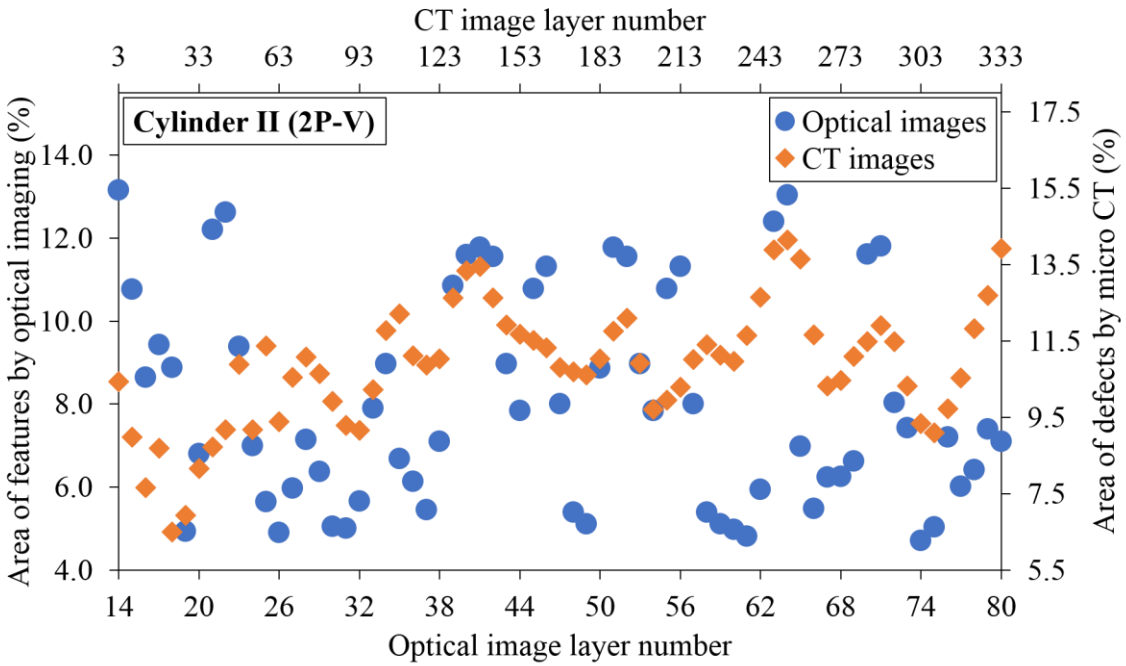

Figure F2 Area of features and defects across each layer for cylinder II (in percentages).

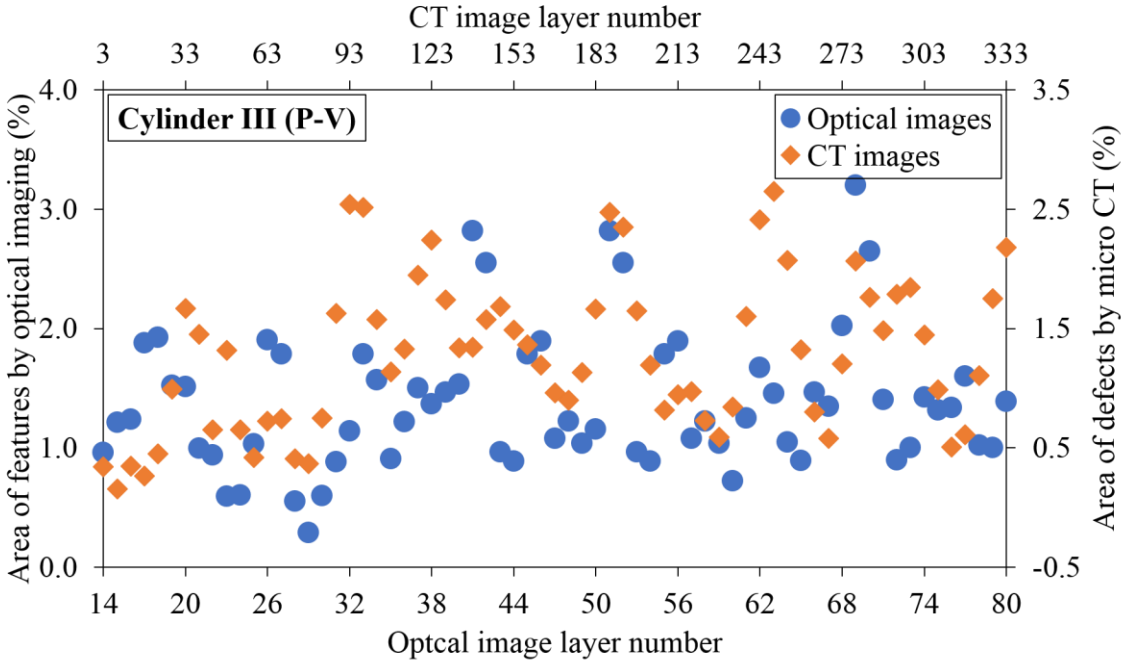

Figure F3 Area of features and defects across each layer for cylinder III (in percentages).

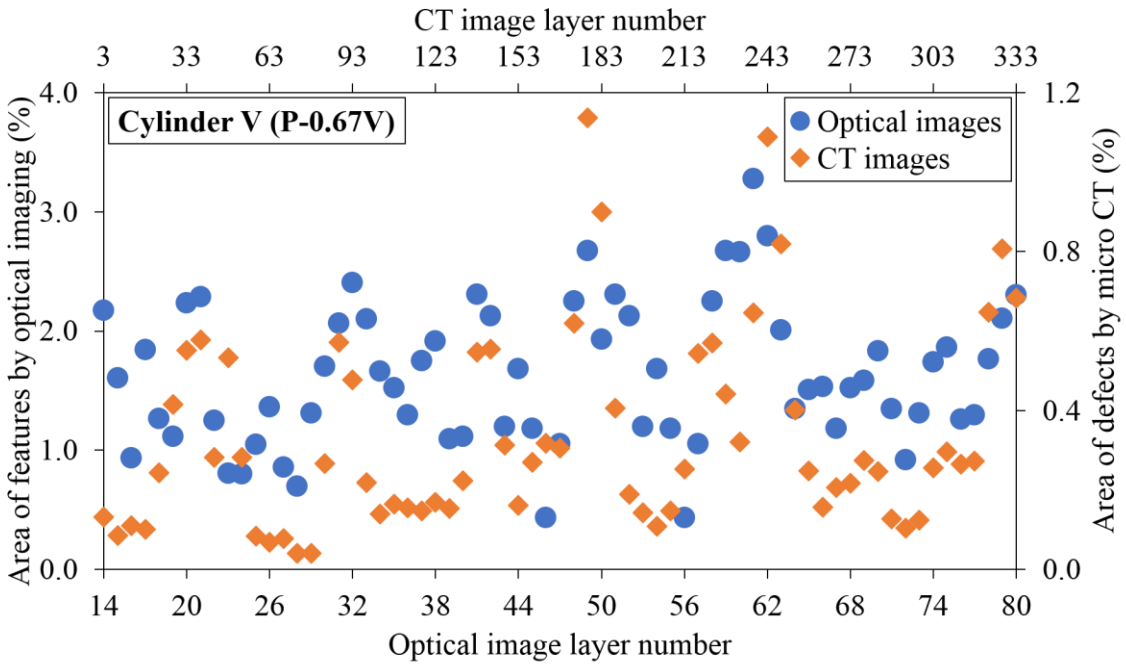

Figure F4 Area of features and defects across each layer for cylinder V (in percentages).

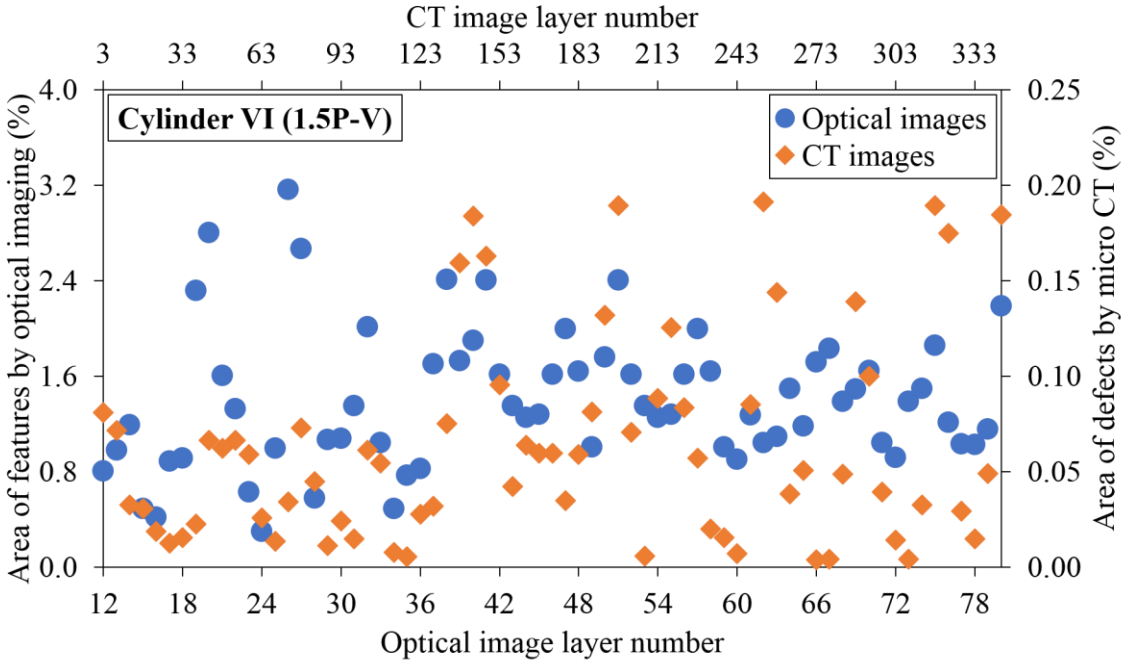

Figure F5 Area of features and defects across each layer for cylinder VI (in percentages).

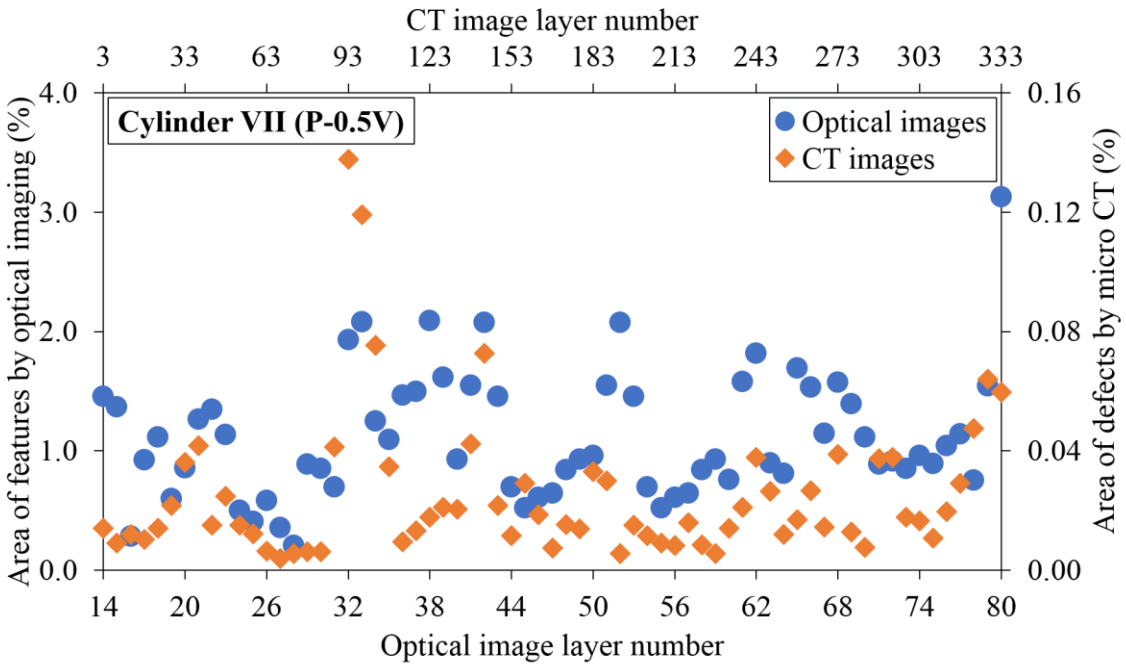

Figure F6 Area of features and defects across each layer for cylinder VII (in percentages).

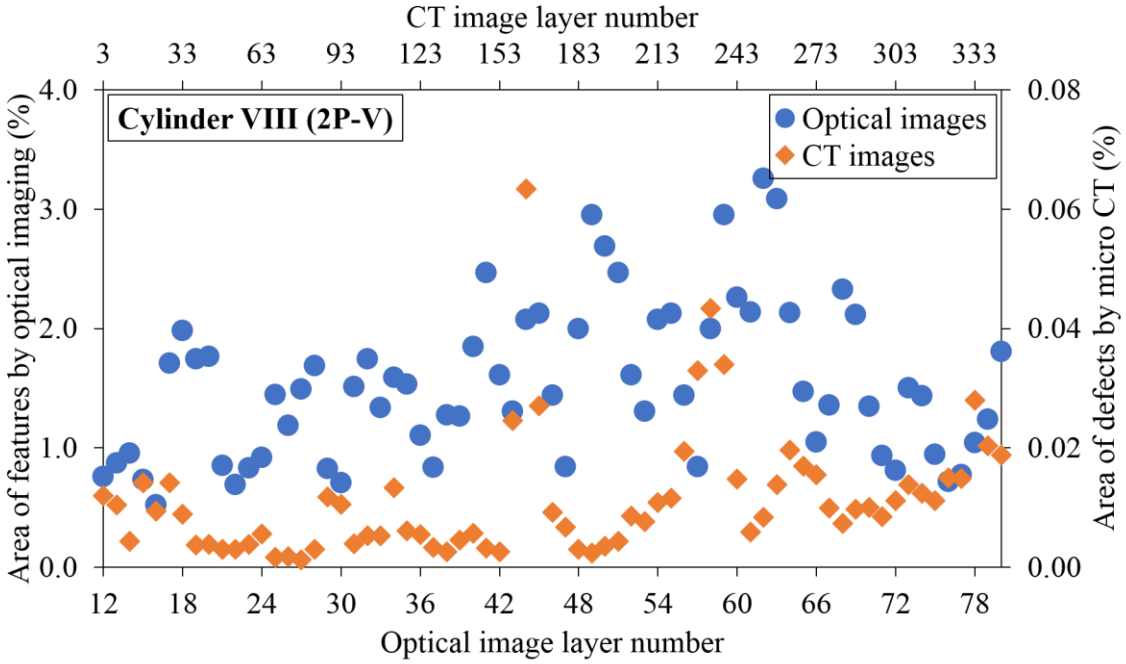

Figure F7 Area of features and defects across each layer for cylinder VIII (in percentages).

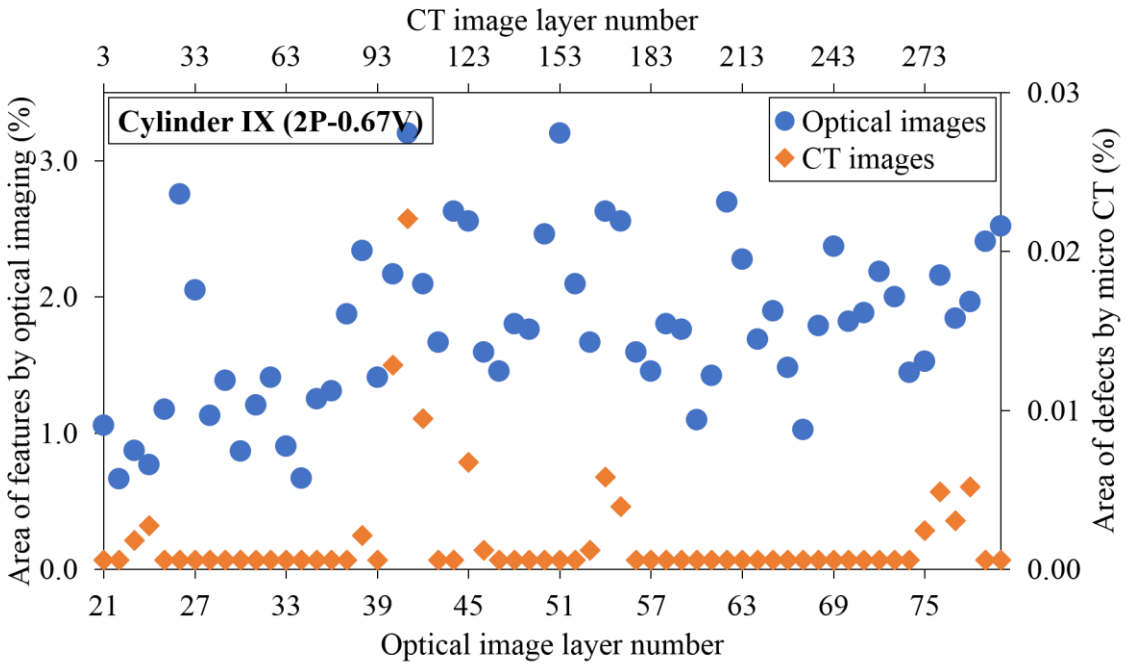

Figure F8 Area of features and defects across each layer for cylinder IX (in percentages).

The 3D volumetric models of cylinders I to III, V to VII and IX to X based on optical and CT imaging are illustrated in Figure F9. The pink regions represent the features captured

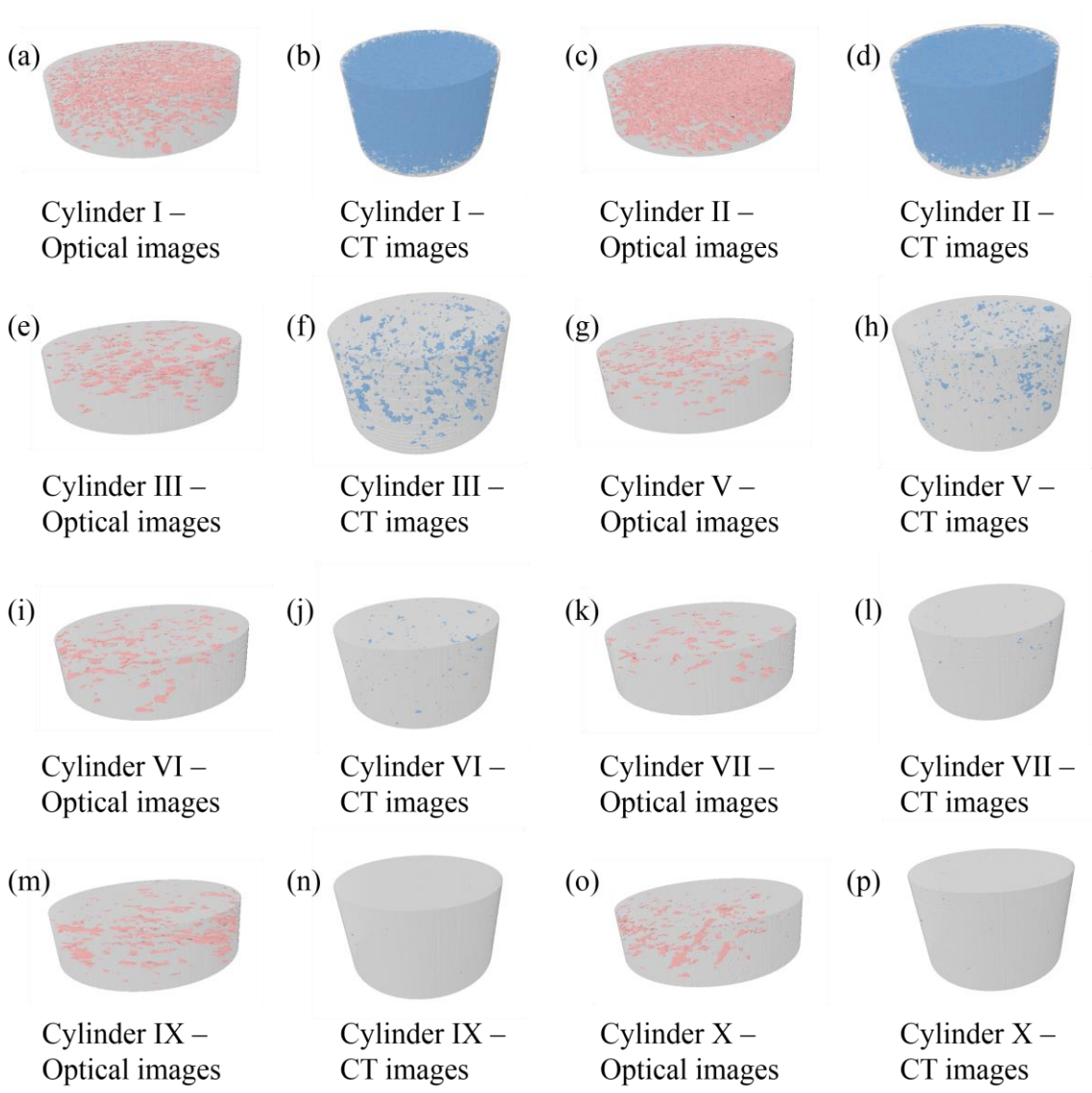

Figure F9 3D volumetric models of cylinders I to III, V to VII and IX to X based on optical images and CT images.